TUM School of Engineering and Design

Virtual development of non-crimp fabrics: numerical textile description at the scale of the filaments and forming simulation.

David Colin

Vollständiger Abdruck der von der TUM School of Engineering and Design der Technischen Universität München zur Erlangung des akademischen Grades eines

Doktors der Ingenieurwissenschaften

genehmigten Dissertation.

Vorsitzender:

Prof. Dr.-Ing. Florian Holzapfel

Prüfer der Dissertation:

1. Prof. Dr.-Ing. Klaus Drechsler
2. Prof. Dr. Philippe Boisse
3. Prof. Dr.-Ing. Horst Baier

Die Dissertation wurde am 05.07.2021 bei der Technischen Universität München eingereicht und durch die TUM School of Engineering and Design am 06.12.2021 angenommen.

Technische Universität München
TUM School of Engineering and Design
Lehrstuhl für Carbon Composites
Boltzmannstraße 15
D-85748 Garching bei München

Tel.: +49 (0) 89 / 289 – 15092
Fax.: +49 (0) 89 / 289 – 15097
Email: info@lcc.lrg.tum.de
Web: www.lrg.tum.de/lcc

ACKNOWLEDGEMENTS

First of all, I would like to express my gratitude to my supervisor Prof. Dr.-Ing. Klaus Drechsler for giving me the opportunity to work at the Chair of Carbon Composites, for the judicious advice regarding my research topic and for his continuous support throughout these years. I would also like to thank my second supervisor Prof. Philippe Boisse for the kind discussions and guidance during my research activities.

Additionally, I would like to thank in particular Prof. Assist. Dr. Sylvain Bel for his precious mentorship. He gave me a valuable support (both technical and personal) for which I will always be grateful. Our intense discussions, his pertinent questions and his constructive comments all contributed to my personal development and the quality of this work. I hope that we will have the chance to collaborate professionally once again in the near future and I will definitely keep training for our next run!

Since the beginning of my research, I had the chance to work with Dr. Thorsten Hans. Our regular technical discussions were a great chance. He gave me all tools I needed to start this work and always took time to read, correct and question my activities, which constantly pushed me forward throughout these years.

Furthermore, I am hugely grateful to Klaus Heller. He was the best colleague I could dream of, always ready to hear my doubts and to discuss my existential problems. I must also thank all the staff of the Chair of Carbon Composites, especially Andi Kollmannsberger, Benno Böckl and Ralf Knott for our friendship, the laughs and all good moments we shared. I wholeheartedly enjoyed doing my research activities at this chair, where I found faultless support, no matter the issues I was facing. I would like to thank Mathias Hartmann for his guidance in the first years of my work. I also would like to thank Swen Zaremba, a never-ending source of creativity who is constantly ready to motivate his team regardless of the challenges ahead.

My friends, in particular Sabi, Coco, Max and David, have played an important role in my life and have contributed to the completion of this work. They always brought me the motivation and forces I needed to overcome difficulties, for which I am sincerely grateful. I am also thankful to Théo for his patience, his comments and kind discussions about this work.

Last but certainly not least, I would like to express my deepest gratitude to my family, my parents and Sarah. They always encouraged and helped me towards new challenges. The completion of this work would not have been possible without their trust and continuous support.

KURZFASSUNG

Die Nachfrage nach leichteren Strukturen zur Reduzierung von Treibhausgasemissionen (bspw. im Fahrzeugbau oder in der Luftfahrt) lässt den Bedarf an kohlenstofffaserverstärkten Kunststoffen stetig steigen. Die automatisierte Herstellung trockener Preforms, die im Anschluss in Füllprozessen verarbeitet werden, hat einen signifikanten Einfluss auf die Faserorientierung innerhalb des finalen Bauteils. Ein unerwartetes Versagensverhalten kann immer dann auftreten, wenn während des Umformungsprozesses ursprünglich flacher Textilien in die endgültige Bauteilgeometrie Defekte in die Preform induziert werden. Numerische Methoden, die den Umformungsprozess simulieren (bezeichnet als Umformsimulation), können die Konstruktion der neuen Bauteile unterstützen, wobei eine umfangreiche Materialcharakterisierung unerlässlich ist, um die Modelle zu kalibrieren. Dabei ist für jede Textilart eine eigene Charakterisierung erforderlich, um mögliche Defekte während der Umformung genau vorhersagen zu können. Daher ist es unbedingt erforderlich, Ingenieuren bereits in einer frühen Entwurfsphase neuer Bauteile numerische Methoden zur Verfügung zu stellen, die den experimentellen Charakterisierungsaufwand reduzieren.

In dieser Dissertation wird ein Ansatz entwickelt, der auf zwei unterschiedlichen Modellierungsskalen basiert. Zuerst wird der Umformungsprozess trockener Textilien auf der makroskopischen Skala so modelliert, dass er auf ein ganzes Bauteil übertragen werden kann. Danach wird eine detaillierte Beschreibung der Textilarchitektur auf der Skala der Filamente implementiert, um deren Verformbarkeit vorherzusagen. Die in dieser Arbeit vorgestellten numerischen Methoden werden für biaxiale Gelege entwickelt, die aufgrund ihrer hohen mechanischen Eigenschaften, guten Handhabbarkeit und hohen Produktionsraten gerne in Hochleistungsbauteilen eingesetzt werden.

Die Umformsimulationsmethode verwendet kommerzielle Softwarelösungen, um den Umformprozess einer einzelnen Textillage zu modellieren. Unter Verwendung hinterlegter Materialmodelle werden Anpassungen vorgeschlagen, sodass die Genauigkeit der Umformsimulation trockener Textilien erhöht wird. Es werden geeignete Charakterisierungsmethoden entwickelt und eine Validierung des Ansatzes anhand einer generischen Werkzeuggeometrie vorgestellt. Zudem werden Kriterien gebildet, die die Qualität einer Preform auf Basis der Simulationsergebnisse quantifizieren. Indem die Materialeingangsparameter variiert werden, kann das optimale Verformungsverhalten Textilverstärkungen für einen gegebenen Umformprozess ermittelt werden. Somit ist es möglich, eine passende Materialauswahl vorzunehmen und den Umformprozess zu optimieren.

Es wird ein Ansatz erarbeitet, der die Modellierung einer großen Vielfalt von Gelegen auf der Skala der Filamente ermöglicht, einschließlich verschiedener Wirkarchitekturen oder Faserlagenorientierungen. Die Interaktion zwischen den Filamenten und mit dem Wirkgarn wird in der Simulation abgebildet. Eine wesentliche Neuheit ist die Einführung von Variabilität in der Orientierung der Filamente. Somit werden alle

Verformungsmechanismen eines Geleges berücksichtigt und lokale Defekte können in den Faserschichten genau modelliert werden. Diese vollständig mechanische Textilbeschreibung kann darüber hinaus auch in weiterführenden Simulationen verwendet werden, um das mechanische Verhalten des Textils vorherzusagen. Im Zuge dieser Arbeit werden Untersuchungen zum Scherverhalten sowohl in Abhängigkeit der Modellgröße, als auch der Variabilität der Filamentorientierung und des Einflusses der Wirklänge vorgestellt. Damit wird der Einfluss der Herstellungsparameter der Gelege auf das Verformungsverhalten des Textils nachgewiesen.

ABSTRACT

The demand for lighter structures, particularly within the automotive and aerospace sectors, is driving an ever-increasing need for carbon fiber reinforced plastics. For such materials, the production of dry preforms, used in automated liquid composite molding processes, is a crucial step that determines the orientation of the fibers within a component. Unfavorable mechanical behavior including dramatic failures can occur if defects are generated during the deformation of originally flat textiles into the final component geometry. Numerical methods modelling the preforming step (referred to as forming simulations) can support the design of new components. However, an extensive material characterization of each textile type is necessary to reach accurate simulation results, limiting the use of forming simulation in the early design phase of new components. Thus, it becomes essential to provide engineers with methods that can alleviate the time-consuming material characterization in order to facilitate the use of forming simulations.

This doctoral thesis proposes an approach based on two distinct modeling scales. First, the forming simulation of dry textiles is performed at the macroscopic scale to account for a whole component. Second, a detailed description of the textile architecture is implemented at the scale of the filaments to predict their deformability. The numerical methods presented in this work are developed for biaxial non-crimp fabrics, which are popular in high performance applications due to their high stiffness, good handling capabilities and high production rates.

The presented forming simulation uses commercially available software solutions to model the preforming process of a single textile ply. Adjustments of material models already implemented in the simulation software are proposed to increase the accuracy of the forming simulation. Adequate characterization methods are developed and a validation of the approach is presented using a generic tool geometry. Moreover, criteria quantifying the quality of a preform based on simulation results have been developed. A methodology to vary the material input parameters is presented, which enables deriving the optimal deformation behavior of textiles for a given preforming process.

A framework is developed to model a large variety of non-crimp fabric configurations at the scale of the filaments, including various stitching architectures and fibrous layer orientations. The interaction between filaments and with the stitching yarns is reproduced in the simulation. One major novelty is the introduction of variability in the orientation of the filaments. With this approach, all deformation mechanisms are considered and local defects in the fibrous layers can be modelled accurately. This complete mechanical textile description can be used in further simulations to predict the mechanical behavior of the textile. In this work, studies are presented on the shear behavior of the textile depending on the virtual sample size, the variability in the filament orientation and the stitching length, highlighting the influence of manufacturing parameters on the textile deformability.

Contents

Contents ix

Nomenclature xiii

List of abbreviations xix

List of figures xxi

List of tables xxix

1 Introduction 1

1.1 Motivation 1

1.2 Objectives 3

1.3 Reference textiles 4

1.4 Outline 5

2 State of the art 9

2.1 Manufacturing of composites with NCF reinforcements 9

2.1.1 Automated manufacturing processes 9

2.1.2 NCFs as textile reinforcements 11

2.1.3 Behavior of NCFs during draping 14

2.1.4 Defects of NCFs 17

2.2 Mechanical characterization of dry textiles 19

2.2.1 Friction behavior 19

2.2.2 Shear behavior 21

2.2.3 Bending behavior 24

2.3 Numerical methods for virtual textile development applied to the preforming process 26

2.3.1 Modeling the structure of dry NCFs 26

2.3.2 Simulation of the forming process 30

2.3.3 Prediction of the mechanical behavior of dry NCFs 36

3 Development of a forming simulation framework for dry NCFs 41

3.1 Selection of the approach 42

3.2 Development of the material model 42

3.2.1 Description of the *FABRIC material model 42

3.2.2 Review of bending modeling approaches with *FABRIC 43
3.2.3 Development of a bi-linear bi-material model.....45
3.3 Calibration of the material model.....49
3.3.1 Frictional behavior.....49
3.3.2 Shear behavior 53
3.3.3 Bending behavior.....56
3.4 Validation of the forming simulation approach 67
3.4.1 Forming experiment.....67
3.4.2 Simulation model.....68
3.4.3 Validation criteria 69
3.4.4 Results.....71
3.5 Conclusion.....79
4 Numerical prediction of the preform quality 83
4.1 Background 83
4.1.1 Definitions of the preform quality 83
4.1.2 Identification of defects in the simulation 84
4.2 Objectives.....85
4.3 Definition of the criteria.....86
4.3.1 Shear deformation.....86
4.3.2 Out-of-plane deformation 87
4.4 Applications 88
4.4.1 Forming simulation model.....89
4.4.2 Case study 1: influence of both shear and bending stiffness 90
4.4.3 Case study 2: influence of the shear stiffness 93
4.4.4 Case study 3: influence of the bending behavior.....97
4.5 Outcomes for textile development 100
5 Numerical description of NCFs at the microscopic scale..... 103
5.1 Investigation of the NCF fibrous layers 104
5.1.1 Distribution of the filament orientation 104
5.1.2 Size of the defects 106
5.2 Generation of the “as-manufactured” geometry.....107

5.2.1 Numerical description of the filaments 107
5.2.2 Generation of the fibrous mat 107
5.2.3 Averaged periodic boundary conditions 109
5.2.4 Stepwise model generation 111
5.2.5 Simulation parameters 113
5.3 Validation of the fibrous layers 114
5.3.1 Numerical description of NCFs with variability of the filament orientation 114
5.3.2 Comparison of the filament orientations 115
5.3.3 Comparison of the local defects 116
5.4 Calibration of the NCF thickness 120
5.4.1 Experimental compaction of the dry NCFs 120
5.4.2 Virtual compaction 121
5.5 Conclusion 124
6 Virtual shear characterization of NCFs 127
6.1 Methodology of the virtual shear characterization 127
6.1.1 Normalization of shear forces 127
6.1.2 Generation of a virtual shear deformation 128
6.2 Validation of the kinematic behavior 130
6.2.1 Shear deformation 130
6.2.2 Stitch sliding 132
6.3 Numerical investigation of the mechanical behavior 137
6.3.1 Influence of the size of the RVE 138
6.3.2 Influence of the orientation variability 141
6.3.3 Influence of the stitch length 143
6.4 Conclusion 146
7 Conclusions, potential application of the multiscale approach and future works 149
7.1 Identification of optimal deformation behaviors 149
7.2 Prediction of the shear behavior of dry NCFs 151

7.3 Potential application of the multiscale approach: example of the stitch length 153
7.4 Future applications towards virtual textile development 155
References 159
A Appendix 178
a Definition of the ROIs for the comparison of the fiber orientation 178
b *FABRIC material card of the ±45° NCF 180
c Case study 1: shear and bending input parameters of the extreme cases 182
d Case study 3: bending moment-curvature relationships 183
e Influence of the RVE size on the virtual material thickness 184
f Results of the sensitivity analysis of the virtual thickness measurement 186
g Virtual shear deformation of NCFs with 0° and 90°-layers 188
h Identification procedure of non-realistic results of the virtual shear characterization 190
B Publications 193
C Supervised student theses 195

Nomenclature

Symbol	Unit	Description
Greek letters		
α_{rope}	° or rad	Inclination angle of the rope
$\alpha_{rope,0mm}$	° or rad	Inclination angle of the rope at the beginning of the experiment
$\alpha_{rope,180mm}$	° or rad	Inclination angle of the rope at a cumulated sliding distance of 180 mm
γ	° or rad	Textile shear angle
Γ_{BB}	-	Set of design variables (Case study 3)
Γ_{DV}	-	Set of design variables
γ_M, γ_N	°	Shear angle of points M and N
Γ_{SB}	-	Set of design variables (Case study 1)
$\Gamma_{SC}.$	-	Set of design variables (Case study 2)
Δt_c	s	Critical increment size
ε	-	Strain
ε_{lock}	-	Compressive strain at the locking curvature
ε_{soft}	-	Compressive strain at the onset of the softening
θ_{layer}	° or rad	Orientation of the fibrous layer
θ_W	° or rad	Polar angle
κ	mm^{-1}	Curvature
κ_{lock}	mm^{-1}	Locking curvature
μ	-	Friction coefficient
μ_d	-	Dynamic friction coefficient
μ_s	-	Static friction coefficient
ν	-	Poisson's ratio
ρ	kg/mm^3	Density
ρ_f	g/cm^3	Density of the filaments
σ	MPa	Stress

Symbol	Unit	Description
σ_G	°	Standard deviation of the Gaussian distribution
φ_{chain}	-	Packing coefficient of filaments in a digital chain
$\bar{\varphi}_k$	° or rad	Element angle of the mesh element k
φ_{layer}	-	Prescribed FVF of the fibrous layers
Ω_{angles}	-	Set of elements used for the objective related to the surface angles.
$\Omega_{ROI}.$	-	Set of elements located in the region of interest.
Ω_{shear}	-	Set of elements used for the shear objective.
Latin letters		
A	g/m²	Areal weight of the layers
A^*	mm²	Reference area
a_B	-	Weighting factor of the objective on surface angles
A_i	mm²	Area between the deformed mesh geometry and the experimental curve of test ID i
A_{mean}	mm²	Mean value of the computed areas
a_V	-	Weighting factor of the objective on the geometry
$C_{bending}$	-	Scaling factor of the bending behavior
C_{fabric}	N.mm/mm²	Normalized shear torque
C_{shear}	-	Scaling factor of the shear behavior
C_{sM}, C_{sN}	-	Scaling factors of the normalized shear force in positive direction at points M and N
d_A	-	Normalized distance of the objective function characterizing the deformed geometry.
D_{chain}	µm	Diameter of a digital chain element
d_F	-	Normalized distances of the objective function characterizing the reaction force.
d_{frame}	mm	Crosshead displacement
$di_{C,k}$,	mm	Draw-in of corner k
di_{ratio}	-	Draw-in ratio

Symbol	Unit	Description
d_j	-	Normalized distance between the simulation result j and the reference point
d_w	mm	Distance between the center of the setup and the projected laser line
E	MPa	Elastic modulus
E_{comp}	MPa	Compression modulus of the bending behavior
E_{lock}	MPa	Compressive modulus after locking
E_{soft}	MPa	Compression modulus of the plateau
E_{tens}	MPa	Tensile modulus of the bending behavior
E_W	N.mm	Work of external forces (ABAQUS history output)
F^*	N	Reference force
f_B	° or rad	Objective related to the surface angles
F_{exp}	N	Experimental reaction force
F_{fabric}	N/mm	Normalized shear force
$F_{fabric+}$, $F_{fabric-}$	N/mm	Normalized shear force in positive and negative directions
F_{frame}	N	Force measured at the load cell
f_S	° or rad	Objective related to the shear deformation
$\widetilde{f_S}$	-	Normalized value of f_S
F_{sim}	N	Simulated reaction force measured
F_{sledge}	N	Force applied to the sledge
f_V	mm³	Objective related to the geometrical deviation
$\widetilde{f_W}$	-	Normalized objective related to the wrinkling of the preform
g	N/kg	Gravitational field
h_k	mm	Distance between the barycenter of the triangle k and the reference plane
l	mm	Width of the RVE
l_{el}	mm	Characteristic length of the mesh element
l_{frame}	mm	Distance between the pivots of the picture frame

Symbol	Unit	Description
L_{min}	mm	Smallest element length of the mesh
l_{sample}	mm	Side length of the textile sample
M	N.mm/mm	Normalized bending moment
M_{lock}	N.mm/mm	Normalized bending moment at the locking curvature
m_{sledge}	kg	Mass of the sledge
M_{soft}	N.mm/mm	Normalized bending moment at the softening point
n_{chains}	-	Number of chains to model a fibrous layer
$\vec{n}_{right}$, $\vec{n}_{left}$, $\vec{n}_{front}$, $\vec{n}_{back}$	-	Normal vectors of the elements located on the right, left, front and back of the element k
P	-	Reference plane
r_W, r_L	-	Number of repetitions of the RVE perpendicular to the machine direction and in machine direction
s_1, s_2	-	Shape functions
$S_{T,k}$	mm²	Area of the projected triangle k
t	mm	Thickness
T_{12}	N/mm²	Nominal shear stress
t_{layer}	mm	Final thickness of the fibrous layers
t_{sample}	mm	Initial thickness of the sample
u_i	mm	Displacement of node i
u_{RP}	mm	Displacement of the reference point
$u_{Shear12}$	mm	Displacement of the dummy node to apply a shear deformation to the RVE
v_{frame}	mm/min	Crosshead velocity
V_{ROI}	mm³	Volume under the elements included in region of interest
$V_{T,k}$	mm³	Volume under the triangle k
V_{Tool}	mm³	Volume under the tool surface
w	mm	Width of the RVE
W_{fabric}	N.mm/mm²	Normalized shear energy

Symbol	Unit	Description
X_{disp}, Y_{disp}	mm	Deformation of the RVE in x and y directions
z_0	mm	z-coordinate of the neutral axis
z_p	mm	z-coordinate the axis of softening

List of abbreviations

Abbreviations	Description
1D, 2D, 3D	One-, Two-, Three-dimensional
BLBM	Bi-Linear Bi-Material
CFRP	Carbon Fiber Reinforced Plastic
CPU	Central Processing Unit
DCE	Digital Chain Element
DoE	Design of Experiments
EU	European Union
FE	Finite Element
FEA	Finite Element Analysis
FEM	Finite Element Methods
FVF	Fiber Volume Fraction
KES-FB	Kawabata Evaluation Systems for Fabric Bending
LCC	Chair of Carbon Composites
LCM	Liquid Compression Molding
LHS	Latin Hypercube Sampling
NCF	Non-Crimp Fabrics
PF	Picture Frame
ROI	Region Of Interest
RP	Reference Point
RTM	Resin Transfer Molding
TUM	Technical University of Munich

List of figures

Fig. 1-1: Main steps of a preforming process with dry textiles (a) and example of stabilized preform in the production of the BMW i3 (b, adapted from [13]) 2

Fig. 1-2: NCFs selected for the development of the methods in the context of this doctoral thesis. 4

Fig. 1-3: Research activities and outline of the thesis 7

Fig. 2-1: Illustration of a Resin Transfer Molding (RTM) process adapted from [39]. 10

Fig. 2-2: Schematic of a warp-knitted NCF adapted from [48]. 12

Fig. 2-3: Modern knitting machine COP MAX 5 from Karl Mayer for the manufacture of warp-knitted NCFs [50]. 12

Fig. 2-4: Steps of the warp-knitting process (a, adapted from [52]) and common knitting patterns (b). 13

Fig. 2-5: Shear directions for a ±45° biaxial NCF (a) and example of forces required to shear the textile depending on the direction of the shear deformation (b, adapted from [57]) 15

Fig. 2-6: Local buckling of NCF filaments during shear adapted from [61]. 16

Fig. 2-7: Representative bending behavior of a dry NCF for a full load-unload pure bending cycle adapted from [64]. 17

Fig. 2-8: Local defects in the fibrous layers of NCFs: channels (a, adapted from [52]) and cracks (b, adapted from [70]). 18

Fig. 2-9: Typical defects of NCF generated during the draping process. 19

Fig. 2-10: Difference between the static and dynamic friction forces, adapted from ASTM G115-98 [86]. 20

Fig. 2-11: Usual experimental methods for the characterization of the friction behavior of textiles: inclined plane (a), sliding sledge (b), pull-out (c) and pull-through (d) methods. 21

Fig. 2-12: Details of the picture frame device and working principle of picture frame tests 21

Fig. 2-13: Working principle of the bias extension test method adapted from [103]. 23

Fig. 2-14: Illustration of the bending characterization methods proposed by Pierce in [83] for the characterization of soft materials: cantilever (a) and hanging loops (pear (b), ring (c) and heart (d) loops). 24

Fig. 2-15: Illustration of the macroscopic simulation scale for a stack with multiple layers. 27

Fig. 2-16: Illustration of the mesoscopic scale in which the layers of a NCF are modeled with continuum elements (adapted from [114]): discretization of the NCF in shell an bar elements (a) and resulting model of a rectangular NCF sample (b). 27

Fig. 2-17: Generation of mesoscopic geometries of NCFs discretizing the layers in tows without defects (a, adapted from [17]) and with defects using TexGen (b, adapted from [119]) and WiseTex (c, adapted from [69]). 28

Fig. 2-18: Discretization of a fibrous tow using the multifilament approach (a, adapted from [117]) and geometry of a woven fabric at the microscopic level (b, adapted from [124]). 29

Fig. 2-19: Isometric view of the initial geometry of a NCF at the microscopic level (a) and side view of the model before and after pretension of the stitching yarn (b) adapted from [123]. 30

Fig. 2-20: Illustration of the kinematic algorithm (a, adapted from [129]) and example of a kinematic draping result with their draping directions (b, adapted from [128]). 31

Fig. 2-21: Forming simulation of single plies of NCFs at the macroscopic scale according to Steer (a, adapted from [60]) and study of the influence of local cuts on the preforming result (b, adapted from [81]). 33

Fig. 2-22: Simulation of the forming process of a NCF ply at the mesoscopic scale with continuum elements for each fibrous layer adapted from [114]. 34

Fig. 2-23: Forming simulation results of NCFs at the mesoscopic scale with a discretization of the tows with volumetric elements (a, adapted from [116]) and shell elements (b, adapted from [123]). 35

Fig. 2-24: Forming simulation of a 3D angle-interlock textile at the microscopic scale (adapted from [160]). 36

Fig. 2-25: Virtual characterization of dry NCFs at the mesoscopic scale: bending characterization (a, adapted from [116]) and simulation of a bias extension test (b, adapted from [17]). 37

Fig. 2-26: Virtual characterization at the microscopic level with multifilament approach to study the bending (a, adapted from [121]) and shear

behavior of woven textiles (b, adapted from [124] and c, adapted from [117]). 38

Fig. 3-1: Illustration of the stress-strain relationship for a pure bending moment applied to a material with a lower compression modulus than the tensile modulus, adapted from [170]. 44

Fig. 3-2: Stress-strain relationship of the bi-linear bi-material model. 45

Fig. 3-3: Illustration of the stress-strain relationship for a pure bending moment applied to a material described with the BLBM model, in the case of $\boldsymbol{\kappa soft < \kappa < \kappa lock}$. 47

Fig. 3-4: Examples of the moment-curvature relationship according to the BLBM model for curvatures smaller than the locking curvature. 48

Fig. 3-5: Experimental method for the characterization of the frictional behavior to reduce the moment applied on the sledge. 50

Fig. 3-6: Test result of a sample representative of the friction characterization: raw measurement of the force at the crosshead (a) and calculated friction coefficient depending on the crosshead displacement (b). 51

Fig. 3-7: Results of the experimental characterization of the frictional behavior (a) and summary of the results for each configuration (b). 52

Fig. 3-8: Illustration of the picture frame test rig developed by Leutz [89] (a) and improved preparation of the test specimen (b). 53

Fig. 3-9: Results of the shear characterization in positive (a) and negative (b) shear directions with respective mean curves. 55

Fig. 3-10: Working principle of the bending tests for material calibration: sample preparation (a) and successive steps of the experiment (b) to (d). 57

Fig. 3-11: Experimental bending test setup for the calibration of the bending behavior of dry textiles. 58

Fig. 3-12: Final configuration of a bending experiment with a ±45° NCF sample. 58

Fig. 3-13: Results of the mean left/right deflection for each bending experiment and computed mean value of all experiments (a) and experimental curvature calculated with the mean result (b). 60

Fig. 3-14: Result of the DoE study implemented with 500 sets of inputs for the calibration of the bending model. 64

Fig. 3-15: Comparison of the deformed shape of the samples between the simulation result DoE_354 and the experiments. 64

Fig. 3-16: Resulting deflections (a) and bending moment-curvature relationships (b) of simulation results with various input parameters.....66

Fig. 3-17: Experimental forming setup of the hemisphere punching test bench (a) and example of a forming experiment (b).....68

Fig. 3-18: Definition of the ROIs for the comparison of the fiber orientation (a) and experimental setup with the F-Scan sensor (b).....70

Fig. 3-19: Measurement of the corner draw-in of the preform and definition of the parameters to quantify the wrinkling profile. 71

Fig. 3-20: Pictures of the finale state of the experimental forming trials used for the geometrical criteria (a to c) and illustration of the corresponding forming simulation result (d).....72

Fig. 3-21: Comparison between the reaction force on the stamp (a) and lift of the blank-holder (b) depending on the forming stroke of the experimental and simulation results. 73

Fig. 3-22: Azimuthal results of the optical measurement of the filament directions before post-treatment (a), results of the filtering (b) and final azimuthal results after post-treatment (c).....74

Fig. 3-23: Azimuthal angles in ROIs defined along the x-axis (a) and y-axis (b), along the paths defined in bias direction with positive (c) and negative shear deformations (d), and evolution of the azimuthal angle at ROI 24 depending on the forming stroke (e).....76

Fig. 3-24: Comparison of the corner draw-in of the experimental and simulation results.....77

Fig. 3-25: Distance between the axis of the stamp and the contour of the outer surface of the preform at a height of 21 mm: experimental (a to c) and simulation results (d). 79

Fig. 4-1: Illustration of fiber waviness generated in thick preforms at the corner (a, adapted from [187]) and in the flat region of a CFRP part (b, adapted from [193]). 84

Fig. 4-2: Calculation of the volume under the mesh elements in order to identify large wrinkles (a) and definition of the normal vectors used to compute element angles (b).....88

Fig. 4-3: Illustration of the forming process with the “Pole Peak” stamp geometry. 89

Fig. 4-4: Simulation results of the reference configuration. 90

Fig. 4-5: Results of the normalized objective functions for shear deformations (a) and wrinkling (b) from case study 1, depending on the shear and bending scaling factors. 91

Fig. 4-6: Forming simulation results of four configurations close to the boundaries of the design space. 93

Fig. 4-7: Shear behavior of the reference configuration (a), definition of the shape functions (b) and examples of shear curves generated with two sets of scaling factors (c). 95

Fig. 4-8: Results of the normalized objective functions for shear (a) and wrinkling (b) from case study 2, focusing on the shape of the input curves of the shear behavior. 96

Fig. 4-9: Forming simulation results obtained with two extreme couples of scaling factors. 97

Fig. 4-10: Results of the normalized objective functions for shear (a) and wrinkling (b) from case study 3, focusing on the influence of the non-linear bending behavior. 98

Fig. 4-11: Forming simulation results of four configurations close to the boundaries of the design space with identification of the elements for which the bending softening is reached in the final state of the forming process. 100

Fig 5-1: Local deviation of the filament orientation from the layer orientation on the 0°/90° NCF (a and b) and ±45° NCF (c and d) with identification of the local defects. 105

Fig. 5-2: Probability density of the deviations of the local filament orientation from the layer orientation. 105

Fig. 5-3: Measurement procedure of the defect size of a channel (a) and crack (b). 106

Fig. 5-4: Resolution of the interpenetration in fibrous layers including variability in the filament orientation. 108

Fig. 5-5: Fibrous layers homogeneously generated without variability of the filament orientation (a) as well as with Gaussian distributed filament orientation featuring standard deviations from 0.3° (b) to 3.0° (d). 109

Fig. 5-6: Regular rectangular mesh defined at the boundary of the RVE with corresponding reference points and contact surfaces. 110

Fig. 5-7: Flowchart of the automated framework for the stepwise generation of the “as-manufactured” geometry. 112

Fig. 5-8: Detailed view of the stepwise generation of the “as-manufactured” geometry. 112
Fig. 5-9: Illustration of the packing coefficient of filaments in a digital chain. 113
Fig. 5-10: Elementary RVEs of the “as-manufactured” geometries of a 0°/90° biaxial NCF using purely periodic chains (a) as well as with increasing standard deviations of the sampling (b to d). 115
Fig. 5-11: Elementary RVE of the “as-manufactured” geometry of the ±45° NCF. 115
Fig. 5-12: Comparison of the DCE orientation (Sim.) with the measurement on the samples (Exp.) of the 0°/90° (a) and ±45° NCFs (b). 116
Fig. 5-13: Comparison of the overall defect formation in the 0°-layer (a) and 90°-layer (b) between the 0°/90° NCF samples (left) and simulation results (right). 117
Fig. 5-14: Comparison of the overall defect formation in the 45°-layer (a) and -45°-layer (b) between the ±45° NCF samples (left) and simulation results (right). 118
Fig. 5-15: Comparison of the defect width (a) and length (b) between the measurements performed on the NCFs samples and on simulation results. 119
Fig. 5-16: Experimental setup to measure the thickness at 1.0 kPa of the reference NCFs 121
Fig. 5-17: Results of the virtual thickness measurement of the 0°/90° NCF. 123
Fig. 5-18: Results of the virtual thickness measurement of the ±45° NCF. 123
Fig. 6-1: Identification of the RVE deformation in $\boldsymbol{x}$ (a) and $\boldsymbol{y}$ (b) directions of a ±45° NCF in the case of positive (orange) and negative (blue) shear deformations. 129
Fig. 6-2: Simulation results of the ±45° NCF modeled with a 2x2 RVE before deformation (a), at a negative shear angle of -30° (b) and at a positive shear angle of +30° (c). 131
Fig. 6-3: Results of the virtual shear deformation of the NCF for positive and negative shear deformations. 132
Fig. 6-4: Illustration of the experimental setup (a), front face of the NCF with uncolored stitching yarns (b) and back face with colored regions of the stitching yarns before testing (c). 133
Fig. 6-5: Original microscope picture (a), segmented image after opening (b) and subsequent closing operations (c). 134

Fig. 6-6: Image analysis (raw picture (a), image after post-treatment (b) and fitted ellipse (c)) of a same stitch segment before testing (i.e. 0° shear angle), at 10° and 27° shear angle. 135

Fig. 6-7: Comparison between the measured sliding distance and the theoretical segment elongation depending on the shear angle. 135

Fig. 6-8: Measure of the numerical stitch sliding of the simulation results: reference length (a) and corresponding lengths at a shear deformation of 15° (b) and 30° (c). 136

Fig. 6-9: Comparison between the experimental and numerical stitch sliding distance. 137

Fig. 6-10: Examples of the RVEs generated in order to study the influence of the RVE size on the shear behavior: 1x1 (a), 3x3 (b) and 5x5 RVEs (c). 138

Fig. 6-11: Normalized shear torque measured at a shear deformation of 11.5° in positive (a) and negative (b) directions depending on the RVE size. 140

Fig. 6-12: Evolution of the shear asymmetric ratio depending on the RVE size. 140

Fig. 6-13: Virtual NCFs (before virtual shear characterization) generated with various standard deviations of the Gaussian distribution used to sample used to sample the orientation of the digital chains. 141

Fig. 6-14: Normalized shear torque measured at a shear deformation of 11.5° in positive (a) and negative (b) directions depending on the standard deviation used to sample the orientation of the chains modeling the fibrous layers. 143

Fig. 6-15: Evolution of the shear asymmetric ratio depending on the standard deviation used to sample the orientation of the chains modeling the fibrous layers. 143

Fig. 6-16: Virtual NCFs (before virtual shear characterization) with a constant stitch gauge of 5.08 mm and stitch lengths of 1.1 mm (a), 2.2 mm (b) and 4.4 mm (c). 144

Fig. 6-17: Normalized shear torque measured at a shear deformation of 11.5° in positive (a) and negative (b) directions depending on the stitch length. 145

Fig. 6-18: Evolution of the shear asymmetric ratio depending on the stitch length. 146

Fig. 7-1: Results of forming simulations using the virtual shear characterization to generate the shear input parameters of NCFs with various stitch lengths. 154

Fig. 7-2: Criteria measuring the quality of the preform of forming simulations using the virtual shear characterization to generate the shear input parameters of NCFs with various stitch lengths. 155

Fig. A-1: Identification of the ROIs for the comparison of the fiber orientation at the surface of the textile samples from the forming experiments. 178

Fig. A-2: Shear input curves of the case study 1 calculated with the extreme values of the shear scaling factor $\boldsymbol{Cshear}$ 182

Fig. A-3: Bending-moment relationships of the case study 1 calculated with the extreme values of the bending scaling factor $\boldsymbol{Cbending}$. 182

Fig. A-4: Bending moment-curvature relationships of the four sets of input parameters used in section 4.4.4 and of the reference configuration (resulting from the calibration presented in chapter 3). 183

Fig. A-5: Thickness at 1.0 kPa of the 0°/90° NCF (a) and ±45° NCF (b) depending on the area of the RVE 185

Fig. A-6: Results of the virtual thickness measurements for each repetition and configuration of the 0°/90°NCF listed in Tab. A-5. 187

Fig. A-7: Results of the virtual thickness measurement for each repetition and configuration of the ±45°NCF listed in Tab. A-5. 187

Fig. A-8: Identification of the RVE boundaries (a), as well as $\boldsymbol{x}$ and $\boldsymbol{y}$ deformations of the back face of a NCF with 0° and 90°-layers for an applied shear angle $\boldsymbol{\gamma}$ 188

Fig. A-9: Examples of tensile stresses during virtual shear characterization and ratios between the 99.5th percentile and the maximum tensile stress in the respective models. 190

Fig. A-10: Example of spurious localized stresses at the corner of a simulation result during virtual shear characterization. 191

List of tables

Tab. 1-1: Technical data of the “0°/90° NCF” and “±45° NCF”. 5

Tab. 3-1: Parameters of the BLBM model for the generation of the bending moment-curvature relationships illustrated in Fig. 3-4. 49

Tab. 3-2: Summary of the results of the friction characterization. 53

Tab. 3-3: Experimental parameters of the shear characterization. 54

Tab. 3-4: Test results of the bending experiments according to the selection criterion 59

Tab. 3-5: Input parameters of the structural model of the indirect bending calibration 62

Tab. 3-6: Boundaries of the optimization variables for the indirect characterization of the bending model. 63

Tab. 3-7: Input parameters of the set DoE_354 and results of the objective functions 65

Tab. 3-8: Input parameters of selected sets of the DoE study, corresponding normalized distances of the objective functions and Euclidian distance to the reference point. 65

Tab. 3-9: Summary of the bending characterization with the BLBM bending model. 67

Tab. 3-10: Input parameters for the validation of the simulation approach. 68

Tab. 3-11: Results of the corner draw-in and corresponding draw-in ratios. 77

Tab. 4-1: Simulation parameters of the forming process with a “Pole Peak” stamp geometry. 89

Tab. 4-2: Results of the objective functions for the reference configuration. 90

Tab. 4-3: Extreme results of the objective functions for the set of design variables $\boldsymbol{\Gamma SB}$ (application case study 1). 91

Tab. 4-4: Extreme results of the objective functions for the set of design variables $\boldsymbol{\Gamma SC}$ (application case study 2) 96

Tab. 4-5: Boundaries of the design variables (application case study 3) 98

Tab. 4-6: Extreme results of the objective functions for the set of design variables $\boldsymbol{\Gamma BB}$ (application case study 3) 99

Tab. 4-7: Parameters of the BLBM model of the four configurations illustrated in Fig. 4-11. 99

Tab. 5-1: Size of the local defects measured on the NCFs. 106
Tab. 5-2: Input parameters for the numerical description of the NCFs 114
Tab. 5-3: Measured local defects on the simulation results. 119
Tab. 5-4: Experimental gap thickness at a compaction pressure of 1 ± 0.01 kPa....121
Tab. 5-5: Boundaries of the numerical parameters for virtual thickness measurement....122
Tab. 5-6: Definition of the coefficients $\boldsymbol{\varphi layers}$ and $\boldsymbol{\varphi chain}$ for the simulation of the reference NCFs according to the experimental and virtual investigations of the textile thickness. 124
Tab. 5-7: Summary of the input parameters for the simulation of the "as-manufactured" geometries of the reference NCFs with adequate defect and thickness description....125
Tab. 6-1: Configurations and respective results of the numerical study on the influence of the RVE size on the shear behavior of the ±45° NCF.....140
Tab. 6-2: Configurations and respective results of the numerical study on the influence of the orientation variability on the shear behavior of the ±45° NCF. 142
Tab. 6-3: Configurations and respective results of the numerical study on the influence of the stitch length on the shear behavior of the ±45° NCF. 145

Tab. A-1: Coordinates of the ROIs 179
Tab. A-2: Parameters of the BLBM model of the four configurations illustrated in Fig. 4-11. 183
Tab. A-3: RVE configurations used to investigate the influence of the RVE size on the virtual textile thickness. 184
Tab. A-4: Input parameters of the simulation for the investigation of the influence of the RVE size on the textile thickness. 185
Tab. A-5: Detail of the configurations for the parametric analysis of the virtual thickness. 186

1 Introduction

Environmental initiatives have become increasingly important in our societies. The European Union (EU) defined a clear environmental strategy in its European Green Deal in order to significantly reduce the greenhouse gas emissions by 2030 [1, 2] and to achieve a climate-neutral EU by 2050. A broad action plan has been established to support this strategy, affecting all economic sectors. Among them, the fuel combustion of the transport industry, being responsible for 22% of the total CO2-equivalent emissions in the EU in 2017 [3], has a major role to play in the fulfillment of the objectives set in the European Green Deal. Although the development of CO2-free energies and of alternative fuels is key to improve the sustainability of the transport industry, the use of light structures contributing to the reduction of the fuel combustion is a key aspect towards a clean mobility [4].

Due to its unique lightweight potential, the introduction of Carbon Fiber Reinforced Plastic (CFRP) in structural applications has been constantly increasing over the last decades. It was identified as a promising substitute to reduce the weight of vehicles and thus of the greenhouse gas emissions [5]. In the aerospace industry, CFRP crossed the symbolic 50% weight share of the materials used in aircrafts with the Airbus A350XWB [6] and Boeing B787 Dreamliner [7]. In addition, this material is extensively used in automotive structural parts. The example of the BMW i3 is a breakthrough in the automotive industry, within which CFRP components represent almost 50% of the total weight of the life-module structure [8]. Finally, CFRP is gathering interest for further application sectors, such as in energies, maritime transport, electronics and for the onboard hydrogen storage with pressure vessels in aircrafts and vehicles [9, 10].

1.1 Motivation

The increasing demand for CFRP components requires high production rates and, therefore, challenges the traditional manufacturing techniques in terms of quantity and reproducibility. An answer to these challenges is the use of dry carbon reinforcements in automated processes instead of manual processes [11], which are still widespread in the production of CFRPs (about 32% of the market size in 2019, as reported in [9]). Liquid Compression Molding (LCM) processes have proven their compatibility with a high degree of automation [12]. For LCM processes, carbon fibers are usually processed into textiles to increase the production rates of CFRP components. The draping of the carbon fiber reinforcement textiles into the final shape of the part is a key operation to reach a high structural performance. The main steps of the draping process are illustrated in

Fig. 1-1a starting from the dry textiles until the final preform. An example of the result of a draping process with dry carbon fibers for the production of the BMW i3 is shown in Fig. 1-1b.

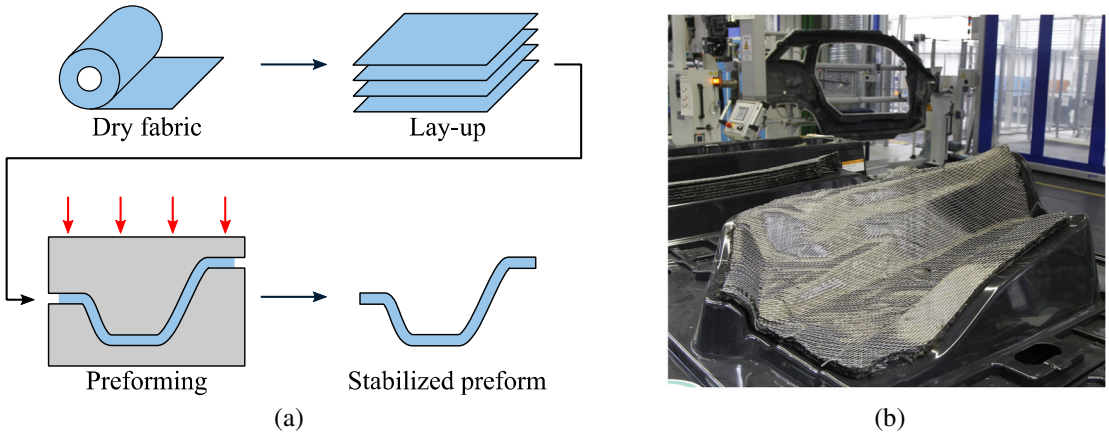

Fig. 1-1: Main steps of a preforming process with dry textiles (a) and example of stabilized preform in the production of the BMW i3 (b, adapted from [13])

Due to the high anisotropy of fiber reinforced materials, the orientation and rectitude of the filaments are crucial for the performance of the final part. Various preforming processes using rigid or flexible tools can be selected depending on the textile type and on the complexity of the targeted component. Additional components such as grippers or blank-holders can help to reduce the defects during the draping process [14]. Even though different actions can improve the quality of the preforming process, their implementation with an experimental "trial and error" approach induces high development and material costs.

The quest for stiffer and lighter parts requires adapted reinforcement textiles. Multilayer multiaxial Non-Crimp Fabrics (NCFs) are very attractive to the automotive industry [15]. They are constituted of single or multiple unidirectional fibrous layers bound together with a binding yarn (usually referred to as "stitching yarn"), which enables tailoring the stiffness and strength of the laminate. Compared to woven fabrics, the undulation of the fibers is considerably reduced, leading to superior mechanical performance while offering comparatively good handling capabilities [16]. Moreover, the current manufacturing techniques of NCFs enable high production rates, which makes them even more attractive for use in large volume applications. However, the introduction of the binding yarn induces complex deformation mechanisms during the draping of flat textiles into the desired part shape [17]. The relative importance of these mechanisms varies for each individual NCF configuration, resulting in a different deformability of each textile [18]. For instance, the compaction, shear or bending behavior of the NCF may vary depending on the textile architecture [19, 20]. The shear deformability is a key factor in adapting to geometries with a double curvature, whereas the bending stiffness of the textile strongly influences the generation of wrinkles [21]. As a consequence, each

textile behaves differently in the draping process and will result in different preform qualities [22–25].

Numerical models of the forming process can be implemented to verify the manufacturability and support the design of new composite parts. For that purpose, the preforming process is modeled, including the reinforcement material, the tooling geometry and the sequence of events. Process parameters are considered in the simulation to accurately reproduce the forming process conditions. Simulation results can predict the fiber orientations and potential defects in the preform depending on the deformation behavior of the fibrous material [26]. Thus, numerical methods can be used to develop preforming processes, to improve their robustness and to predict which fibrous structure is adequate for a given part geometry. Nevertheless, the models of the textile behavior implemented in draping simulations require intensive experimental characterization of their deformability to deliver accurate results. Due to the high variety in the deformability of NCFs, this material characterization must be performed for any change of the knitting parameters or textile architecture.

An efficient development process of new CFRP parts requires approaches that can ensure the manufacturability of the components in the early phases of the design process [27]. Since the type of textile reinforcement may not be defined at this stage of the development process, it is crucial to provide the engineers with simulation methods that predict the behavior of a large range of textiles with reduced experimental effort. In this case, predictive models of NCFs can be implemented in order to reduce the costly and time-intensive material characterization [28]. With predictive capabilities, a virtual characterization can model the deformation of the textile in detail in order to generate a deep understanding of its behavior during the draping process. Moreover, it enables studying the influence of manufacturing process parameters in a wide range. For example, the influence of the stitch length, stitch gauge or stitching pattern on the deformation behavior of the textile can be investigated numerically without expensive manufacture of textile samples.

1.2 Objectives

The aim of this doctoral thesis is to develop numerical methods to support the design of new textiles and to identify suitable textile architectures for the manufacture of a given composite component with NCF reinforcements. An approach on two distinct modeling scales is adopted.

First, the simulation of the forming process of a whole part (i.e. at the scale of the component) shall be proposed. This includes the development of a method able to predict the quality of a preform. Combined with a flexible way to model the deformability of the textile, this enables identifying the optimal deformation behavior of a textile for the forming of a given component. Second, a framework able to predict the deformability of dry NCFs shall be implemented. This includes a realistic numerical generation of the

textile geometry (i.e. at the scale of the filaments) based on its manufacturing parameters and a virtual characterization of its mechanical behavior.

In order to reach these goals, following objectives shall be achieved in this doctoral thesis:

- Forming simulation: design of an approach for the development of forming simulations for dry NCFs using simplified and flexible input parameters. This includes the application and validation of the approach with a reference NCF.
- Preform quality: development of an automated analysis of forming simulation results in order to predict the quality of the preform.
- Numerical "as-manufactured" geometry: development of a framework to predict and generate a realistic virtual geometry of the textile based on the textile manufacturing parameters. The virtual description of the NCF shall consider all relevant deformation mechanisms and local defects of dry NCFs.
- Virtual shear characterization: development of a virtual testing approach for the shear characterization of the numerically generated NCF geometries.

1.3 Reference textiles

The methods listed above shall be able to consider various NCF configurations. In order to support their development and implementation, two fabrics representative of the high variety of NCF configurations are selected:

- Biaxial 0°/90° tricot-chain stitched NCF from SGL KÜMPERS®.
- Biaxial ±45° tricot stitched NCF from SGL Group®.

The fabrics are illustrated in Fig. 1-2 and their respective characteristics are listed in Tab. 1-1. In this doctoral thesis they will be referred to as the "0°/90° NCF" and "±45° NCF", respectively.

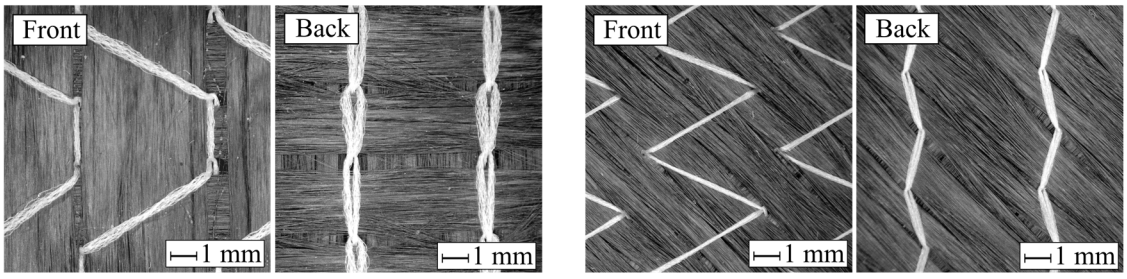

(a) 0°/90° NCF (b) ±45° NCF

Fig. 1-2: NCFs selected for the development of the methods in the context of this doctoral thesis.

These two NCFs are representative of potential differences between NCF configurations which result in different deformation behaviors. First, the orientation of the layers influences the shear behavior: ±45° biaxial NCFs show a potential asymmetric shear behavior

due to the stiffness of the stitching yarn introduced in the bias direction. Moreover, the stitching pattern may considerably influence the deformation mechanisms of the textile. Finally, the fibrous layers exhibit local defects at the stitching points with local deviation of the filament path from the theoretical layer orientation. The type and size of these defects may also have an influence on the interaction mechanisms in the textile and modify its mechanical behavior.

Tab. 1-1: Technical data of the "0°/90° NCF" and "±45° NCF".

Parameter	**0°/90° NCF**	**±45° NCF**
Designation	HPT 310 – C090 (90°//0°//P)	SIGRATEX C B310-45-ST-E214-5g
Type of fabric	Biaxial carbon NCF	Biaxial carbon NCF
Total areal density [g/m²]	300	308
Orientation of the plies [°]	0°/90°	+45°/-45°
Filament material	SGL Sigrafil CT24-4.8/240	SGL Sigrafil CT50-4.4/255
Filament count in tow [-]	24 K	50 K
Filament tensile modulus [GPa]	240	255
Filament density [g/cm³]	1.81	1.78
Stitching pattern	Tricot-chain	Tricot
Stitch gauge [needles per inch]	5	5
Stitch length [mm]	2.8	2.2
Stitching yarn	PES 7.6 tex	PES 5.0 tex

1.4 Outline

This work is divided in seven chapters. A schematic presentation of the research activities is shown in Fig. 1-3, highlighting the connections between the different chapters.

Chapter 1 introduces the motivation of this doctoral thesis and presents the overall aim of the work. It leads to the definition of four detailed objectives. Each objective will be considered in a different chapter (chapter 3 to chapter 6). Also, the textile material used for the demonstration of the numerical methods is detailed.

Chapter 2 gives an overview of the state of the art related to the global aim of the work. It focuses first on the challenges associated with the automated manufacture of CFRP with NCFs. The mechanical behavior of dry NCFs is a central part of this chapter since it influences the defects induced in the preform during the draping process. Afterwards, the experimental methods to characterize dry textiles for the development of an accurate draping simulation are analyzed and particular attention is paid to their suitability for NCFs. Then, the chapter presents numerical methods able to describe dry NCFs from the microscopic to the macroscopic scale. Their applicability to model the preforming

process and to predict the mechanical behavior of NCFs are reviewed with examples from the literature.

Chapter 3 proposes the development and validation of a forming simulation able to predict the results of the preforming process with dry NCFs in an industrial context. It includes the development of a method using commercially available models and numerical solvers to model the shear and the bending behavior of a dry NCF as well as the relevant parts of the preforming process. An appropriate experimental characterization is performed to generate the inputs for the material model and interaction parameters. The validation of the approach is proposed through forming experiments with a generic stamp geometry. Quantitative validation criteria are used to compare the simulation with the experimental results (e.g. the orientation of the fibers and the final geometry of the preform).

Chapter 4 is dedicated to the analysis of forming simulation results. Criteria and corresponding objective functions are developed to identify the shear deformation and the occurrence of wrinkles in the simulation. With this method, numerical investigations are performed to identify the influence of the material behavior on the preform quality. The shear and bending deformability of the NCFs are used as variables for parametric studies. Their impact is observed on the shear deformation and wrinkling behavior. Finally, outcomes of these investigations that should be considered in the development or selection of adequate textiles are summarized.

In **Chapter 5**, a framework able to model dry NCFs at the scale of the filaments is detailed in order to achieve predictive capabilities. The orientation variability is measured on the two reference NCFs. Based on these measurements, a method to model the “as-manufactured” geometry of dry NCFs is presented, in which the orientation of the filament may deviate from the theoretical orientation of the layer. This enables predicting the onset of local defects in the fibrous layers. An extended comparison between the numerically generated NCFs with the real material is proposed focusing on the filament orientation and size of the defects. In addition, a method to calibrate numerical parameters is introduced, using the thickness of the NCF as comparison criterion.

Chapter 6 describes the development of a virtual test bench to characterize and predict the shear behavior of a dry NCF using its virtual “as-manufactured” description at the scale of the filaments. Firstly, the kinematic behavior of the textile is validated using the orientation of the fibrous layers and the sliding of the stitching yarn depending on the applied shear deformation. Secondly, the shear torque is used to evaluate the mechanical behavior of the NCF with a focus on the predicted asymmetric shear behavior. Thirdly, the influence and importance of the variability in the fibrous layers is highlighted. Fourthly, the evolution of the shear torque and asymmetric behavior depending on the stitch length is tested virtually.

In **Chapter 7**, the work performed and the results achieved in this doctoral thesis are analyzed with regards to their respective objectives. Conclusion on the methods are

drawn and major outcomes are summarized. A connection between the developed forming simulation methods and the virtual shear characterization is proposed to highlight the potential applications of this work in the context of textile development. This chapter delivers a critical discussion on the usability of each method and associated challenges for industrial applications. Further work is proposed based on this doctoral thesis towards the vision of virtual textile development.

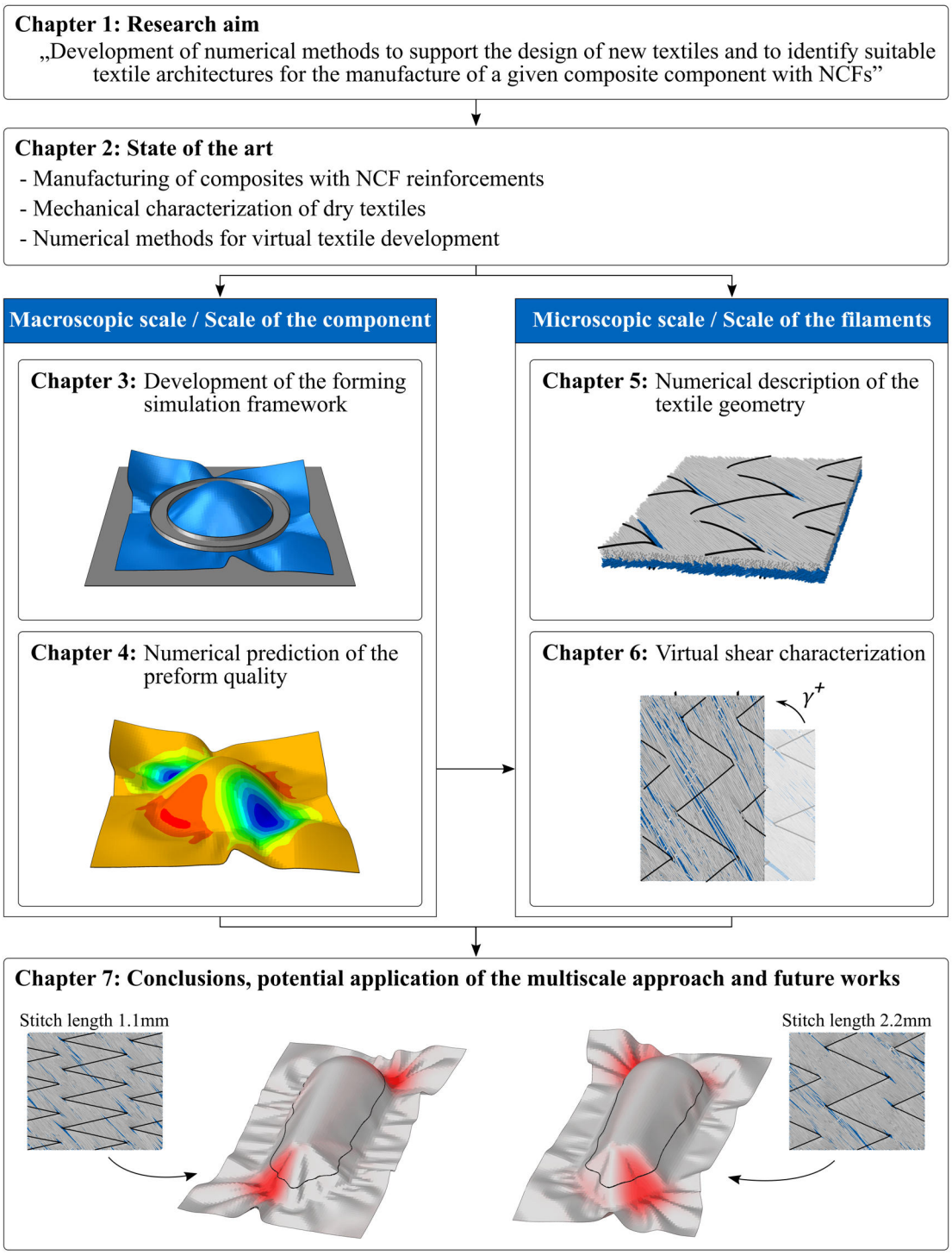

Fig. 1-3: Research activities and outline of the thesis

2 State of the art

This chapters gives an overview of all key aspects required to achieve the objectives of this doctoral thesis. First, the challenges related to the manufacture of Carbon Fiber Reinforced Plastics (CFRPs) with Non-Crimp Fabrics (NCFs) are outlined. Then, the experimental methods to characterize the friction and mechanical behavior of dry textiles for preforming applications are reviewed. Finally, the numerical methods to model dry NCFs are presented with a focus on their suitability for forming simulations and on their prediction capabilities.

2.1 Manufacturing of composites with NCF reinforcements

Composite materials are constituted of continuous or discontinuous reinforcements embedded in a matrix that protects the fibers and transfers the load between the filaments [29]. Different materials can be used for the filaments (glass, carbon, aramid, metal) depending on the required performance and type of loads applied to the structure. The high specific properties of carbon filaments make them attractive for the production of high-performance components in which the stiffness and strength are the main decision-driving factors. The most common matrix materials are types of plastics (thermoset or thermoplastics), which constitutes more than 50% of the volume in the world-wide composites market in 2019 [9]. Nevertheless, metal or ceramic matrices can be required for structures subjected to very high temperatures, such as for disk brakes [30].

A large variety of processes can be used to manufacture continuous carbon fiber reinforced plastics. Many processes were developed over the last decades to meet the requirements of each industrial field and its associated challenges. These processes range from manual processes, such as the wet lay-up widely used in the manufacture of sail planes [31] and from the use of prepregs for the aerospace industry [32], to fully automated processes of fiber reinforced thermoplastics for the manufacture of brake pedals used in electric sports car [33].

2.1.1 Automated manufacturing processes

Focusing on the automotive industry, the demand for CFRPs has constantly been increasing since their introduction in the 1950s to reduce the weight of cars [15, 34]. The associated high production volumes led to new challenges in terms of production rates. For example, the use of thermoset resins, widespread in the aerospace industry (which require curing times of many hours [35]), is not applicable to the automotive

requirements. Thus, processes with low cycle times of a few minutes per part are required [36]. The use of liquid composite molding processes offers a high degree of automatization, mandatory to meet those requirements. Among them, the Resin Transfer Molding (RTM) process used for the manufacture of BMW i3 parts relies on the use of preforms — dry fibrous material previously shaped to the final component geometry — infused with a thermoset resin and cured at high temperatures (see Fig. 2-1) [37]. High performance part can be achieved with high Fiber Volume Fraction (FVF) and good surface quality. Variants of the RTM process are described in the literature (e.g. high-pressure RTM or compression RTM [38]) to further reduce the cycle times and increase the part performance.

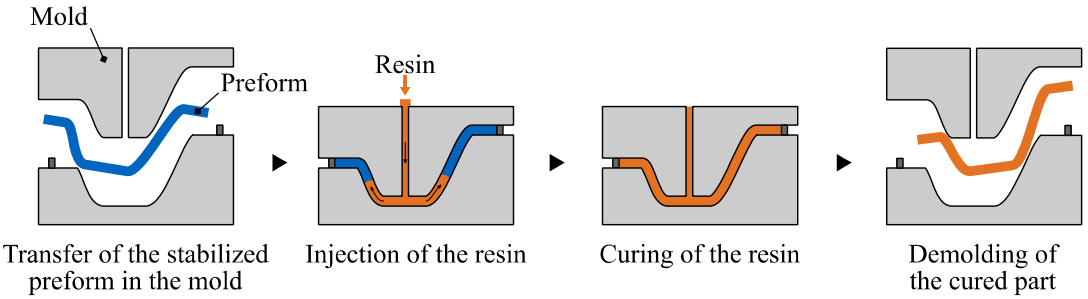

Fig. 2-1: Illustration of a Resin Transfer Molding (RTM) process adapted from [39].

All those processes rely on the use of dry preforms shaped at the geometry of the final component. One can differentiate the production of preforms in a direct or a sequential preforming process. A direct preforming, such as the braiding process, shapes the preform to its final shape in a single process. The sequential preforming mainly uses textiles that are first cut, then stacked and subsequently formed into a three-dimensional geometry close to the final component geometry. This step is usually called the “draping process”. A binding material can be applied to the textile e.g. as a powder to maintain the preform in the final shape. In this case, the binder must be activated at high temperature to diffuse the binding material in the fibrous layers. After cooling of the preforms and, thus, consolidation of the binder, the preform is stabilized. This increases the handling capabilities of the preform and facilitates its transfer to the filling station [40].

The use of textile preforming enables a parallelization of all processes and reduces the manufacturing time of single parts. Moreover, all steps of the manufacturing process can be automated as shown by the production line of the rear axle spring leaf of the Volvo XC90. A production rate of 500,000 parts per years are expected using fully automated processes [41].

2.1.2 NCFs as textile reinforcements

2.1.2.1 Definition

In order to manufacture fibrous reinforcements, rovings — group of many thousands of filaments — are bound together using different techniques to generate a planar fabric (weaving, knitting, braiding, etc.). Depending on the manufacturing processes of the textile, it results in various filament architectures that influence the stability of the preform (i.e. handling properties) and the mechanical performance of the final part. Thus, the selection of the adequate textile requires an extensive study based on the composite manufacturing process, the geometry of the component and the required lay-up. [40]

Woven fabrics are produced by the weaving of rovings. The resulting planar textiles are constituted of two perpendicular filament orientations (i.e. warp and wefts). The stability of the woven fabrics is ensured by the interlacing of the filaments. The resulting fibrous architecture exhibits an undulation of the filaments that depends on the weaving pattern. Patterns with higher entanglements increase the preform stability but reduce the performance of the part due to filament undulation. [42]

Another textile manufacturing process was introduced for the production of carbon reinforcement textiles, in which a supplementary yarn is used and knitted in different shapes to maintain the filaments. The warp-knitted multiaxial multilayer fabrics — also called Non-Crimp Fabrics (NCFs) — are the predominant type of knitted textiles used for the manufacture of composites. In this case, different unidirectional layers of filaments are bound together. Different quantities of layers with different orientations can be manufactured; unidirectional (a single layer), biaxial (two layers, usually with 0°/90° or ±45° orientation), quadriaxial (in a quasi-isotropic lay-up) or even in combination with fibrous mats (see Fig. 2-2) can be found [43]. This process enables high production rates since a large number of layers can be processed at once. Manufacturing rates up to 180 m/h are reported by LIBA Textilmaschinenfabrik GmbH [44] against a maximum of 42 m/h[1] for a woven fabric manufactured with the DORNIER P1rapier weaving machine [45]. Compared to woven fabrics, the filaments do not exhibit out-of-plane undulation, leading to higher mechanical properties of the composite parts [46]. As a consequence, NCF reinforcements have the highest share in CFRP production for structural automotive applications [47].

[1] Calculated with the maximum speed and a yarn width of 2 mm

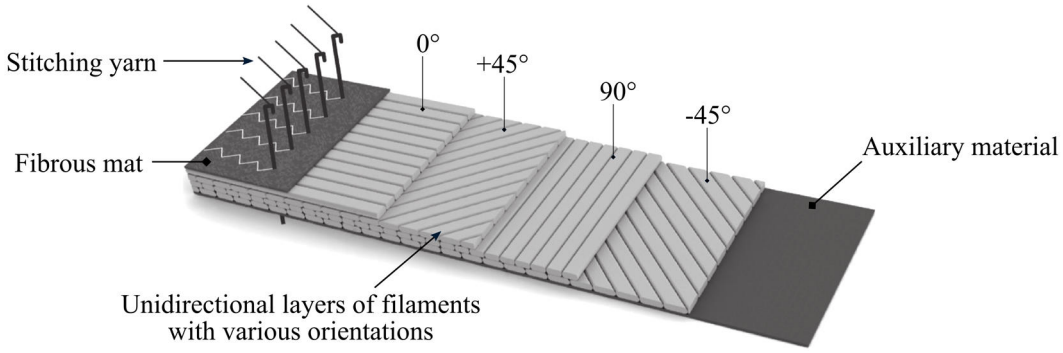

Fig. 2-2: Schematic of a warp-knitted NCF adapted from [48].

NCFs are defined according to the standard EN 13473 [49] by

- the fibrous nature of the layers and respective areal density,
- the fiber direction of the layers,
- the nature of the binding yarn and areal density,
- and the stitching pattern.

Note that the 0° direction is defined as the machine feeding direction.

2.1.2.2 Manufacturing steps

The manufacture of a NCF requires various steps that may influence the textile quality and the resulting mechanical properties of the part. A large number of patents were published on NCF manufacturing techniques. An extensive presentation and the details of these processes can be found in [48]. This subsection gives an overview of the manufacturing process steps with a focus on the warp-knitting process and modern knitting machines such as the COP MAX 5 from Karl Mayer Textilmaschinenfabrik GmbH illustrated in Fig. 2-3.

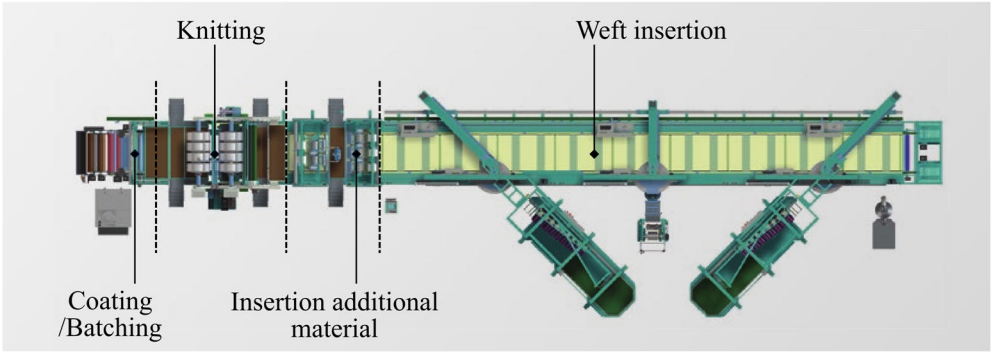

Fig. 2-3: Modern knitting machine COP MAX 5 from Karl Mayer for the manufacture of warp-knitted NCFs [50].

First, the filament rovings must be spread in flat layers to meet the desired areal weight. The use of rovings made of a large number of filaments (superior than 46k filaments – usually called “heavy tows” [51]) increases the economic efficiency of the knitting

process but requires an advanced spreading process to generate thin layers with uniform distribution of the filaments. It can be done either directly at the knitting machine or in a separate step. In the latter case, wide tapes are spread and subsequently laid on the transport chain to build the stacking sequence of the NCF with the desired fiber orientations. In the case of the use of wide tapes, special care must be taken to avoid gaps or overlaps in the process. The stack is clamped on the transport chain and moved to the knitting unit, in which the layers are bound together with a knitting yarn – often referred to as "stitching yarn". The knitting unit is constituted of movable guides and needles. The principle of the knitting process is shown in Fig. 2-4a for a warp-knitting process. In this case, the yarn is fed through a guide. The knitting needles move up and down through the textile and the guide moves simultaneously around the needles. This creates loops on the back side of the fabric in the transportation direction (i.e. in the machine direction). Different knitting patterns (usually referred in the literature to as "stitching pattern") can be produced depending on the moving sequence of the guides. Common stitching patterns used for the manufacture of NCFs are illustrated in Fig. 2-4b, showing the chain, tricot or tricot-chain patterns. A detailed description of the knitting patterns and their coding be found in [52]. At the end of the knitting process, a chemical binder can be spread directly on the textile to facilitate the handling of the future preform [53, 54].

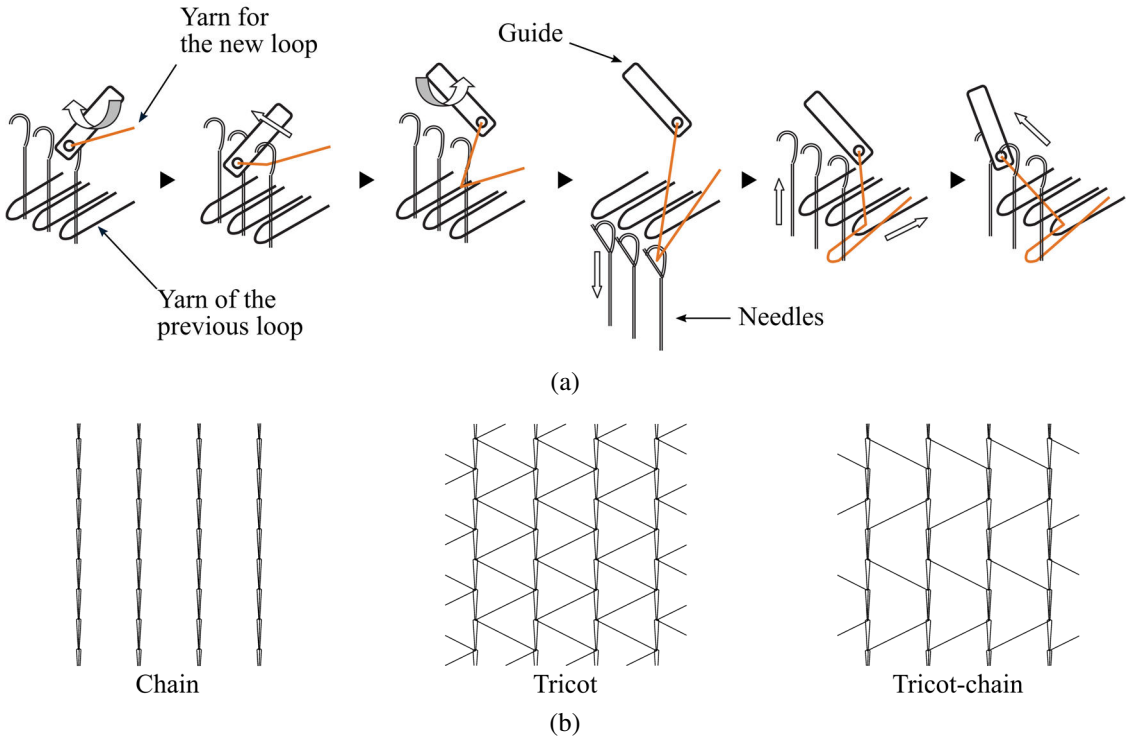

Fig. 2-4: Steps of the warp-knitting process (a, adapted from [52]) and common knitting patterns (b).

2.1.3 Behavior of NCFs during draping

2.1.3.1 Deformation mechanisms

During the draping of reinforcement textiles, the fibrous structure is subjected to complex deformations in order to adapt to the final three-dimensional geometry of the component. Due to the high stiffness of the fibers, the structure of the filament layers is modified to accommodate different geometries. In order to adapt to doubly curved surfaces, a combination of in-plane shear and bending deformation of the NCF is necessary. In addition, compaction, tensile and out-of-plane shear stresses or inter-layer sliding might be generated depending on the preforming process [55]. The introduction of the binding yarn induces complex deformation mechanisms, which influence the mechanical behavior of the textile. These global deformations of the textile are obtained through combined movements and deformations of the filaments and of the stitching yarn [17], involving various interactions that can be gathered into three groups:

- Inter-filament: relative translations or rotations of the filaments. This corresponds to interactions of filaments within the same layer and with adjacent layers.
- Inter-stitch: interaction of the stitching yarns with themselves and with the adjacent yarns due the loops that are generated during the knitting process. This leads to tension in the yarns and potential relative sliding movements.
- Stitch-to-filament: interaction between the stitching yarn and the filaments of the fibrous layers. It is responsible for the cohesion of the layers and the stability of the NCF.

The relative importance of each interaction mechanism varies for each individual NCF configuration, resulting in different deformation behaviors of the textile [18].

2.1.3.2 Shear behavior

A pure shear deformation of a NCF results from relative motions of the filaments within the layers, without elongation in fiber direction. It generates a modification of the angle between the layers, which is defined as the “shear angle”. In the case of layer orientations deviating from the machine and orthogonal directions (i.e. in the case layers different from 0° and 90°-layers), a pure shear induces a length change in the machine direction. This results in an extension or contraction of the stitching yarn loops. A shear deformation leading to an extension in machine direction is referred to as a “positive shear”. It induces a high tension in the stitching yarn to accommodate the elongation. On the contrary, a contraction in machine direction corresponds to a “negative shear” deformation [17]. As shown in Fig. 2-5a, a buckling of the stitching yarn is generally observed leading to looser loops on the back side of the textile [56]. These two types of deformations require different levels of energy, leading to a potential asymmetric shear behavior. Fig. 2-5b illustrates the difference of force required to shear a biaxial ±45° NCF

in positive and negative directions, showing a clear difference in shear forces. Maximum ratios between positive and negative shear forces of five or more can be found in the literature [18, 57, 58]. In addition, potential breakage of the stitching may be observed due to the extension of the stitching loops and induced tensile stress [56].

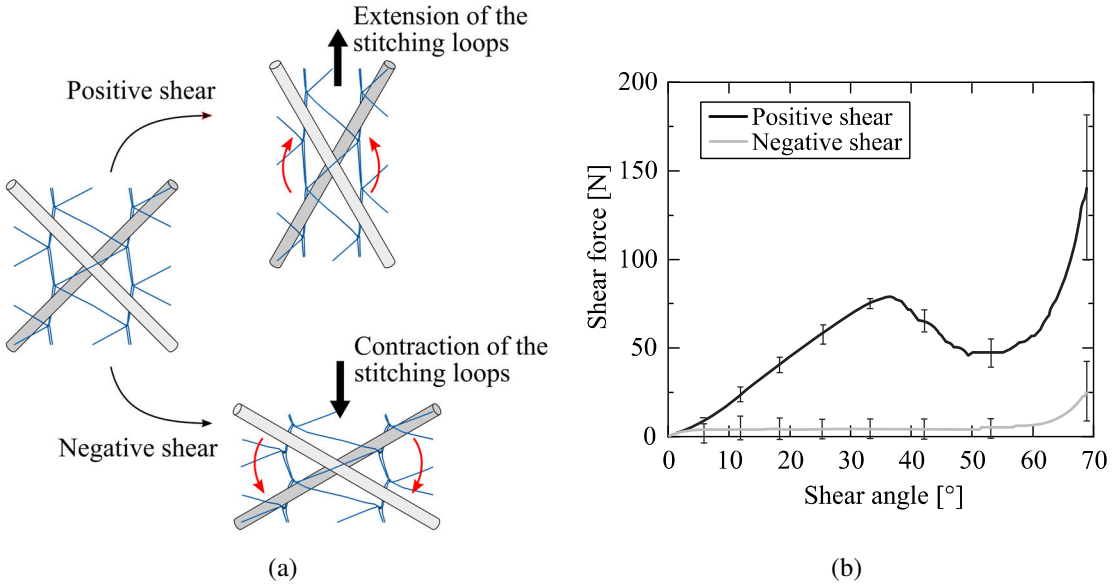

Fig. 2-5: **Shear directions for a ±45° biaxial NCF (a) and example of forces required to shear the textile depending on the direction of the shear deformation (b, adapted from [57]).**
The results shown in (b) correspond to the shear characterization of a ±45° biaxial NCF with a chain stitching pattern presented by Long et al. in [57].

While the orientation of the fibrous layers determines whether the shear behavior is potentially asymmetric, the stitching pattern significantly influences the shear behavior. This has been extensively investigated and reported in various studies. A few examples are detailed here to emphasize the interactions between the parameters of the stitching architecture and the mechanical behavior of the fabrics. Lomov et al. [18] investigated the shear behavior of two NCFs: a ±45° NCF with a tricot pattern and a 0°/90° with a tricot-chain stitching pattern. It was found that the textile with tricot-chain pattern leads to lower shear forces. It was attributed by the authors to the layer orientations and the tricot-stitching pattern that facilitate the sliding of the tows. This type of deformation was also observed experimentally by Bel et al. [23] for a 0/90° NCF with a tricot pattern. Furthermore, the influence of the stitching pattern was studied by Stolyarov et al. [59] for 0°/90° NCFs and concluded that the density of the stitching pattern increases the shear stiffness. An experimental study on the influence of the stitch length was performed by Steer [60] for a ±45°NCF with a tricot stitching pattern. He found that the forces required to shear the sample in positive direction increases with the stitching length. Moreover, he reported higher forces in negative shear than in positive shear direction for the shortest stitch length (stitch length of 1.5 mm and a stitch gauge of 5 mm).

Krieger et al. [61] and Kong et al. [62] found that the stitching parameters influence the shear force at higher shear angles only.

During the shear deformation, the thickness of the textile increases due to the reduction of the projected area. Experiments on the thickness change were performed by Lomov et al. [18], showing that the evolution of the thickness can be approximated based on a constant volume calculation for low shear angles. Nevertheless, they observed a buckling of the filaments and of the stitching yarn at high shear angles, leading to higher thicknesses than expected. Similar observations of local buckling were published by Krieger et al. [61], as illustrated in Fig. 2-6. This buckling is due to the reduction of the distance between the stitching points; and to the tension in the stitching yarn that prevents further rotation of the filaments.

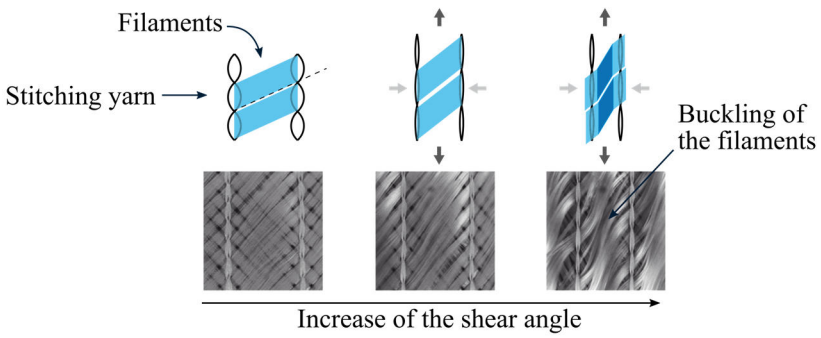

Fig. 2-6: Local buckling of NCF filaments during shear adapted from [61].

2.1.3.3 Bending behavior

The bending behavior of a dry textile significantly influences the wrinkling behavior during preforming. Boisse et al. [63] demonstrated numerically the influence of the bending behavior on the forming result. Therefore, a detailed knowledge of the bending behavior of the textile is necessary for accurate forming predictions. The bending stiffness of a dry textile is very low compared to the tensile modulus of the fibers and no direct relation can be made between them due to the potential slippage of the filaments. Various experiments were published on the bending behavior of dry NCFs. A typical result from Bilbao et al. [64] is illustrated in Fig. 2-7, in which the bending moment is measured depending on the applied curvature for full loading and unloading cycle. First, a strong non-linear behavior of the fabric can be observed in the first loading phase. Moreover, a hysteresis can be noticed since the unloading curves do not follows the loading curve. This is may be attributed to the non-reversible slippage of the filaments [19, 64–66].

Lomov et al. investigated in [19] the bending behavior of various NCFs. They observed that the stitching pattern does not directly influence the bending behavior. However, they concluded that the tightness of the filaments within the fibrous layers and any mechanism preventing their relative displacement considerably influence the bending stiffness of the NCFs, and thus their drapeability.

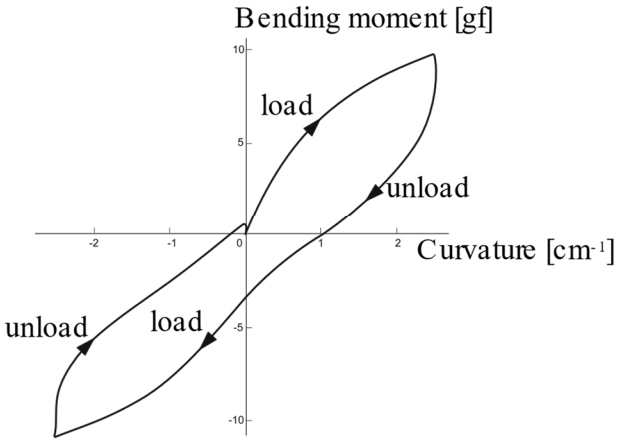

Fig. 2-7: Representative bending behavior of a dry NCF for a full load-unload pure bending cycle adapted from [64].
This experimental result was obtained with a pure bending deformation applied to a dry 2.5D carbon fabric, as presented by Bilbao et al. in [64].

2.1.4 Defects of NCFs

The high mechanical performance of CFRP structures derives from the high strength and high stiffness of the carbon filaments, whereas the matrix ensures a transfer of the load between the filaments. Therefore, the local architecture of the filaments is a key parameter to achieve a high stiffness and strength of the material. During the whole manufacturing process, from the production of the filaments until the final assembly, different operations can alter the material properties [67]. Here, a focus is put on the defects resulting from the production of the textile and from the preforming step.

Fibrous layers of NCFs exhibit local defects at the stitching points, locally deviating the filaments from their theoretical orientation. As illustrated in Fig. 2-8, the defects can be continuous gaps that connect many stitching points (referred to as “channels”) or local fish-eye distortions, commonly defined as “cracks”. These defects are generated during the knitting process when the needle penetrates the fibrous mat. The type and size of these defects may have an influence on the interaction mechanisms, modifying the mechanical behavior of the dry textile. Moreover, the local defects have an influence on filling behavior, since channels are created in which the resin can propagate faster. Finally, the resulting resin-rich regions and the local deviation of the filaments from the intended path may impact the performance and the strength of the structure. [68]

Schneider reported in [69] the classification of the defects defined by the “Airbus Industry Material Specifications” to quantify the quality of the textile during the production. Thresholds on the criteria are usually defined in material specifications and depend on the manufacturer or application fields.

A non-exhaustive list of the defects is presented hereafter:

- Defects in the fibrous mats: gaps, waviness, wrinkles, filament breakage.
- Defects related to the stitching yarns: missing loops, yarn breakage.
- External material on the textile, such as fuzz balls.

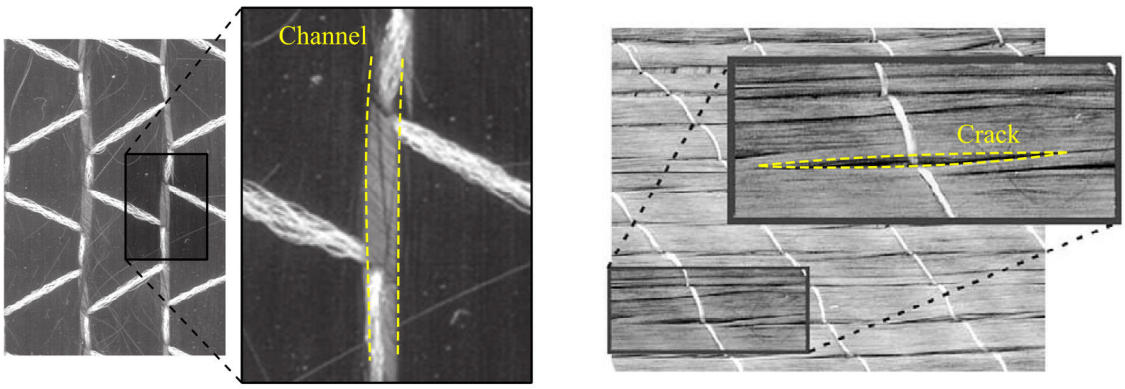

Fig. 2-8: Local defects in the fibrous layers of NCFs: channels (a, adapted from [52]) and cracks (b, adapted from [70]).

In the preforming step, the macroscopic deformation of the fabric results from relative displacements of the fibers and deformation of the stitching yarn. This may lead to local defects, such as the deviation of the filaments from their intended path. Due to the anisotropic properties of fiber reinforced textiles, the achievement of the desired final orientation of the filaments represents the main challenge of the draping process. For example, Jones showed that a deviation of 10° of the filaments in an unidirectional graphite-epoxy material leads to a stiffness reduction of more than 50% [71]. Moreover, misalignment of the filaments can change the failure mechanisms of the structure, leading to an early and unexpected failure of the component [46].

Further defects can be generated during the preforming step, as listed in [15, 23, 72–74]. Defects relevant for the development of NCF are listed hereafter and partly illustrated in Fig. 2-9:

- Wrinkles: out-of-plane deformation of the textile leading to a geometrical deviation of the preform or local accumulation of material.
- Waviness: local in-plane waviness of many filaments in the textile.
- Gaps: local absence of filaments due to compaction or distortion of the fibrous mat.
- Tow buckling: local out-of-plane buckling of many filaments between two stitching points.
- Tow sliding: sliding of a group of filaments due to a weak interaction between the stitching yarn and the filaments.
- Breakage of the stitching yarn due to high tensile stress in the yarn.

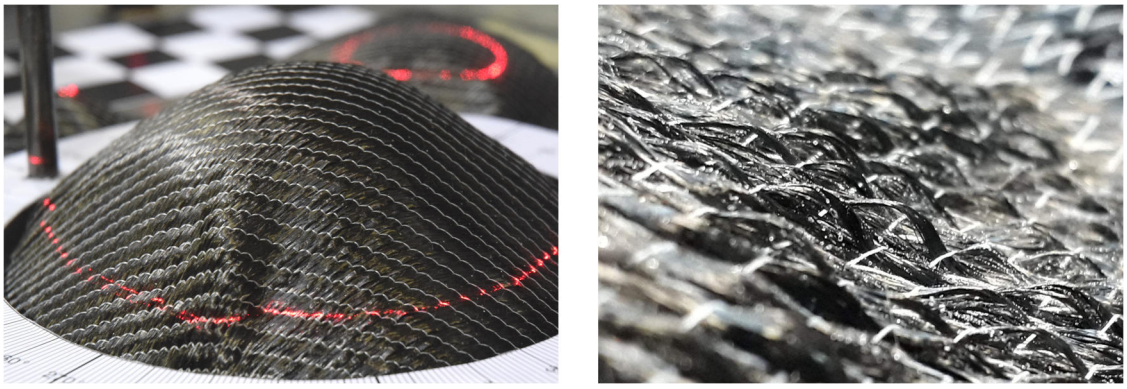

(a) Wrinkles (b) Tow buckling

Fig. 2-9: Typical defects of NCF generated during the draping process.

The occurrence of these defects depends on many material parameters, such as the fiber orientation or the stitch architecture, as shown in [22, 23, 61, 75, 76] and [S1]. Different methods can be used in the draping process to reduce them. For instance, the use of grippers, blank-holders, local stitches or local cuts in the preforms can improve the drapeability of the textile [14, 77–81].

2.2 Mechanical characterization of dry textiles

First studies aiming at the characterization of the mechanical behavior of textiles were published by Peirce. His objective was to correlate the feel of a textile material with mechanical properties that can be quantitatively investigated to support the development of new textiles [82]. With the same objective, diverse characterization methods were developed and adapted to standards (e.g. the DIN EN 53362 for the characterization of the bending rigidity [83]). Nevertheless, these methods are not always suitable for the mechanical characterization of textile reinforcements. This section proposes a review of methods to experimentally investigate the behavior of textiles in the context of the preforming process.

2.2.1 Friction behavior

The characterization of the friction behavior requires the application of a homogeneous contact pressure on the interface that is being characterized. A relative displacement between the contact pairs must be generated while the force required for the displacement is measured. Two friction coefficients can be determined according to the standard DIN EN 14882 [84] (see Fig. 2-10):

- Static friction coefficient μ_s: relation between the tangential and normal force required to initiate a relative displacement at the contact interface.
- Dynamic friction coefficient μ_d: relation between the normal and tangential force required to maintain a relative displacement with a constant velocity at the contact interface.

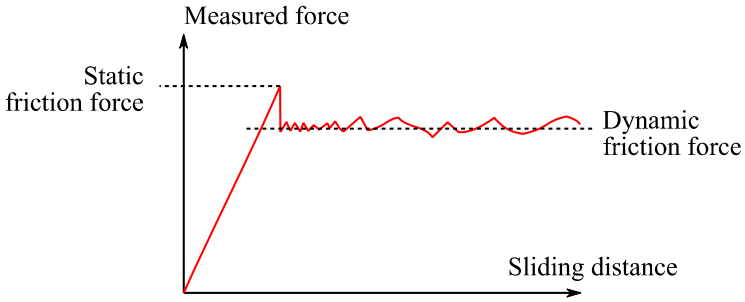

Fig. 2-10: Difference between the static and dynamic friction forces, adapted from ASTM G115-98 [85].

According to these requirements, various test methods were developed. First, the "inclined plane" method described by Dong et al. [86] uses the own weight of a sledge to generate a contact pressure and a tangential force (see Fig. 2-11a). The static friction coefficient can be calculated based on the inclination angle. To measure the dynamic friction coefficient, the angle of the inclined plane must be precisely controlled to ensure a constant sliding velocity. This method is very attractive to measure the static friction because it only involves rudimentary equipment. Nevertheless, the measure of a dynamic friction coefficient is only possible with precise controlling devices. Also, the contact pressure at the interface results from the weight of the sledge and from the inclination.

The "sliding sledge" or "horizontal plane" method described in the standards DIN EN 14882 [84] and ASTM D1894-01 [87] is a common test for the characterization of the friction behavior of textiles. As illustrated in Fig. 2-11b, the contact pressure results from the weight of the sledge. It can be adjusted to characterize the friction behavior at various contact pressures. The sledge is pulled over a horizontal plane at a prescribed velocity. The measure of the force depending on the sliding displacement allows for calculation of the static and dynamic friction coefficients precisely. This method has been used in various studies to characterize the friction behavior of dry textiles at room temperature [88–90]. This test principle was adapted to perform tests at different temperatures (e.g. as developed by Margossian [91]), enabling the characterization of the interface of carbon reinforced thermoplastic materials. The main drawback reported on this method is the torque generated at the front of the sledge due to the distance between the anchor of the sledge and the contact interface. The torque leads to an inhomogeneity of the contact pressure and, in the case of interfaces with high friction coefficients, to a lifting of the rear part of the sledge.

The "pull-out" and "pull-though" methods are improvements of the sliding sledge tests that involve the simultaneous characterization of two interfaces (ref. Fig. 2-11c and Fig. 2-11d). In this configuration, the spurious torque described above vanishes and a pure tangential force is generated. The test method is referred to as "pull-out" if the contact area reduces when the sledge is pulled through the testing device. Various test setups were developed to characterize the friction coefficient of prepreg materials at

different pressures, temperatures and sliding velocities [88, 92, 93]. The main challenge lies in the generation and conservation of a predefined contact pressure.

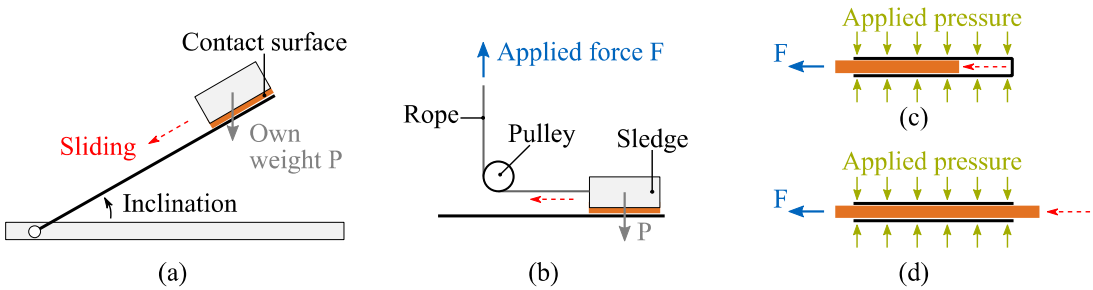

Fig. 2-11: Usual experimental methods for the characterization of the friction behavior of textiles: inclined plane (a), sliding sledge (b), pull-out (c) and pull-through (d) methods.

2.2.2 Shear behavior

The shear deformation is the predominant deformation mode during the forming of textiles. It has been extensively investigated in the last decades [94]. Experimental setups developed to characterize the shear properties of dry fabrics can be divided into two categories.

2.2.2.1 Direct shear deformation

The first category refers to setups that directly apply a pure shear deformation to a textile sample. These experimental devices are referred to as Picture Frame (PF) test setups. A schematic of shear tests with a PF test device is proposed in Fig. 2-12.

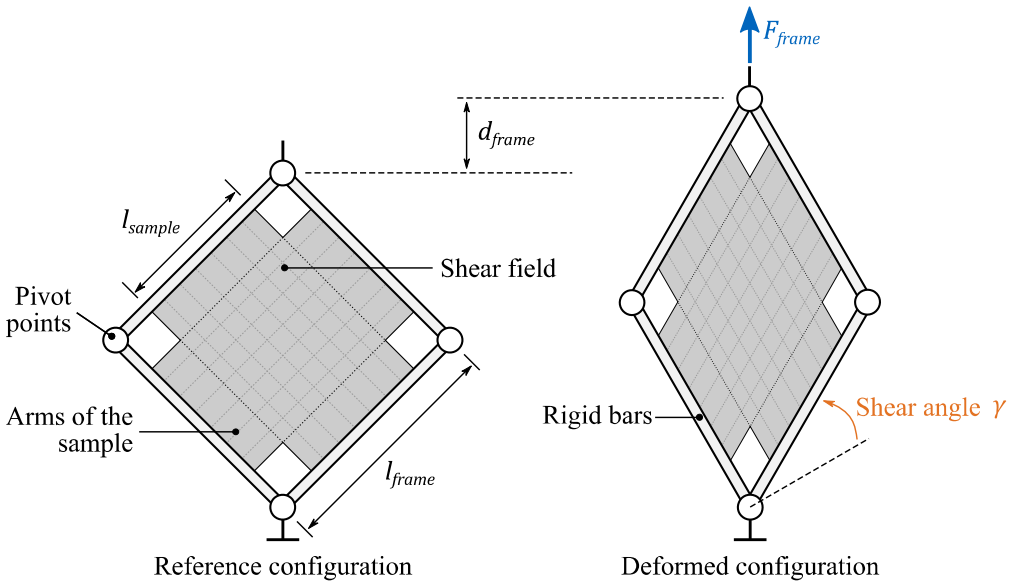

Fig. 2-12: Details of the picture frame device and working principle of picture frame tests

A PF test device is generally constituted of a rigid frame with frictionless articulations. The controlled displacement of one articulation enables the application of a defined pure

shear deformation to the textile sample. The shear angle γ of the frame is related to the displacement of the crosshead d_{frame} as follows:

$$\gamma = \frac{\pi}{2} - 2\cos^{-1}\left(\frac{\sqrt{2}\, l_{frame} + d_{frame}}{2\, l_{frame}}\right) \tag{2-1}$$

where l_{frame} corresponds to the length of the frame, i.e. to distance between the pivots of the frame. The force F_{frame} measured at the load cell depends on the frame geometry and on the sample size. A common approach to present the experimental results of PF tests is to calculate the normalized shear force F_{fabric} using the side length of the sample l_{sample} [95]:

$$F_{fabric} = \frac{F_{frame} l_{frame}}{{l_{sample}}^2} \frac{1}{2\cos\left(\frac{\pi}{4} - \frac{\gamma}{2}\right)} \tag{2-2}$$

A large number of studies were published over the last years on the shear characterization of various reinforcement materials with the PF method, such as dry woven fabrics [96], dry NCFs [18], woven fabric reinforced thermoplastic sheets [97] or unidirectional fiber reinforced thermoplastic sheets [91]. Although the PF test method is widely used to characterize the shear behavior of textile reinforcements, this method is still not standardized and various aspects of the test method (such as the geometry and features of the frame, the preparation of the sample or the test parameters) still differ from one research institute to the other. Peng et al. [98] developed an approach to compare the results of the shear characterization of woven textiles performed with different picture frame rigs and various sample dimensions. The methodology is based on the work done by the forces applied on the frame to shear the sample. This method was applied in a benchmark gathering seven research institutes to investigate the behavior of three different woven textiles, as published in [96]. The results have shown a high variability between the results, which has been attributed to the influence of the clamping force and to the sample preparation. One main drawbacks of the PF test setup reported in the literature is the large influence of the filament orientation: due to the high stiffness of the filament, a misalignment of the textile sample relative to the edges of the PF setup yields high tensile stresses in the filaments. This may result in slippage of the filaments in the clamps and non-realistic high shear forces. Evolutions of the PF equipment were proposed to control the force induced between two opposite edges of the frame during the experiment. The method was applied on woven textiles in refs [95, 99]. On the one hand, it has shown that the tension in the yarn increases during the shear tests. On the other hand, it was observed that the application of a pretension on the sample influences the shear behavior of the textile. Another drawback of the PF is the kink introduced in the filaments at the boundaries due to the fixation of the rotational movement of the filaments in the clamp: the filaments are forced to remain perpendicular to the rigid frame while to onset of a pure shear angle requires an evolution of this angle. This leads to potential

wrinkles at the clamp (as reported in the characterization of unidirectional tapes [88]). In addition, Cao et al. [96] reported that this kink introduces an influence of the size of the sheared field on the shear properties of the fabric. Orawattanasrikul [100] developed a dedicated clamping system using needles to enable a rotation of the filaments at the clamp. Similarly, Dangora et al. [101] proposed to reduce the shear stiffness of the arms of the sample to reduce the influence of the clamping system on the measurement.

2.2.2.2 Indirect shear deformation

The second category refers to working principles that apply an indirect shear deformation to the sample (i.e. the shear deformation in the textile results from external loads). The most common method for the characterization of biaxial textiles is the "bias extension test". In this case, a rectangular sample cut in a ±45° configuration is clamped at both ends and a uniaxial extension is applied in its bias direction, as illustrated in Fig. 2-13. The deformation results in a pure shear deformation in the middle zone of the sample only if the following three assumptions are verified: [102]

1. The filaments are inextensible.
2. The filaments rotate without sliding.
3. The deformation is homogeneous in each zone without significant transitions.

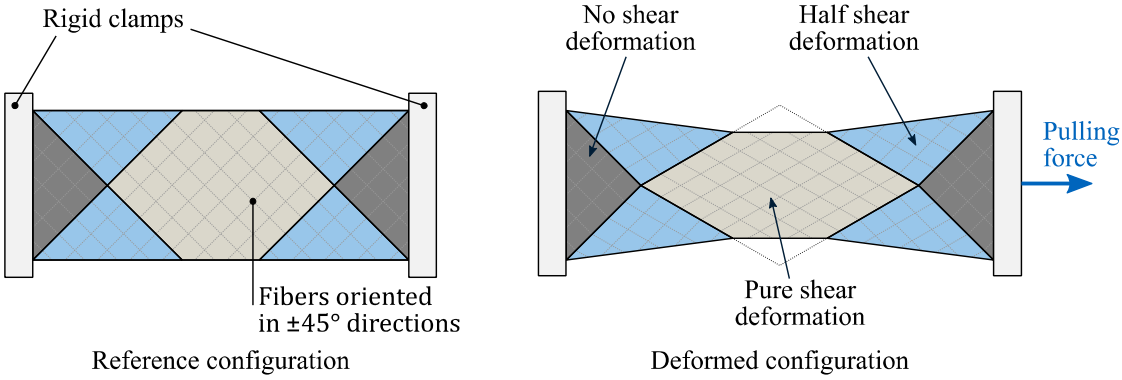

Fig. 2-13: Working principle of the bias extension test method adapted from [102].

Unlike the PF test method, the bias extension test method only requires simple equipment. Also, this method is less prone to spurious tension in the filaments due to the free edges of the sample. The bias extension test method was extensively used for the characterization of woven fabrics in which the yarn crossovers act as pivot joints [102]. Nevertheless, sliding of the yarns at the crossovers can still occur. This was observed by Harrison et al. [103] during the characterization of thermoplastic prepregs at high temperature. This leads to a non-homogenous distribution of the shear deformation and requires advanced equipment to measure the effective shear deformation [104]. The applicability of this method to biaxial NCFs is even more challenging since the filament layers are only bound together through the stitching yarn. An extended study of the deformation behavior of NCFs in bias extension tests was published by Bel et al. [23],

reporting significant sliding of the yarns depending on the textile configuration. More recently, Pourtier et al. [105] presented a new method to analyze the test results of NCFs by including potential slippage in the sample kinematic. Nevertheless, it was shown that the occurrence of the slippage leads to a high dependency of the results on the sample width.

2.2.3 Bending behavior

Although many standards can be found on the characterization of bending behavior, they are mostly only suitable for stiff structures. Due to the soft properties of the fabric, standard bending devices, such as the "3-point bending test" of the DIN EN ISO 14125 [106], are not applicable to reinforcement textiles. A first characterization method of soft materials and plastic foils was presented by Peirce in 1930 [82] in which bending deformation of a sample is generated using its own weight. This method, referred to as the "single cantilever" test method, has been adapted in the standard DIN 53362 [83]. A sample of the material is moved horizontally in order to progressively increase its free length until a total deflection of 41.5° is achieved (see Fig. 2-14a). The bending stiffness can be calculated using mathematical equations introduced by Peirce. This testing method relies on very simple equipment to obtain information on the bending characteristics of the textile easily. Nevertheless, the experiments are challenging for materials exhibiting highly non-linear behavior, which leads to a sudden kink of the sample at the clamping or a twist of the free end [107]. As a consequence, it is difficult to reach an exact deflection of 41.5°. Further methods were proposed by Peirce in [82] for textile not suitable to the single cantilever test method. He introduced various hanging loops, in which both ends of the sample are clamped and juxtaposed at various angles, as illustrated in Fig. 2-14b to Fig. 2-14d. In all configurations, the loop is placed vertically and deforms under its own weight. The height of the loop can be readily used as an indicator of the bending rigidity of the textile. The calculation of the bending stiffness as presented by Peirce relies on the strong assumption of linear elastic bending behavior, which was often refuted for dry textiles, as reported in [19, 64–66].

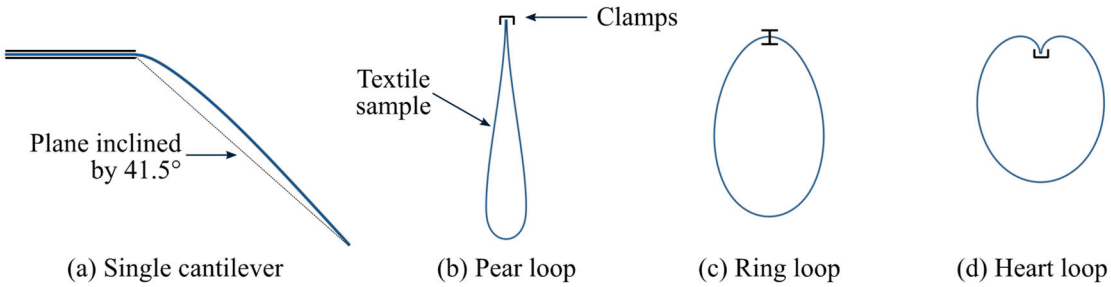

Fig. 2-14: Illustration of the bending characterization methods proposed by Pierce in [82] for the characterization of soft materials: cantilever (a) and hanging loops (pear (b), ring (c) and heart (d) loops).

The measure of the bending rigidity depending on the curvatures is mandatory in order to calibrate advanced bending models. The different test setups published on that topic can be separated into three groups.

The first setups were derived from modifications of the single cantilever tests. Clapp et al [108] proposed a method to generate the bending moment-curvature relation of fabrics by recording the shape of the specimen in a cantilever configuration. The correlation of the sample deformation with the calculation of the bending moment distribution enables the characterization of the bending behavior for non-linear materials. Nevertheless, the induced curvatures strongly depend on the stiffness of the material. Based on a similar approach, Bilbao et al. [64] developed a characterization method able to generate higher curvatures, even for stiffer material. Their test device generates a succession of cantilever tests with an increasing free length. The shape of the specimen is recorded at the equilibrium of each free length. Supplementary weight can be added to the sample to increase the curvature for stiffer materials. The characterization of the hysteresis is also possible with the correlation of the deformation history induced in the various test steps. Since the stiffness of the material is a priori not known, many test configurations with different supplementary masses may be required to generate the full bending moment vs. curvature relationship. Also, difficulties to compute the curvature of the sample were reported, leading to a high scatter of the results. Contrary to the previous configurations, Dangora et al. [107] proposed to hang a textile sample vertically and to apply a predefined horizontal force at the tip. With this method, the curvature remains small (about 1.0 m^{-1}), which is not representative of the curvature in the formation of wrinkles during the preforming process. In order to generate higher curvatures in a continuous deformation process, Krollmann et al. [K1] developed a cantilever test bench with a rotating clamp to apply the deformation to the tip of the sample. This method was used to characterize soft materials [109]. However, the localization of the curvature near the clamps reduces the usability of this setup for dry textiles. A similar test principle was developed by Sachs [110] for the characterization of thermoplastic unidirectional tapes at high temperatures. A free translation of the specimen in the clamp is introduced to adapt the change in length of the deformed part. The calculation of the bending properties relies on the calculation of the curvature and, thus, on assumptions on the material behavior.

The second group of experimental approaches aims at the application of a pure bending load to the sample. The application of a pure bending load is challenging since it requires a precise control of the clamps. The Kawabata Evaluation Systems for Fabric Bending (KES-FB) has been used to study the bending behavior of textile for many years. In this case, both the rotation and distance of the clamps are precisely controlled to apply a circular arc to the sample, whose radius corresponds to the radius of curvature [66]. The KES-FB enables to record a full load-unload cycle up to high curvatures and has been successfully used to investigate the bending behavior of various reinforcement textiles [64, 68]. The control of the clamp requires sophisticated equipment. Moreover, the free length of the sample is small (1 cm reported in [19]), which may lead to high variability

in the results if the unit cell of the textile exhibits the same order of magnitude as the free length.

Supplementary setups were proposed in which a bending deformation is induced through complex and combined stress states. Wang et al. [111] applied a compressive load on a small sample of unidirectional uncured prepregs. The global buckling of the sample induced a deformation used to investigate the viscous bending behavior of the material. It allows the generation of a large range of curvatures and the measure of the resulting forces. Nevertheless, a manual operation is necessary to induce the global buckling of the sample. Similarly, Dangora et al. [107] developed a test device to generate wrinkles with various curvatures in a textile, referred to as the “double compression” test method. This approach enables studying the onset of wrinkles and comparing their precise shape with simulation results. However, the measure of the required forces is not possible and, thus, is not applicable to the characterization of the bending stiffness.

2.3 Numerical methods for virtual textile development applied to the preforming process

The development of solutions to improve the preforming quality exclusively using experimental approaches induces high development time and cost to find the adequate textiles and corresponding process parameters. Numerical methods can significantly reduce the need for expensive tooling, can avoid the manufacture of textile coupons and can decrease the number of experimental trials. These methods can be implemented with different levels of detail. This section firstly introduces the modeling scales of dry NCFs. Since this doctoral thesis addresses the prediction of the preforming quality on the one hand and the prediction of the textile deformability on the other hand, the applicability of the modeling scales with regard to these objectives are review separately. As a result, numerical approaches modeling the forming process are presented in a second part and the methods to predict the mechanical behavior of dry NCFs are reviewed in a third part.

2.3.1 Modeling the structure of dry NCFs

Three main modeling scales can be identified to numerically describe dry NCFs depending on their discretization level.

2.3.1.1 Macroscopic scale

The macroscopic scale homogenizes the properties of the reinforcement with a continuum description (i.e. without any discontinuity). The textile is usually modeled as a 2D medium, as shown in Fig. 2-15. Thereby, tensile, compressive, shear and bending deformation can be modeled. Inner deformation mechanisms such as tow slippage and further interactions cannot be represented numerically and must be considered in the

constitutive equations. Moreover, sliding between the textile layers and contact with the tools can be modeled with various interaction laws [21, 56, 72, 112].

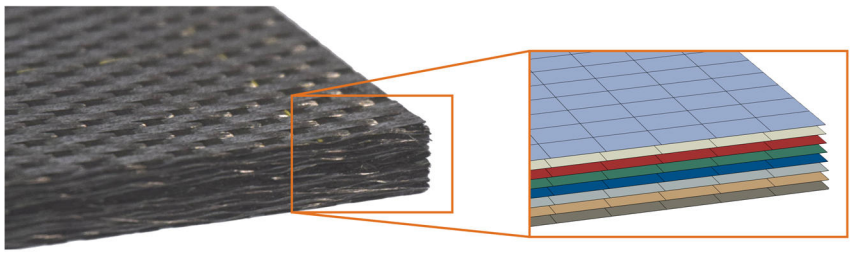

Fig. 2-15: Illustration of the macroscopic simulation scale for a stack with multiple layers.

2.3.1.2 Mesoscopic scales

The discretization of the fibrous mat modeling the textile architecture is referred to as "mesoscopic approach". This modeling scale is easily defined for woven textile, in which the textile architecture refers to the tows generated during the weaving process. Nevertheless, NCFs are constituted of different unidirectional layers without any interlacing of the filaments of various layers. Moreover, it includes a supplementary component: the stitching yarn. As a result, two mesoscopic scales are introduced in this doctoral thesis.

The first mesoscopic level corresponds to approaches discretizing a multiaxial NCF with continuum elements per layer, as proposed by Bel et al. [113] and illustrated in Fig. 2-16. Note that the stitching yarn is modeled separately. This enables accounting for interlayer and stitch-to-filament interactions. Tow-sliding can be simulated with this method.

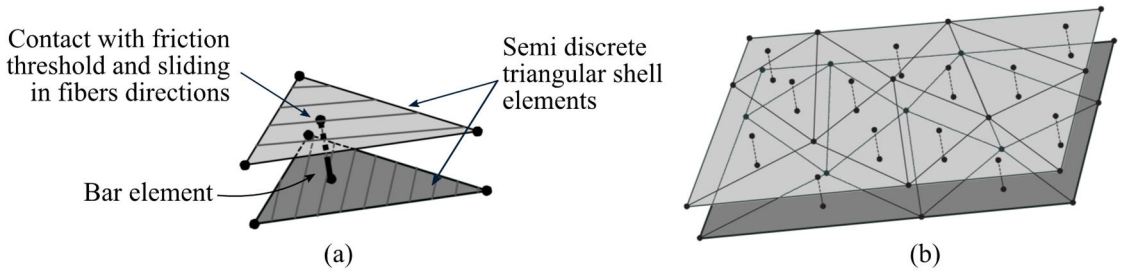

Fig. 2-16: Illustration of the mesoscopic scale in which the layers of a NCF are modeled with continuum elements (adapted from [113]): discretization of the NCF in shell an bar elements (a) and resulting model of a rectangular NCF sample (b).

In the second mesoscopic modeling scale, the mesoscopic structure of each layer is modeled. It results in the simulation of filament tows and of the respective interactions between these tows. Different methods can be found in the literature to generate a mesoscopic geometry of dry textiles. First, mesoscopic models can be extracted from experimental measurements of the textile architecture. An approach modeling woven fabrics based on X-ray computed tomography was presented by Naour et al. [114]. The main advantage of this method is the high fidelity of the numerical model. However,

experimentally extracted geometries require high effort in the segmentation of the results and local adaption of the structure may be necessary to ensure a periodic model.

Another approach is the generation of idealized mesoscopic NCF geometries based on the stitching pattern. While studies were published assuming a perfect and rectangular description of the tows [17, 115] (see Fig. 2-17a), two programs are available to generate realistic mesoscopic structures of NCFs.

- The software TexGen was developed by the university of Nottingham [116–118]. The generation of the model requires a few parameters to create the stitching yarn and the fibrous structure. A large variety of stitching pattern can be implemented. A 90°/0° NCF with a tricot pattern is depicted in Fig. 2-17b.
- The software Wisetex from the KU Leuven [119] is able to produce unit-cells of a large number of NCFs based on parameters of the fibrous layers, on the stitching architecture and on experimental measurements. Moreover, local cracks in the fibrous mats are considered. The experiments required to generate a realistic mesoscopic unit-cell of the material are presented in [68]. For instance, the ratio between the crack length and crack width must be measured on the preform but suggestions for different NCF architectures are proposed if the required parameters cannot be measured. An example of the models generated with WiseTex is illustrated in Fig. 2-17c.

The geometries modeled with TexGen and WiseTex can be exported to simulation software packages to predict the mechanical behavior of the preform, its permeability or the mechanical performance of the textile composite material. Nevertheless, the definition of tows and their discretization remains a challenge for NCFs with non-orthogonal layer orientations (e.g. for a ±45° NCF) if the ratio between the stitch gauge and length is not appropriately selected.

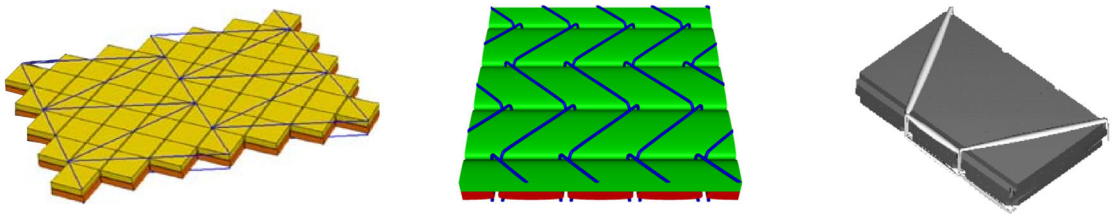

(a) (b) (c)

Fig. 2-17: Generation of mesoscopic geometries of NCFs discretizing the layers in tows without defects (a, adapted from [17]) and with defects using TexGen (b, adapted from [118]) and WiseTex (c, adapted from [68]).

2.3.1.3 Microscopic scale

The third main discretization level of a dry textile is the “microscopic scale” [120]. The objective of this discretization level is to model the interactions between the filaments within the tows and the interactions with the stitching yarn. As a result, all interaction

mechanisms listed in section 2.1.3.1 are modeled. Usually, the microscopic scale is defined as the consideration of each filament separately [71]. Such approach would include a non-feasibly large number of elements to model a unit-cell of the textile architecture. To consider all interaction mechanisms of a NCF with realistic computation effort, an intermediate discretization level is introduced in the literature: the multifilament approach (also called "discrete approach"). Here, the tows of the layers are discretized with Digital Chain Elements (DCEs), and a reasonable number of filaments are grouped in one chain. Green et al [121] reported the discretization of a 12k yarn with 19 to 91 chains and concluded that an optimal discretization of a yarn with their approach shall include about 61 chains. Based on these conclusions, Thompson et al. [122] reported a group of 155 filaments in one chain to model the fibrous layers of NCFs. Note that the multifilament approach corresponds to the usual description of the microscopic scale if each element models a single real filament only. An example of the simulation of a tow at the microscopic scale are illustrated in Fig. 2-18a.

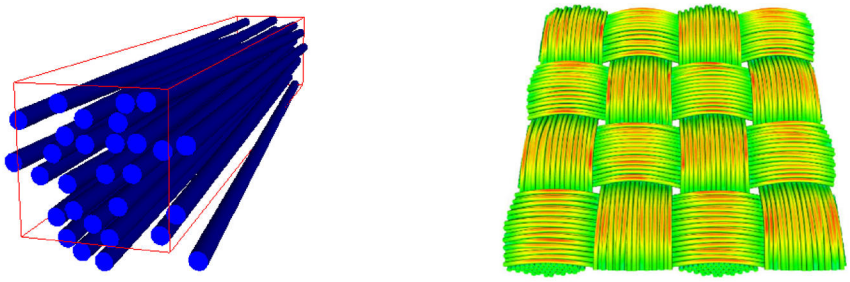

(a) (b)

Fig. 2-18: Discretization of a fibrous tow using the multifilament approach (a, adapted from [116]) and geometry of a woven fabric at the microscopic level (b, adapted from [123]).

First multifilament approaches of dry textiles using DCE were presented by Zhou et al. [124]. They consist in chains of rod-elements connected with frictionless pins. The frictionless hinges between the rod-elements ensure a free rotation at the connecting nodes. It is assumed that the forces induced by the bending deformation of the single filaments are negligible compared to the forces induced by the interactions within the textile. The modeling technique was used to study the geometry of woven fabrics and braids through a detailed stepwise manufacturing process, leading to high computation time. More recently, Huang et al. [125] proposed to start from an idealized geometry of the weaving pattern and applied tension to the yarns to generate a realistic woven geometry. This approach enables reducing the computation time while reaching a realistic model of the microscopic geometry. However, this method is limited to textile architectures with a high level of interlacing, such as 3D-woven fabrics. In addition, Durville proposed the modeling of reinforcement textiles at refined scale. In [123] many filaments are merged in a single element. Using an enriched kinematic beam model, it allows accounting for the bending stiffness and the deformation of the cross-section of filament bundles. The approach presented by Durville is based on a progressive resolution of interpenetration

of the bundles to generate the textile geometries, as shown in Fig. 2-18b for a plain weave fabric. The calculation method relies on an implicit integration scheme, which requires intensive development efforts of the contact algorithms to reach a reasonable convergence rate with commercial Finite Element (FE) solvers.

Discrete modeling approaches have been mostly applied to fibrous material with woven or braided architectures. Thompson et al. [122] proposed a workflow to predict the mesoscopic geometry of the tows of a biaxial 0°/90° NCF with the use of the multifilament approach (see Fig. 2-19). The virtual description of the NCF was generated starting from an idealized periodic alignment of the chains with predefined gaps between the tows. A negative temperature was subsequently applied to the stitching yarn to reproduce the manufacturing process.

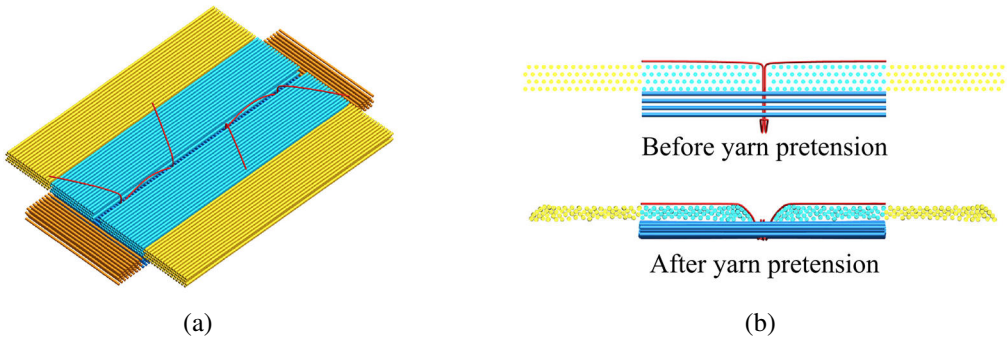

Fig. 2-19: Isometric view of the initial geometry of a NCF at the microscopic level (a) and side view of the model before and after pretension of the stitching yarn (b) adapted from [122].

2.3.2 Simulation of the forming process

Forming simulations (also referred to as draping simulations) find applications at many stages of the development process. The main goal of these numerical approaches is to describe the deformation of the textile during the forming process in order to support the development of new components as well as adequate manufacturing processes. By consideration of the textile deformability, it is possible to study the manufacturability of a given geometry in the early design phase. Also, simulations in which all components of the forming process are considered allow studying numerically the compatibility of various manufacturing processes with the reinforcement textile and the component geometry. For example, a stamping process with rigid elements can be compared with a diaphragm process involving flexible tools. In addition, numerical analyses enable the investigation of the influence of a large set of process parameters and their optimization to reduce the forming defects.

Many numerical approaches have been developed over the last decades to model the deformation process of a textile into its final 3D geometry. These approaches can be divided into two categories. The first category, referred to as “kinematic approach”, is a purely analytical approach that only relies on geometric parameters of the textile. The

second category uses the Finite Element Methods (FEM) to model the whole preforming process and account for the mechanical behavior of the textiles. A review of these categories with their respective applicability to the prediction of the preforming quality of reinforcement textiles is proposed here. Note that careful attention will be paid during the review of the methods to study their applicability to the simulation of NCFs.

2.3.2.1 Kinematic approach

The first kinematic approaches were developed for the clothing industry in order to study how a textile can adapt to a given surface geometry [126]. It is a simple method that enables predicting the shear deformation that a textile undergoes. The main assumption of the kinematic approach is that the textile is assimilated to a regular mesh constituted of rigid bars that can rotate freely at the connection points. In order to predict the result of the preforming step, a mapping of the final component geometry is performed: starting at a given point, the surface is iteratively mapped along two prescribed directions with the single condition that the distance between two points of the mesh remains constant (ref Fig. 2-20a). Thus, the shear deformation can be directly measured by the deformation of the cells of the mesh, as shown in Fig. 2-20b. [127]

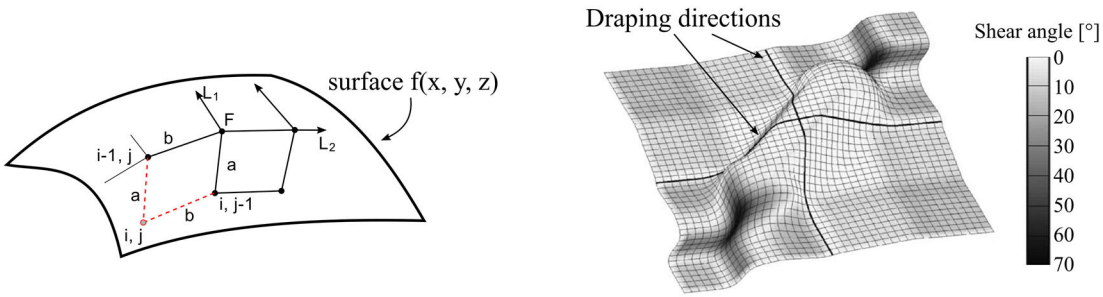

Fig. 2-20: Illustration of the kinematic algorithm (a, adapted from [128]) and example of a kinematic draping result with their draping directions (b, adapted from [127]).

Kinematic approaches are implemented in numerous commercially available software packages such as in Catia V5 from Dassault Systèmes (module “Composites Part Design”) [129–131]. They are very popular in the industry to assist the development of new components since they require a reduced number of inputs and compute in a few seconds. The distribution of the shear angle is a useful information that can be used to prove the manufacturability of a geometry. For instance, the shear angle can be compared to a maximum shear angle that a textile can deform (usually referenced to as “shear locking” [57]). If higher shear deformations are necessary, the textile is more likely to create wrinkles and generate defects. Moreover, the alignment of the filaments can be derived from the deformed mesh. Thereby, the manufacturability of the designed lay-up can be investigated and potential deviation be identified in a very early design phase. [27]

Nevertheless, the analytical descriptions neglect the material properties and process parameters. The rigidity of the textile is not considered and important deformation

mechanisms are not modeled. Moreover, textiles like NFCs or unidirectional textile layers do not exhibit any rotation point and involve complex deformation mechanisms. Evolutions of the kinematic approach can be found in the literature in order to account for the textile stiffness and diverse process parameters [132–134]. As an example, Long et al. [135] proposed a method in which the shear strain energy required to deform the mesh is calculated based on experimental shear data. This method is able to account for the asymmetric shear behavior of NCFs and improvements considering the friction with the blank-holder showed the influence of the blank-holder force on the forming result of NCFs [136]. Although the approach is very attractive to assist the development of new structures, the prediction capability is limited since the occurrence of defects such as wrinkles are neglected. Moreover, process parameters and interactions with the forming tools are not considered.

2.3.2.2 Finite element approaches

Further approaches have been developed aiming at a detailed description of the process and of the material. The simulation is commonly performed with the use of FEM to describe the preforming process and solve the respective partial differential equations. In those cases, the consideration of the material behavior plays a central role. FE approaches are very attractive compared to kinematic approaches since they are able to consider the deformation mechanisms of a textile and are a realistic representation of the manufacturing process. The interaction with the tools and further components, such as grippers and blank-holders, can be considered and investigated. Also, the evolution of the forming process over time is modeled, which enables accounting for the whole history of the material deformation. Simulations accounting for the evolution of the temperature, the hysteresis of the material behavior or the sequence of the preforming process have been recently published [137, 138].

As introduced above, the description of the textile can be done at various scales: macroscopic, mesoscopic and microscopic scales. Depending on the level of detail, they can predict the occurrence of defects in the fibrous mat (e.g. gaps, undulation) or bigger geometrical deformation such as wrinkles and folds. The deformation mechanisms that are modeled and their resulting interactions depend on the discretization level.

Macroscopic approach

The deformation behavior of a textile is very complex and depends on its fibrous architecture. Compared to usual materials, reinforcement textiles exhibit a very high tensile stiffness in the filament direction and comparable very low shear or bending stiffnesses. As a result, conventional constitutive equations are not directly adapted to describe the behavior of reinforcement textiles in the preforming step and special care must be taken in order to decouple the deformation mechanisms [139]. Thus, different material models have been developed depending on the textile that were investigated. A non-exhaustive

review of macroscopic simulations is proposed here with a focus on their applicability to dry NCFs.

A large number of studies performed at the macroscopic scales have been published over the last decades using commercially available FE software packages with dedicated material or interaction models. The software package ABAQUS from Dassault Systèmes / SIMULIA is widely used in industrial applications and is strongly integrated in the portfolio of Dassault Systèmes [140]. Using explicit solvers, various studies of the forming behavior of NCFs with ABAQUS were published [56, 80, 141, 142]. On the one hand, forming simulations of dry textiles can be modeled with the material models *FABRIC or *VFABRIC which use non-orthogonal constitutive equations to model the behavior of woven textiles [143]. On the other hand, user subroutines can be implemented if the constitutive equations already available are not sufficient to accurately describe the forming process. This offers a high flexibility of the software for forming simulations. One application case is illustrated in Fig. 2-21a, in which the influence of local cuts in the textile was studied.

The research laboratory LaMCoS from the INSA Lyon developed the code PLASFIB dedicated to forming simulations of textile reinforcement [144]. It bases on explicit solvers, and various material models were developed to predict the forming result of dry reinforcements [145] or prepregs [138, 146]. A refined model accounting for the influence of the stitching yarn on the deformation modes has recently been proposed by Steer et al. [147] in which the deformation energy induced by the deformation of the stitching threads and the inter-stitch interactions is computed analytically (see Fig. 2-21b). Even though this code is commercially available, its use requires a high level of expertise.

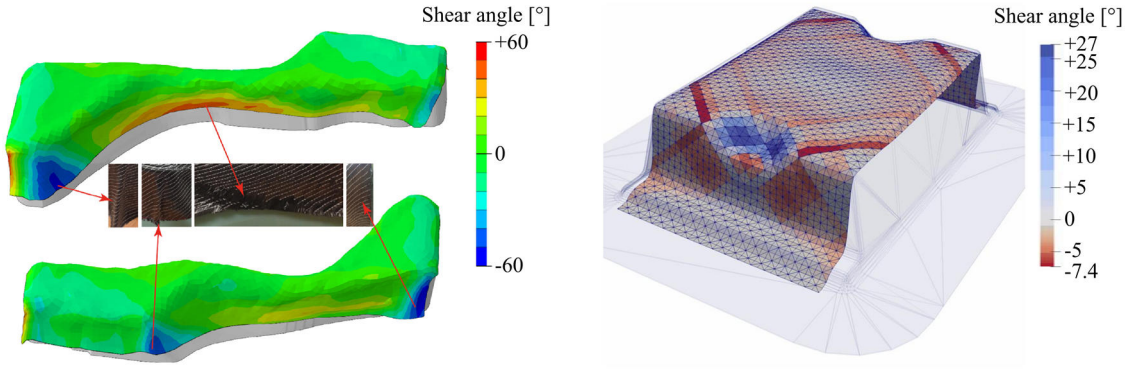

(a) (b)

Fig. 2-21: Forming simulation of single plies of NCFs at the macroscopic scale according to Steer (a, adapted from [60]) and study of the influence of local cuts on the preforming result (b, adapted from [80]).

ESI Group proposes a platform for the virtual manufacturing of CFRP components. The included package PAM-FORM focuses on the simulation of the forming process. The material model MAT140 released after 2015 offers a high flexibility to model the behavior of dry and prepreg textiles [148–150]. A recent approach developed by Kaiser et

al. [151] enables modeling the behavior of textile through a coupling with simplified unit-cells.

Contrary to the other solutions reviewed in this paragraph, the software package AniForm from AniForm Engineering B.V. uses an implicit solver to model the forming process. The solver is based on the work published by Ten Thije et al. [152]. A large number of material models is available depending on the fibrous architecture (including dry NCFs) [153].

Further studies were published on the forming of dry textiles with other software packages such as LS-DYNA [154]. Dörr et al. [155] presented a detailed analysis of usual software packages (AniForm, ABAQUS, PAM-FORM and LS-DYNA) and their respective features available for forming simulations of unidirectional thermoplastic tapes.

Mesoscopic approaches

The mesoscopic level of detail models the architecture of the fibrous layers, which makes it very interesting to gain information on the local defects during the preforming process. Studies published on the forming process at mesoscopic scale of NCFs have shown the ability of the approach to model the tow sliding or occurrence of gaps. Also, local compaction of the fibrous mat can be simulated.

Focusing on the tow sliding observed experimentally [23], Bel et al. developed a mesoscopic approach in which the layers of NCFs are modeled with continuum elements. This method is not able to reproduce all defects in the fibrous mat but proposes an efficient way to calculate the tow siding [113], as illustrated in Fig. 2-22.

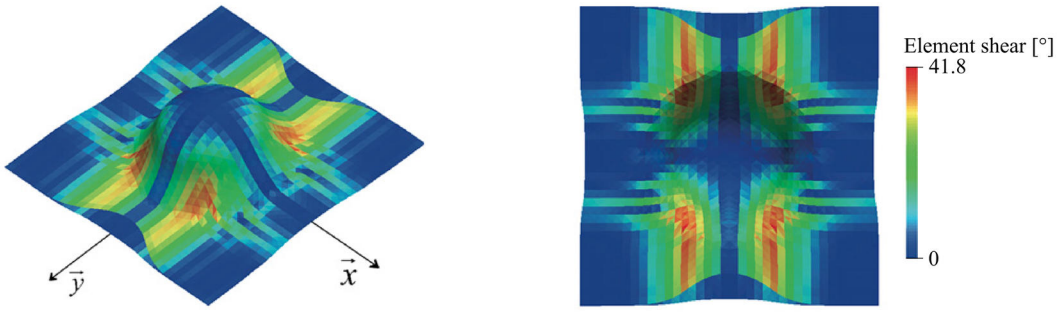

Isometric view Bottom view

Fig. 2-22: Simulation of the forming process of a NCF ply at the mesoscopic scale with continuum elements for each fibrous layer adapted from [113].

Models in which the fibrous layers are discretized in tows with idealized geometries were applied to forming simulations. Creech and Pickett published in 2006 [17] a study to link the result of forming simulations with the failure analysis of a CFRP part. The tows and the stitching yarns were modeled with volumetric and bars elements, respectively. Limitations were shown in the constitutive modeling of the tow, which was not able to decouple the deformation modes. Similarly, Sirtautas et al. [115] proposed a mesoscopic approach to extract information from the forming process for subsequent

filling simulation (see Fig. 2-23a). Dedicated care was taken to model the gaps between the tows for accurate representation of the permeability of the textile. Finally, Pham et al. [156, 157] modeled the tows with beam elements to reduce the computational effort and apply this level of details to an industrial forming process. The forces calculated in each tow allow identifying critical locations of the textile. The comparison with results obtained using a macroscopic approach and experimental trials showed promising results.

Studies aiming at a more realistic description of the tow geometry were suggested by Vorobiov et al. for the forming simulation of unidirectional NCFs [158]. The well-defined tows of the fibrous structure were discretized with volumetric elements. The material behavior of the tows was calibrated through virtual characterization at the tow level, focusing on the transverse compaction behavior. On the contrary, Thompson et al. proposed a discretization of tows with shell elements to reduce the quantity of elements [122]. This method was applied to the forming of a single layer of biaxial NCF over a tetrahedron, as illustrated in Fig. 2-23b. The outer surface of the tows is modeled to accurately reproduce the geometry of the tows and compute the contacts during preforming. A realistic mechanical behavior of the tows is achieved using two dimensional supports in the hollow structure of the outer shell elements. Nevertheless, the high level of refinement induces high computation time and reduces the usability of this simulation scale for industrial applications.

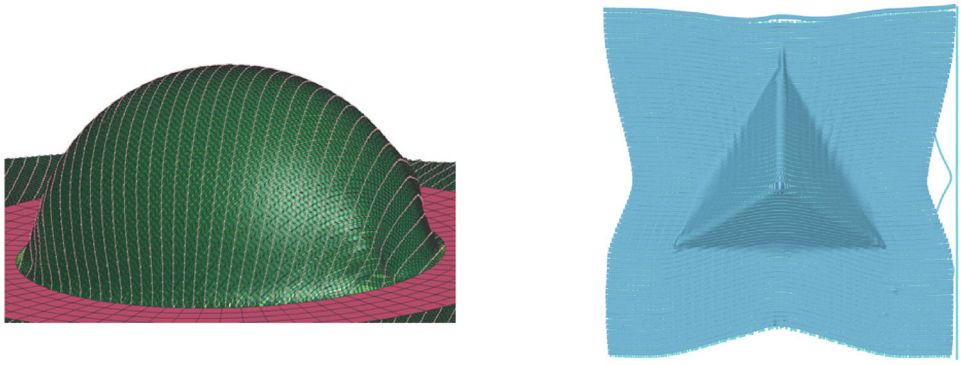

(a) (b)

Fig. 2-23: Forming simulation results of NCFs at the mesoscopic scale with a discretization of the tows with volumetric elements (a, adapted from [115]) and shell elements (b, adapted from [122]).

Microscopic approaches

At this high level of refinement, interaction within the tows can be modeled more accurately. Also, in the case of NCFs, interactions with the stitching yarn are reproduced and defects in fibrous layers can be introduced. The main advantage of microscopic approaches is that further defects induced during the preforming process can be modeled. For instance, local buckling of the filaments resulting in an in-plane or out-of-plane waviness during the preforming can be calculated [159–161]. An example of

microscopic forming simulation of a 3D angle-interlock textile is illustrated in Fig. 2-24. Nevertheless, simulating the forming of a whole component is not feasible due to the high number of elements and contact surfaces.

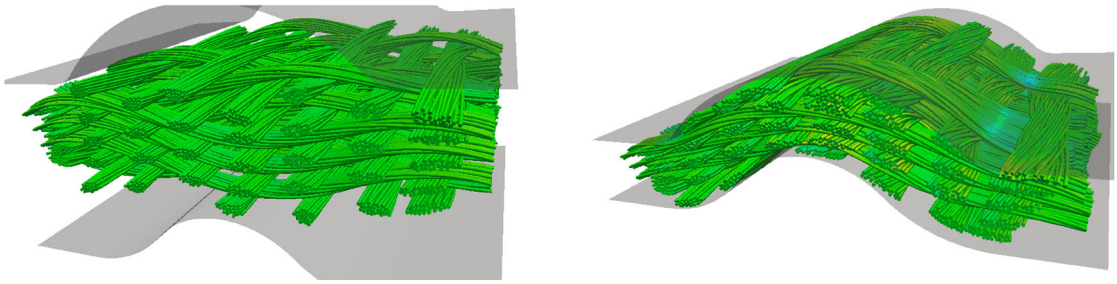

(a) (b)

Fig. 2-24: Forming simulation of a 3D angle-interlock textile at the microscopic scale (adapted from [159]).

2.3.3 Prediction of the mechanical behavior of dry NCFs

The development of numerical approaches to model the complex behavior of NCFs represents an attractive method to understand and predict their deformation behavior. With a numerical approach, it is possible to investigate interactions between manufacturing parameters and to reduce the costly experimental trials listed in section 2.2. Moreover, complex loading conditions — such as a combined shear and compaction deformation — can be applied virtually with a reduced effort compared to the development of advanced experimental devices. This subsection reviews the modeling scales introduced in section 2.3.1 and their suitability for the prediction of the mechanical behavior of dry NCFs.

2.3.3.1 Macroscopic scale

Since the macroscopic scale homogenizes the behavior of the textile, time-consuming material characterization is required to generate the appropriate inputs. Nevertheless, relative influences of the stitching patterns can be predicted based on the deformation behavior of the stitching yarn. For instance, Krieger et al. [61] developed an analytical approach using the stitching yarn strain to predict the asymmetric behavior of the textile. It only uses the characteristics of the stitching architecture. Furthermore, Wiggers [162] and Steer et al. [147] proposed different methods to calculate the energies resulting from the deformation of the stitching yarn and from the interaction with the fibrous layers. These energies can be combined or superimposed to the behavior of the fibrous mats to predict the behavior of NCFs at the macroscopic scale with varying stitching architectures.

2.3.3.2 Mesoscopic scale

Since the mesoscopic scale considers the fibrous architecture, it is possible to calculate the interaction forces in the textile. Peng et al. [98] developed a numerical analysis of the shear behavior on unit cells of woven fabrics at the mesoscopic scale. They modeled the boundary conditions of the picture frame on the unit cell to reproduce the experimental conditions, leading to rigid lateral surfaces. Similarly, Lin et al. [117] studied the influence of boundary conditions on the shear behavior of woven fabrics at the mesoscopic scale. They showed that the intra-tow shear induced by the clamping of the picture frame has a significant influence on the shear force.

The investigation of the behavior of NCFs at the mesoscopic scale was mainly performed on a whole sample in order to model the experimental trials directly rather than at the unit-cell level [17, 115, 122, 163]. Examples of bending and bias extension tests are illustrated in Fig. 2-25. Despite an enhanced description of the deformation mechanisms, a homogenization of the tow behavior is still necessary to gain results on part level within an acceptable computation time. This makes this approach inflexible, as adaptions are necessary for any new NCF configuration even with only slight changes (e.g. other stitch length).

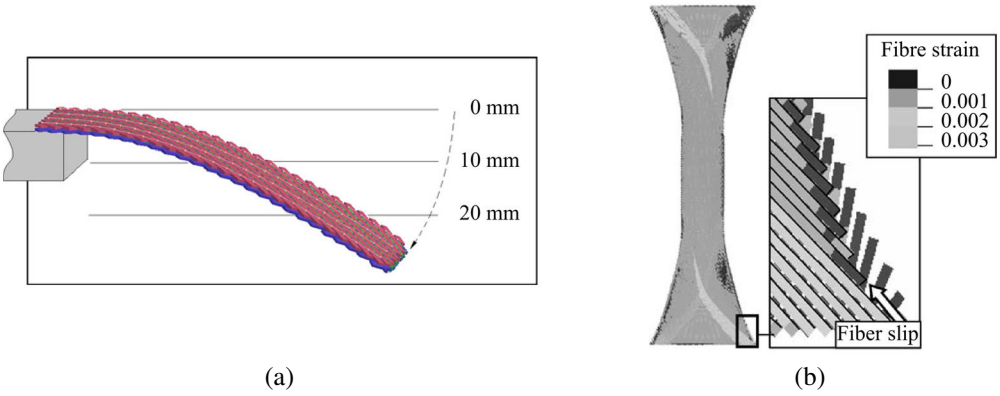

Fig. 2-25: Virtual characterization of dry NCFs at the mesoscopic scale: bending characterization (a, adapted from [115]) and simulation of a bias extension test (b, adapted from [17]).

2.3.3.3 Microscopic scale

This level of refinement models explicitly the relative motion between the filaments. The predictive capabilities are improved, since the homogenization is reduced to a smaller number of real filaments and all relevant interaction mechanisms are considered.

Such approaches have been mainly reported for the virtual characterization of textiles with well-defined tows. Durville published numerical investigations of woven fabrics modeled at the level of the filaments. [120, 123]. The unit cells of the fabric are simulated based on the repetition of the waving pattern in which each tow is discretized with 48 chains of enhanced beam elements. Dedicated boundary conditions were developed

to relate the displacements of each chain in a tow with a reference point at the border of the unit cell. This relation constrains the average displacement of the nodes of a tow. With this approach, the macroscopic deformation of the unit-cell is applied on the reference points while local deformation of the tow is possible. Virtual characterization was proposed for various deformation modes. Fig. 2-26a and Fig. 2-26b show the results of virtual bending and shear characterization. This framework was also applied to the simulation of rovings for braided textiles in order to study their compression behavior [164].

Daelemans et al. [165] published a study on the tensile and shear behavior of 3D woven textiles using the DCE approach in an explicit integration scheme (ABAQUS/Explicit). Although the bending stiffness of the chains was neglected, a good correlation with experimental results was achieved. Moreover, a realistic initial bending stiffness of the textile was reached.

A similar approach was proposed by Sherburn in order to predict the behavior of fibrous tows [116]. It was adapted to predict the behavior of a unit-cell of woven fabrics for a shear deformation, as illustrated in Fig. 2-26c. The simulation is performed on a quarter of the unit-cell based on the symmetry of the pattern to reduce the computational effort. The boundary conditions applied to the numerical filaments ensure a moment-free rotation and a symmetric displacement with respect to the midplane of the tow.

A further discrete modeling technique of textiles was proposed by Green et al. to study the compaction behavior of 3D woven textiles using conventional beam elements [121]. However, merging many filaments in one conventional beam element would lead to an overestimation of the bending stiffness. To tackle this problem, Green et al. used an elastic-plastic model in order to reduce the bending stiffness of the bundles when a deflection threshold is exceeded. The geometry of the simulation results correlated well with computed tomography scans even though they concluded that this approach is not able to reproduce the forces in the woven fabric accurately when deformed. Moreover, the results are sensitive to the yield strength used to reduce the bending stiffness of the chains.

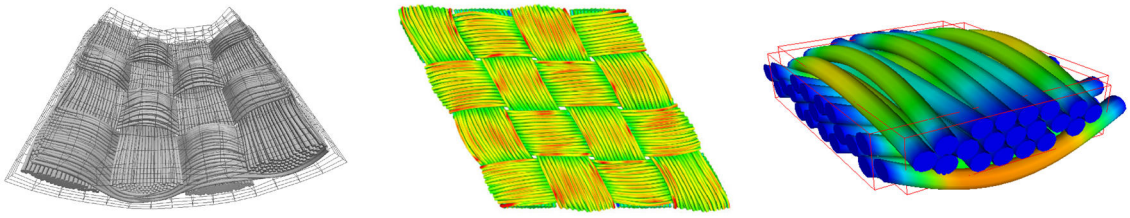

(a) (b) (c)

Fig. 2-26: Virtual characterization at the microscopic level with multifilament approach to study the bending (a, adapted from [120]) and shear behavior of woven textiles (b, adapted from [123] and c, adapted from [116]).

Applied to the simulation of NCFs, discrete modeling approaches enable to account for the inter-filament, the inter-stitch and the stitch-to-filament interactions. Moreover, the

local defects listed in section 2.1.4 (e.g. cracks and channels) can be reproduced. To the author's knowledge, the study presented by Thompson et al. in [122] is the only work published so far focusing on the application of discrete modeling to NCFs. Nevertheless, their approach is limited to NCFs constituted of 0° and 90°-layers, in which well-defined tows can be identified. Moreover, the elements used to discretize the fibrous layers and the stitching yarns rely on the elastic-plastic model introduced by Green et al. [121]. As a result, the multifilament approach of the NCF presented by Thompson et al. is not able to predict the forces induced in the material during the deformation. Also, the assumption of periodic and perfect alignment of the chains does not account for local deviations of the chain orientation from the idealized path. Therefore, it fails to model the occurrence of various local defects and, thus, might underestimate interactions in the textile.

3 Development of a forming simulation framework for dry NCFs

Numerical descriptions of the preforming step can support the development of manufacturing processes by reducing conventional experimental trial and error approaches. The aim of this chapter is to develop a simulation framework able to study and predict the forming behavior of dry NCFs. First, the numerical approach is selected according to the following objectives of the framework:

1. Simulation of a whole component in an industrial context. The whole simulation approach, including iteration loops, should be possible in a usual duration of under 12 hours.
2. Description of defects induced during the preforming step.
3. Use of simulation software packages able to model the behavior of dry textiles using only "built-in" solutions.
4. Possibility to integrate the forming simulation in a conventional scripting environment (e.g. Python).

Then, a methodology is proposed to develop and calibrate the material models. Finally, the accuracy of the simulation approach is validated with experimental trials performed using a generic demonstrator geometry. Since the preforming step of reinforcement textiles is a complex process including different physical phenomena, the draping results and the accuracy of the simulation might be influenced by a large number of parameters. In order to reduce the modeling complexity while efficiently proving the ability of the whole framework to numerically predict the preforming behavior, following restrictions are applied in this doctoral thesis:

- Forming at room temperature without previous activation of the binder.
- Forming of a single NCF ply.
- Use of solid metallic tools.
- Forming experiments are performed with a low velocity in order to reduce the influence of strain-rate material dependencies.

The demonstration of the framework is done using the ±45° NCF material presented in section 1.3. This material exhibits a higher complexity than the 0°/90° NCF due to its potential asymmetric shear behavior.

3.1 Selection of the approach

The kinematic approach is well established in the industry due to its high computation efficiency in predicting the shear deformation of the textile. However, the outputs achievable with this approach are not suitable for the objectives listed above, since only the fiber orientation can be observed. Therefore, FE based approaches describing the mechanical behavior of the textile reinforcement are selected. According to the review of the modeling scales presented in section 2.3 and the objectives of this doctoral thesis, the macroscopic FE approach is identified as the most suitable simulation scale to study the preforming process of dry NCFs. Even though single simulation results at the mesoscopic scale can be reached in 12 hours, iterations and optimization procedures are not feasible. As a consequence, the preforming induced defect considered in this study are the shear deformation, the fiber orientation and the occurrence of wrinkles.

The material model and corresponding calibration procedures must be adequately selected for the development of a macroscopic forming simulation framework. As reviewed in section 2.3.1.1, many software packages propose solutions to model the forming process of dry textiles. Since the present work aims to develop a method suitable in an industrial context, commercially available software packages are favored against academic solutions that require dedicated expertise to perform forming simulations. The software package selected for this doctoral thesis is ABAQUS from Dassault Systèmes / SIMULIA [140]. It is a common FE software package widely adopted in the industry for various applications, such as structural analyses, crash simulations or simulation of manufacturing processes. Moreover, the built-in material model *FABRIC, able to model textile reinforcements, is readily available. Nevertheless, dedicated adaptions of the input data may be required to accurately model the bending behavior of dry NCFs.

One main advantage of multipurpose FE software packages is the possibility to rely on different built-in material behaviors and interaction algorithms. Moreover, the extensive documentation, support and available examples with ABAQUS solvers is a significant benefit. Also, dedicated user subroutines can easily be integrated in the analysis in order to compensate gaps or enhance the built-in solutions. Finally, ABAQUS pre and post processing commands (e.g. the generation of a model geometry or extraction of specific results) rely on the open-source software Python, which has been ranked 3rd by the TIOBE index in January 2021 [166] . As a consequence, ABAQUS modules can easily be integrated in a reliable scripting environment.

3.2 Development of the material model

3.2.1 Description of the *FABRIC material model

The commercially available software package ABAQUS/Explicit from Dassault Systèmes / SIMULIA offers a material model *FABRIC suitable for the simulation of

textiles [143]. The numerical framework is implemented to model the behavior of materials that exhibit two main directions which do not remain orthogonal during the deformation. Applied to a 2D woven fabric, these two main directions correspond to the warp and weft yarn directions. In the present work, the main directions are assimilated to the fiber orientations to generalize the applicability of the *FABRIC model. The definition of the material behavior can be divided into three components: the behavior in the first and second fiber direction, as well as the behavior relative to the change in angle between the fiber directions. The stress-strain relationship of the material can be implemented following two concepts:

- Test-data relation for each component separately.
- Constitutive equations implemented in a user subroutine *VFABRIC. This enables the consideration of interrelations between the components.

The use of test-data relations allows for the inclusion of a large number of phenomena: plasticity, damage, strain-rate dependency, etc. Also, each component can be defined separately in tension and compression, enabling the definition of an asymmetric shear behavior. Using test-data relations, the behavior of each component is defined independently and no interaction between them is possible. On the contrary, the definition of constitutive equations is more flexible and many dependencies between the three components can be implemented. For instance, a tensile-shear dependency could be defined, as presented in [167]. Interactions between the tensile and in-plane shear properties of a biaxial NCFs can be induced by the increase of interaction mechanisms within the textile. Nevertheless, this dependency is difficult to investigate experimentally and is expected to remain small in NCFs compared to other textiles that have interlacing filaments from many layer orientations, such as in woven fabrics. Therefore, interactions between in-plane shear and tensile deformations will be neglected in this doctoral thesis.

3.2.2 Review of bending modeling approaches with *FABRIC

The material model *FABRIC can be used with either membrane or shell elements. In order to accurately model the bending behavior, elements exhibiting rotational degrees of freedoms (i.e. shell elements) are necessary. Using either test-dated based relations or constitutive equations, the calculation of the out-of-plane deformation with *FABRIC material model is based on the in-plane properties of each component. The high tensile modulus of the filaments would yield non-realistic bending properties if conventional integration computation methods of the in-plane properties were used, as is done in the shell elements of ABAQUS/Explicit. A direct decoupling of the in-plane and out-of-plane behaviors is not possible with the use of the material model *FABRIC.

The implementation of a material model that decouples the in-plane and out-of-plane mechanical behaviors was presented by Dörr et al. [168] with newly developed user subroutines for the simulation of thermoplastic fiber reinforced tapes. They used two

distinct kinetically coupled meshes to model the membrane and bending behavior separately.

Other approaches readily usable with conventional shell elements introduce a lower compression modulus to reduce the bending stiffness of the material, as presented by Yu et al [169]. In this case, the neutral axis of the material is shifted toward the stiffer region, leading to an asymmetric stress-strain relationship for a pure bending deformation, as illustrated in Fig. 3-1. The distance between the neutral axis and the mid-plane z_0 depends on the E-Moduli of the two materials, as given in Eq. (3-1). The relation between the bending moment per unit width[1] M and the curvature κ is expressed in Eq. (3-2):

$$z_0 = t\frac{E_{comp} + E_{tens} - 2\sqrt{E_{comp}E_{tens}}}{2\left(E_{comp} - E_{tens}\right)} \tag{3-1}$$

$$M = \frac{\kappa}{24}\left(E_{tens}(t^3 + 3t^2 z_0 - 4{z_0}^3) + E_{comp}(t^3 - 3t^2 z_0 + 4{z_0}^3)\right) \tag{3-2}$$

where E_{tens} and E_{comp} correspond respectively to the tensile and compressive moduli of the bending behavior, and t to the thickness of the textile.

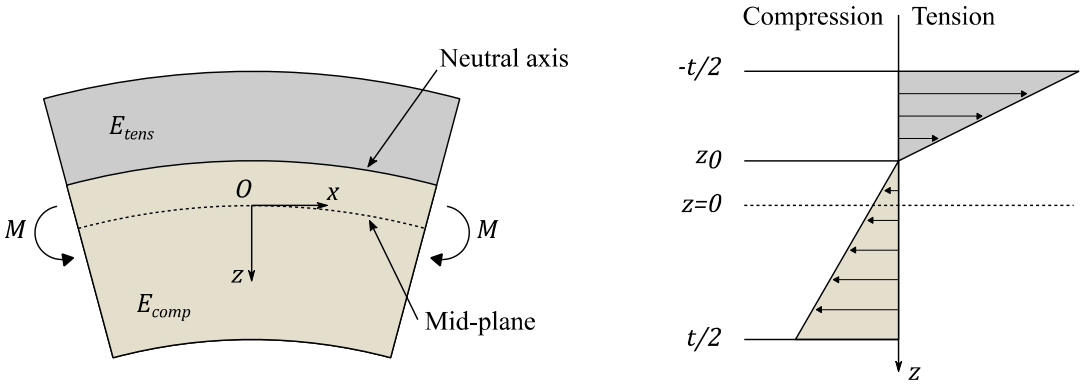

Fig. 3-1: Illustration of the stress-strain relationship for a pure bending moment applied to a material with a lower compression modulus than the tensile modulus, adapted from [169].

This method was successfully applied in diverse studies to model the deformation behavior of dry textiles (e.g. in [107] to model the bending behavior of a woven textile). A priori, this approach is compatible with the *FABRIC material model since the stress-strain relationship in compression can be defined independently from the tensile behavior. Nevertheless, the bending stiffness of dry fabrics exhibit a strong non-linear

[1] In the following, the specification "per unit with" will be omitted for convenience and only "bending moment" will be used.

behavior as reported in section 2.2.3. Therefore, the “bi-material” approach from Yu et al. in [169] must be adapted to improve the description of the bending behavior.

3.2.3 Development of a bi-linear bi-material model

A bi-linear curve is introduced in the compression part of the stress-strain relationship in order to accurately model the loss of stiffness of the material at higher curvatures. Moreover, a locking angle is defined to avoid non-realistic localized high curvatures and to prevent a collapse of the elements. The resulting stress-strain relationship of the material model, referred to as “Bi-Linear Bi-Material (BLBM) model”, is illustrated in Fig. 3-2. Following parameters are introduced:

- E_{tens}: tensile modulus.
- E_{comp}: compression modulus until the onset of the softening.
- E_{soft}: compression modulus of the plateau.
- ε_{soft}: compressive strain at the onset of the softening.
- ε_{lock}: compressive strain at the onset of the locking of the bending deformation.

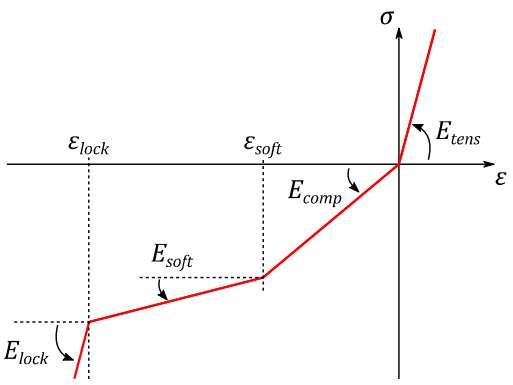

Fig. 3-2: Stress-strain relationship of the bi-linear bi-material model.

At the onset of the softening — referred to as the softening point — the curvature κ_{soft} is related to the parameters of the models due to Kirchhoff–Love theory as follows:

$$\varepsilon_{soft} = \kappa_{soft}\left(\frac{t}{2} - z_0\right) \tag{3-3}$$

From Eqs. (3-1) and (3-3), it ensues:

$$\kappa_{soft} = \frac{\varepsilon_{soft}}{t}\frac{E_{comp} - E_{tens}}{-E_{tens} + \sqrt{E_{comp}E_{tens}}} \tag{3-4}$$

3.2.3.1 $|\kappa| < \kappa_{soft}$

At small curvatures (i.e. until the curvature κ_{soft} is reached) the BLBM model corresponds to the model from Yu et al. [169]. Thus, the bending moment M and the curvature κ follow the linear relation given by Eqs. (3-1) and (3-2).

3.2.3.2 $|\kappa| = \kappa_{soft}$

The bending moment at the softening point M_{soft} can be calculated using the equilibrium of the moments applied to the cross section:

$$M_{soft} = \kappa_{soft}\left(\int_{-\frac{t}{2}}^{z_0} E_{tens} z(z - z_0)dz + \int_{z_0}^{\frac{t}{2}} E_{comp} z(z - z_0)dz\right) \tag{3-5}$$

Using Eq. (3-4):

$$M_{soft} = \frac{\varepsilon_{soft}}{t}\frac{\left(E_{comp} - E_{tens}\right)^2}{24\left(-E_{tens} + \sqrt{E_{comp}E_{tens}}\right)}\left(\frac{t^3\left(E_{comp} + E_{tens}\right)}{E_{comp} - E_{tens}} + \frac{3t^2 z_0\left(-E_{comp} + E_{tens}\right)}{E_{comp} - E_{tens}} + 4{z_0}^3\right) \tag{3-6}$$

3.2.3.3 $\kappa_{soft} < |\kappa| < \kappa_{lock}$

At curvatures larger than κ_{soft}, the relation between M and κ becomes non-linear. The distribution of the stress is characterized by two variables:

- The neutral axis z_0.
- The axis of softening z_p.

These variables can be calculated using the equilibrium of the forces applied on the cross section. It ensues:

$$z_0(\kappa) = \frac{\left(E_{comp}\varepsilon_{soft} - E_{soft}\varepsilon_{soft} + E_{soft}\kappa\frac{t}{2} + E_{tens}\kappa\frac{t}{2}\right)}{\kappa\left(E_{soft} - E_{tens}\right)} \tag{3-7}$$

and

$$z_P(\kappa) = \frac{\varepsilon_{soft}}{\kappa} + z_0 \tag{3-8}$$

Note that the neutral axis z_0 and the axis of softening z_p depend on the curvature applied to the material. Again, the relation between M and γ is calculated using the equilibrium of the moments:

$$M = \kappa\left(\int_{-\frac{t}{2}}^{z_0} E_{tens} z\big(z - z_0(\kappa)\big)dz + \int_{z_0}^{z_p(\kappa)} E_{comp} z\big(z - z_0(\kappa)\big)dz + \int_{z_p(\kappa)}^{\frac{t}{2}} E_{soft} z\big(z - z_0(\kappa)\big)dz\right) + \frac{\big(E_{comp} - E_{soft}\big)\varepsilon_{soft}}{8}\big(t^2 - 4z_p(\kappa)^2\big), \quad \forall\, \kappa_{soft} < |\kappa| \leq \kappa_{lock} \tag{3-9}$$

According to the previous equations, the stress distribution over the thickness in the material can be illustrated as shown in Fig. 3-3.

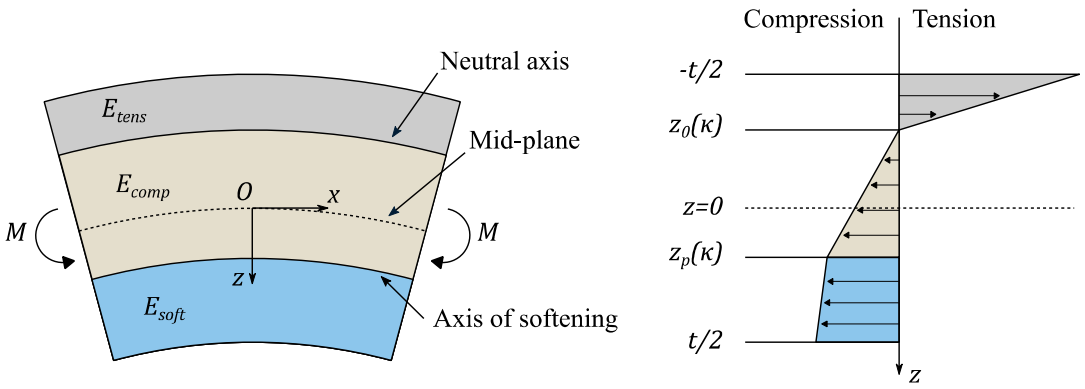

Fig. 3-3: Illustration of the stress-strain relationship for a pure bending moment applied to a material described with the BLBM model, in the case of $\kappa_{soft} < |\kappa| < \kappa_{lock}$.

3.2.3.4 $\kappa = \kappa_{lock}$

The locking curvature is a parameter that depends on the mesh size. It is calculated based on the characteristic length of the mesh elements l_{el} used to discretize the textile in the simulation:

$$\kappa_{lock} = \frac{\sqrt{2}}{l_{el}} \tag{3-10}$$

The corresponding compression strain ε_{lock} at the locking curvature is given by:

$$\varepsilon_{lock} = \frac{\sqrt{2}}{l_{el}}\left(\frac{t}{2} - z_0(\kappa_{lock})\right) \tag{3-11}$$

with $z_0(\kappa_{lock})$ calculated according to Eq. (3-9). The bending moment M_{lock} directly results from Eqs. (3-7) to (3-10).

3.2.3.5 $|\kappa| > \kappa_{lock}$

At curvatures larger than κ_{lock} the compression modulus $E_{lock} = E_{tens}$ is used in the stress-strain relationship to avoid a non-physical collapse of the elements. It leads to a sudden increase of the bending moment, which can be calculated using the equilibrium relations as proposed in the previous sections.

3.2.3.6 Bending moment-curvature relationship

Fig. 3-4 illustrates typical moment-curvature relationships resulting from the BLBM model for curvatures smaller than the locking curvature. The linear part and the onset of the softened behavior are clearly identified in the diagram (the softening point is shown with dashed lines). The softening occurs in two steps. First, a strong non-linear behavior can be observed directly after the softening point. Then, it is followed by an approximately linear portion. Different curves were generated according to the input parameters listed in Tab. 3-1 in order to highlight their influence on the moment-curvature relationship.

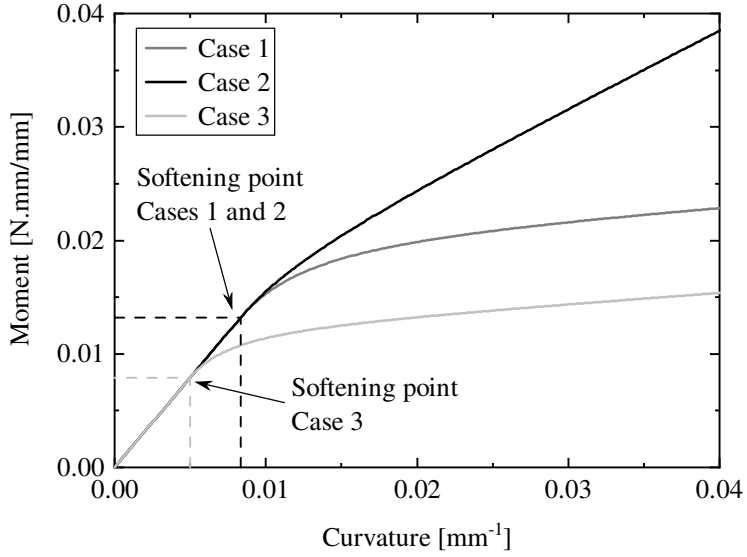

Fig. 3-4: Examples of the moment-curvature relationship according to the BLBM model for curvatures smaller than the locking curvature.
The input parameters of the cases illustrated in this figure are detailed in Tab. 3-1.

The influence of the compression modulus E_{soft} is highlighted by *Case 1* and *Case 2*. Here, the onset of the softened behavior is located at the same curvature (κ_{soft}= 0.0083 mm^{-1}). The linear regime of the softened part is reached faster in *Case 2* than in *Case 1*, due to the smaller difference between E_{comp} and E_{soft}. The difference between *Case 1* and *Case 3* shows two BLBM models with a different softening point. It can be observed that the curves are almost parallel after onset of the softened behavior even though the linear regime is achieved at a smaller curvature in *Case 3*. Finally, it can be concluded that the behavior of the BLBM model is coherent with experiments

reported in the literature and with the characteristic shape of the bending behavior of dry textiles shown in section 2.1.3.3.

Tab. 3-1: Parameters of the BLBM model for the generation of the bending moment-curvature relationships illustrated in Fig. 3-4.

Designation	Case 1	Case 2	Case 3
E_{tens} [GPa]	2.0	2.0	2.0
E_{comp} [MPa]	20	20	20
E_{soft} [MPa]	1.0	8.0	1.0
ε_{soft} [-]	5.0E-3	5.0E-3	3.0E-3
Thickness [mm]	0.66	0.66	0.66

3.3 Calibration of the material model

Experimental characterization methods are used to investigate the material behavior depending on environmental and loading conditions. The description of the material behavior results in the formulation of a material model that relates the applied deformation with the resulting forces. In the context of Finite Element Analysis (FEA), the parameters of a material model are usually referred to as the "material card". The experimental characterization must be performed with regard to the considered deformation mechanisms and modeled physical phenomena.

According to the selected macroscopic simulation approach and the restrictions of this doctoral thesis, following properties must be thoroughly investigated:

- Frictional behavior between the metallic tool and the textile
- In-plane shear behavior of the textile
- Out-of-plane bending behavior of the textile

3.3.1 Frictional behavior

The sliding sledge configuration developed by Leutz [88] was improved to characterize the frictional behavior of the NCF at room temperature. The pulley was shifted upwards in order to reduce the moment generated at the front of the sledge, as illustrated in Fig. 3-5. With this adaptation the force is applied to the anchor with an angle α_{rope} chosen so that the moment applied to the sledge vanishes at the middle of the sliding distance. The distance between the pulley and the sledge was increased to the maximum distance allowed by the testing device to reduce the variation of α_{rope} during the movement of the sledge. Note that the vertical component of the force applied to the sledge reduces the vertical force. This must be considered in the calculation of the friction coefficient as follows:

$$\mu = \frac{F_{sledge} \cdot \cos \alpha_{rope}}{m_{sledge} \cdot g - F_{sledge} \cdot \sin \alpha_{rope}} \tag{3-12}$$

where F_{sledge} corresponds to the force applied to the sledge by the rope and m_{sledge} the mass of the sledge. The angle of the rope at the beginning of the experiment is calculated at $\alpha_{rope,0mm}$= 8.58° and increases to $\alpha_{rope,180mm}$= 22.4° for a cumulated sliding distance of 180 mm.

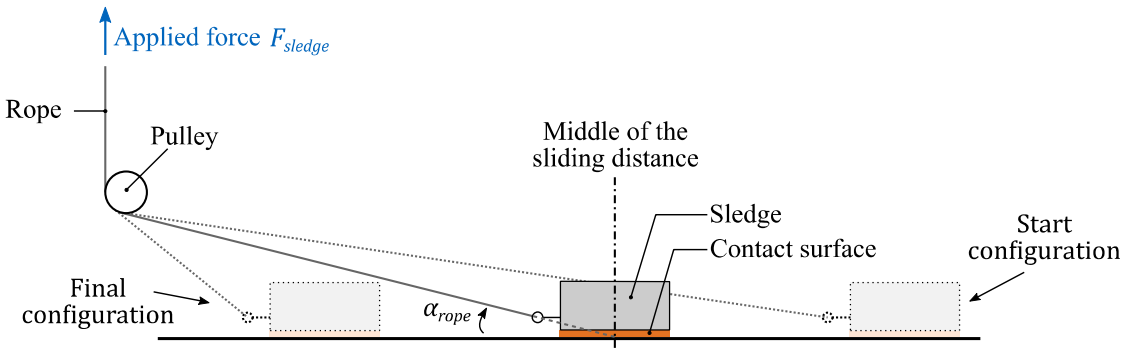

Fig. 3-5: Experimental method for the characterization of the frictional behavior to reduce the moment applied on the sledge.

Due to the different surface properties and the powder binder present on the front surface of the textile, the frictional behavior was tested parallel and perpendicular to the fiber orientation at the front and back surfaces of the textile. This results in four test configurations designated as follows:

- Face of the textile in contact with the metallic plate (“front” or “back”).
- Sliding direction of the sledge with respect to the fiber orientation (0° or 90°).

The sledge used for these experiments has a contact surface of 150x100 mm² and a total weight of 1.21 kg. The experiments were performed at a constant sliding velocity of 100 mm/min and repeated three times for each configuration. A stainless-steel plate representative of the material of forming tools was used in the experiments.

The friction tests were performed in the context of a student thesis [S2]. Fig. 3-6a illustrates the force measured at the crosshead of one representative test. This diagram can be divided into two parts:

- The first part corresponds to an increase of the load applied to the sledge until onset of the displacement, often referred to as the “stick” phase. The end of the first part corresponds to the static friction coefficient μ_s
- The second part represents the force required to apply a constant sliding to the sledge, which is used to calculate the dynamic friction coefficient μ_d

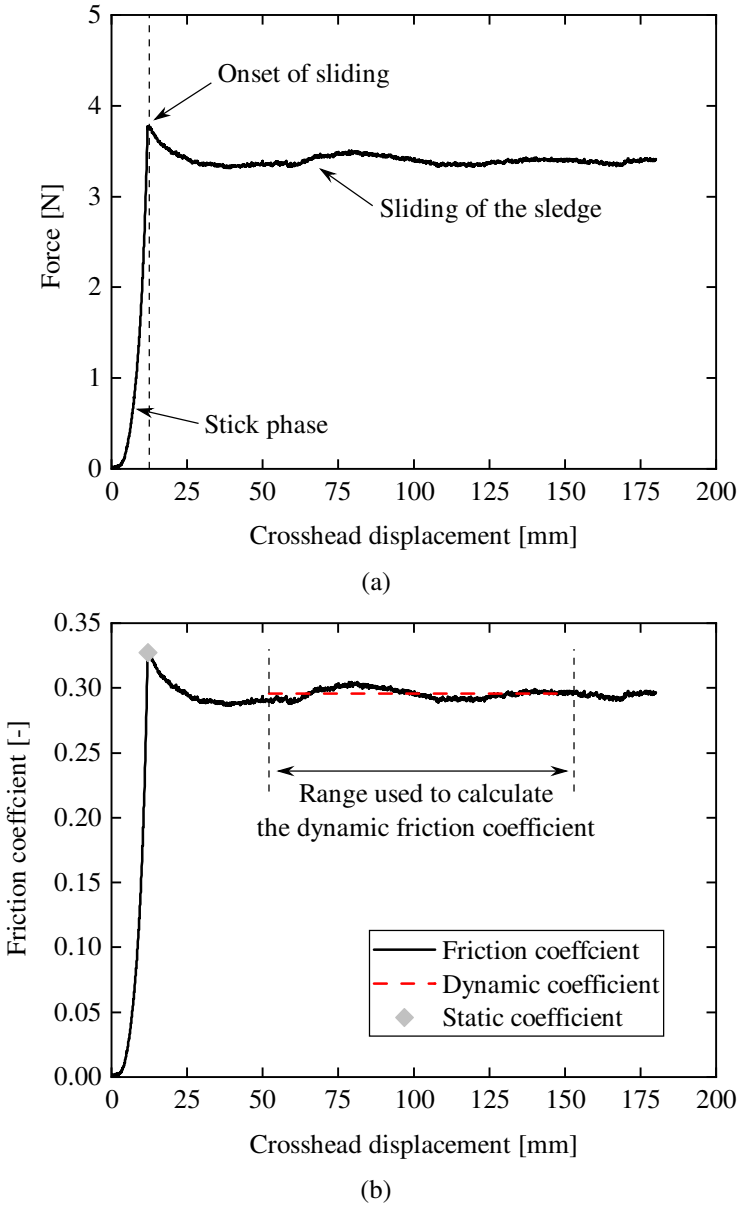

Fig. 3-6: **Test result of a sample representative of the friction characterization: raw measurement of the force at the crosshead (a) and calculated friction coefficient depending on the crosshead displacement (b).**

The static and dynamic friction coefficients are computed separately for each repetition and illustrated in Fig. 3-7a. The mean coefficient of each configuration is shown in Fig. 3-7b and listed in Tab. 3-2 along with their corresponding standard deviations. First, a recurrent difference between the static and dynamic friction coefficients can be observed in all configurations. The dynamic friction coefficient is 6.9% smaller than the static friction coefficient[2]. Moreover, the friction coefficients are higher when sliding

[2] This difference corresponds to the mean of the differences between the dynamic and static coefficients of all configurations.

perpendicular to the fiber direction, with an increase of dynamic friction coefficient of 19% and 14% for the front and back faces, respectively. A possible explanation is that the filaments can slide over microscopic irregularities of the steel plate when they are aligned with the sliding direction. On the contrary, sliding perpendicular to the fiber orientation would lead to a higher adhesion to the steel plate. Finally, no significant difference between the friction coefficients of the front and back faces were observed. As a result, higher dependency of the frictional behavior can be observed on the sliding direction, which should be considered in priority in the interface modeling of the draping simulation.

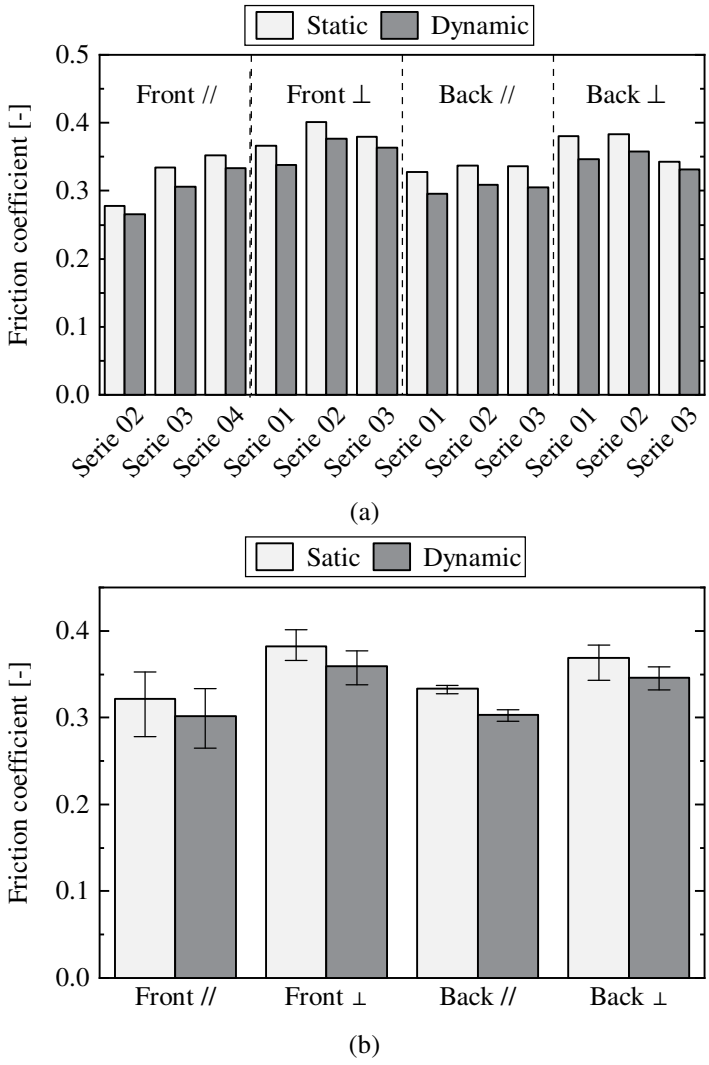

Fig. 3-7: Results of the experimental characterization of the frictional behavior (a) and summary of the results for each configuration (b).
The error bars represent the minimum and maximum values of the respective test series.

Tab. 3-2: Summary of the results of the friction characterization.

	Static coefficient			Dynamic coefficient		
	Mean	**Min**	**Max**	**Mean**	**Min**	**Max**
Front ∥	0.322	0.278	0.353	0.302	0.265	0.333
Front ⊥	0.382	0.366	0.401	0.359	0.338	0.377
Back ∥	0.334	0.328	0.337	0.303	0.296	0.309
Back ⊥	0.369	0.343	0.383	0.346	0.332	0.358

3.3.2 Shear behavior

Due to the reduced applicability of the bias extension test method to NCFs (ref. section 2.2.2.2), the PF test method was preferred to characterize the shear behavior of the dry NCF. The experiments were performed using the PF device illustrated in Fig. 3-8a, which was previously developed by Leutz [88] at the Chair of Carbon Composites of the Technical University of Munich (TUM-LCC).

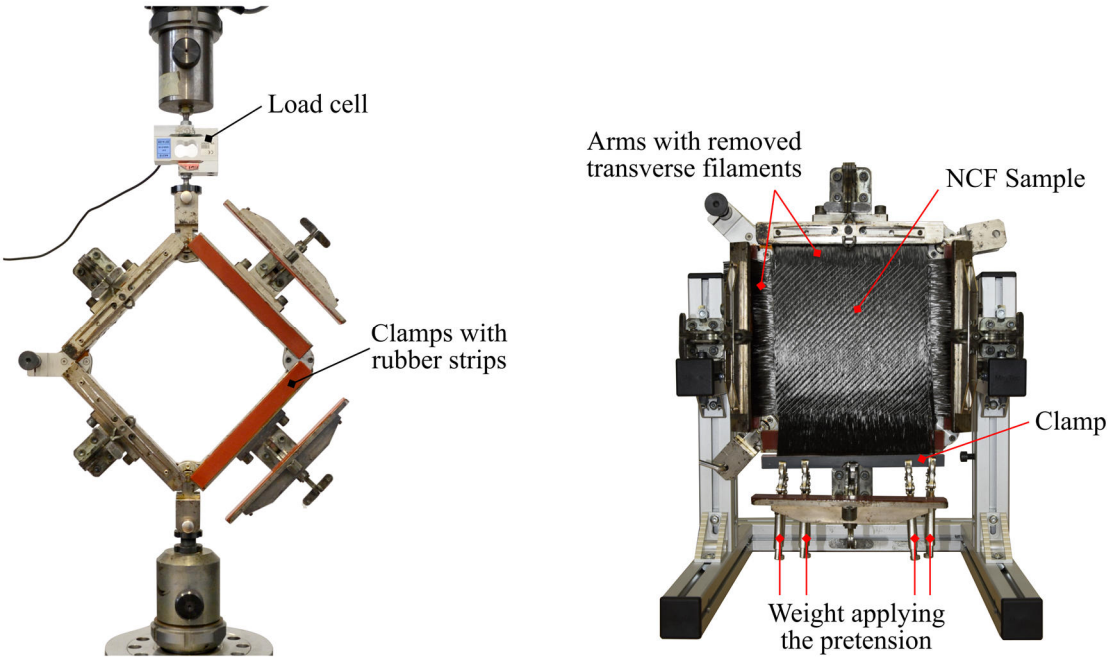

Fig. 3-8: Illustration of the picture frame test rig developed by Leutz [88] (a) and improved preparation of the test specimen (b).

Different measures were taken during the sample preparation to improve the robustness of the experiments. Firstly, the filament in transverse direction and the stitching yarn were removed in the arms of the sample. This reduces the influence of the region outside the sheared zone on the shear behavior. This measure was also presented by the Hong Kong University of Science and Technology in the benchmark of the shear behavior of woven fabrics published in [96]. With this modification of the samples, the shear stiffness of the outer regions is reduced, leading to an increased homogeneity of the

deformation in the sheared zone [18]. The second measure tackles the misorientation and tension in the filaments. A predefined tension of 0.021 N/mm was applied to the sample using a dead weight mounted at the edges of the sample before the clamps of the PF device are closed (see Fig. 3-8b). Although the pretension is not controlled during the test, this procedure enables adjusting the filament orientation and reduces the misorientation of the filaments within the frame.

According to the ABAQUS user manual [143], the material model *FABRIC based on test-data relations requires the calculation of a "nominal shear stress" T_{12} defined as follows:

$$T_{12} = \frac{F_{frame}\, l_{frame}}{{l_{sample}}^2} \frac{\sin\left(\frac{\pi}{4} - \frac{\gamma}{2}\right)}{t_{sample}} \tag{3-13}$$

where, t_{sample} is the initial thickness of the sample. It was measured to 0.66 mm by Bichlmaier in [S2] according to the standard DIN EN ISO 5084 [170].

Note the relation between T_{12} and F_{fabric} (normalized shear force, see Eq. (2-2)):

$$T_{12} = \frac{\cos(\gamma)}{t_{sample}} F_{fabric} \tag{3-14}$$

The influence of test parameters, such as the width of the sample, the pretension of the filaments or the crosshead velocity, were extensively investigated in [S2]. A sample width of 175 mm has been identified as the optimum size to reduce the influence of the boundary effects. For the development of the simulation approach presented in this doctoral thesis, the experiments were performed at room temperature and at a constant crosshead velocity v_{frame} of 100 mm/min. The tests were repeated three times in each shear direction. The relevant parameters are listed in Tab. 3-3.

Tab. 3-3: Experimental parameters of the shear characterization.

Parameter	Unit	Value
l_{frame}	mm	201.5
l_{sample}	mm	175
v_{frame}	mm/min	100
t_{sample}	mm	0.66

The shear characterization was performed in the context of a student thesis [S2]. In this section, the results of the PF tests are illustrated using the normalized shear force F_{fabric}. Note that different opinions can be found in the literature on the loading cycle that should be used for the characterization of dry textiles [18, 95]. Since the forming behavior of the textile is of interest, only the first loading cycle of the sample is considered here.

This choice is supported by the study presented in [S3], showing that forming simulations performed with the second loading cycle only result in a non-realistic forming behavior.

The results of the shear characterization in positive and negative shear directions are presented in Fig. 3-9a and Fig. 3-9b, respectively. Considering that the material model *FABRIC requires a single table for each shear direction, respective mean curves were calculated based on the three repetitions. The mean curves are also illustrated in Fig. 3-9.

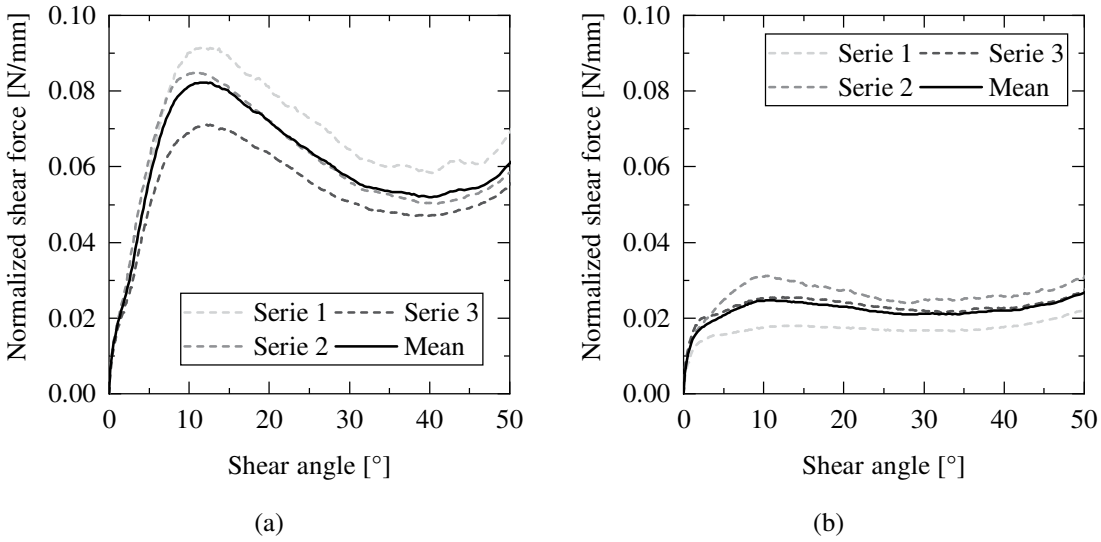

Fig. 3-9: Results of the shear characterization in positive (a) and negative (b) shear directions with respective mean curves.

A similar behavior can be observed in the positive and negative directions. After a linear increase of the shear force, a non-linear part can be observed until a maximum force is reached at a shear angle of approximately 10°. Between shear angles of 10° and 40°, a significant decrease of the shear force is identified in positive direction. This can be attributed to an accommodation of the extension of the stitching yarn on the back face by the transversal displacement (compression) of the yarns on the front face or to the breakage of the binder network at the surface of the textile. Finally, an increase of the shear force is shown at shear angles larger than 40°. This is explained by the loading of the stitching yarn combined with the transverse contact between the filaments and the stitching yarns that restrain the shear deformation of the layers.

A significant asymmetric behavior is found. The ratio between the shear forces in positive and negative directions reaches its maximum at a shear angle of 11.5° and is calculated at 3.35. Note that no difference is noticeable between the positive and negative shear forces for small shear deformations (smaller than 1°). It may be due to a slack in the stitching yarn that requires an extension larger than the initial slack to show a significant contribution to the shear force.

During the shear deformation the onset of local buckling was observed (corresponding to the loops illustrated in Fig. 2-6 as reported by Krieger et al. in [61]. The onset of the first buckles was detected in the range of 5° to 8° shear angle.

The nominal shear stress T_{12} for each shear direction is calculated using the respective mean curves with Eq. (3-14).

3.3.3 Bending behavior

A method to calibrate the BLBM bending model with simple equipment is proposed. First, the experimental method is presented. Due to the complex behavior of textiles, various curvatures must be applied to the textile while accurately measuring the reaction forces. Then, the calibration of the model input parameters is performed using an indirect approach. To that purpose, the bending test is simulated and the results are compared with the experimental results using criteria on the deformed geometry and on the reaction force. Finally, an optimization strategy is implemented to calibrate the input parameters of the material models.

3.3.3.1 Experimental method

In order to calibrate the material model, the bending moment-curvature relationship must be measured experimentally. According to the complexity of pure bending test devices, the generation of a pure bending deformation is not further considered in this thesis. Therefore, the experimental method must be able to fulfill following objectives:

1. Generate an adequate range of curvatures representative of the deformation during preforming.
2. Observe and extract the deformed geometry of the sample.
3. Measure the forces applied to the sample (i.e. the reaction forces).

The test method consists of the buckling of a rectangular textile sample on a planar surface. For this experiment, a sample is constituted of two strips of textile cut along the fiber orientation and joined with a soft tape (ref. Fig. 3-10a). The tape ensures a pivot articulation between the two strips, which facilitates the handling of the sample in order to avoid any deformation of the sample prior to the bending experiment. First, the sample is fold at its pivot, clamped at the free end, and hang vertically (as illustrated in Fig. 3-10b). This step resembles the pear loop configuration described by Peirce in [82]. Then, the sample is formed over a horizontal plate in order to generate various curvatures in the sample (see, Fig. 3-10c). The experiment is stopped when a sufficient contact length between the strips and the horizontal plate is reached, as shown in Fig. 3-10d. The shape of the sample is recorded with a digital camera and the reaction force is measured at the clamp or at the horizontal plate.

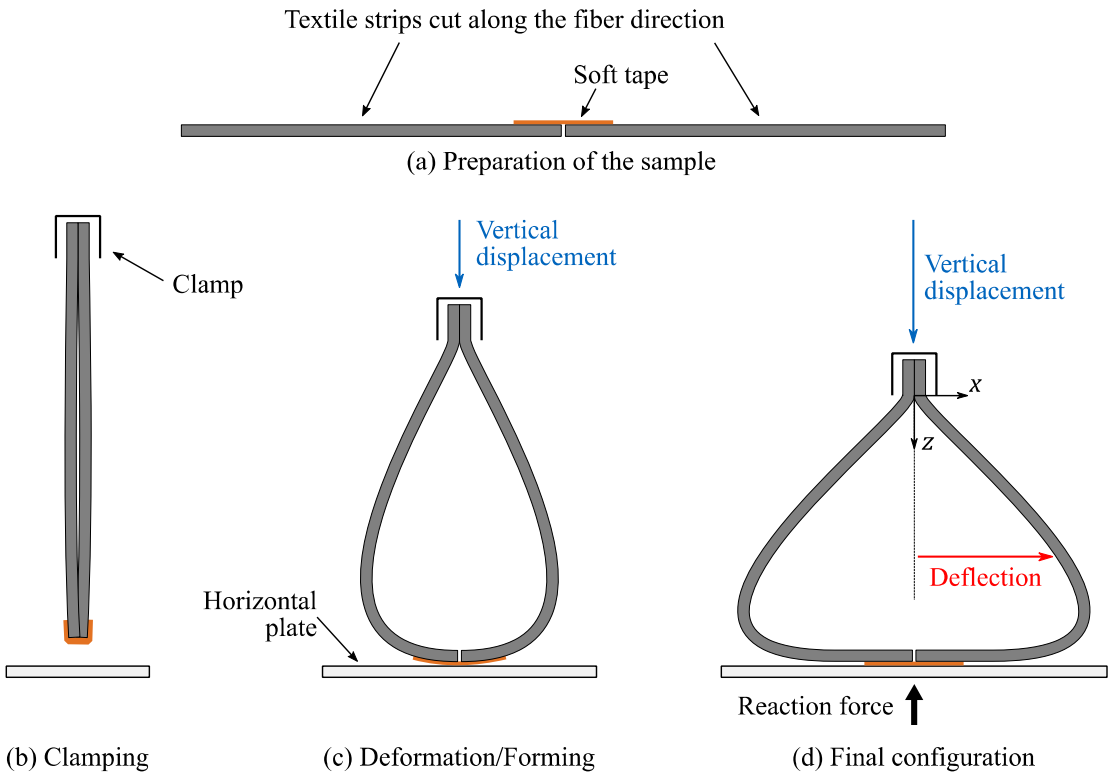

Fig. 3-10: Working principle of the bending tests for material calibration: sample preparation (a) and successive steps of the experiment (b) to (d).

This rather simple method fulfills the three objectives listed above. The main advantage is that rudimentary devices can be used to generate the displacement as long as the final configuration is precisely achieved and recorded in each experiment. Also, the reaction force can be measured with a precise weighing scale or with a load cell. Depending on the bending behavior of the textile, the final configuration can be adapted to generate different curvatures. In this doctoral thesis, the test method uses manual sliders for the linear displacement and a weighing scale for the reaction force measurement. The test setup was partly developed in [S4] and adapted in [S5]. The final device is shown in Fig. 3-11. Spacers are used to precisely determine the final position of the clamp. Note that sand paper was applied to the horizontal plate in order to avoid any slippage of the sample at the contact surface with the plate.

In the development of this test method, a dedicated attention was paid to the load introduction of the textile to reduce the influence of transversal forces. As reported in [S4] and [S5], deformation of the textile induced by local transverse contacts may lead to local buckling of the filament and, thus, to a localization of bending deformation that can hardly be considered in forming simulations. Here, the contact surface between the two strips at the upper clamp stabilizes the textile. In addition, the distributed contact with the horizontal plate ensures a smooth distribution and transition of the transverse force. The clamp designed for this test bench is divided into two parts. The first part maintains the sample in the folded configuration while being hung to the test bench. The

second part of the clamp is applied to the sample shortly before the start of the experiment (configuration showed in Fig. 3-10b) to ensure that the remaining free length of the sample — especially near the clamp — was not deformed prior to the experiment (e.g. during the preparation of the sample).

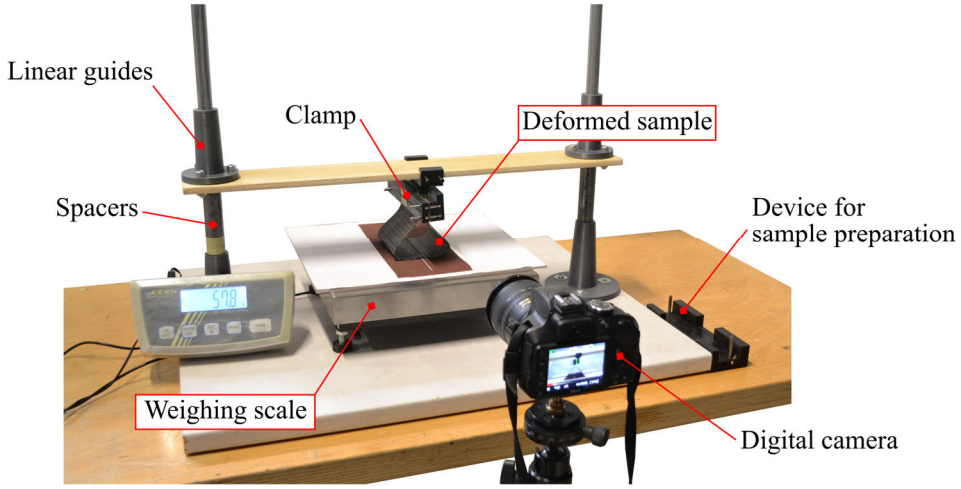

Fig. 3-11: Experimental bending test setup for the calibration of the bending behavior of dry textiles.

The textile strips have a width of 100 mm and a free length of 125 mm each. The final distance between the clamp and the horizontal plane is set to 75 mm. The front face of the NCF is placed at the external face of the sample and, thus, comes into contact with the horizontal plate. The final configuration of a representative test result is shown in Fig. 3-12.

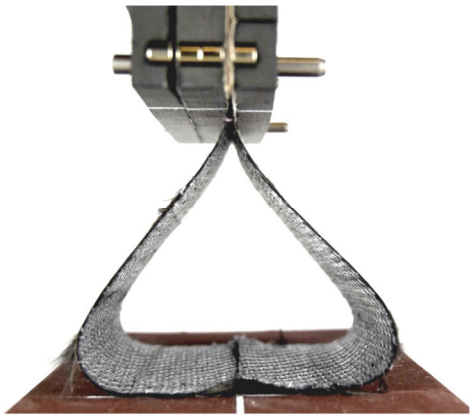

Fig. 3-12: Final configuration of a bending experiment with a ±45° NCF sample.

The geometry of the sample in the final configuration is recorded with a digital camera. The deformed geometry is manually extracted with a minimum of hundred points distributed over the whole sample length and the deflection is separately computed for each side of the sample. In order to reduce the influence of spurious waviness at the contact

of the plate, the extraction of the sample geometry is stopped 2 mm before the plate (along the vertical axis).

The main drawback is the potential asymmetric deformation of the sample if the textile strips were deformed prior to the experiment or if the contact of the tip with the horizontal plate is not exactly aligned with the clamp. Thus, specific criteria for the acceptability of tests must be defined. In order to discard experiments with non-symmetric deformations, i.e. not in accordance with the test requirements, a threshold is set on the finale shape of the sample. To that end, the difference between the deflection of the left and right parts is computed at a height of 37.5 mm. The test result is discarded if the difference exceeds 15% of the mean deflection at this height. Finally, the mean deflection of the left and right parts is computed for each of these experiments.

3.3.3.2 Experimental results

Nine experimental trials were performed. According to the symmetric deformation criterion, five repetitions were selected for the characterization of the textile behavior. The corresponding results are listed in Tab. 3-4. The resulting left/right mean deflection of each experiment is illustrated in Fig. 3-13a along with the mean value of all experiments. The curvature calculated with the mean result of all experiments is shown in Fig. 3-13b.

Tab. 3-4: Test results of the bending experiments according to the selection criterion

Serie ID	Reaction force [mN]	Left to right deflection difference [%]
1	179	13.7
2	182	13.2
3	224	8.95
5	159	4.91
8	167	8.68
Mean	182	

An initial curvature is observed near the clamps and decreases until a straight part at the mid height of the deformed sample. A subsequent localization of the curvature is observed, which reaches a maximum of 0.11 mm^{-1} at a vertical axis of 64.5 mm. This corresponds to a minimum radius of curvature of 9.28 mm. As a consequence, the experimental approach is able to generate a large range of curvatures with a localization of the deformation, which is representative of a local wrinkle.

In addition, the results show a small variability between the experiments. A maximum deviation of 2.4 mm is measured at a vertical axis of 40.1 mm, which corresponds to 8.3% of the mean deflection at this position.

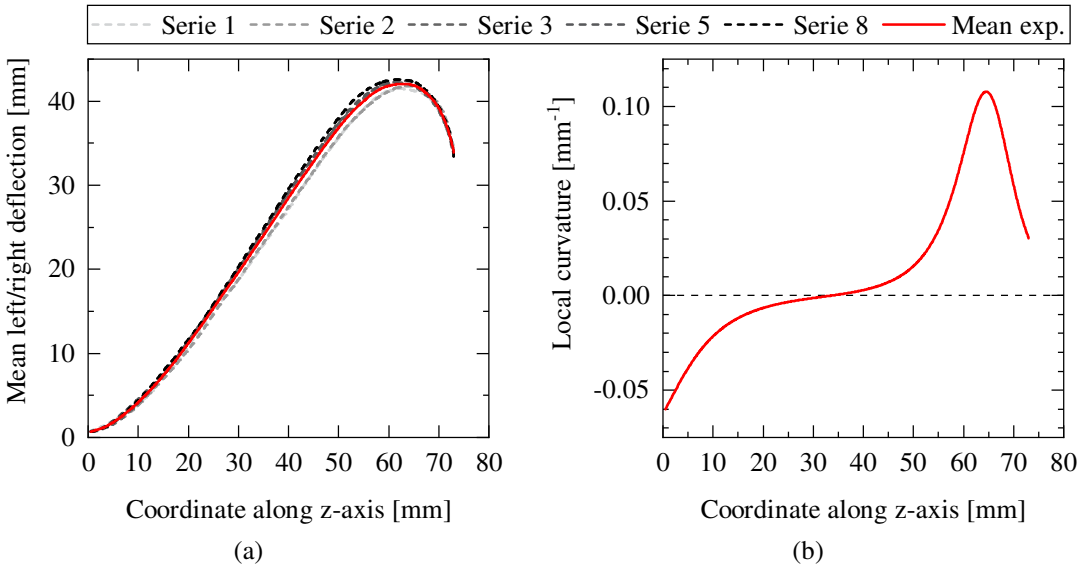

Fig. 3-13: **Results of the mean left/right deflection for each bending experiment and computed mean value of all experiments (a) and experimental curvature calculated with the mean result (b).**

3.3.3.3 Indirect calibration

Due to the high complexity of the deformation and of the stress state induced in the textile sample, an indirect approach is proposed. Here, the experiments are numerically simulated using the material model introduced in section 3.2.

In order to calibrate the material card (i.e. inputs of the material model), simulations are performed with various model inputs. The respective comparison of the numerical results with the experiments enables the identification of the most suitable set of parameters. Therefore, the indirect approach can be assimilated to a structural optimization problem. As presented in [171], a structural optimization problem consists of the structural model (or structural analysis), the optimization model and the optimization algorithm.

Structural model:

According to the symmetry of the material and of the test setup, the model of the experiments is reduced to a quarter of the sample. The upper edge of the sample is fully clamped and a pivot articulation is defined at the lower tip. The deformation of the samples is applied through vertical displacement of the clamp until the final configuration is reached. The simulation is performed using the explicit solver ABAQUS/Explicit.

The FEA is based on the solver ABAQUS/Explicit. This integration scheme involves a large number of successive integration step to model the whole process. This is an efficient method to account for large displacements and non-linearity but the accuracy of the simulation is directly related to the size of the increments. Thereby, the increment size must remain smaller than the critical increment size Δt_c, which is calculated based

on the mesh size, the stiffness of the material and its density. It ensures that the fastest deformation only propagates to the subsequent element in one increment. An approximate calculation of the critical increment size neglecting damping parameters is given in Eq. (3-15).

$$\Delta t_c \approx L_{min} \sqrt{\frac{\rho(1-2\nu)}{E}} \tag{3-15}$$

with L_{min} the smallest element length of the mesh, ρ the density, ν the Poisson's ratio and E the elastic modulus of the material.

Explicit integration schemes are principally dedicated to model transient cases with highly dynamic deformations and short durations, such as for impact analysis [172]. The use of the explicit integration scheme for the simulation of the forming experiment requires the introduction of scaling factors to increase the size of the critical time step and reduce the number of increments required to model the whole process. Based on (3-15) different methods can be proposed:

- Reduce the stiffness of the material.
- Increase the density of the material.
- Increase the mesh size.
- Increase the displacement velocity to reduce the number of increments required for the whole simulation.

In the context of this doctoral thesis, the tensile stiffness and the density of the material are varied to increase the critical time step.

First, the tensile stiffness of the textile is reduced. Due to its fibrous structure, the textile exhibits a high tensile stiffness in filament direction compared to the shear and bending stiffness. Thus, the tensile stiffness can be reduced as long as it remains significantly higher than the shear and bending stiffness. Due to the low velocity of the stamp, the deformations can be approximated as quasi-static deformations. Therefore, the mass can be increased to reduce the computation time but it is necessary to ensure that the kinematic energy involved in the model remains small compared to the other energies [173]. The final parameters selected for the simulation are listed in Tab. 3-5. These parameters were optimized to increase the critical time step while maintaining their influence on the final result negligible. The optimization of the calculation duration is presented in [S5], which results in a total duration of one hour on one Central Processing Unit (CPU).

Tab. 3-5: Input parameters of the structural model of the indirect bending calibration

Variable	Unit	Value
E_{tens}	[GPa]	2.0
L	[mm]	2.5
ρ	[ton/mm³]	1.93E-07
Δt_c	[s]	2.21E-05

Optimization model:

The design of an optimization model covers the definition of the objectives, the variables and their boundaries. The objective functions are defined as the quantified comparison between the simulation and experimental results. Two objective functions are required for the absolute characterization of the bending model parameters:

- The shapes of the final state are compared in order to characterize the relative evolution of the bending rigidity depending on the curvature (i.e. to calibrate the non-linearity of the material). To that end, the area between the deformed mesh geometry of the simulation and the experimental curves is calculated for each experiment, referred to as A_i, were i corresponds to the test ID. The mean value A_{mean} of all experiments is computed.
- The comparison of the reaction force (measured on the horizontal plate) between the simulation F_{sim} and the mean experimental result F_{exp} ensures the absolute calibration of the parameters.

The use of multiple objective functions for the indirect parameter calibration is analogous to a multi-criteria optimization. One common approach presented in [174] relies on the minimization of the Euclidian norm of the normalized distance d_j between the simulation result j and the reference point, defined as follows:

$$\left|d_j\right| = \sqrt{{d_{A,j}}^2 + {d_{A,j}}^2} \tag{3-16}$$

with

$$d_{A,j} = \frac{A_{mean,j} - A^*}{A^*} \tag{3-17}$$

$$d_{F,j} = \frac{\left|F_{sim,j} - F^*\right|}{F^*} \tag{3-18}$$

where $A^*$and F^* correspond to the reference area and the reference force, respectively.

The reference force F^* is defined as the mean force of the experimental results. According to Tab. 3-4, F^*= 182 mN.

The reference area A^* is zero in the ideal case. Nevertheless, a zero area can be achieved only in the perfect case where all experimental results are exactly the same. Due to the variations previously observed, the reference area is defined as the lowest result achievable with the set of experimental results. To that end, a separate optimization was performed to find the deflection curve that minimizes the area A_{mean}. Using a curve discretized in fifty points, it was found that A^*= 34.4 mm².

The variables of the optimization problems are the three parameters of the material models: E_{comp}, E_{soft}, ε_{soft}. The boundaries of the variables are set according to Tab. 3-6. They derive from a previous manual calibration of the parameters presented in [S3], which uses experimental results of single cantilever tests.

Tab. 3-6: Boundaries of the optimization variables for the indirect characterization of the bending model.

Variable	Minimum	Maximum
E_{comp} [MPa]	5	100
E_{soft} [MPa]	0.1	5
ε_{soft} [-]	2.50E-04	5.00E-03

Optimization algorithm:

Due to the high duration of a single simulation, a response surface method is used to find the optimum material parameters with a sampling of the parameters based on a stochastic Design of Experiments (DoE). The response of the numerical model is observed for different sets of input parameters, which are distributed within the design space. Since this method only provides an estimation of the optimum solution, a sufficiently high number of input sets shall be used. In addition, the distribution of the sets of input parameters is performed using the Latin Hypercube Sampling (LHS) method, which is a stochastic approach that randomly distributes the input parameters within the design space with improved filling properties [175]. The distribution is performed using the LHS method with space-filling option available in the python library DOEPY [176] to generate 500 sets of input parameters.

The response surface method offers the advantage of easier parallelization of the FEA since the input configurations are defined at the beginning of the DoE study and do not depend on previous configurations to generate the following set of inputs.

Results

The results of the DoE study are shown in Fig. 3-14. The normalized distances of the objective functions d_A and d_F are illustrated for each set of inputs.

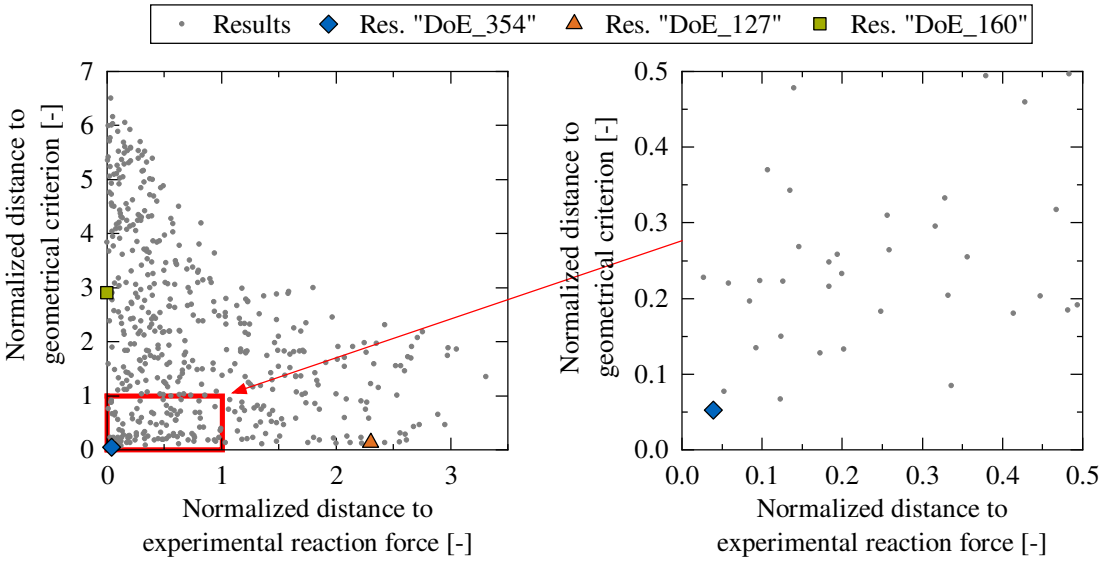

Fig. 3-14: Result of the DoE study implemented with 500 sets of inputs for the calibration of the bending model.

A wide range of results was achieved showing a strong density around the reference configuration. According to the minimization of the normalized distance d_j, the set of parameters *DoE_354* is identified as the best set from all five hundred configurations. Fig. 3-15 illustrates the comparison of the deformed shape between the simulation and the experimental results. The input parameters and the results of the objectives functions A_{mean} and F_{sim} are listed in Tab. 3-7. It can be observed that A_{mean} increases of only 5.2% compared to the reference area. Moreover, the relative error of the reaction force is smaller than 4% and the simulation result lies within the range of experimental results.

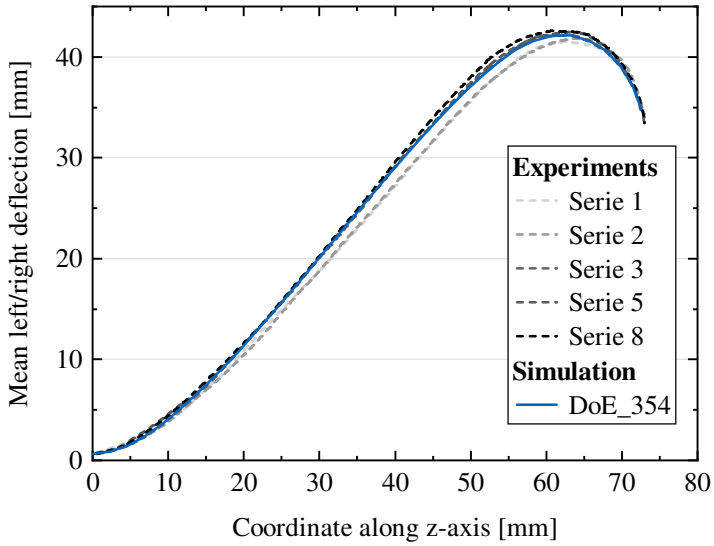

Fig. 3-15: Comparison of the deformed shape of the samples between the simulation result DoE_354 and the experiments.

Tab. 3-7: Input parameters of the set DoE_354 and results of the objective functions

Variable	Unit	Value
E_{comp}	[MPa]	20.2
E_{soft}	[MPa]	0.925
ε_{soft}	[-]	3.90E-03
A_{mean}	[mm²]	36.1
F_{sim}	[mN]	175

Further observations

In order to emphasize the importance of both objective functions and, thus, of fitting both the forces and the deformations, two further results of the DoE study are observed. Firstly, *DoE_127* (identified as a red triangle in Fig. 3-14) delivers a good fit of the final shape of the sample (comparable to that of *DoE_354*), whereas the reaction force strongly deviates from experimental results. Similarly, *DoE_160* (identified as the red cross in Fig. 3-14) delivers the best fit of the reaction force but fails to reproduce the geometry of the final shape. The input parameters and the corresponding results are listed in Tab. 3-8. The moment-curvature relationships of those input sets are illustrated in Fig. 3-16 along with their respective final deformed shapes.

Tab. 3-8: Input parameters of selected sets of the DoE study, corresponding normalized distances of the objective functions and Euclidian distance to the reference point.

DoE ID	E_{comp} [MPa]	E_{soft} [MPa]	ε_{soft} [-]	d_A [-]	d_F [-]	$\lvert d \rvert$ [-]
354	20.2	0.925	3.93E-03	5.21E-2	3.91E-2	6.51E-2
127	98.7	1.88	3.90E-03	0.127	2.30	2.30
160	43.6	0.267	2.51E-03	2.90	2.02E-3	2.90

Although the moment of the parameters *DoE_160* is larger than that of *DoE_354* for all curvature values, the strong localization of the curvature creates a low reaction force close to the experimental result (i.e. close to *DoE_354*). On the contrary, the geometry of the simulation result *DoE_127* is very close to the deformed shape of the sample but the forces are strongly overestimated (factor 3.3 between the reaction forces). As a consequence, using the input parameters of *DoE_127* would significantly overestimate the absolute bending stiffness of the textile, which emphasizes the importance of both criteria.

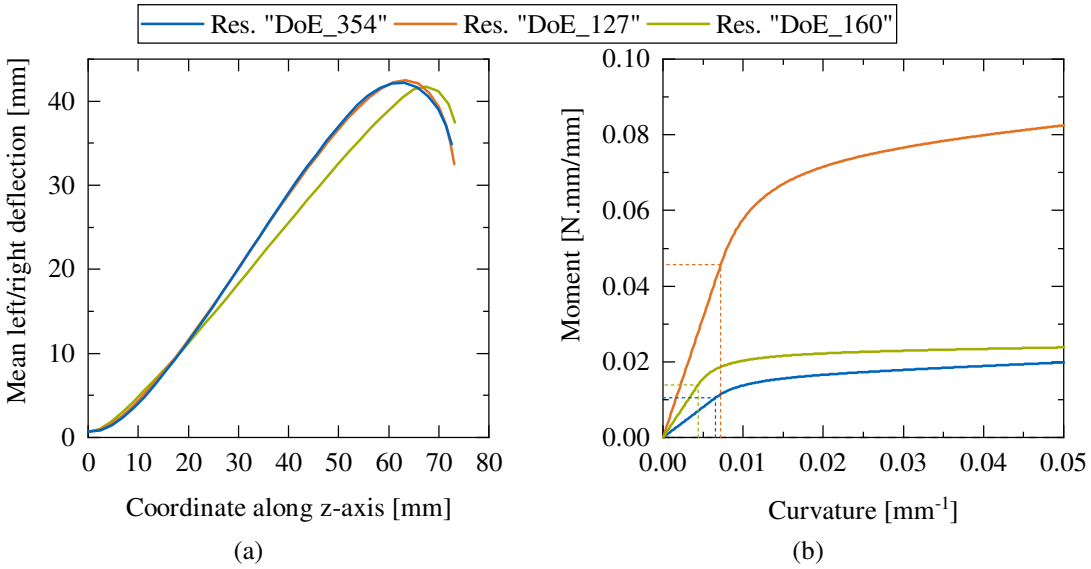

Fig. 3-16: Resulting deflections (a) and bending moment-curvature relationships (b) of simulation results with various input parameters.
The dotted lines in diagram (b) show the softening points (i.e. onset of the non-linear behavior) of the respective bending moment-curvature relationships.

3.3.3.4 Conclusion

A method was presented to calibrate the bending properties of soft materials that exhibit a strong non-linear behavior, such as dry NCFs. The experimental principle is based on a forming experiment that induces a large range of curvatures in the sample. The measurement of the reaction force and the extraction of the final sample geometry enables an indirect calibration of the material models. A sampling of five hundred configurations was performed using the LHS method. The best configuration was identified based on the normalized distance of objectives on the deformed geometry and on the reaction force. Moreover, it was shown that the consideration of the deformed geometry and the resulting force is crucial for the calibration. The material parameters of the best result and the corresponding characteristics are listed in Tab. 3-9. These parameters will be used in the subsequent sections to describe the bending behavior of the ±45° NCF.

Tab. 3-9: Summary of the bending characterization with the BLBM bending model.

Variable	Unit	Value
E_{comp}	[MPa]	20.2
E_{soft}	[MPa]	0.925
ε_{soft}	[-]	3.90E-03
M_{soft}	[mN.mm/mm]	10.5
κ_{soft}	[m^{-1}]	6.56

3.4 Validation of the forming simulation approach

Numerical simulations of the forming behavior of textile are useful at different steps of the development of a new component. Nevertheless, the accuracy of the simulation approach is primordial to draw the right conclusions and support the development process. Therefore, an intermediate step aiming at the validation of the simulation approach is necessary. This subsection focuses on the validation of the developed approach to accurately predict the deformation behavior of the textile applied to the forming of a generic component geometry. First, the forming experiments and the corresponding simulation model are described. Afterwards, the validation criteria are defined. Finally, experimental and simulation results are compared to assess the accuracy of the simulation approach.

3.4.1 Forming experiment

The forming process selected in this doctoral thesis is a stamping process with one punch pushed through the textile and a blank-holder, as depicted in Fig. 3-17. Since there is no opposite mold, the deformed geometry results from a combination of forces induced by the punch, the blank-holder and the base plate only. Here, the blank-holder is able to move vertically, applying a constant force to the textile due to its own weight. This setup allows for observations of the deformed geometry of the textile during the whole experiment without releasing any force or removing components. Therefore, various criteria can be used to validate the simulation approach.

The geometry of the punch is a hemisphere with a radius of 63.5 cm. The deformation of the textile over the hemisphere induces double curvatures in the textile, which is representative of industrial part shapes. Moreover, the deformation of textiles over a hemispheric geometry involve large shear and bending deformations to accommodate the surface. Therefore, this geometry enables an accurate validation of the shear and bending behaviors. The circular blank-holder has an internal and external radius of 90 mm and 120 mm respectively and weights 1.65 kg. The experiments were carried out on square samples of single plies of NCFs with a geometry of a 350x350 mm^2 aligned with the fiber orientations (i.e. the direction of the loops of the stitching yarns is aligned with the

diagonal of the sample). This setup can highlight and quantify the asymmetry of the preform deformation. The experiments were performed at room temperature and with constant punch velocity of 100 mm/min in the context of a master's thesis [S3].

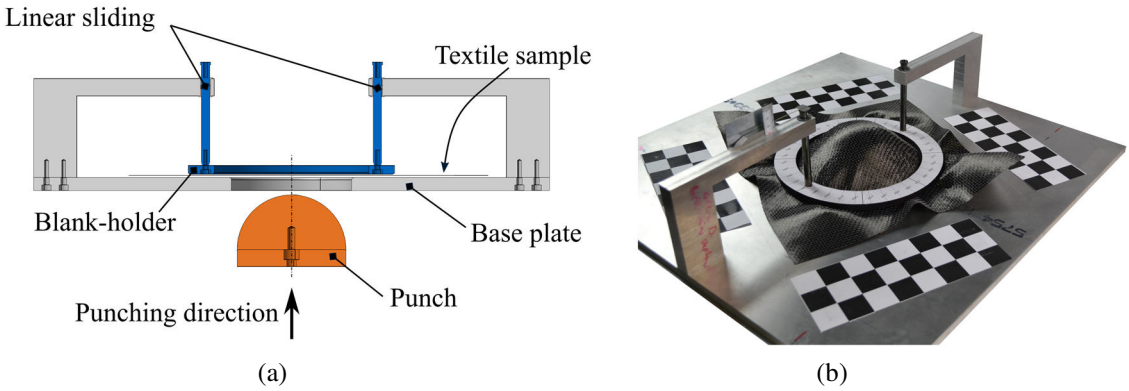

Fig. 3-17: Experimental forming setup of the hemisphere punching test bench (a) and example of a forming experiment (b).

3.4.2 Simulation model

In order to validate the simulation approach, the experimental process must be reproduced numerically. The selected macroscopic scale models all components, interactions and process parameters. Due to the high stiffness of the metallic parts (blank-holder, ground plate and stamp) compared to the deformability of the textile, only the outer surfaces of the metallic parts in contact with the textile are considered. They are modeled as rigid surfaces. The weight of the blank-holder is applied as an external force to the blank-holder to reduce the dynamic effects. The textile is modeled with the *FABRIC material model presented in section 3.2 using the calibrated input parameters of sections 3.3.2 and 3.3.3. The stamp velocity is adapted in order to optimize the calculation and to reduce dynamic effects. The resulting parameters are listed in Tab. 3-10. They lead to a total computation duration of about twelve hours on four CPUs. More details on the optimization of the material and processes parameters can be found in [S3].

Tab. 3-10: Input parameters for the validation of the simulation approach.

Variable	Unit	Value
E_{tens}	[GPa]	2.0
l_{el}	[mm]	5.0
ρ	[ton/mm³]	4.84E-08
Δt_c	[s]	2.22E-05

The interaction between the textile and the metallic part is modeled with an anisotropic friction model. This model was released in the version ABAQUS2017, which accounts for differences in friction coefficients depending on the material orientation and relative displacement directions [177]. The input parameters are derived from the material and interface characterization presented in section 3.3.1.

3.4.3 Validation criteria

A large number of comparison criteria are used to prove the ability of the simulation method to predict the fiber orientation, reproduce the asymmetric shear deformation, locate the onset of wrinkles and predict the forces involved in the process.

3.4.3.1 Fiber orientation

. Due to the anisotropic properties of composite parts, deviations of the fiber orientation from the designed path can considerably impact the part performance. Therefore, the prediction of the fiber orientation is the most important output of the forming simulation and is selected as the first criterion. To that end, a procedure to measure and compare the fiber orientation on the surface of the textile was developed. The experimental measurements were performed using an optical sensor FScan from the Profactor GmbH [178, 179]. The sensor measures the direction of the filaments on the surface of the preform and the results are computed over an area of 12.5x30 mm² with a resolution of 15 µm/px. The mean value over this area is used to characterize the fiber orientation of the surface. A total of twenty-five Regions Of Interest (ROIs) were defined to study the distribution of the fiber orientation in different regions of the preform, as shown in Fig. 3-18a and listed in appendix a.

The ROIs are defined tangential to the surface of the textile. The measurement field of the sensor is aligned with the projection of the y-axis presented in Fig. 3-18a (corresponds to the fiber orientation of the upper layer before forming). This projection is used as reference in order to measure the fiber orientation and quantify the variations. Therefore, all angles are measured in the respective planes of the ROIs and are referred to as “azimuthal angle” in the following. The ROIs are located along the symmetry plane of the setup (x-axis and y-axis) and in the regions of high shear deformation. Changes of fiber orientation along the intersection of the symmetry planes and asymmetric deformation in the sheared zones would be a first evidence of the asymmetric shear behavior of the textile. More details on the locations and orientations of the ROIs can be found in [S3].

The optical sensor is mounted on a robot to ensure a precise and reproducible positioning of the sensor. As the textile surface is accessible during the whole experiments, the measurements can be performed before forming and at different stages of the forming process (here at 49.7 mm and 65 mm forming stroke). The final setup is illustrated in Fig. 3-18b. The azimuthal angle of the simulation is computed with a similar procedure for each ROI. First, an algorithm searches the mesh elements located within the ROI. Then, the fiber direction of each element is projected onto the surface of the ROI. Finally, the azimuthal angle is calculated, defined as the mean direction of all projected directions. More details on the procedure to compare the results of the simulation with the experiments can be found in [S6].

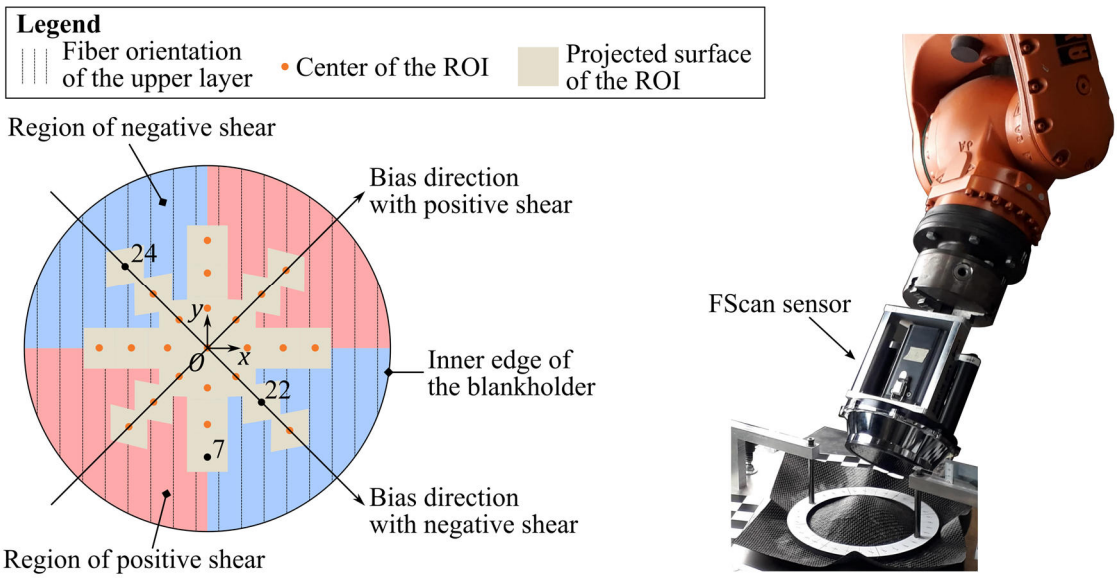

Fig. 3-18: Definition of the ROIs for the comparison of the fiber orientation (a) and experimental setup with the F-Scan sensor (b).

3.4.3.2 Textile draw-in

The shape of the outer part of the preform and the respective draw-in is a common criterion for the comparison of forming simulations with experimental results. The textile draw-in highlights the cumulated deformation, and thus enables verifying the deformation behavior of the whole sample. In this section, the draw-in is used in order to quantify the asymmetric deformation of the textile. To that end, pictures of the final shape of the preforms were recorded and the projected distance between each corner and the center of the setup was measured using image post-treatment. The draw-in of a corner k, referred to as $di_{C,k}$, is defined as the change in length between the initial and final configuration. The corners are labelled as presented in Fig. 3-19. The draw-in ratio di_{ratio} — quantifying the asymmetric deformation — is given by:

$$di_{ratio} = \frac{di_{c,1} + di_{c,3}}{di_{C,2} + di_{C,4}} \tag{3-19}$$

3.4.3.3 Wrinkling profile

The third criterion targets the onset of wrinkles in the inner part of the blank-holder. In this region, the balance between bending and shear stiffness is essential to predict the onset of out-of-plane deformations. During the experiments, a line at a height of 21 mm is projected on the textile surface with linear lasers. Pictures of the preforms were recorded at the final stage of the experiments. The distance d_w between the center of the setup and the red line was manually measured in the pictures with a polar angle pitch of 2.5° (see Fig. 3-19 for the definition of the polar angle θ_W).

This procedure is close to the experimental approach proposed by Arnold et al. [180], in which the 3D deformation geometry of the whole textile surface was recorded. Here, the size and location of the wrinkles can be identified efficiently.

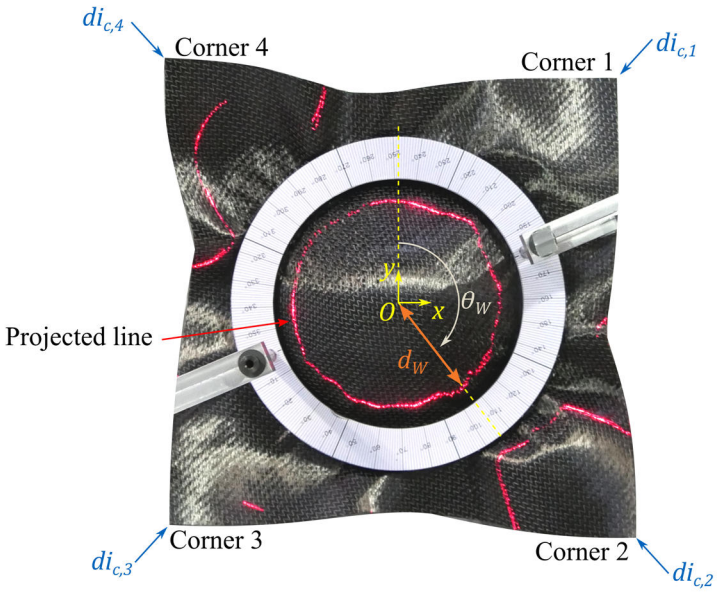

Fig. 3-19: Measurement of the corner draw-in of the preform and definition of the parameters to quantify the wrinkling profile.

3.4.3.4 Forces involved in the process

The last criterion identifies the level of forces involved during the forming process. The vertical lift of the blank-holder and the reaction force on the stamp were measured during the experiments. Theses quantities are complementary, since the blank-holder applies a defined force to the textile due to its own weight and the stamp imposes the forming deformation. Note that the reaction force and the blank-holder displacement result from the stiffness of the textile, the onset of wrinkles and the friction between the textile and the metallic parts.

3.4.4 Results

Experimental trials were performed in order to generate three results for each criterion. Various test setups were required to obtain the necessary data. Here, four test configurations were used, leading to a total of twelve experimental trials.

Pictures of the final shapes of the three experimental trials used for the geometrical criteria (Series 1 to 3) are illustrated in Fig. 3-20 along with the simulation result.

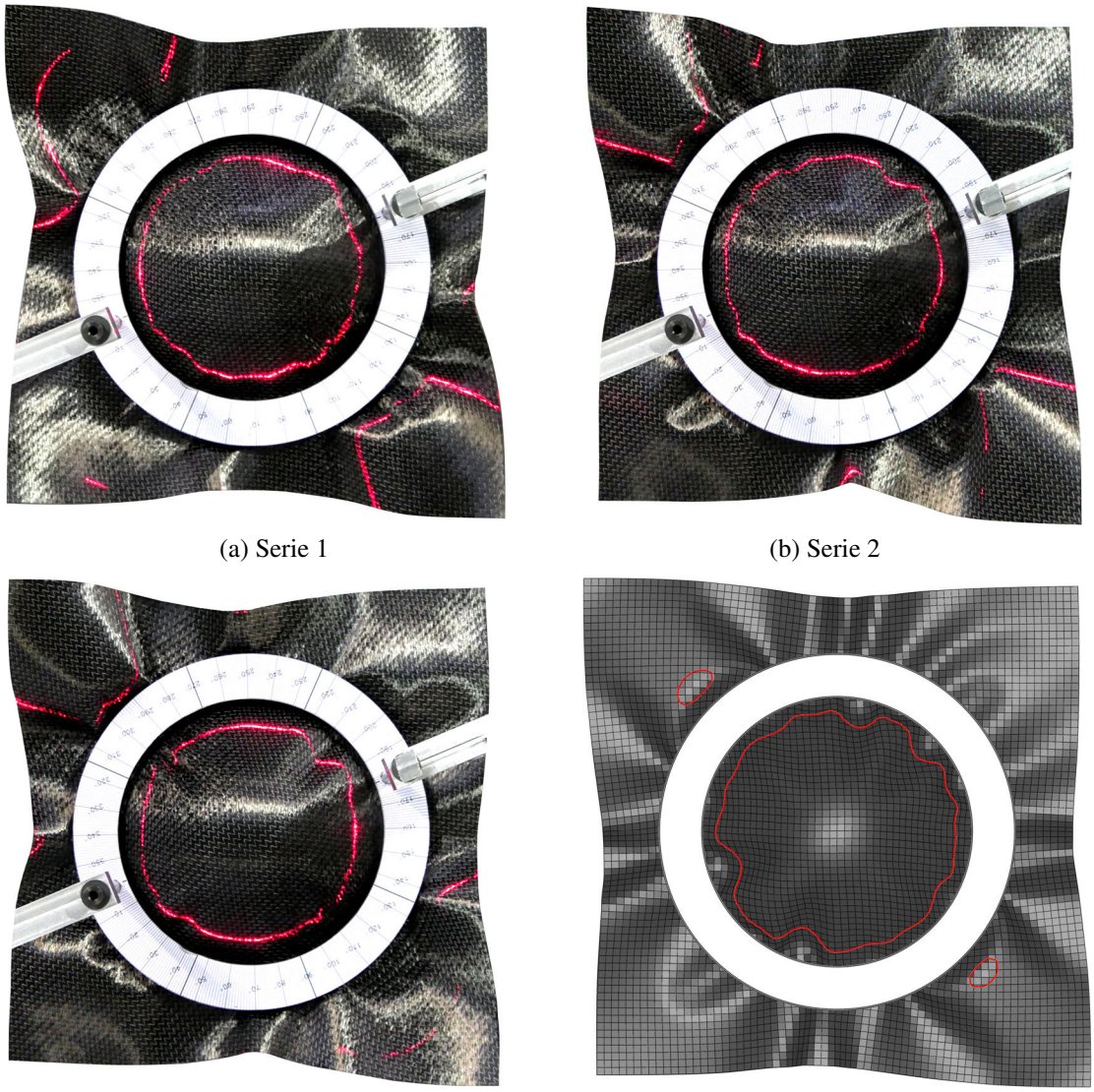

(a) Serie 1 (b) Serie 2

(c) Serie 3 (d) Simulation result

Fig. 3-20: Pictures of the finale state of the experimental forming trials used for the geometrical criteria (a to c) and illustration of the corresponding forming simulation result (d).

3.4.4.1 Reaction force and blank-holder displacement

The reaction force and the vertical lift of the blank-holder are illustrated in Fig. 3-21 depending on the forming stroke (i.e. vertical displacement of the stamp). The experimental measurements of the reaction force show a bilinear behavior for all repetitions, with a kink at about 23 mm stamp displacement. This kink can be attributed to the nonlinear bending behavior of the textile. The bilinear evolution of the force is also observed in the simulation but the kink is located at a stamp displacement of ca. 35 mm. A good correlation can be observed between the experimental and simulation results until the kink of the experimental curves. For larger stamp displacements, the simulation slightly overestimates the reaction force. The difference increases progressively until the kink in

the simulation result and remains constant afterwards. A mean force of 11.9 N is measured at the end of the forming experiments and 14.5 N is reached in the simulation.

The results of the blank-holder displacement reveal large differences between the simulation and experiments. A bilinear behavior of the simulation result is also identified with a kink at a stamp displacement of 35 mm. Above those values, the blank-holder displacement is significantly overestimated, with a final difference of 7.0 mm. A reasonable explanation for those deviations may be that the simulation fails to predict the flattening of wrinkles or overestimates the bending stiffness for larger curvatures. Potential friction in the guide of the blank-holder may also contribute to the overestimation of the vertical lift.

These two criteria show that the simulation is able to predict the bilinear evolution of the reaction force on the stamp. Nevertheless, the significant differences between the simulation and experimental results suggest that the calibrated material model overestimates the bending stiffness for large curvatures and that the softening of the bending stiffness should be shifted towards smaller curvatures. The deviation of the blank-holder lift is an important result for the subsequent validation criteria focusing on the geometrical deformations, since the geometry is partly defined by the blank-holder.

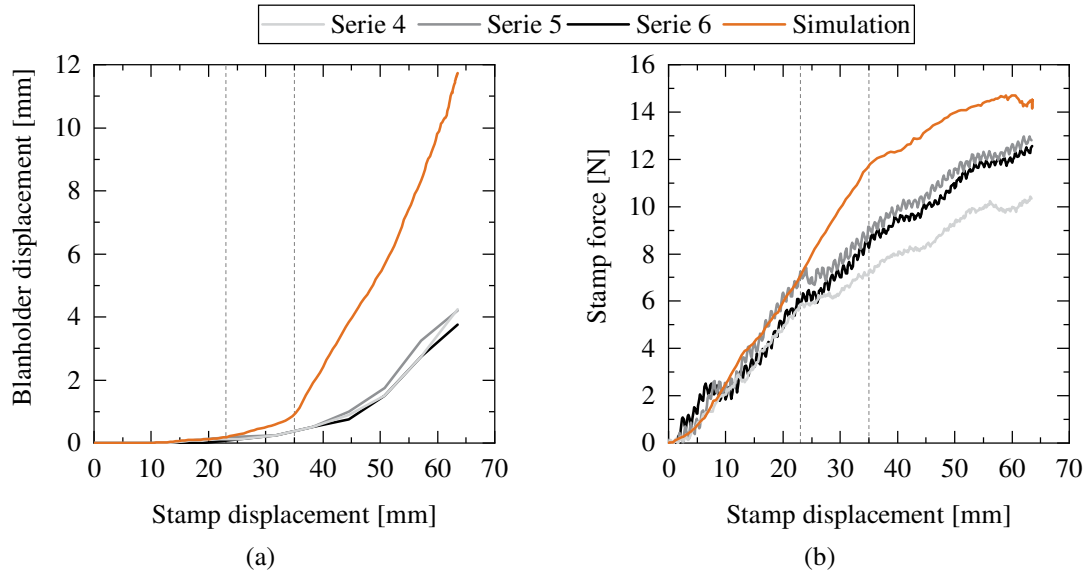

Fig. 3-21: Comparison between the reaction force on the stamp (a) and lift of the blank-holder (b) depending on the forming stroke of the experimental and simulation results.

3.4.4.2 Fiber orientation

Fig. 3-22 illustrates an example of the optical measurements of the filament directions (before and after post-treatment of the data) in order to determine the fiber orientation of the upper layer only. Local defects, particles and local filament buckling are also excluded from the data using the polar and specular values of the pixels.

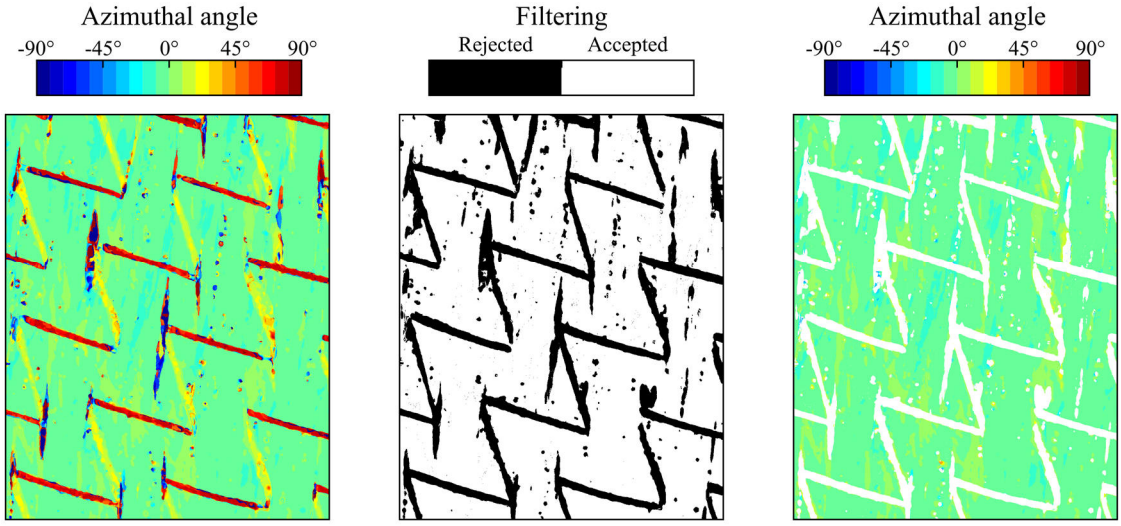

Fig. 3-22: Azimuthal results of the optical measurement of the filament directions before post-treatment (a), results of the filtering (b) and final azimuthal results after post-treatment (c).

Fig. 3-23a and Fig. 3-23b illustrate the measured azimuthal angles along the projected x-axis and y-axis at the end of the forming experiment, respectively. In the case of a textile with symmetric shear behavior, change of the fiber angle would be only measured in the sheared zones and not on the principal axes of the setup. Therefore, the azimuthal angles measured along the x-axis and y-axis indicate an asymmetric shear behavior. Fig. 3-23c and Fig. 3-23d show the azimuthal angle in the region of positive and negative shear at the final forming stroke, respectively. In the region of positive shear, an azimuthal angle of about 8° is measured at the outermost ROIs, while angles up to 20° are reached in the region of negative shear deformation. The difference of absolute values between the azimuthal angles in the zone of high shear deformation is a further evidence of non-symmetric shear behavior.

At the final forming stroke, the variation of the measurements between each repetition reveals a maximum difference of 5.63°, which is obtained in the ROI 22 (outermost ROI in the region of negative shear and area with the highest shear deformations). Nevertheless, the mean maximum difference between the three repetitions is 1.14°, which is close to the precision of the optical sensor (it is showed in [178] that 95% of the measurements are located in an range of ±0.8° for flat samples of dry textiles). Differences measured between the negative and positive projected locations may exhibit spatial variability of the textile behavior, potential pre-shearing of the textile, misalignment of the sample or non-symmetric onset of the wrinkles.

The comparison of the azimuthal angles between the simulation results and the experimental measurements shows a very good correlation. The largest deviation between the simulation and the mean value of the experimental results is observed at ROI 7 with a difference of 3.92°. This ROI is located along the fiber orientation of the upper layer at

a coordinate along the y-axis of -53 mm. It can be explained by the occurrence of a large wrinkle at this location, which introduces a supplementary rotation angle and influences the projection of the local filament orientation (ref Fig. 3-20 and section 3.4.4.3). The mean difference between the simulation result and the respective mean values of the three experiments is 1.25°, with a standard deviation of 0.89°.

Fig. 3-23e represents the evolution of the azimuthal angle measured at ROI 24 (region with negative shear deformation) depending on the forming stroke. It is used to evaluate the ability of the simulation framework to predict the behavior of the textile during the whole forming process. An increase of the azimuthal angle is observed in the experimental and simulation results, with a difference between them smaller than 1.0°. Note that direct conclusions on the evolution of the shear angle are not possible due to the different orientations of the ROIs for each forming stroke.

The differences observed between the experimental and simulation results corresponds to usual variability and tolerances for the fiber orientation (e.g. ±1° in guidelines for the preparation of sample [181] or ±5° for the production of composite parts with dry fiber reinforcements in the aerospace industry [46, 182]). As a result, it can be concluded that the simulation method is able to accurately predict the fiber orientation of the textile.

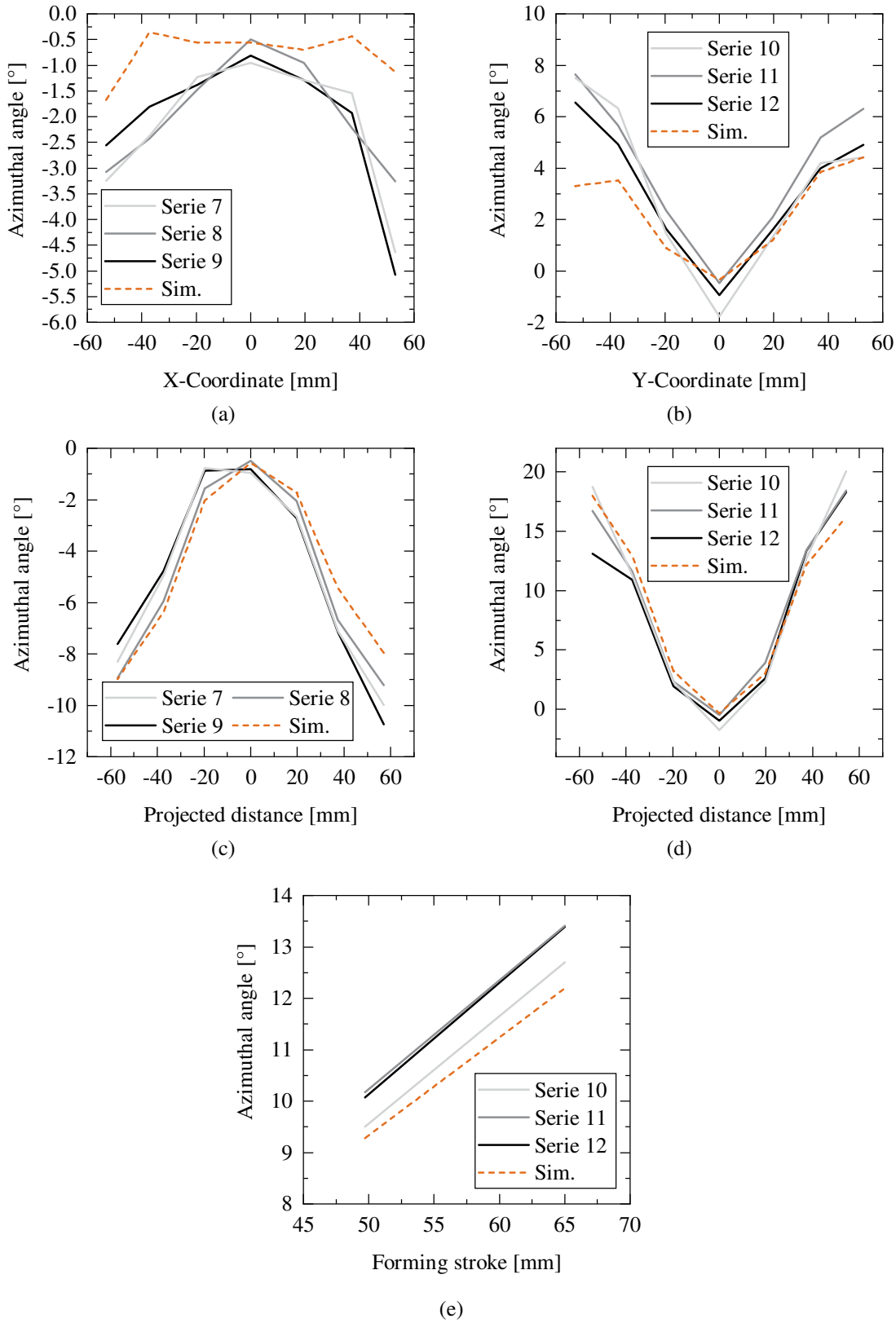

Fig. 3-23: Azimuthal angles in ROIs defined along the x-axis (a) and y-axis (b), along the paths defined in bias direction with positive (c) and negative shear deformations (d), and evolution of the azimuthal angle at ROI 24 depending on the forming stroke (e).

3.4.4.3 Textile draw-in

Fig. 3-24 illustrates the draw-in results for each corner. The results of the draw-ins and corresponding draw-in ratios, as introduced in Eq. (3-19), are listed in Tab. 3-11. The draw-in of the corners located in the region of positive shear (i.e. corners 1 and 3) is significantly larger than the draw-in of the corners 2 and 4. A mean draw-in ratio of 2.8 is reached in the experiments. This is evidence of the asymmetric shear stiffness, which induces larger shear deformation in the region of negative shear and, therefore, to a smaller cumulated draw-in. The deviations between the measurements can be explained by the difference of the deformation behavior of each corner. In Fig. 3-25 it can be seen that some corners bend downwards, while other bend upwards or remain straight. In order to increase the robustness of this criteria, a large blank-holder surface can be used (e.g. as introduced by Krieger et al. in [183]).

The simulation results show a slight underestimation of the draw-in. Nevertheless, the asymmetric behavior of the textile is accurately predicted and remains in the experimental scatter. A possible explanation for the smaller draw-in is the difference in blank-holder lift. Since the blank-holder is lifted to a higher distance from the ground plate, it results in a smaller deformation of the textile and, therefore, to a smaller corner draw-in.

Tab. 3-11: Results of the corner draw-in and corresponding draw-in ratios.

Draw-in	Sample 1	Sample 2	Sample 3	Mean value experiments	Simulation
Corner 1 [mm]	21.5	21.7	19.2	20.8	16.7
Corner 2 [mm]	8.37	7.59	8.83	8.26	6.44
Corner 3 [mm]	18.9	23.6	23.5	22.0	18.3
Corner 4 [mm]	4.50	5.65	10.5	6.88	7.05
Draw-in ratio [-]	3.14	3.42	2.21	2.83	2.59

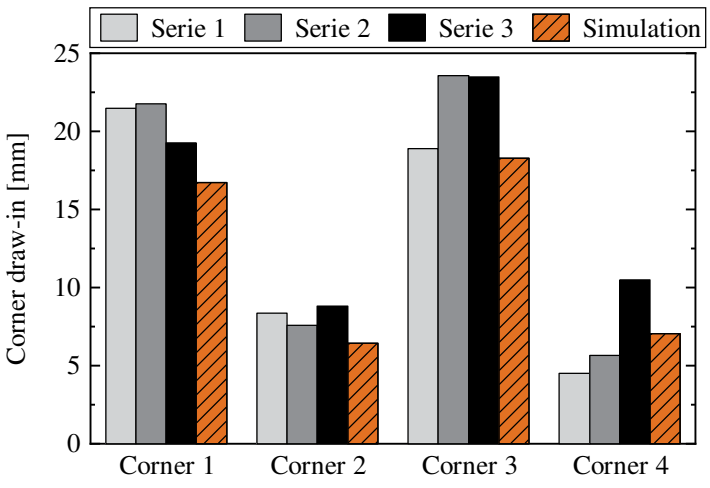

Fig. 3-24: Comparison of the corner draw-in of the experimental and simulation results.

3.4.4.4 Wrinkling profile

The distance between the center of the setup and the contour of the laser projected on the surface of the textile is illustrated in Fig. 3-25, along with the simulation results. The diagrams are divided in four zones, representing each quadrant of the setup. Moreover, it is indicated for each corner of the sample if the corner deforms downwards, upwards, or if no bending of the corner can be observed. First of all, it can be observed in the experiments that the deformation of the corners (i.e. the deformation of the textile outside the blank-holder) is not reproducible, excepted for the first quadrant. Therefore, it is considered that the use of the corner deflection is not a robust criterion to validate the simulation results. The mean distance between the center of the setup and the contour is measured to 73.5 mm. From the experimental results it can be observed that the regions with positive shear deformations lead to a recurrent onset of large wrinkles. On the contrary, a non-reproducible onset of wrinkles (with small amplitudes or localized deformations) is found in the regions with negative shear deformations. Because of the variable number and amplitude of the wrinkles, further conclusions on the geometrical deformations cannot be drawn.

The simulation result shows a clear distinction between the regions of positive and negative shear. In the first and third quadrant (positive shear), large wrinkles with an amplitude larger than 10 mm can be observed. In the contrary, only small wrinkles with an amplitude smaller than 5 mm are generated in the second and fourth quadrant (negative shear). The mean distance is measured to 78.3 mm, which is significantly larger than the experimental results. This can be also explained by the difference in blank-holder lift observed in section 3.4.4.1. It can be concluded that the simulation is able to accurately predict the regions in which large wrinkles are likely to occur. Therefore, the simulation can be used to identify critical regions of wrinkling.

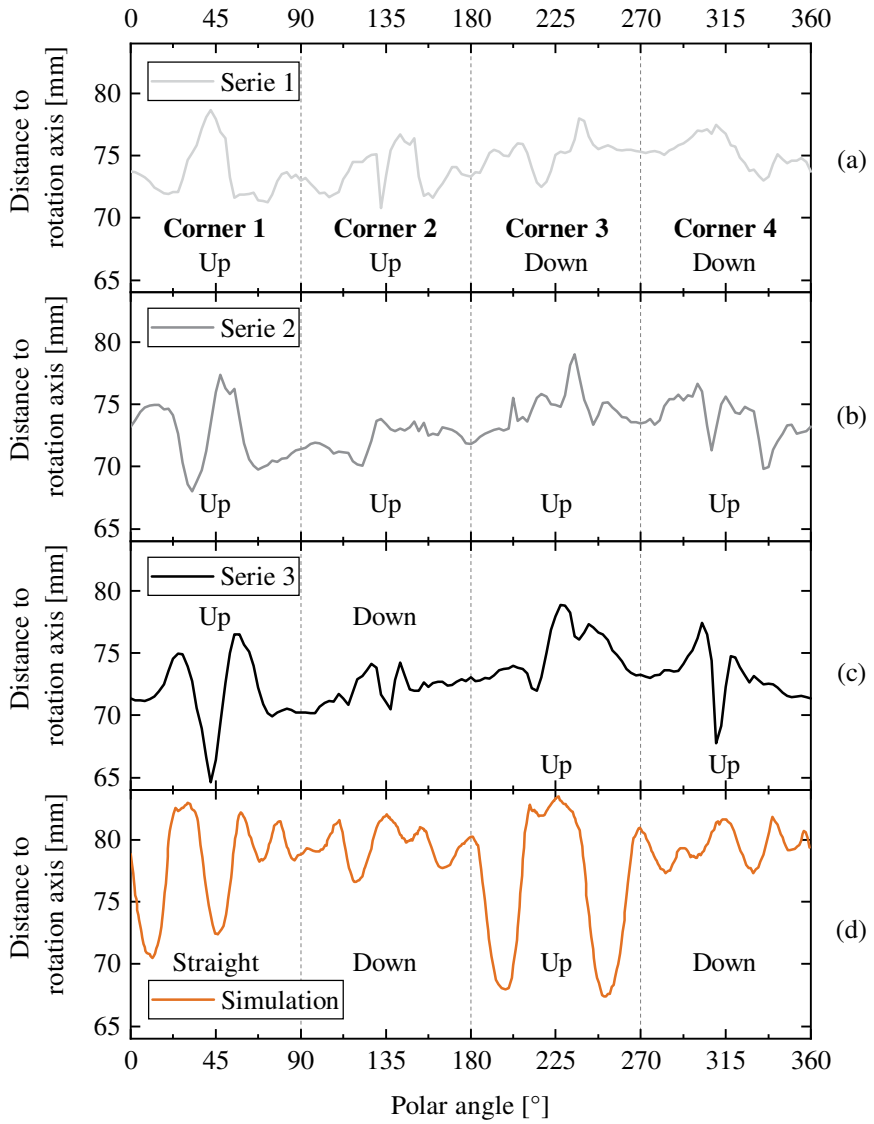

Fig. 3-25: **Distance between the axis of the stamp and the contour of the outer surface of the preform at a height of 21 mm: experimental (a to c) and simulation results (d).** The range of the polar angles are divided in four regions corresponding to the four quadrants of the textile. The deformation of each corner is added to the diagram for easier interpretation of the results.

3.5 Conclusion

A forming simulation was developed using the commercially available software package ABAQUS. The material model *FABRIC is selected to reproduce the deformation behavior of a dry NCF. A bi-linear bi-material model was proposed in order to account for the bending behavior without development of new constitutive equations. It describes the material using one linear material for tensile deformations and a bi-linear soft material in compression. With this approach, the non-linear bending behavior of dry textile can be accurately approximated with only three parameters.

A calibration of the friction, shear and bending parameters was performed. The friction measurements between the textile and metallic surfaces have shown an anisotropic frictional behavior. The friction coefficient for sliding in fiber direction was smaller than for sliding perpendicular to the filament direction. The anisotropic behavior was implemented using the anisotropic surface interaction properties available in ABAQUS. The asymmetric shear behavior of the textile was observed, which is due to the different contribution of the stitching yarn in positive and negative shear directions. In that case, the forces required to shear the fabric with a positive shear was about three times higher than for negative shear. The experimental curves for both shear directions were discretized and implemented in the simulation. In order to calibrate the parameters of the bending model, a new testing device was developed. A buckling of the textile is selected as test principle in order to generate a bending deformation. The new setup enables the observation of the textile deformation in order to study localizations of the curvature. Moreover, it is possible to measure the reaction force on the sample with rudimentary equipment. Thus, the non-linear behavior of the material can be adequately characterized. The calibration of the parameters was performed with an indirect approach by comparing simulation and experimental results for a large number of input parameter sets. Nevertheless, variability was observed in the experimental results and a threshold on the deflection was set to discard non-symmetric deformations. In order to increase the repeatability of the test and the precision of the measurement, this test method can be adapted in a universal test machine. This would also enable controlling the displacement velocity and measure the reaction force during the whole deformation process of the sample.

Finally, an extended validation of the forming simulation was performed using criteria on the fiber orientation of the upper layer, on the geometrical deformation of the fabric, on the reaction forces generated on the stamp and on the vertical lift of the blank-holder. A good correlation of the fiber orientation was found between the experiments and the simulation. Due to some wrinkles in the simulation results, the projection of the fiber orientation has led to deviations at the outermost regions of interest. In further validation studies, it is recommended to mainly consider regions with reduced wrinkling. The asymmetric shear deformation, characterized by the corner draw-in, was accurately reproduced. The observation of the wrinkling behavior has shown a large variability in the experimental results. Therefore, an exact comparison of the wrinkle size and respective amplitude was not further considered. Nevertheless, the simulation method was able to locate the critical regions where wrinkling may occur. Although deviations were observed in the vertical lift of the blank-holder, the reaction forces measured on the stamp have shown a better correlation. These deviations can be attributed to a lack of characterization of the bending behavior at high curvatures. To that end, the bending characterization method could be adapted with various sample length to improve the robustness of the calibration method for higher curvatures.

The material card and interaction parameters resulting from this extent characterization is presented in appendix b. It can be concluded that the approach developed in this chapter is able to accurately predict the forming behavior of dry NCFs. Moreover, the use of flexible input parameters offers a high flexibility of the simulation for further investigations on the influence of material parameters on the forming results.

4 Numerical prediction of the preform quality

Forming simulations can be used to improve composite manufacturing processes, identify relevant process parameters or adapt the design of components according to manufacturing limitations. Compared to experimental trials, the flexibility of forming simulations enables extensive studies at reduced cost in order to investigate the influence of material parameters on the forming behavior. Although the manufacturability of textile materials for each material configuration is not guaranteed at this stage, it is possible to establish requirements on the textile deformability that can improve the quality of the preforming process.

This chapter focuses on the development of an automated framework able to predict the preform quality based on forming simulation results. First, definitions of the preform quality and methods to identify defects are reviewed. Afterwards, the objectives of the framework are presented and the corresponding criteria are developed to measure the quality of the preform based on simulation results only. Then, the method is applied to a generic demonstrator geometry to identify the influence of the shear and bending behaviors on the preforming results. Finally, important outcomes of this study are summarized and guidelines for textile development are derived.

The content of this chapter is partly derived from [K2].

4.1 Background

4.1.1 Definitions of the preform quality

The quality of a preform can be defined according to various criteria, depending on the objectives that a preform must fulfill:

- Fiber orientation: the design of lightweight components with carbon fiber reinforced material relies on their strong anisotropic behavior to optimize the mechanical performance. Thus, the proper orientation of the filaments in the final component is a central parameter that must be considered during the manufacturing process. In order to support the design of the process, forming simulations combined with optimization algorithms have been widely investigated [27, 184]. They are used to define the cut-out, the orientation of the fibrous layers or to optimize the process parameters.

- Mechanical properties of the final component: local defects of the fibrous architecture may significantly reduce the performance of the composite part. For example, it has been shown in different studies that waviness of the filaments might reduce the stiffness of the part [185–187] but can also change the failure modes, resulting in unexpected and critical failure of the structure [46, 188, 189].
- Stability of the preform: a high stability of the preform increases the handling capabilities between the process steps in automated manufacturing processes. This definition is generally applied to a stack made of many plies, in which the thermal management of the preforming process plays a central role [76, 190].

In the context of this doctoral thesis, the quality of a preform is defined based on the occurrence of local defects in the fibrous layers. An extensive overview of the effects leading to fiber waviness in composite structures was published by Thor et al. [191]. The waviness can be a result of the textile architecture, the filament type, the design of the preforms, the preforming process or even mismatch of thermal deformations during the injection process. Illustrations of local fiber waviness can be found in Fig. 4-1a, in which waviness is identified at the corner of a thick preform consolidated using a vacuum bagging process. Moreover, forming induced waviness resulting from the forming of a thick stack of unidirectional prepreg tapes is illustrated in Fig. 4-1b.

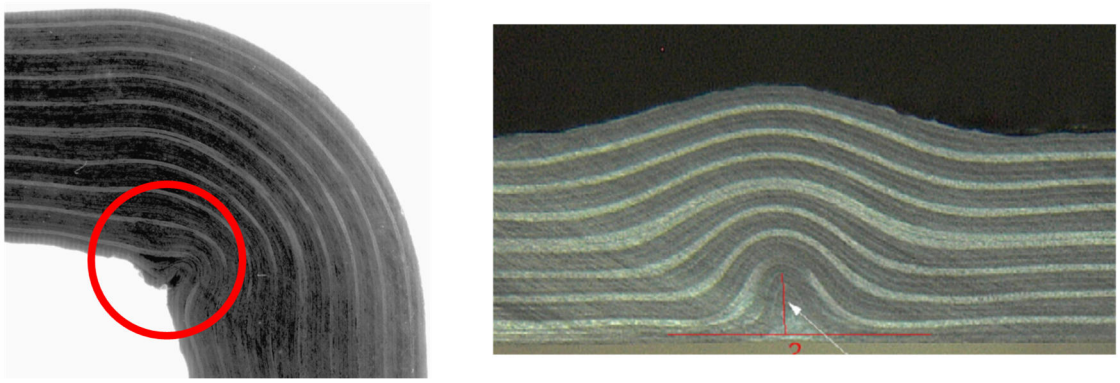

(a) (b)

Fig. 4-1: Illustration of fiber waviness generated in thick preforms at the corner (a, adapted from [186]) and in the flat region of a CFRP part (b, adapted from [192]).

4.1.2 Identification of defects in the simulation

As presented in chapter 2, the numerical description of textiles can be performed at various scales. Depending on the level of discretization, various defects can be reproduced and directly identified.

The most efficient method to model the mechanical behavior of the textile is the macroscopic approach. Since the whole textile is modeled with one continuum, only macroscopic-level-defects can be described. First, it is possible to predict the change of angle

between the directions of the textile layers, defined as the shear angle. The quantification of the shear deformation can be done using either the maximal shear angle reached in the preform [193], or its distribution over a predefined zone. for the numerical optimization of inter-ply stitching points in woven preforms, as presented by Chen et al [81]. The identification of wrinkles is the second defect that can be described with macroscopic approaches. To identify them, one can compute the local deviation between the position of the textile and the tool geometry, as used to compensate the tool geometry to avoid resin rich regions in an RTM process (module “Die Spotting” in PAM-FORM [194]). Another solution to identify wrinkles is to compute the local curvature of the fabric based on the node coordinates of the simulation result [195]. In addition, a study presented by Chen et al. [56] has shown relations between in-plane fiber waviness observed on experimental results and the stress state in fiber direction predicted with a macroscopic forming simulation. However, no total equivalency between them could be determined. Finally, a recent approach coupling macroscopic and mesoscopic analyses was developed by Iwata et al. [196]. It combines the computational efficiency of macroscopic forming simulations with the ability to predict the local architecture of the textile offered by a mesoscopic analysis (gaps, tow buckling, etc.).

4.2 Objectives

The objective of the present chapter is to improve the quality of the preform based on simulation results only. An automated approach is proposed to relate the simulation results with the expected preform quality. In the context of industrial applications, forming simulations at mesoscopic or microscopic scale are not suitable due to their high computation time. Therefore, the preforming quality shall be quantified based on macroscopic forming simulation results. The fiber waviness is identified as critical defects and deformations likely to induce fiber waviness in the preform will be tackled in this chapter.

Although shear deformations are necessary to accommodate surfaces with double curvatures, their occurrence should be minimized. First, shear deformations lead to an increase of the textile thickness. This can be shown analytically due to the conservation of the filament volume and the reduction of the sheared area [18]. Even though the variation of the textile thickness is a priori not a defect, its local variation over the component geometry may generate defects during the manufacturing process. During the closure of the molds in RTM processes, the preform is compressed to the final FVF. Various compaction states are induced if the preform exhibits thickness variations and, thus, generates an out-of-plane waviness of the filaments. Moreover, the shear of NCFs may generate local buckling of filament bundles for larger shear angles, resulting in a high level of fiber waviness as observed in section 3.3.2 or reported in [61].

The onset of out-of-plane deformations, whether it is a spurious localized wrinkle or a deviation from the theoretical geometry, also results in a waviness of the filaments.

During the closing of the tool before resin injection, the wrinkles (i.e. the exceeding material) are pushed together. In the case of small wrinkles, this may result in a local increase of the preform thickness and, thus. to fiber waviness. Moreover, folds of the textiles can be produced due to large wrinkles.

As a result, the occurrence of shear and out-of-plane deformations must be minimized. In this doctoral thesis, an automated method is developed to identify these deformations in the simulation results. The approach is subsequently applied to identify the influence of the material deformability on the preform quality. The influence of the shear and the bending stiffnesses is studied and resulting requirements on the textile deformability are specified.

4.3 Definition of the criteria

The criteria defined in this section measure the preform quality of simulation results. Since the quality is related to the final part performance, the criteria are computed using only the elements located in the region corresponding to the final component at the end of the simulation. The set of these elements is referred to as Ω_{ROI}. As a consequence, the preform quality is a local measure and wrinkles or shear deformations outside this region do not influence the preform quality.

The criteria defined in this subsection were partly implemented in the context of a student thesis [S7].

4.3.1 Shear deformation

The shear deformation is identified in the simulation based on the output variable EFABRIC12. It indicates the change of angle between the two directions of the fibrous layers. Therefore, the shear angle γ in the textile can be directly quantified for each mesh element using this output. In order to derive a single measure from the shear deformation of a large number of mesh elements, different information can be used:

- Maximum absolute shear angle: This can be used to reduce the extreme deformations. Nevertheless, this criterion may spread the shear deformation over a larger surface of the component.
- Averaged shear angle: This criterion can reduce the overall shear deformation but allows local severe deformations that can generate dramatic defects in the preform.

In order to target both aspects, the set Ω_{shear}, which contains 20% of all elements in Ω_{ROI}, includes the following subsets:

- 10% of those elements in Ω_{ROI} which have the highest shear deformation in the positive direction.

- 10% of those elements in Ω_{ROI} which have the highest shear deformation in the negative direction.

The shear objective f_S is computed as the mean of the absolute values of shear deformation of all elements in Ω_{shear}. It is normalized as follows:

$$\widetilde{f_S} = \frac{\max\left(f_S(\Gamma_{DV})\right) - f_S}{\max\left(f_S(\Gamma_{DV})\right) - \min\left(f_S(\Gamma_{DV})\right)} \tag{4-1}$$

where Γ_{DV} is the set of all design variables investigated.

4.3.2 Out-of-plane deformation

Two criteria are necessary to identify out-of-plane deformations and, thus, wrinkles in the preform. First, large wrinkles (i.e. significant deviation from the ideal part geometry with low curvatures) are identified. To that end, the volume under the textile is calculated based on the nodal coordinates of the deformed mesh. Ideally, the preform lays exactly on the tool surface and the volume under the deformed textile corresponds to that of the tool geometry. In order to calculate the volume between the preform and a reference plane P, the point cloud constituted of the node of Ω_{ROI} is first tessellated using the Delaunay triangulation algorithm available in the Python library Scipy [197]. Each triangle is subsequently projected onto the reference plane, as illustrated in Fig. 4-2a. The area of the projected triangle k, referred to as $S_{T,k}$, can be calculated using the cross product of the projected edges as follows:

$$S_{T,k} = \left\| \frac{\overrightarrow{P_1P_2} \wedge \overrightarrow{P_1P_3}}{2} \right\| \tag{4-2}$$

Then, the volume $V_{T,k}$ is calculated by multiplying $S_{T,k}$ with the distance h_k between the barycenter of the triangle and its projection on the reference plane. The criterion used to quantify the geometrical deviation f_V is the difference between the volume under all elements of Ω_{ROI} and the corresponding volume under the tool V_{Tool}:

$$f_V = \sum_{k \in \Omega_{ROI}} \left(S_{T,k} \times h_k\right) - V_{Tool} \tag{4-3}$$

The second geometrical criterion tackles the onset of localized wrinkles. These out-of-plane deformations have large curvatures but do not change the volume under the preform significantly. The criterion f_B is introduced to quantify the angle between adjacent elements and, thus, identify the regions with high curvatures. First, a normal vector is calculated for each mesh element. Then, for each element k, the mean angle between the normal vectors (ref. Fig. 4-2b) is derived according to Eq. (4-4). The resulting quantity — referred to as the element angle $\bar{\varphi}_k$ — is assigned to the central element.

$$\bar{\varphi}_k = \frac{\cos^{-1}\left(\vec{n}_{right} \cdot \vec{n}_{left}\right) + \cos^{-1}\left(\vec{n}_{front} \cdot \vec{n}_{back}\right)}{2} \tag{4-4}$$

The element set Ω_{angles} is introduced. It contains 20% of the elements in Ω_{ROI} and takes those with the highest element angles. The criterion f_B is the mean value of the element angles in Ω_{angles}. This approach accounts for both the extreme and the global values of the small wrinkles.

Finally, a single scalar value $\widetilde{f_W}$ is derived from f_V and f_B to quantify the wrinkling of the textile. To that end, the criteria are normalized based on the respective maximum and minimum values computed from the set of all design variables Γ_{DV}. It results:

$$\widetilde{f_W} = a_V \frac{\max\left(f_V(\Gamma_{DV})\right) - f_V}{\max\left(f_V(\Gamma_{DV})\right) - \min\left(f_V(\Gamma_{DV})\right)} + a_B \frac{\max\left(f_B(\Gamma_{DV})\right) - f_B}{\max\left(f_B(\Gamma_{DV})\right) - \min\left(f_B(\Gamma_{DV})\right)} \tag{4-5}$$

where a_V and a_B are the weighting factors of the objectives f_V and f_B, respectively. In this thesis, the weighting factors are set to 0.5 in order to account for localized wrinkles and large geometrical deviations equally.

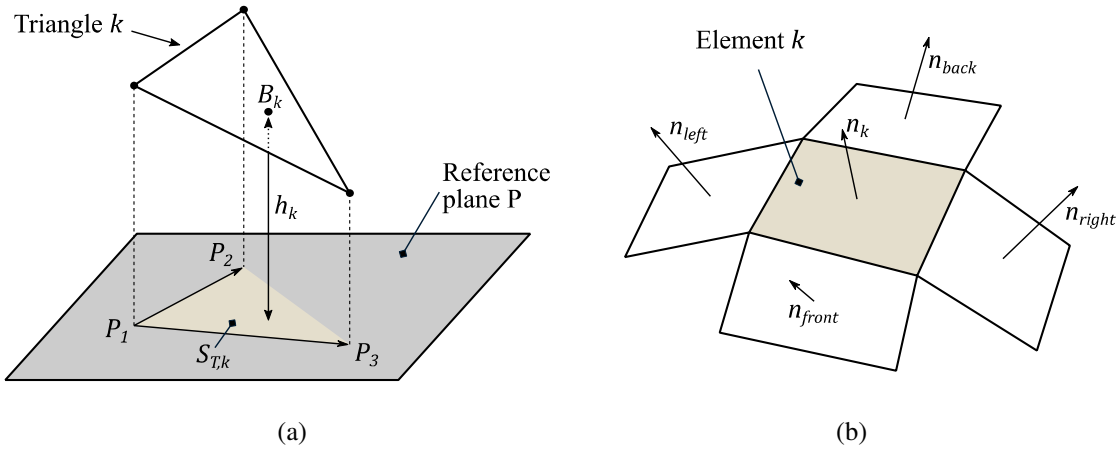

Fig. 4-2: Calculation of the volume under the mesh elements in order to identify large wrinkles (a) and definition of the normal vectors used to compute element angles (b).

4.4 Applications

The applications of the simulation framework investigate the importance of the material behavior on the preform quality. Although it is recognized that the bending stiffness and the shear behavior influence the wrinkling [21, 198], their respective impacts on the shear deformation, geometrical deviations and local curvatures must be quantified. To that end, a complex stamp geometry representative of usual composite parts is selected. First, the forming process and the simulation parameters are presented. Then, the evolution of the criteria is observed depending on the ratio between the shear and bending

stiffness. Afterwards, an in-depth study is proposed on the influence of the shear and bending behaviors separately to increase the overall preform quality.

4.4.1 Forming simulation model

In this subsection, the criteria are applied to the forming process designed by Eisenhauer and Drechsler [199]. The geometry of the stamp (called "Pole Peak" geometry) is constituted of a half-hemisphere on one end, of a pyramid on the other end, and of a transition geometry (see Fig. 4-3). This process is selected due to the complexity and diversity of the geometric features. The blank-holder follows the contour of the stamp base, on which a large range of forces can be applied. For this study, the blank-holder is modeled as a unique part, to which a constant force of 70 N is applied. The simulation parameters to model the forming process are listed in Tab. 4-1.

Tab. 4-1: Simulation parameters of the forming process with a "Pole Peak" stamp geometry.

Parameter	Unit	Value
Mesh element size	mm	5.0
Forming duration	s	5.0
Stamp stroke	mm	72
Blank-holder force	N	70
Density of fabric material	tons/mm³	4.84E-07

Note that the stamp, the blank-holder and the ground plate are modeled as rigid bodies. For all applications in this chapter, the reference configuration is defined as the forming simulation result using the material and interaction parameters calibrated in chapter 3. Finally, the region used to compute the criteria of the preform quality is defined as the inner region of the blank-holder.

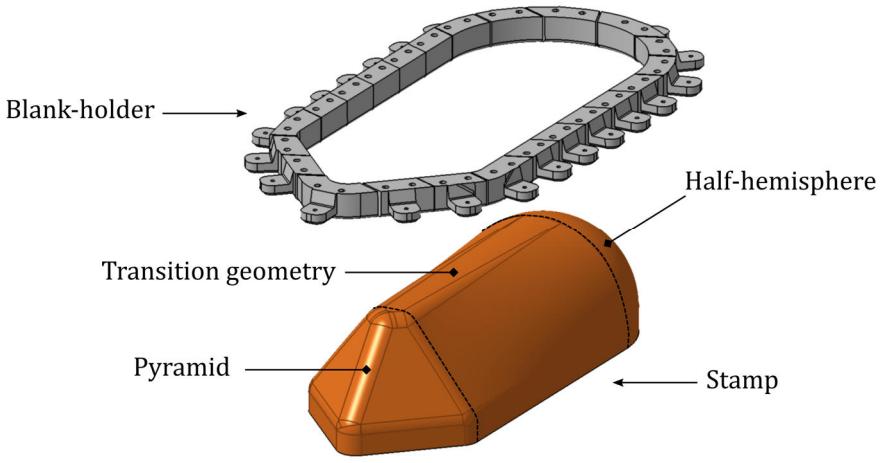

Fig. 4-3: Illustration of the forming process with the "Pole Peak" stamp geometry.

The simulation result of the reference configuration is illustrated in Fig. 4-4, in which the wrinkling profile is shown at height of 25 mm. The asymmetric deformation of the

preform can be clearly recognized in the corners. Also, large wrinkles can be observed on the side of the pyramid in which the textile is sheared in positive direction, whereas only small wrinkles are generated in the zone of negative shear. This correlates well with the observations made in the previous chapter. In order to compare the results of the subsequent applications, the objective criteria computed with the reference configuration are listed in Tab. 4-2.

Tab. 4-2: Results of the objective functions for the reference configuration.

f_S [°]	f_B [°]	f_V [dm³]
22.9	17.2	2.27

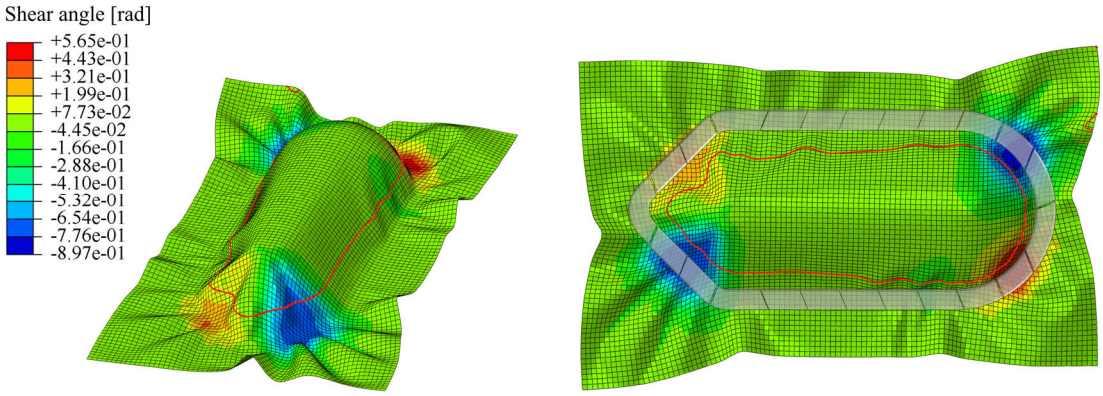

Fig. 4-4: Simulation results of the reference configuration.
The red line shows the contour of the outer surface of the preform at a height of 25 mm.

4.4.2 Case study 1: influence of both shear and bending stiffness

4.4.2.1 Design variables

A parametric variation of the shear and bending input parameters is proposed in order to analyze the influence of the balance between the shear and bending stiffness. To that end, the shear and bending behaviors of the reference configuration are scaled according to factors C_{shear} and $C_{bending}$. Each data point of the shear input curve as defined in Eq. (3-13) is scaled according to the factor C_{shear}. Note that the curves of the negative and positive shear directions are scaled using the same factor. In order to vary the stiffness of the BLBM bending model, only the parameters E_{comp} and E_{soft} are scaled according to the factor $C_{bending}$. The parameter ε_{soft}, which characterizes the onset of the non-linearity, is adapted according to Eq. (3-4) to keep the softening point at a constant curvature κ_{soft}= 6.56 m^{-1} for all design variables.

Both scaling factors vary between 0.1 and 2.0 to propose a large number of material configurations. The shear and bending input parameters of the extreme cases are

illustrated in appendix c. The design space of the scaling factors is covered using a full factorial design with sixteen equally spaced levels for each parameter, leading to a total of 225 configurations. This defines the set of the design variables Γ_{SB}.

4.4.2.2 Results

The results of the normalized objective functions $\widetilde{f_S}$ and $\widetilde{f_W}$ are shown in Fig. 4-5 depending on the shear (horizontally) and bending (vertically) scaling factors. The maximum and minimum results of the respective objective functions are listed in Tab. 4-3.

Tab. 4-3: Extreme results of the objective functions for the set of design variables Γ_{SB} (application case study 1).

	$f_S(\Gamma_{SB})$ [°]	$f_B(\Gamma_{SB})$ [°]	$f_V(\Gamma_{SB})$ [dm³]
Minimum	8.16	11.4	2.21
Maximum	28.6	31.0	2.35

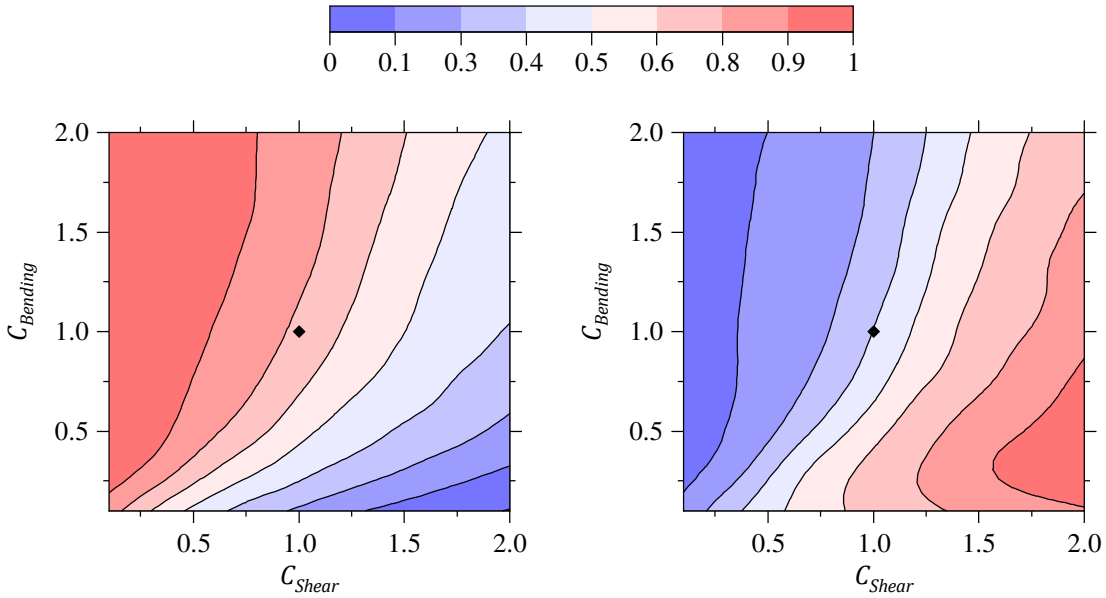

(a) Shear deformation characterized by $\widetilde{f_S}$ (b) Wrinkles characterized by $\widetilde{f_W}$

Fig. 4-5: Results of the normalized objective functions for shear deformations (a) and wrinkling (b) from case study 1, depending on the shear and bending scaling factors. The black point in the diagram indicates the reference configuration.

It can be observed that the criteria quantifying the shear deformation and the wrinkles are conflicting objectives: a higher shear stiffness combined with a low bending stiffness reduces the shear deformation but promotes the onset of wrinkles. On the contrary, a low shear stiffness associated with a high bending stiffness causes the compliance of the textile with larger shear deformations. These two cases are illustrated in Fig. 4-6a and Fig. 4-6d, showing the large differences in shear deformation and wrinkling in the simulation results.

The contour plots of Fig. 4-5 show that both criteria follow the same dependency on the scaling factors. Therefore, it would be possible to define a path $C_{bending} = f(C_{shear})$ along which neither the criterion $\widetilde{f_S}$ nor $\widetilde{f_W}$ vary significantly. Thus, it is possible to achieve the same quality of the preform if the shear stiffness and the bending stiffness are scaled accordingly. For example, the selection of a textile with a higher shear stiffness can be compensated with a softer bending stiffnesses. This highlights the importance of the balance between shear and bending stiffness to control the shear deformation of the textile and the onset of wrinkles during preforming. More generally, it argues that the selection of an adequate textile requires the investigation of the shear and bending stiffnesses simultaneously.

Finally, it can be observed that for $C_{shear} < 0.25$ (i.e. at very low shear stiffness) the objective functions have a smaller dependency on the bending stiffness. In this case, the textile mainly complies to the stamp geometry through shear deformation. Nevertheless, it can be observed that a low bending stiffness is still necessary to adapt sharp edges of the stamp geometry. Otherwise, the textile smoothens the deformation at sharp corners, as shown in Fig. 4-6 by the black contour at a height of 25 mm. In Fig. 4-6c the shear deformation is slightly reduced compared to Fig. 4-6a and small wrinkles are detected but the sharp edges of the stamp can be adapted by the textile.

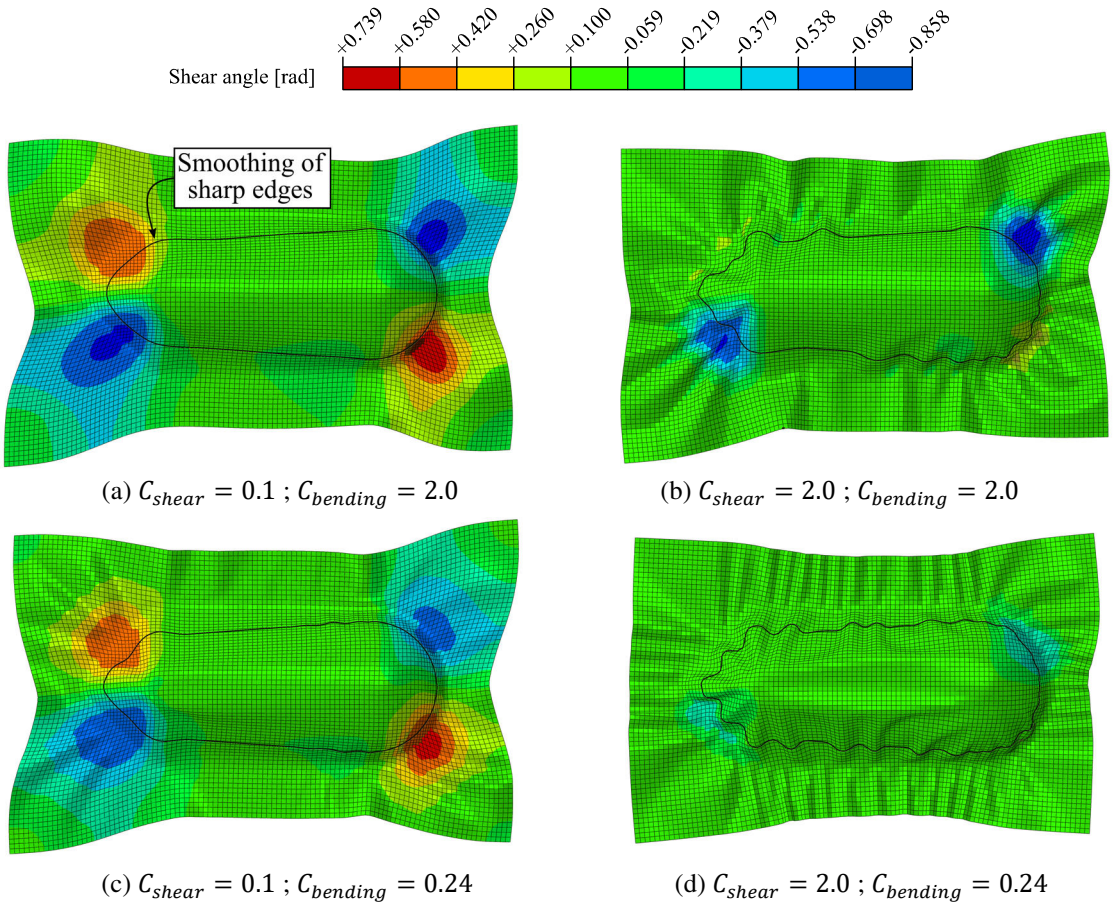

(a) $C_{shear} = 0.1$; $C_{bending} = 2.0$ (b) $C_{shear} = 2.0$; $C_{bending} = 2.0$

(c) $C_{shear} = 0.1$; $C_{bending} = 0.24$ (d) $C_{shear} = 2.0$; $C_{bending} = 0.24$

Fig. 4-6: Forming simulation results of four configurations close to the boundaries of the design space.

4.4.3 Case study 2: influence of the shear stiffness

It is common knowledge that the stitching yarn influences the shear stiffness. Besides the influence on the ratio between the positive and negative forces, the stitching pattern, stitch length and stitch gauge influence the whole shear behavior. The shape of the shear force-shear angle relationship strongly differs between NCF configurations. Thus, it is necessary to study the influence of the shape of the curves on the preforming quality to support the development or the selection of adequate textiles. As a consequence, a large range of characteristic shapes of shear input curves shall be considered. For example, a linear increase over a large range of shear angles, a potential decrease after a first peak, or the onset of a locking towards high shear angles should be investigated.

4.4.3.1 Design variables

Chen et. al [56] investigated the influence of the stitching yarn on the shear stiffness of a ±45° biaxial NCF. They performed different picture frame tests on a dry NCF before and after removal of the stitching yarn. They showed that the force necessary to shear the textile in negative direction equals the force to shear the textile of which the stitching

yarn was previously removed. Therefore, the shear stiffness in negative direction can be assimilated to the minimum shear stiffness of the fibrous layers.

Based on these outcomes, the normalized shear force in positive direction $F_{fabric+}$ is generated based on the normalized shear force in negative direction $F_{fabric-}$ with different ratios. As illustrated in Fig. 4-7a, the characterization of the reference material showed that the asymmetric ratio (defined as the ratio between $F_{fabric+}$ and $F_{fabric-}$) varies between 1.23 and 3.35. In order to generate a large set of potential shear behaviors, the curve is divided into two regions.

- The first region ends at the shear angle γ_M= 11.5° (defined as point M). It corresponds to the segment in which the asymmetric ratio increases monotonously. Note that the maximum asymmetric ratio is reached at γ_M.
- The second region ends at the maximum shear angle γ_N= 45° (defined as point N). Two scaling factors C_{sM} and C_{sN} are introduced to set the scaling of the positive shear force $F_{fabric+}$ at the end of each region (i.e. at points M and N). The interpolation of the scaling factors is obtained by means of two shape functions s_1 and s_2 defined as follows:

$$s_1 = \begin{cases} 1, \forall \gamma \in [0,11.5°[\\ -\frac{1}{33.5}(\gamma - 45), \forall \gamma \in [11.5°, 45°] \end{cases} \tag{4-6}$$

$$s_2 = \begin{cases} 0, \forall \gamma \in [0°, 11.5°[\\ \frac{1}{33,5}(\gamma - 11.5), \forall \gamma \in [11.5°, 45°] \end{cases} \tag{4-7}$$

The shape functions are illustrated in Fig. 4-7b. Note that in the region $[\gamma_M, \gamma_N]$ they resemble the functions used to interpolate the results between nodes in the case of FEA with first order polynomials.

Finally, the positive shear force $F_{fabric+}$ is calculated as follows:

$$F_{fabric+}(\gamma) = F_{fabric-}(\gamma) \times \left(C_{sM}.s_1(\gamma) + C_{sN}.s_2(\gamma)\right) \tag{4-8}$$

The scaling factors vary between 1.0 and 5.0. The design space of the scaling factors is covered using a full factorial design. Sixteen levels are selected to sample the parameter sets, resulting in a total of 289 configurations (referred to as Γ_{SC}). Fig. 4-7c illustrates the resulting shear forces for two sets of scaling factors.

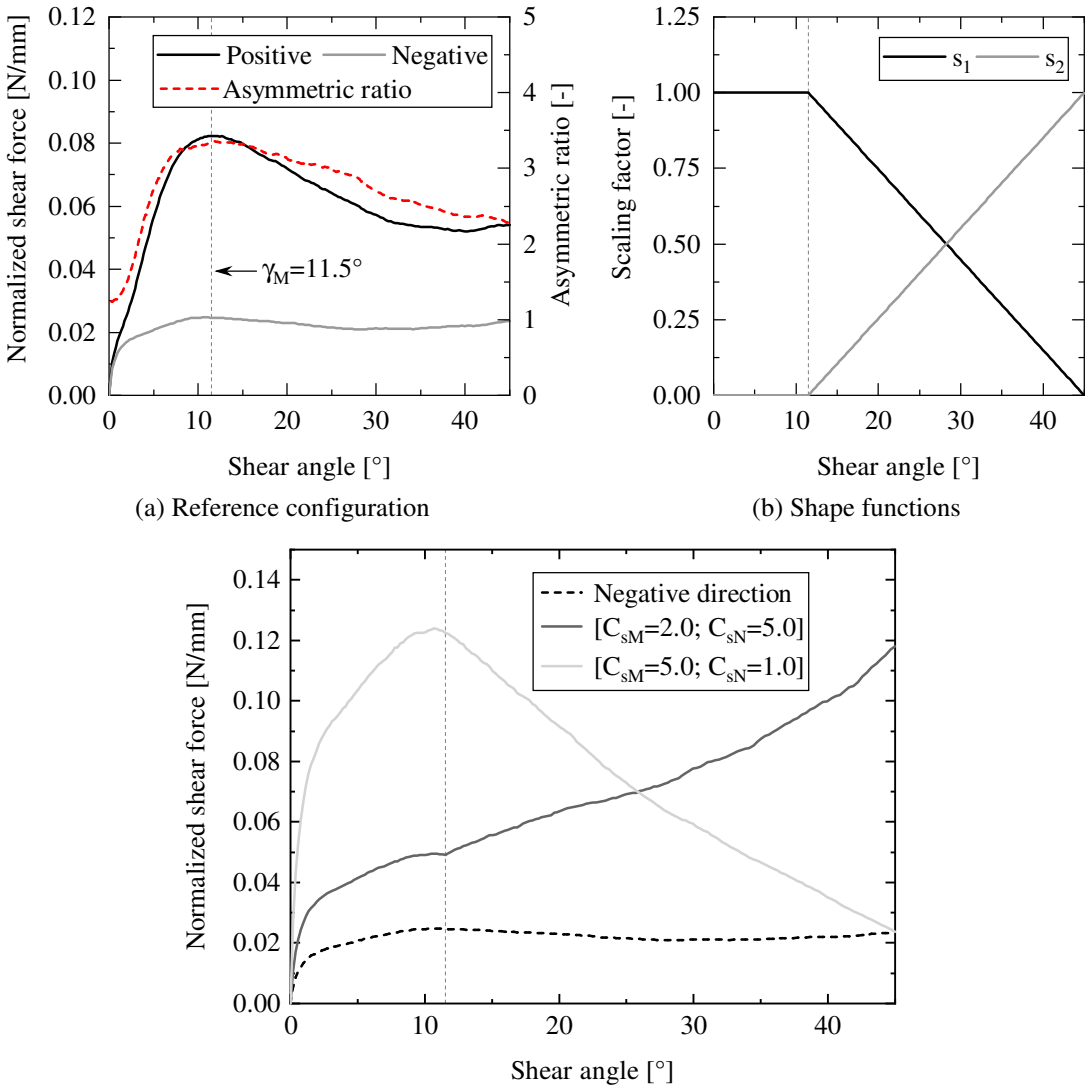

(a) Reference configuration

(b) Shape functions

(c) Examples of simulation inputs

Fig. 4-7: Shear behavior of the reference configuration (a), definition of the shape functions (b) and examples of shear curves generated with two sets of scaling factors (c).
The experimental curves illustrated in (a) are derived from the experimental results described in chapter 3 and represent the mean values of each shear direction.

4.4.3.2 Results

The results of the respective objective functions before normalization are listed in Tab. 4-4. The results of this application case study are shown in Fig. 4-8 depending on the scaling factor C_{sM} (horizontally) and C_{sN} (vertically).

Tab. 4-4: Extreme results of the objective functions for the set of design variables Γ_{SC} (application case study 2)

	$f_S(\Gamma_{SC})$ [°]	$f_B(\Gamma_{SC})$ [°]	$f_V(\Gamma_{SC})$ [dm³]
Minimum	19.7	11.9	2.24
Maximum	27.0	22.3	2.30

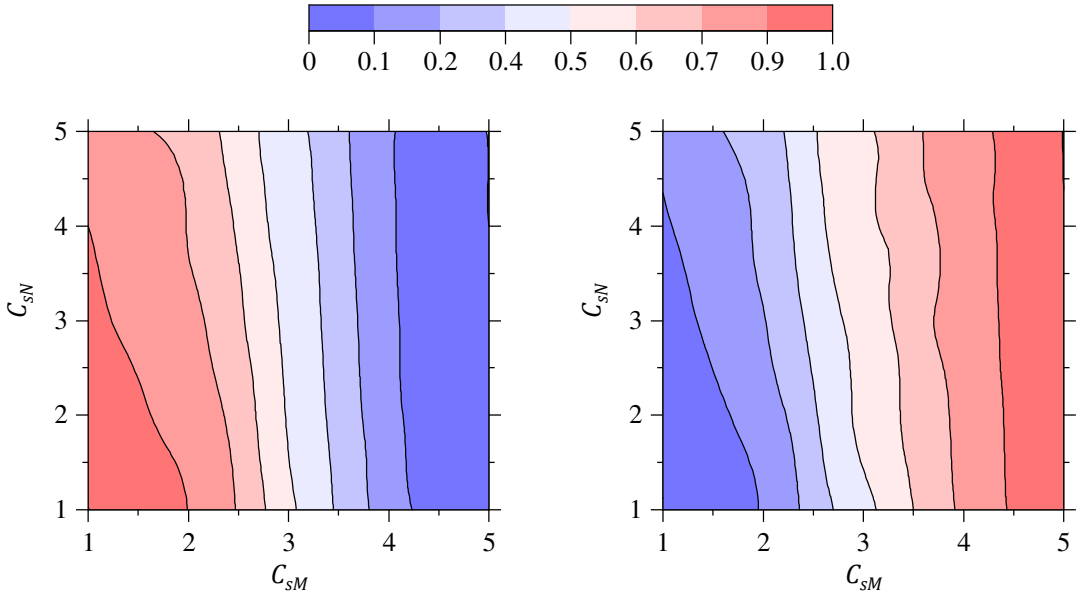

(a) Shear deformation characterized by $\widetilde{f_S}$ (b) Wrinkles characterized by $\widetilde{f_W}$

Fig. 4-8: Results of the normalized objective functions for shear (a) and wrinkling (b) from case study 2, focusing on the shape of the input curves of the shear behavior.

Here again, it can be found that the shear and wrinkling objective functions are conflicting objectives. Moreover, it can be observed that both objective functions only depend on C_{sM} if this scaling factor is higher than 3. It suggests that the level of shear deformation is only defined by this first part of the shear curve if the shear stiffness at small angles is high. For low initial shear stiffnesses, a slight dependency on the scaling factor C_{sN} can be detected but the impact on the objective functions remains small.

The simulations results obtained with the extreme sets of scaling factors [C_{sM}= 1.0; C_{sN}= 5.0] and [C_{sM}= 5.0; C_{sN}= 1.0] are shown in Fig. 4-9a and Fig. 4-9b, respectively. First, it can be observed that the asymmetric deformation of the textile is significantly higher in the case [C_{sM}= 5.0; C_{sN}= 1.0]. Furthermore, the maximum positive shear deformation is reduced by 31% and the maximum negative shear deformation is increased by 20% compared to the values computed with the scaling factors [C_{sM}= 1.0; C_{sN}= 5.0].

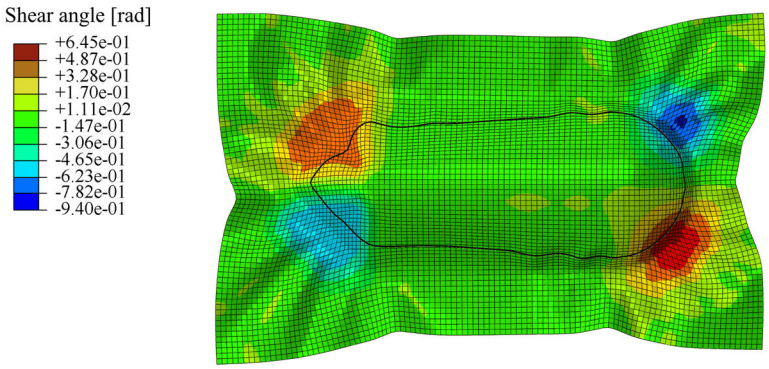

(a) $C_{sM} = 1.0$; $C_{sN} = 5.0$

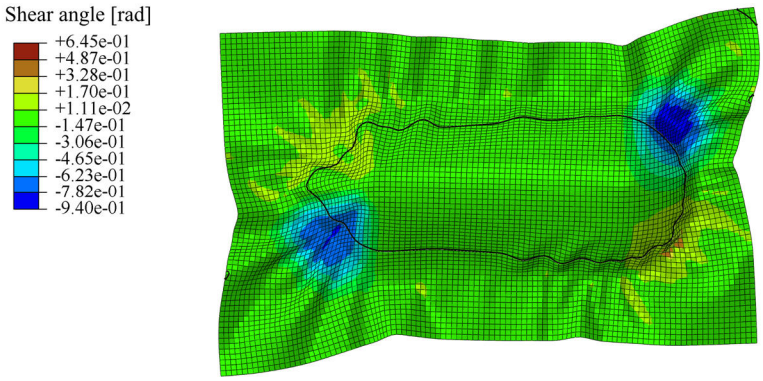

(b) $C_{sM} = 5.0$; $C_{sN} = 1.0$

Fig. 4-9: Forming simulation results obtained with two extreme couples of scaling factors.

Based on these observations, it can be derived that the quality of the preform is mainly defined by the shear behavior of the textile for small shear angles. This can be justified by the fact that the textile either shears or generates out-of-plane wrinkles and do not switch between these two deformation modes. Only a sudden increase of the shear stiffness at large angles would change the shear deformation into wrinkles, as it is found at the shear locking of woven textiles [57]. This also confirms the importance of the balance between shear and bending stiffness highlighted previously.

4.4.4 Case study 3: influence of the bending behavior

The complex bending behavior of dry textiles lead to a localization of the wrinkles that strongly depends on the non-linear moment-curvature relationship. Using the BLBM model introduced in section 3.2.3, it is possible to simultaneously vary the curvature of the softening point and the magnitude of the non-linearity (i.e. stiffness difference before and after the onset of the softening). Knowledge about the influence of the non-linear behavior on the quality of the preform is a crucial parameter for the selection of a textile.

4.4.4.1 Design variables

In order to focus on the non-linear behavior and on the softening point of the bending moment-curvature relationship, only the parameters ε_{soft} and E_{soft} of the BLBM model

are investigated. The remaining parameters are directly derived from the reference configuration. Therefore, the parameters E_{tens} and E_{comp} — responsible for the first linear part of the curve — remain constant in all configurations. Only the curvature κ_{soft} at which the softening starts is shifted and calculated according to Eq. (3-4). The boundaries of the design space and resulting curvatures of the softening points are listed in Tab. 4-5. The full factorial configuration for this study has seventeen levels, inducing a design variable set Γ_{BB} constituted of 289 configurations.

Tab. 4-5: Boundaries of the design variables (application case study 3)

	ε_{soft} [-]	E_{soft} [MPa]	κ_{soft} [m^{-1}]
Minimum	1x10^{-4}	0.1	0.167
Maximum	8x10^{-3}	5	13.3

4.4.4.2 Results

The results of this case study are shown in Fig. 4-10 depending on the compressive strain at the onset of the softening ε_{soft} (horizontally) and on the compression modulus after softening E_{soft} (vertically). The results of the respective objective functions before normalization are listed in Tab. 4-6.

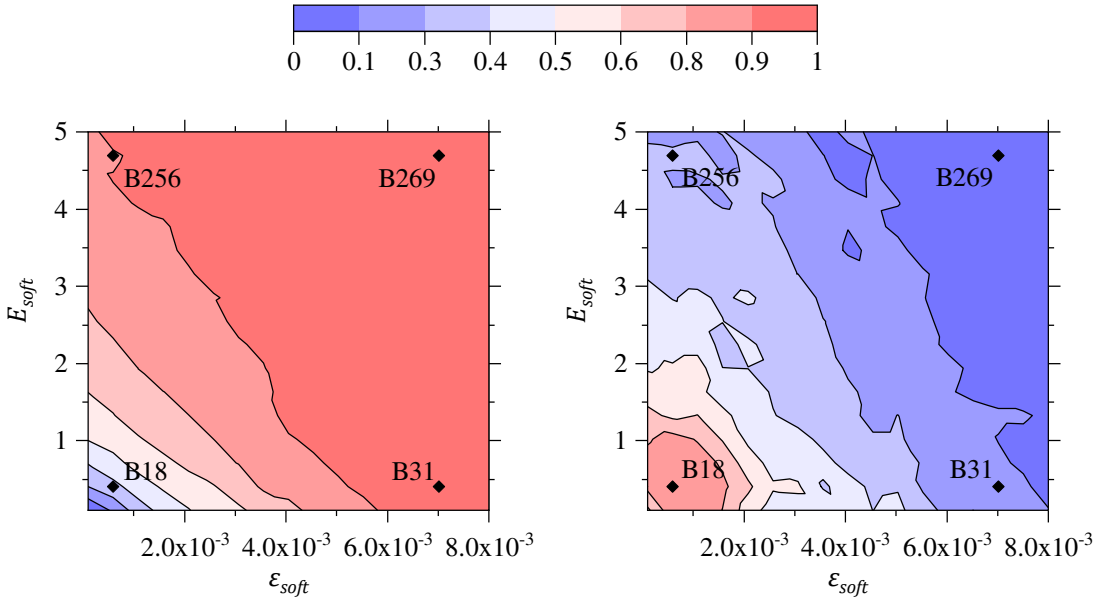

(a) Shear deformation characterized by $\widetilde{f_S}$ (b) Wrinkles characterized by $\widetilde{f_W}$

Fig. 4-10: Results of the normalized objective functions for shear (a) and wrinkling (b) from case study 3, focusing on the influence of the non-linear bending behavior.

Tab. 4-6: Extreme results of the objective functions for the set of design variables Γ_{BB} (application case study 3)

	$f_S(\Gamma_{BB})$ [°]	$f_B(\Gamma_{BB})$ [°]	$f_V(\Gamma_{BB})$ [dm³]
Minimum	11.3	13.6	2.25
Maximum	25.2	29.3	2.30

It can be observed that the shear deformation shows a stronger dependency on ε_{soft} and E_{soft} for the lower values of the design space than the out-of-plane deformations. More precisely, the normalized shear objective function $\widetilde{f_S}$ is higher than 0.8 in more than 80% of the design points. Both variables ε_{soft} and E_{soft} show the same influence on the criteria: their increase leads to high shear and low wrinkling objective functions. In order to facilitate the interpretation of the results, four simulation results were extracted from configurations located close to the boundaries of the design space. The corresponding design variables are listed in Tab. 4-7 and their respective moment-curvature relationships are illustrated in appendix d. The textile shapes of the simulation results are shown in Fig. 4-11. The figures highlight the zones in which the softening of the BLBM model is reached in at least one fiber direction.

Tab. 4-7: Parameters of the BLBM model of the four configurations illustrated in Fig. 4-11.

Designation	**B18**	**B31**	**B256**	**B269**
E_{tens} [GPa]	2.00	2.00	2.00	2.00
E_{comp} [MPa]	20.2	20.2	20.2	20.2
E_{soft} [MPa]	0.406	0.406	4.69	4.69
ε_{soft} [-]	0.593E-3	7.01E-3	0.593E-3	7.01E-3
κ_{soft} [m^{-1}]	0.990	11.7	0.990	11.7

As illustrated in Fig. 4-11a and Fig. 4-11c (i.e. at ε_{soft}= 0.593x10^{-3}) the softening of the bending behavior is reached almost in the whole textile. The compression modulus E_{soft} has a significant influence on the wrinkling behavior. It can be observed that the amplitude of the wrinkles is slightly increased in Fig. 4-11a compared to Fig. 4-11c. However, a high compression modulus E_{soft} increases the width of the wrinkles and significantly reduces their rate of occurrence. According to Fig. 4-11b and Fig. 4-11d (i.e. at ε_{soft}= 7.01x10^{-3}), only elements located in regions where a high curvature is imposed (i.e. near the blank-holder, at the edges of the pyramid or in the hemisphere part of the stamp) achieve curvatures higher than κ_{soft}. Here again, a higher value of E_{sot} reduces the number of the wrinkles and smoothens the geometry. Note that the level of shear is almost constant for the four selected configurations, excepted for the configuration showed in Fig. 4-11a (ε_{soft}= 0.593x10^{-3}, E_{soft}= 0.046 MPa) that exhibits a strong wrinkling.

Based on these results, it can be concluded that, due to the imposed geometry of the stamp, a wide region of the textile is forced to reach the softening part of the bending

behavior independently from the material parameter ε_{soft}. Thus, the bending rigidity of the textile at high curvature is a key parameter of the material model. Moreover, a larger curvature of the softening point (i.e. a higher value of ε_{soft}) reduces the number of wrinkles. Strong localizations of the deformation are still possible and only a higher compression modulus E_{soft} is able to smoothen the out-of-plane deformations.

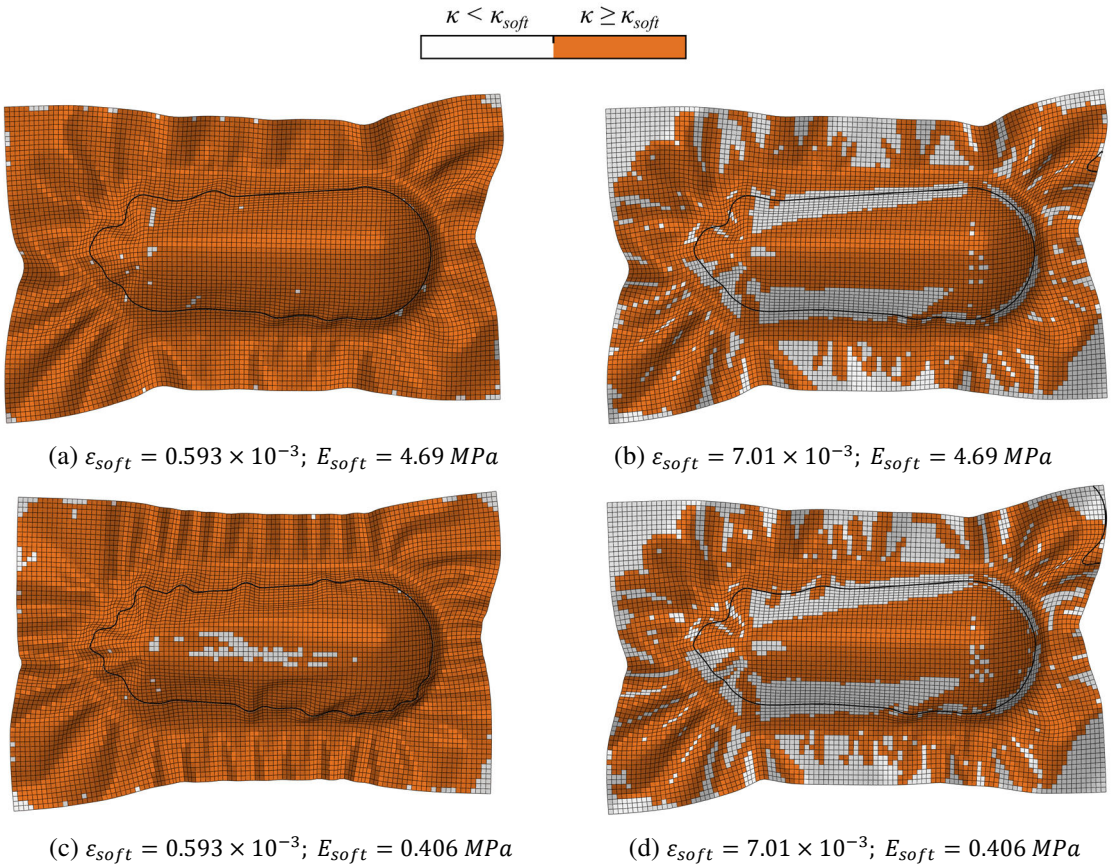

(a) $\varepsilon_{soft} = 0.593 \times 10^{-3}$; $E_{soft} = 4.69\ MPa$

(b) $\varepsilon_{soft} = 7.01 \times 10^{-3}$; $E_{soft} = 4.69\ MPa$

(c) $\varepsilon_{soft} = 0.593 \times 10^{-3}$; $E_{soft} = 0.406\ MPa$

(d) $\varepsilon_{soft} = 7.01 \times 10^{-3}$; $E_{soft} = 0.406\ MPa$

Fig. 4-11: Forming simulation results of four configurations close to the boundaries of the design space with identification of the elements for which the bending softening is reached in the final state of the forming process.

4.5 Outcomes for textile development

This chapter presented a method to measure the quality of a preform based on numerical results of a macroscopic forming simulation. Two deformation modes were identified to compute the objective functions. Firstly, the shear deformation was considered since high shear deformations change the architecture of the textile and might lead to waviness in the final component. Secondly, the out-of-plane deformations should be minimized to avoid wrinkles or folds in the final component. Their quantification was based on the local curvature for localized wrinkles and on the volume under the textile for large geometrical deviations.

This method was successfully applied to a stamping process, in which the stamp geometry is constituted of a half hemisphere and a pyramid with sharper edges. With this forming simulation, the influence of several material parameters was investigated on the preform quality, which increases understanding of the process. According to the objective functions introduced in this chapter, the following outcomes should be considered during the development or selection of adequate textiles:

- The balance between shear and bending forces is crucial for the deformation of the textile. Moreover, a combined increase of the shear and the bending stiffnesses can lead to comparable results if their ratio is appropriately selected. Applied to the development of a textile, these observations suggest that it is possible to compensate an increase of the shear stiffness by influencing its bending stiffness. For example, if the desired stitching pattern of the textile changes the shear stiffness, the preform quality could be improved with dedicated measures to adapt the bending stiffness of the textile.
- The initial shear stiffness of the textile (here for shear angles smaller than 11.5°) is essential for the final preform quality. A high initial stiffness would promote the onset of wrinkles, becoming the principal deformation mode to accommodate the stamp geometry. On the contrary, a reduced initial stiffness might lead to an overall strong shear deformation. The shear stiffness at higher shear angles reduces the maximum shear deformation but its influence is reduced to localized deformations. Considering that the shear objective function is computed using the highest shear deformation with a total of 20% of the elements, the influence of local maxima is restrained. With an increased understanding about the importance of the shear stiffness at low shear angles, it is possible to narrow the range of shear angles crucial for the selection of the textile. For instance, this method can identify the angles above which a locking of the shear behavior might be acceptable.
- The curvature at which the non-linearity of the bending moment-curvature relationships starts directly influences the number of wrinkles. At constant initial bending stiffness, a later start of the softening reduces their quantity. Nevertheless, the maximum curvature in the wrinkles is directly influenced by the magnitude of the softening. A high compression modulus after softening avoids localized kinks and smoothen the overall textile deformation. Thus, a reduced bending stiffness might be preferred if the stamp geometry (i.e. the final component) have sharp edges.

It is important to note that these outcomes are applicable to this precise geometry and forming process. Although the application case is representative of an industrial component geometry, the manufacturing of a component with other geometrical features or using a different forming process changes the boundary conditions and, thus, influences the outcomes of the analysis. Nevertheless, the framework presented in this chapter

details a method with guidelines to support the selection or the development of a textile that can be applied to any material and forming process.

Finally, this method can be used in further studies to optimize process parameters, such as the blank-holder forces or to optimize the locations and forces of grippers. In that case, optimization methods adapted to multi-objectives shall be used to compute a single scalar based on the shear and wrinkling objective functions.

5 Numerical description of NCFs at the microscopic scale

The previous chapters have shown that requirements can be defined on the textile deformability in order to reduce the defects during the preforming process. However, finding the adequate textile architecture that corresponds to a target deformability using an experimental approach would require the extensive manufacture of textile samples and their subsequent experimental characterization. Therefore, the development of numerical approaches modeling the complex behavior of NCFs represents an attractive method to understand and predict their deformation behavior at reduced costs. The objective of this chapter is to develop a model describing the filament architecture and interaction mechanisms of NCFs that can be used in further simulation steps to predict the mechanical behavior of a large range of NCF configurations.

Numerical methods developed in order to model textiles at the microscopic scales were reviewed in chapter 2. Limitations of these methods were identified, especially on the lack of defect prediction in the fibrous layers. Furthermore, they were restricted to the simulation of textiles with well-defined yarns. As a consequence, further development is necessary to apply these methods to any NCF configuration – including layer orientations that do not exhibit a purely periodic structure at the filament level, as is generally the case for ±45°-layers. Moreover, allowing local deviations of the filament orientation from the theoretical orientation is essential for accurate reproduction of the local defects in the fibrous layers.

This chapter proposes a new method to apply the microscopic modeling approach to a large panel of NCFs and model their “as-manufactured” geometries. The variability of the filament orientation is modeled, resulting in fibrous layers that account for the entanglement of the filaments and the local defects in the fibrous mat. The three-dimensional generation of the numerical model is based on the manufacturing parameters of the knitting unit and on the orientation distribution in the fibrous mat before the knitting process instead of usual geometrical inputs generated by micrographs or computed-tomography. Moreover, the proposed method is able to model any layer orientation and stitching pattern.

First, an experimental quantification of the filament orientation distribution and local defects is proposed. Then, the approach modeling the fibrous structure of the NCF including the variability of the filament orientation is detailed, applied and validated with the reference textiles presented in section 1.3 (±45° and 0°/90° NCFs). Finally,

guidelines to adjust numerical parameters of the method is presented based on thickness measurement of the textiles.

The content of this chapter is partly derived from [P1].

5.1 Investigation of the NCF fibrous layers

5.1.1 Distribution of the filament orientation

A characterization of the distribution of the filament directions was first performed to quantify the actual deviation of the filaments from the theoretical path and to study local defects in various NCF configurations. The orientation measurements were performed using an optical F-Scan Sensor from Profactor GmbH [178] on both sides of the 0°/90° and ±45° NCFs (i.e. reference textiles). In this way, each layer can be observed separately. The results are depicted in Fig 5-1, showing the local deviation of the filament orientation from the layer orientation (defined as the median value of the data). Note that the stitching yarn and the underlying fibrous layers are excluded from the measurement in order to consider each layer separately using the procedure introduced in section 3.4.4.2. This also emphasizes the local defects in the fibrous layers. In the 0°/90° NCF, the filaments should theoretically align with the stitching points, resulting in channels only. Nevertheless, it can be observed in Fig 5-1a that a few filaments of the 0°-layers are crossing the channels between the stitching points and that cracks are generated in the 90°-layer (see Fig 5-1b). Therefore, the types of defects not only depend on the orientation of the layers with regard to the stitching points but also on the distribution of the filaments resulting from the spreading and laying processes (i.e. the waviness and fiber misalignment present in the fibrous layers prior to the knitting process). Moreover, cracks are observed in both layers of the ±45° NCF, as illustrated in Fig 5-1c and Fig 5-1d.

The distributions of the local deviations from the layer orientations are illustrated in Fig. 5-2. While comparable distributions are measured on both +45° and -45°-layers, significant differences can be observed for the 0°/90° NCF. The 0°-layer shows a narrower distribution than the 90°-layer, which correlates well with the previous observation of the local defects. Therefore, the types of defects are closely related to the orientation distribution of the fibrous layers. Moreover, it is expected that a greater spread of the filament orientation distribution leads to a higher degree of entanglement of the filaments (i.e. inter-filament interactions) and to an increased interaction with the stitching yarn. As a result, it is expected that the filament orientation distribution influences the overall deformation mechanisms of the textile and must be modeled accurately in the numerical description of the textile.

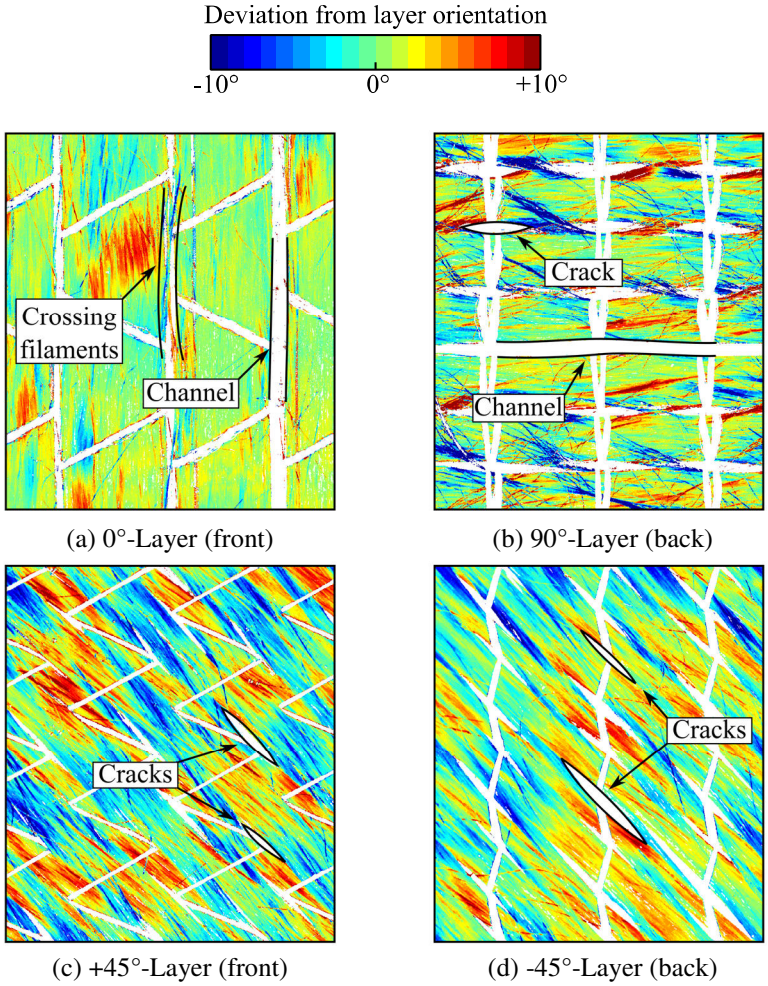

(a) 0°-Layer (front) (b) 90°-Layer (back)

(c) +45°-Layer (front) (d) -45°-Layer (back)

Fig 5-1: Local deviation of the filament orientation from the layer orientation on the 0°/90° NCF (a and b) and ±45° NCF (c and d) with identification of the local defects.

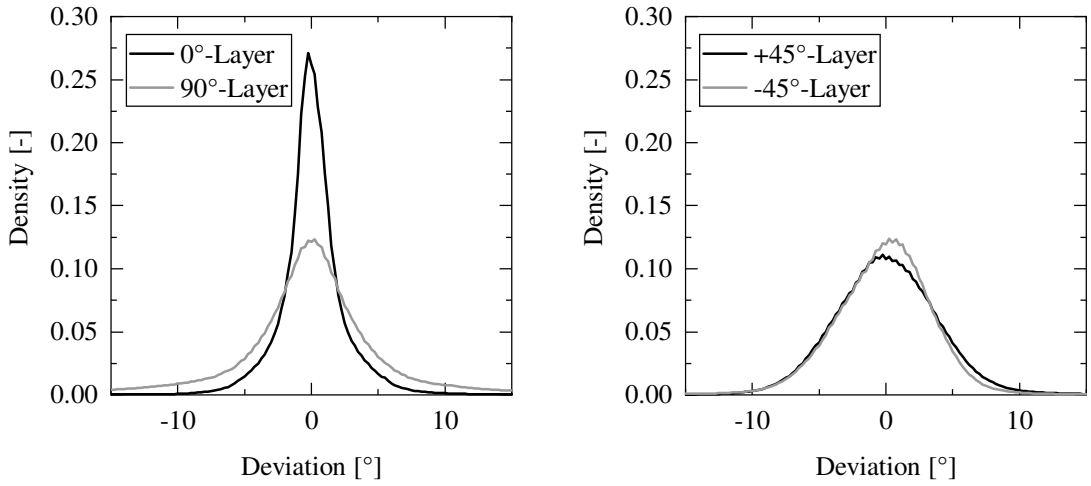

(a) 0°/90° biaxial NCF (b) ±45° biaxial NCF

Fig. 5-2: Probability density of the deviations of the local filament orientation from the layer orientation.

5.1.2 Size of the defects

The size of the local defects was measured in each layer with a minimum of forty measures per layer. As illustrated in Fig. 5-3, the width of the channels in the 0°-layer of the 0°/90° NCF was evaluated in the middle of the tricot segments. Due to the presence of the stitching yarn, the width of the cracks in the 90°-layer could not be evaluated accurately. Therefore, only the crack length of the 90°-layer was measured. In the ±45° NCF, cracks are observed in both layers. As shown in Fig 5-1, the fibrous mat of the +45°-layer covers the stitching yarns at some locations and prevent the measure of any defect. This happened in 35% of the selected locations. In this case, further points were selected to achieve a minimum of forty measures in each layer.

The results of the defect measurement are listed in Tab. 5-1. The local defect in the fibrous layers vary considerably in width and length. In addition, the angular tilt of the loops was investigated in the -45°-layer to quantify their deviation from the machine direction. A mean angle of 14.9° with a standard deviation of 1.3° was determined. These experimental observations will be used to validate the numerical approach. Note that they correlate well with the results reported by Lomov et al. in [68], where the cracks induced in various NCFs and the angular tilt of the stitching loops were extensively characterized.

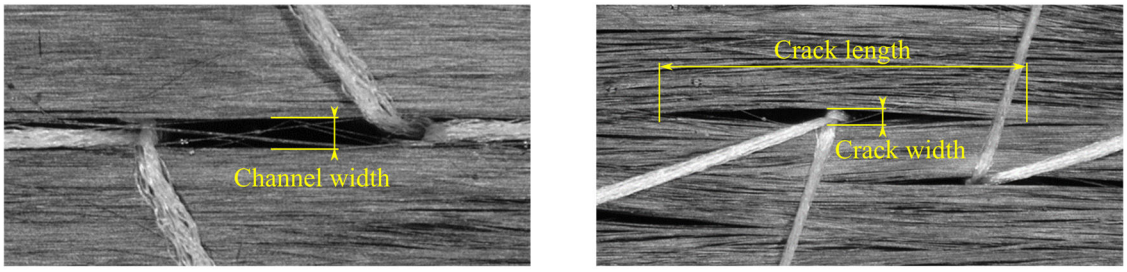

(a) Channel in a 0°-layer (b) Crack in a 45°-layer

Fig. 5-3: Measurement procedure of the defect size of a channel (a) and crack (b).

Tab. 5-1: Size of the local defects measured on the NCFs.

Designation	Layer	Defect type	Characteristic	Mean value [mm]	Standard deviation [mm]
0°/90° NCF	0°	channels	width	0.50	0.24
0°/90° NCF	90°	cracks	length	2.30	0.70
±45° NCF	45°	cracks	length	3.19	0.81
±45° NCF	45°	cracks	width	0.21	0.09
±45° NCF	-45°	cracks	length	3.58	0.89
±45° NCF	-45°	cracks	width	0.22	0.09

5.2 Generation of the "as-manufactured" geometry

5.2.1 Numerical description of the filaments

In this doctoral thesis, digital chains using truss elements have been implemented in the commercially available finite element software package ABAQUS/Explicit. Using this type of elements, the bending stiffness of the chains is neglected. Within this approach, the forces result from the axial deformation of the truss elements and from friction between the chains. The contact between the chain elements is computed using a penalty method that introduces a numerical stiffness at the contact between two elements to compute the forces at the interface. The corresponding penalty stiffness is calculated by the solver to minimize the penetration of the elements while reducing the impact on the critical time increment of the explicit calculation [200]. A conventional Coulomb friction law is used to calculate the frictional forces. Moreover, it is expected that the deformation behavior of the textile in thickness direction mainly derives from the rearrangement and relative displacement of the filaments. Since these DCE have a constant cross-section, the discretization level of the fibrous mat should be sufficiently refined to reproduce the rearrangement and interaction between the chains accurately. This approach is especially attractive because it reduces the number of degrees of freedom and requires few inputs.

5.2.2 Generation of the fibrous mat

Depending on the manufacturing technique and the layer orientation, uniformly distributed fibrous layers are used during the knitting process to manufacture the NCFs. In this case, the needles do not penetrate the layers between precisely laid tows but pierce the fibrous mat [201]. Therefore, it is proposed to generate fibrous layers homogeneously distributed in order to consider a wide variety of multiaxial NCFs and to reproduce the manufacturing process accurately.

In a first step, the variability of the filament directions is introduced with digital chains initially modeled as straight lines with an angle, which is randomly sampled using a Gaussian distribution located at the reference layer orientation. Each chain is modeled at a different out-of-plane coordinate[1] to avoid any non-physical interpenetration of the chains. If a chain crosses the border of the modeled volume element, it is projected onto the corresponding face on the other side of the volume element (see Fig. 5-4a). Hence, the number of digital chains is kept constant for any cross section of the modeled fibrous mat. Subsequently, a simulation step using two rigid plates is necessary to compact the

[1] A supplementary gap of 1% of the chain diameter is introduced between the upper and lower out-of-plane coordinates of the chain surfaces

chains to the final homogeneous fibrous mat. Thereby, the displacement of the end-nodes of the chains is allowed in the vertical direction only. This simulation step offers an efficient resolution of the potential interpenetration with an explicit solver and leads to the onset of undulation and entanglement of the chains – as illustrated in Fig. 5-4b. The compaction stops once the distance between the plates reaches a predefined value. Since the thickness of the NCF material in a relaxed state is a priori not known, a coefficient similar to the FVF is introduced to characterize the packing state of the relaxed material. The thickness t_{layer} of the generated layers after compression is calculated as follows:

$$t_{layer} = \frac{A}{\varphi_{layer} \cdot \rho_f} \tag{5-1}$$

where A corresponds to the areal weight of the layers, φ_{layer} is the prescribed FVF and ρ_f the density of the filaments. The thickness of the fibrous mat before the stitching is calculated based on an overall FVF of φ_{layer}= 20%.

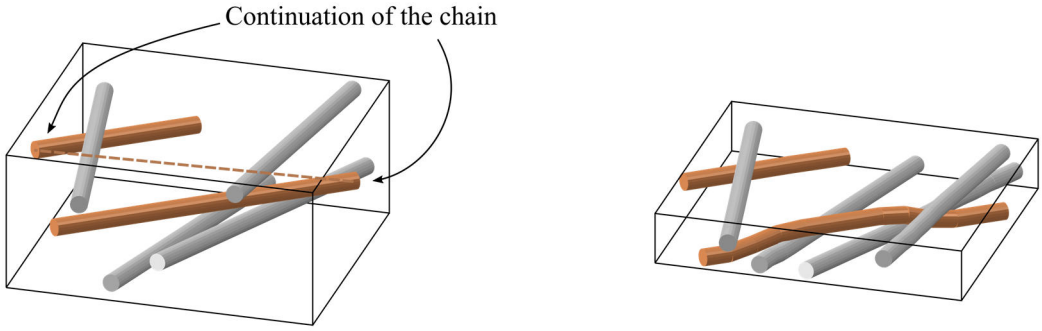

(a) Generation of the chains without interpenetration

(b) Compression and onset of the entanglement

Fig. 5-4: Resolution of the interpenetration in fibrous layers including variability in the filament orientation.

In the case of a purely periodic material (i.e. without variability), the chains are directly distributed homogeneously in a volume with the final thickness t_{layer}. Since the knitting process induces local shifting of the filament directions from the reference path, the sampling of the homogeneous fibrous layers cannot directly rely on the distributions presented in Fig. 5-3. Therefore, various standard deviations are implemented and only the orientation of the chains of the final "as-manufactured" geometry are compared to the experimental results. Fig. 5-5 shows the resulting architecture of the fibrous layer for an exemplary 0°-layer without variability and with normally distributed filament orientations featuring standard deviations of 0.3°, 1.0° and 3.0° respectively. It can be observed that the standard deviation significantly influences the interlacing of the chains and confirms the ability of the approach reproducing the entanglement of filaments.

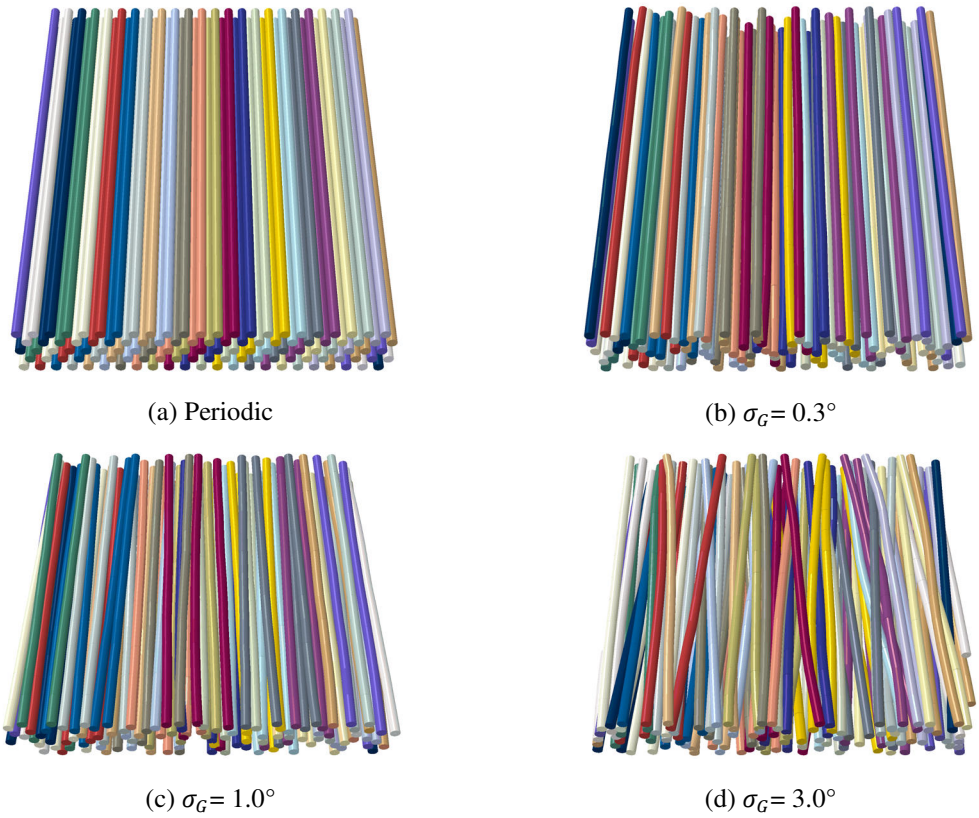

(a) Periodic (b) σ_G= 0.3°

(c) σ_G= 1.0° (d) σ_G= 3.0°

Fig. 5-5: Fibrous layers homogeneously generated without variability of the filament orientation (a) as well as with Gaussian distributed filament orientation featuring standard deviations from 0.3° (b) to 3.0° (d).

5.2.3 Averaged periodic boundary conditions

Due to the high refinement scale of the presented approach, the simulation of a whole textile sample usually required in mechanical characterization would lead to unfeasible calculation times. Therefore, a representative substructure is modeled using adequate boundary conditions to reproduce the behavior of the whole sample. The manufacturing process of multiaxial NCFs is a continuous process in which the knitting process leads to a periodic network of the stitching yarns [201]. Depending on the stitching pattern, the knitting cycle repeats, for example, after each cycle (pillar pattern), two cycles (tricot pattern) or four cycles (tricot-chain pattern). In this approach, the textile is modeled with a RVE based on the periodicity of the stitching pattern. The smallest RVE, defined as the smallest repetitive unit cell of the stitching yarn network, is referred to as the "elementary RVE". The size of the RVE can be derived from repetitions of the elementary RVE and denoted $r_W \times r_L$, where r_W and r_L correspond to the number of repetitions perpendicular to the machine direction and in machine direction, respectively.

After introduction of the variability, the generated digital chains do not exhibit any periodicity at the edge of the RVE. Therefore, appropriate boundary conditions must be applied to the fibrous layer to ensure the representativeness of the model for a continuous textile. The implementation of symmetric boundary conditions would enable a free

movement of the chains at the boundary causing their non-physical rearrangement. On the contrary, fixing the transverse displacement of the end nodes would add an artificial transverse stiffness and would not be able to represent the onset of larger defects, such as gaps in a 0°-layer. Therefore, it is proposed to implement averaged periodic boundary conditions. To that end, a discretization of the RVE with a regular rectangular mesh is introduced at its boundaries, as illustrated in Fig. 5-6. Reference Points (RPs) are defined subsequently in the middle of each mesh element. The end nodes of the digital chains located in each mesh element are connected to the corresponding RP with averaged displacement boundary conditions as follows:

$$u_{RP} = \sum_{i=1}^{n} \frac{u_i}{n} \tag{5-2}$$

where u_{RP} represents the displacement of the reference point, u_i the displacement of node i, and n the total number of nodes in the mesh element.

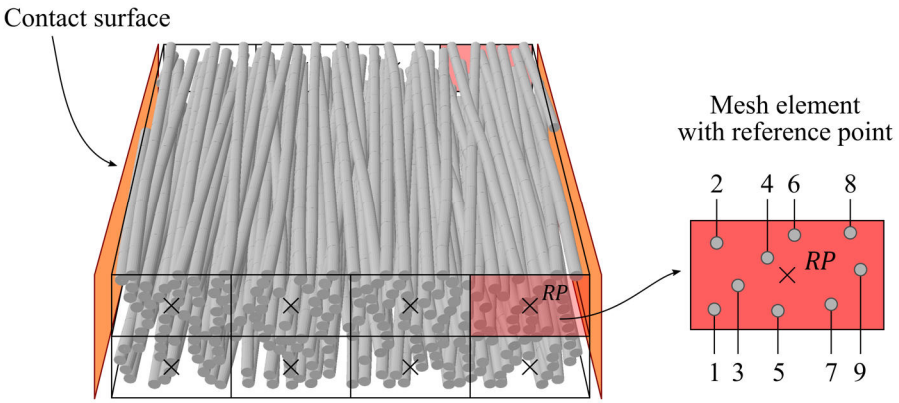

Fig. 5-6: Regular rectangular mesh defined at the boundary of the RVE with corresponding reference points and contact surfaces.
For better clarity, only the lateral surfaces are illustrated.

Since the mesh of the RPs is regular, usual periodic boundary conditions can be applied to the RPs. Thereby, the displacement of periodic nodes, i.e. nodes at corresponding positions on opposed cross sections, are constrained to be equal. The size of the mesh elements is an important parameter of the model and is calculated to ensure that, on average, one end-node is located in a mesh element. This approach is selected to enable a direct comparison with a purely periodic material, which corresponds in this case to the application of usual periodic boundary conditions. If no end-node is located in a mesh element, the element is merged progressively with the closest non-empty element. Thereby, the size of the mesh elements may change but still remains periodic. Moreover, contact surfaces are introduced to all faces of the volume boundary to model the fictive neighboring material and restrain the chains within the modeled volume. Note that standard periodic boundary conditions are applied to the stitching yarn chains since the RVE size correlates with the periodicity of the pattern. Using this approach, the overall

periodicity of the material is ensured while allowing relative movements of the digital chains within the RVE. Moreover, any global deformation of the RVE can be generated by applying relative displacements to the RPs and, thus, enables a virtual characterization of the material.

5.2.4 Stepwise model generation

The manufacturing process must be reproduced accurately in order to generate a realistic mechanical model of the textile – referred to as the "as-manufactured" geometry. In this thesis, a stepwise generation of the "as-manufactured" geometry is achieved through a fully automated framework that connects pre-treatment, simulation and post-treatment operations. The flowchart of Fig. 5-7 illustrates the connections between the input file, the main python scripts used for the pre and post-treatment operations as well as the intermediate simulation steps. The input parameters required for the whole framework are listed in a single text file divided in many categories, depending on the simulation steps for which the input parameters are required. The first python script "main_RandomFiberBed.py" defines all parameters related to the fibrous layers, which includes the number of chains and the sampling of the orientations of the chains. Compaction plates are generated to compress the chains to the required thickness before knitting. The resulting uniformly distributed layers are shown in Fig. 5-8a.The second python script "main_Penetration.py" generates the knitting needles at all stitching points. The periodic mesh and all subsets required for the averaged periodic boundary conditions are defined in this script. The piercing of the fibrous layers by the needles occurs simultaneously at all stitching points and in a single step. Thereby, the digital chains are pushed apart when the needles penetrate the layers, as shown in Fig. 5-8b. The stitching yarns are introduced in the third python script "main_StitchPretension.py". The yarns are initially modeled with simplified geometries using sharp edges at the location of the piercing points (see Fig. 5-8c). Since the digital chains of the stitching yarn have no bending stiffness, the sharp geometries do not induce stress concentrations. The third simulation step consists in the pretension of the stitching yarn. To that end, a negative thermal load is applied to the stitching yarn chains to reproduce the tension induced by the knitting unit during the stitching process, as illustrated in Fig. 5-8d. This procedure reproduces the defects induced during the knitting process and accounts for manufacturing parameters (e.g. the tension in the stitching yarn) with reduced computational cost compared to a simulation of the whole knitting process. Moreover, the simulation approach is applicable using conventional contact algorithms and avoids potential numerical issues due to the resolution of contact overclosure.

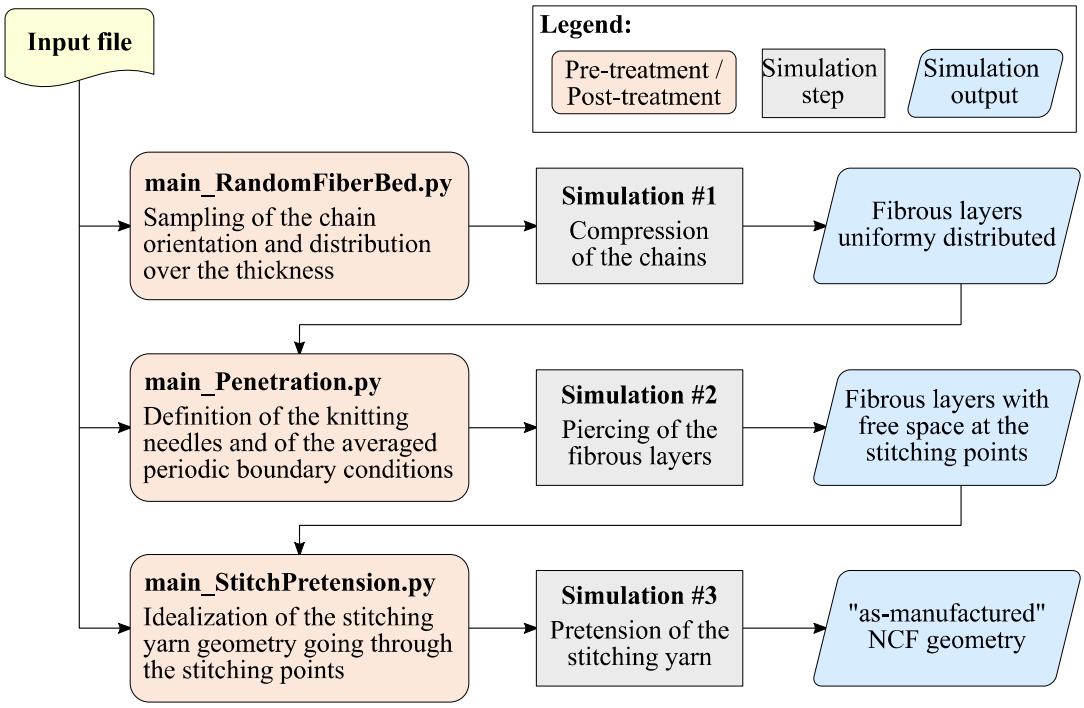

Fig. 5-7: **Flowchart of the automated framework for the stepwise generation of the "as-manufactured" geometry.**

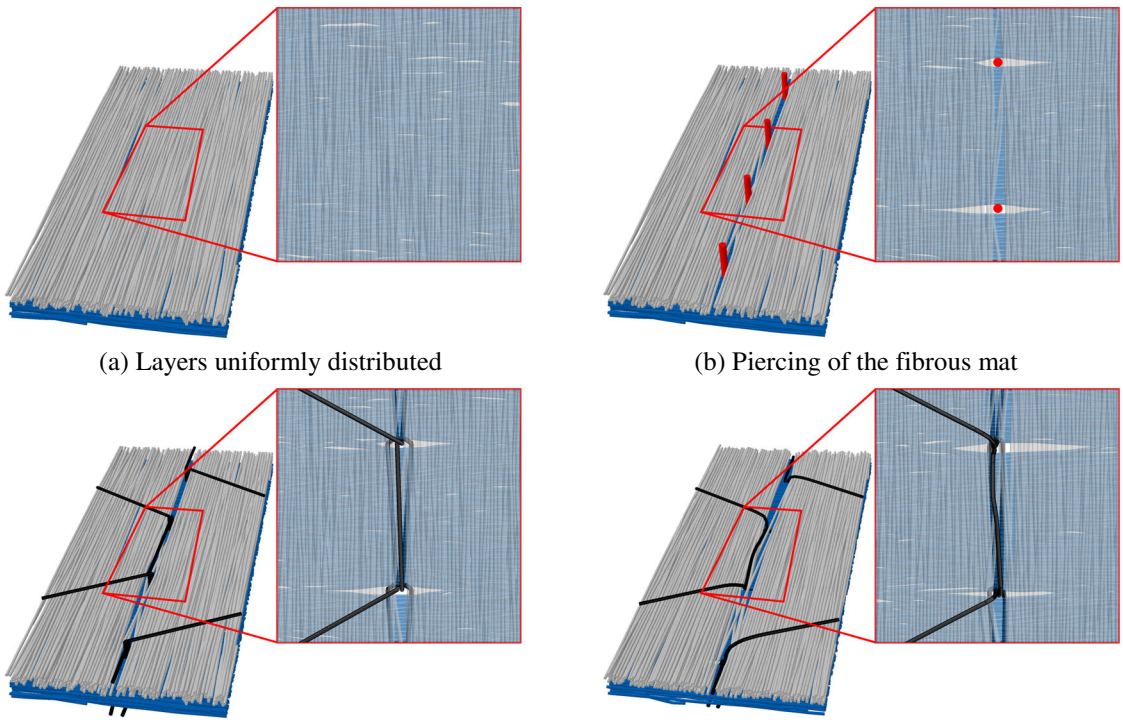

(a) Layers uniformly distributed

(b) Piercing of the fibrous mat

(c) Idealization of the stitching yarn

(d) Pretension of the stitching yarn

Fig. 5-8: **Detailed view of the stepwise generation of the "as-manufactured" geometry.**

5.2.5 Simulation parameters

Due to the high number of filaments in the textile, it is not possible to model each of them separately. Therefore, many filaments are grouped in a single digital chain. In order to generate comparable models with varying refinement levels, the volume of filaments is first calculated based on the areal weight of each layer and on the density of the filaments. A packing coefficient φ_{chain} is introduced as suggested in [202] to account for the packing of the filaments in the relaxed state. This numerical parameter can be approximated as a FVF in each chain (see Fig. 5-9).

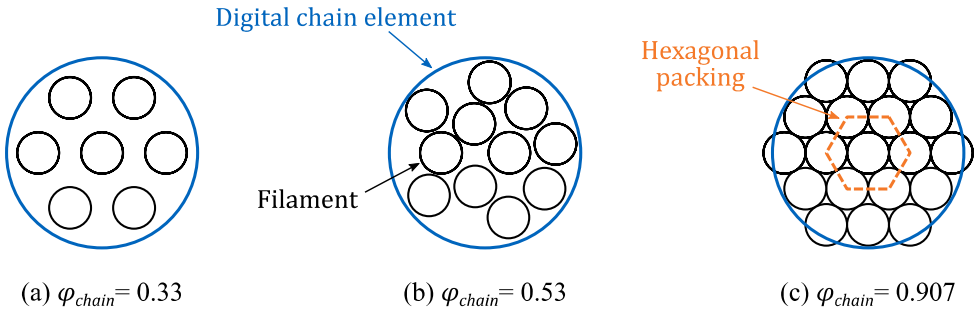

Fig. 5-9: Illustration of the packing coefficient of filaments in a digital chain.

Then, the number of chains n_{chains} required for the simulation of a fibrous layer is calculated according to Eq. (5-3) depending on the layer orientation θ_{layer}, the DCE diameter D_{chain} and the width of the RVE w.

$$n_{chains} = \frac{A \cdot w}{\rho_f \cdot \varphi_{chain}} \frac{4\cos(\theta_{layer})}{\pi \cdot D_{chain}^{\ 2}} \tag{5-3}$$

The number of chains is subsequently rounded up, requiring a slight decrease of the DCE diameter according to Eq. (5-3). The input diameter of the DCEs modeling the filaments is set to 69 µm, which represents a good compromise between calculation time and discretization level. With these parameters, each digital chain models about forty-nine filaments. It should be noted that the stiffness and the density of the chains are calculated depending on the packing coefficient and, thus, depending on the number of filaments grouped in the chains. Moreover, mass scaling is introduced in order to speed up the simulation (initial critical increment size larger than $4x10^{-5}$ sec). Tab. 5-2 summarizes the input parameters used for the numerical description of the NCFs. Although the stitching yarns are also constituted of many filaments, they are modeled with one single digital chain. According to [68], the actual diameter of the stitching yarn varies spatially due to the various compaction states of the yarns (i.e. compacted at the loops or flattened at the top surface). Nevertheless, a unique cross-section of the stitching yarn is assumed in the whole model, since the location of the chain elements may change during the application of the stitching yarn pretension. In order to model the stitching yarn at the region of inter-stitch interactions accurately, the diameter of the chain is calculated assuming a

hexagonal packing, as suggested in [68]. The friction coefficients between the chains is set to a constant value of 0.3. It is representative of the values that can be found in studies focusing on the characterization of friction of carbon filaments at tow or filament level [203–205].

Tab. 5-2: Input parameters for the numerical description of the NCFs

		0°/90° NCF	**±45° NCF**
Filaments	Young's modulus [GPa]	120	127.5
	Density [g/cm³]	0.905	0.890
	Diameter [µm]	69	69
	Packing coefficient [-]	0.5	0.5
	Mesh length [mm]	0.2	0.2
Fibrous layers	Layer thickness before stitching [mm]	0.41	0.43
	Standard deviation for the sampling [°]	1.15 (0°-layer)*	2.0 (+45°-layer)
		4.0 (90°-layer)*	2.0 (-45°-layer)
Stitching yarn	Young's Modulus [GPa]	1.81	1.81
	Density [g/cm³]	1.25	1.25
	Diameter of the chains [µm]	88	71
	Mesh length [mm]	0.1	0.1
	Magnitude pretension [%]	16	17

* these parameters are not applicable to the simulations performed in section 5.3.1

5.3 Validation of the fibrous layers

5.3.1 Numerical description of NCFs with variability of the filament orientation

The influence of the layer orientations and of the standard deviation of the Gaussian distribution used to sample the orientation of the chains is studied on the defects in the fibrous mats. First, various "as-manufactured" geometries of the 0°/90° NCF are illustrated in Fig. 5-10. The simulations are based on the parameters listed in Tab. 5-2 with different orientation variability in the layers (from a purely periodic fibrous mat up to a standard deviation of 3.0°). It can be determined that the purely periodic material (Fig. 5-10a) exhibit straight chains and that only channels are formed. With increasing variability (see Fig. 5-10b to Fig. 5-10d), the channels are closing progressively, starting from a few filaments crossing the channels and evolving to localized cracks. This correlates well with the conclusions drawn from the scans of the textile presented in section 5.1.1. Moreover, the onset of the gap over the whole length of the RVE shows the capability of the averaged periodic boundary condition to model local defects that propagate periodically beyond the RVE.

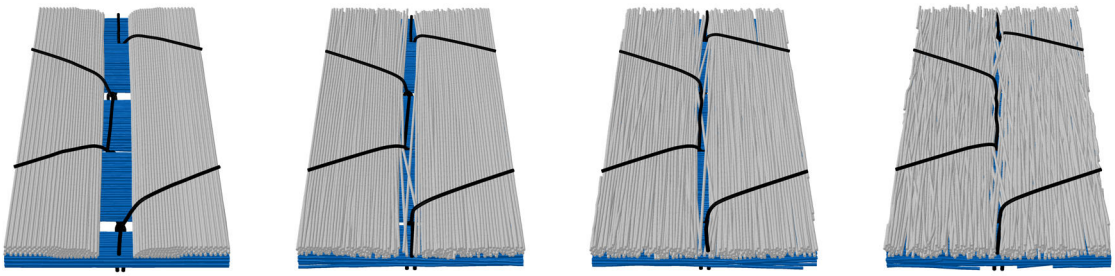

(a) Periodic (b) $\sigma = 0.3°$ (c) $\sigma = 1.0°$ (d) $\sigma = 3.0°$

Fig. 5-10: Elementary RVEs of the "as-manufactured" geometries of a 0°/90° biaxial NCF using purely periodic chains (a) as well as with increasing standard deviations of the sampling (b to d).

The numerical description of the ±45° NCF material is illustrated in Fig. 5-11, where local cracks can be observed at the stitching points and a waviness is induced in the path of the chains. This shows that the modeling approach is able to reproduce various types of defects already using the elementary RVE. A detailed comparison is proposed in the following subsections to assess the accuracy of the simulation approach.

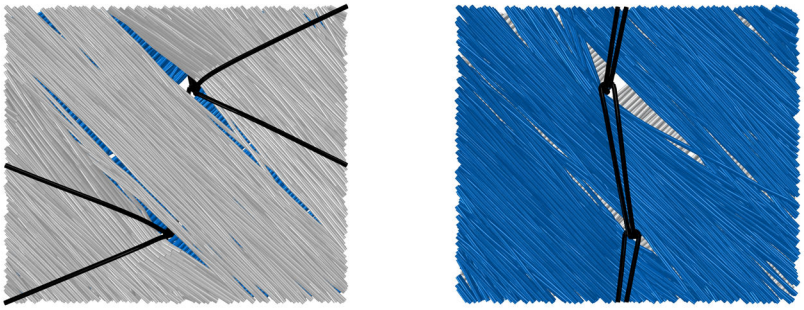

(a) Front face (b) Back face

Fig. 5-11: Elementary RVE of the "as-manufactured" geometry of the ±45° NCF.

5.3.2 Comparison of the filament orientations

The comparison of the simulation results with real samples is performed using larger models, namely 2x2 and 3x3 RVEs for the 0°/90° and ±45° NCF, respectively.

First, the chain orientation is compared with the experimental distributions presented in section 5.1.1 to validate the modeling approach of the fibrous mats. In order to compare the final distributions of the chain orientations, the orientation of all DCEs is computed and projected onto a 2D-plane parallel to the virtual textile. This allows for a direct comparison of the results, as illustrated in Fig. 5-12. Since a random sampling of the chain orientation is used, the final orientation distribution of the numerical results is the mean distribution from three independent calculations. The standard deviation of the Gaussian distributions used to generate the two "as-manufactured" geometries are listed in Tab. 5-2. A good correlation with the experimental distributions can be observed, which confirms the ability of the simulation method to model the variability in the

filament orientation of a textile. A further conclusion is that the standard deviation is a predominant input that can be used to model differences between two fibrous layers in a same NCF material. Nevertheless, slight differences are seen between the simulation and experimental results. For example, the distributions of the 0°/90° NCF can reproduce the peaks accurately, while small deviations occur for angles larger than 5°. Further information on the filament orientation before the stitching process would increase the accuracy of the sampling distribution and, thus, the final distribution of the filament orientations.

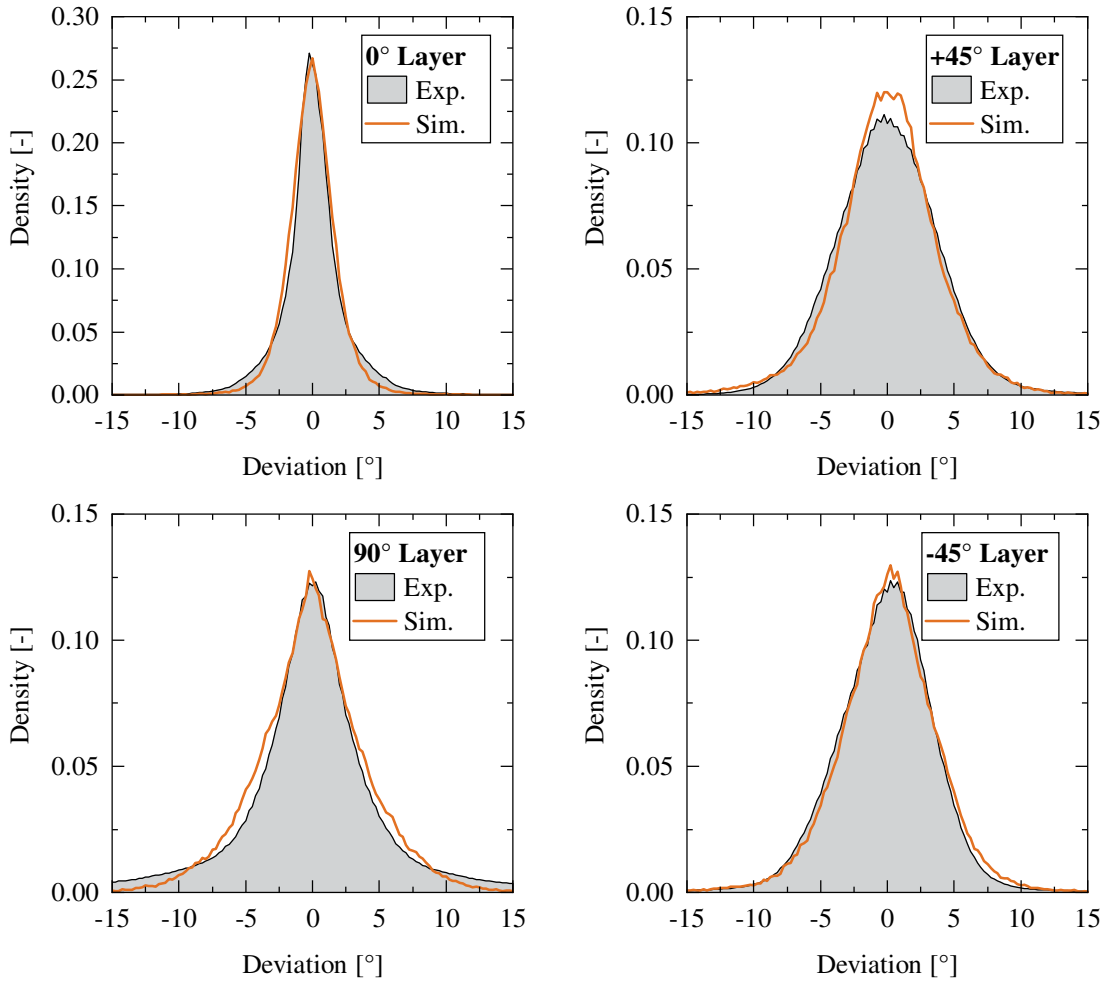

(a) 0°/90° NCF (b) ±45° NCF

Fig. 5-12: Comparison of the DCE orientation (Sim.) with the measurement on the samples (Exp.) of the 0°/90° (a) and ±45° NCFs (b).

5.3.3 Comparison of the local defects

A comparison of the local defects points out the ability of the method to model various deviations induced by the stitching yarn. Using the reflection properties of the carbon filaments, it is possible to emphasize the defects in the NCFs as shown in Fig. 5-13 and Fig. 5-14.

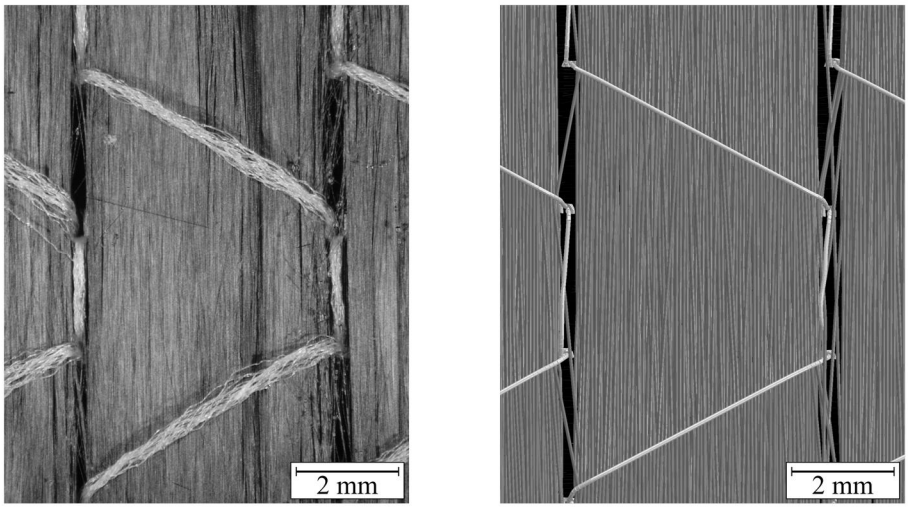

(a) Comparison of the 0°-layer

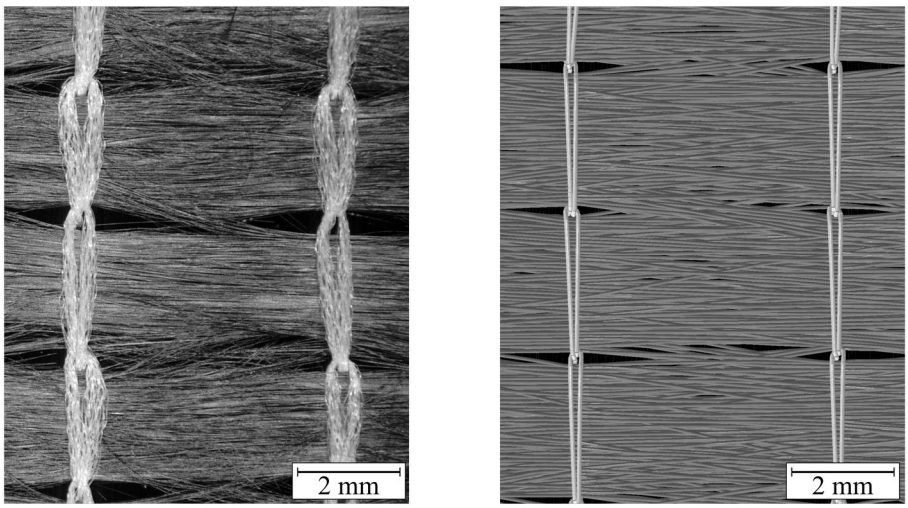

(b) Comparison of the 90°-layer

Fig. 5-13: Comparison of the overall defect formation in the 0°-layer (a) and 90°-layer (b) between the 0°/90° NCF samples (left) and simulation results (right).

As stated in section 5.1.2, a large variability of the defect size is observed in the fibrous layers. In the 0°/90° NCF, the type of defects of the "as-manufactured" geometry are well captured in the model (see Fig. 5-13). Channels are induced in the 0°-layer with filaments crossing from one tow to the neighboring one, while regular localized cracks are formed at the stitching points in the 90°-layer. On the front face of the ±45° NCF (i.e. 45°-layer) the same characteristics as those from real samples can be observed: at some stitching points almost no defects are noticeable while fish eye deformation with a length of several millimeters can be observed at the neighboring stitching point (ref. Fig. 5-14a). On the contrary, the back face (i.e. -45°-layer) shows a regular formation of fish eye defects throughout the layer with various dimensions, as illustrated in Fig. 5-14b.

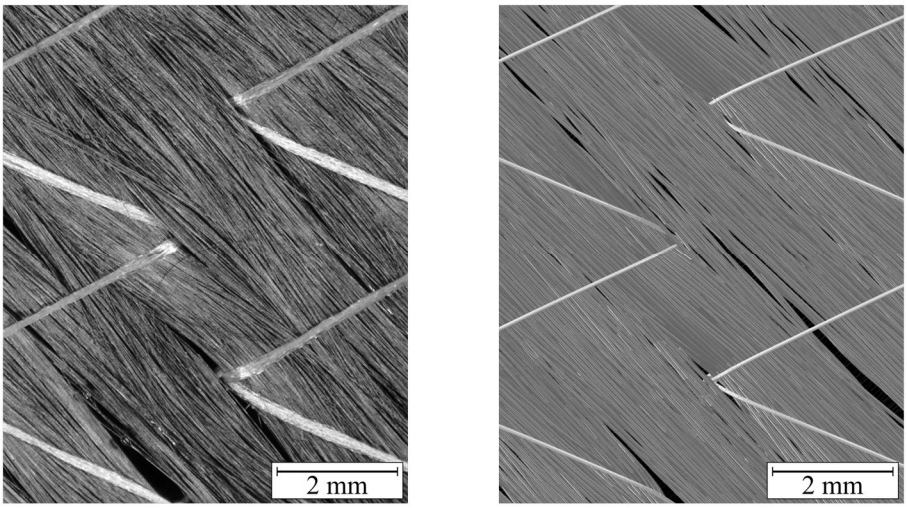

(a) Comparison of the 45°-layer

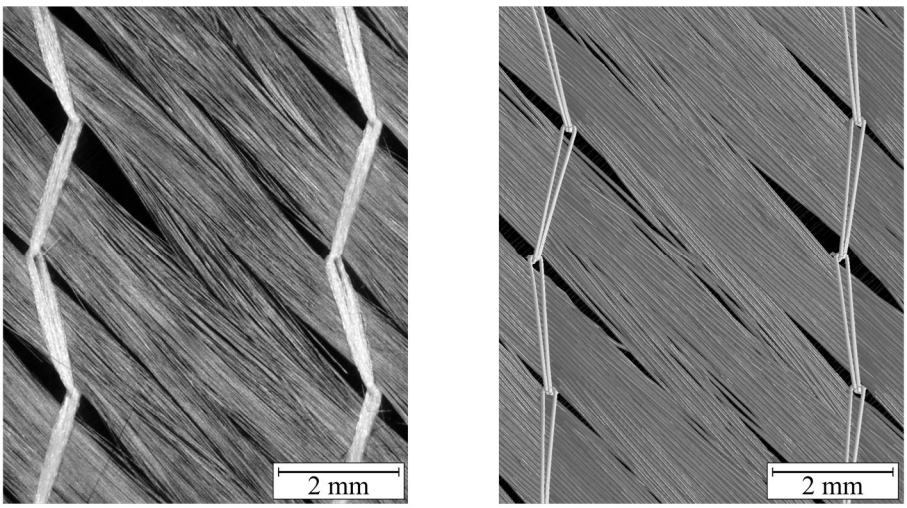

(b) Comparison of the -45°-layer

Fig. 5-14: Comparison of the overall defect formation in the 45°-layer (a) and -45°-layer (b) between the ±45° NCF samples (left) and simulation results (right).

The procedure presented in section 5.1.2 to measure the size of the defects was applied to the simulation results. The measured defect sizes are listed in Tab. 5-3 and a comparison between the experimental and numerical results is proposed in Fig. 5-15.

A good correlation of the mean values and their respective scatter can be observed. The size of the defects measured in the simulation of the ±45° NCF is slightly underestimated. Nevertheless, larger defects are generated in the -45°-layers than in the +45°-layers, an effect that corresponds to the experimental observations. Moreover, the cracks were not observable in the +45°-layer at 31% of the stitching points. This variability in the defect visibility correlates well with the ±45° NCF samples.

The defect length of the cracks generated in the 90°-layers is in complete agreement with the experimental data. In the 0°-layer, the width of the channels is underestimated while the scatter in the simulation results is significantly smaller than in experiments. It should

be noted that the DCEs have a diameter of 69 µm, which constitutes about 45% of the crack width in the ±45° NCF and 20% of the channel width of the 0°-layers. Thus, a single chain can have a considerable influence on the defect width and further refinement of the fibrous mat could increase the accuracy of the defect size. Also, the assumption of a tight packing in the chain elements of the stitching yarn throughout the model might lead to an underestimation of the defect size. Indeed, a reduced packing coefficient would yield larger stitching yarn and, thus, might increase the size of the defects. Finally, the angular tilt of the loops is measured in the simulation to 6.7° with a standard deviation of 3.1°. The numerical angular tilt is significantly smaller than in experiments (ca. 45% of the experimental values). Nevertheless, it shows that the simulation approach is able to capture deviations of the loop orientation from the theoretical alignment.

Tab. 5-3: Measured local defects on the simulation results.

Designation	Layer	Defect type	Characteristic	Mean value [mm]	Standard deviation [mm]
0°/90° NCF	0°	channels	width	0,31	0,10
0°/90° NCF	90°	cracks	length	1,97	0,47
±45° NCF	45°	cracks	length	2,08	0,83
±45° NCF	45°	cracks	width	0,12	0,05
±45° NCF	-45°	cracks	length	2,62	1,13
±45° NCF	-45°	cracks	width	0,17	0,05

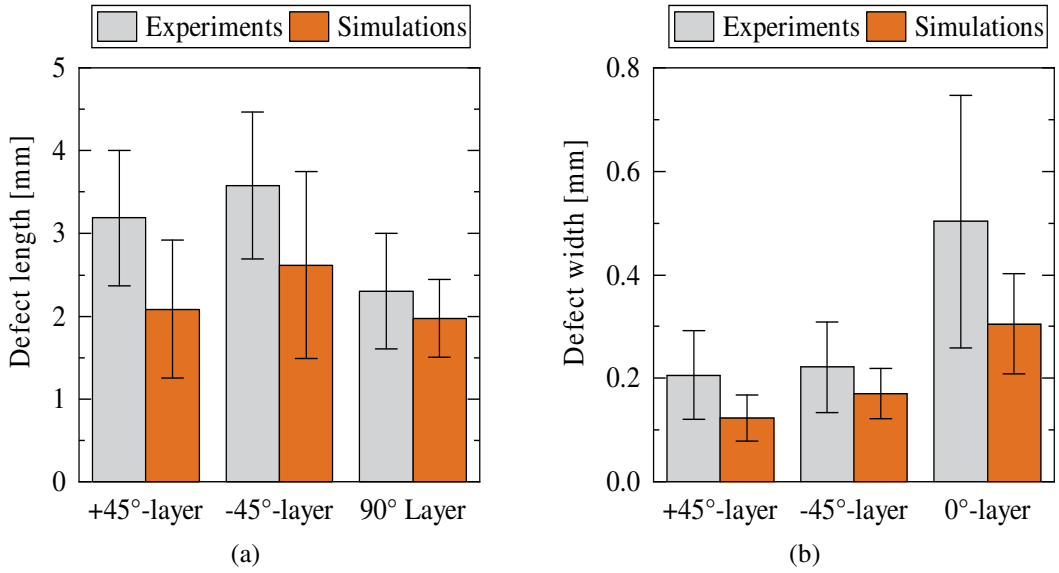

Fig. 5-15: Comparison of the defect width (a) and length (b) between the measurements performed on the NCFs samples and on simulation results.
The error bars represent one pooled standard deviation.

5.4 Calibration of the NCF thickness

In addition to the in-plane architecture validated in the previous sections, a calibration in thickness direction is necessary to generate realistic "as-manufactured" NCF geometries. Note that the approach introduced above is based on two parameters that directly influence the thickness of the material:

- The thickness of the layers before knitting t_{layer} defines the compaction state of the fibrous layers before the knitting process and is characterized by its FVF φ_{layer}.
- The number of chains n_{chains} depends on the packing coefficient in the chains φ_{chain}. Although the areal weight of the NCFs is kept constant, the number of chains necessary to model the fibrous layers vary according to Eq. (5-3).

While the first parameter may be calibrated experimentally before the knitting process, the second parameter is a numerical parameter used to compute an equivalent thickness if many filaments are grouped in the digital chains. In this subsection, it is proposed to investigate the influence of both parameters on the resulting thickness of the material. Moreover, guidelines are defined to calibrate them for further applications.

5.4.1 Experimental compaction of the dry NCFs

Compaction experiments were performed on single NCF plies in order to investigate the thickness of the textile. Note that the compaction of a single ply requires advanced experimental devices, in which the distance between the compaction plates is controlled precisely. A misalignment of the compaction plates or geometrical variation of the plate surfaces would induce non-realistic compaction results. To that end, a rotational rheometer MCR 302 from Anton Paar GmbH was used with parallel platens. The experiments were performed at room temperature with a constant gap closing velocity of 10 µm/sec until a pressure higher than 20 kPa is reached. The circular platen used for these experiments has a diameter of 25 mm. Thus, the compacted area represents the area of 8.6 elementary RVEs of the 0°/90° NCF and 22 elementary RVEs of the ±45° NCF. The experimental setup is shown in Fig. 5-16.

In this section, the thickness of the NCFs is assimilated to the gap thickness (i.e. free space between the upper platen and the base plate of the rheometer) at a compaction pressure of 1 ± 0.01 kPa, as required in the standard DIN EN ISO 5084 [170] to measure the thickness of textiles.

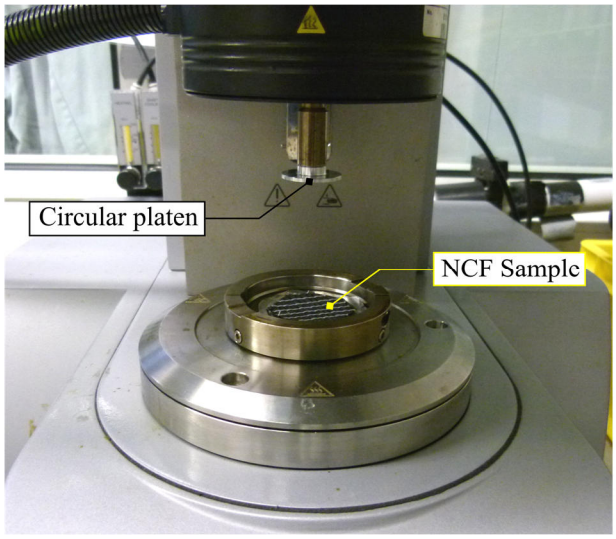

Fig. 5-16: Experimental setup to measure the thickness at 1.0 kPa of the reference NCFs

The results of the thickness measurements with the 0°/90° and ±45 NCFs are listed in Tab. 5-4. Even though both textiles have a similar areal weight (308 and 300 g/m²), it is observed that the mean thickness of the 0°/90° NCF is 29% higher than the thickness of the ±45° NCF. This can be explained by the generation of tows between the stitching points in the 0° and 90°-layers, locally increasing the thickness of the material. Moreover, different spreading techniques of the filament rovings may have influenced the layer architectures and, thus, the thickness of the textile. Also, the scatter — defined as the difference between the maximum and the minimum values — corresponds to 5.6% of the mean value for the 0°/90° NCF and 8.4% for the ±45° NCF.

Tab. 5-4: Experimental gap thickness at a compaction pressure of 1 ± 0.01 kPa.

	0/90° NCF [mm]	**±45° NCF [mm]**
Sample 1	0.870	0.637
Sample 2	0.853	0.662
Sample 3	0.825	0.650
Sample 4	0.823	0.629
Sample 5	-	0.684
Mean	0.843	0.652

5.4.2 Virtual compaction

A python script “main_CompactionTruss.py” automatically imports the “as-manufactured” geometries and prepares the simulation model. The compaction experiments are reproduced using two rigid and infinite plates. The gap between the plates is reduced progressively with a constant plate velocity until a final FVF of 40%. In order to speed-up the calculation while keeping the dynamical effects negligible, the total duration of

the virtual experiment is set to five seconds. This results in gap closing velocities between 215 µm/sec and 42.9 µm/sec. The pressure is computed using the area of the RVE and the reaction forces of the plates. Hence, the numerical thickness is calculated in a similar manner as the experimental thickness, allowing a direct comparison of the results.

First of all, compaction simulations were performed with various RVE sizes in order to identify the dependency of the thickness on RVE sizes. The configurations and corresponding results are detailed in appendix e. It was concluded that elementary RVEs are adapted for the simulation of the 0°/90° NCFs but 2x2 RVEs are required for the analysis of the ±45° NCF.

The influence of the layer thickness before the knitting process t_{layer} and of the packing coefficients φ_{chain} is investigated numerically using a full factorial approach with five levels for each parameter. This results in twenty-five configurations for each NCF. The boundaries of the numerical parameters are listed in Tab. 5-5. Note that the upper limit of φ_{chain} corresponds to a hexagonal packing, which is the maximum physical packing coefficient for circular cross-sections. Furthermore, the simulations must be repeated due to the stochastic generation of the filament orientations that introduces variability in results. Here, the simulations are performed five times for each configuration.

Tab. 5-5: Boundaries of the numerical parameters for virtual thickness measurement

	0/90 NCF		**±45°NCF**	
	φ_{layer} [-]	φ_{chain} [-]	φ_{layer} [-]	φ_{chain} [-]
Minimum	0.15	0.4	0.30	0.5
Maximum	0.25	0.907	0.60	0.907

The response surfaces illustrated in Fig. 5-17 and Fig. 5-18 are computed using the mean results of each configuration for the 0°/90° NCF and ±45°NCF, respectively. The corresponding maximum, minimum and mean experimental results are plot on the response surfaces. The results of the 0°/90° NCF show a linear decrease of the thickness with respect to the packing coefficient and to the FVF of the fibrous layers. Moreover, with a minimum packing coefficient of 40%, FVFs smaller than 22% are required to equal the experimental thickness. On the contrary, the results of the ±45°NCF show that the thickness decreases strongly with the FVF of the layers for values smaller than 40% and a plateau is reached afterwards. The experimental values show that a minimum packing coefficient of 74% is necessary to achieve numerical “as-manufactured” geometries of the ±45°NCF with an adequate thickness.

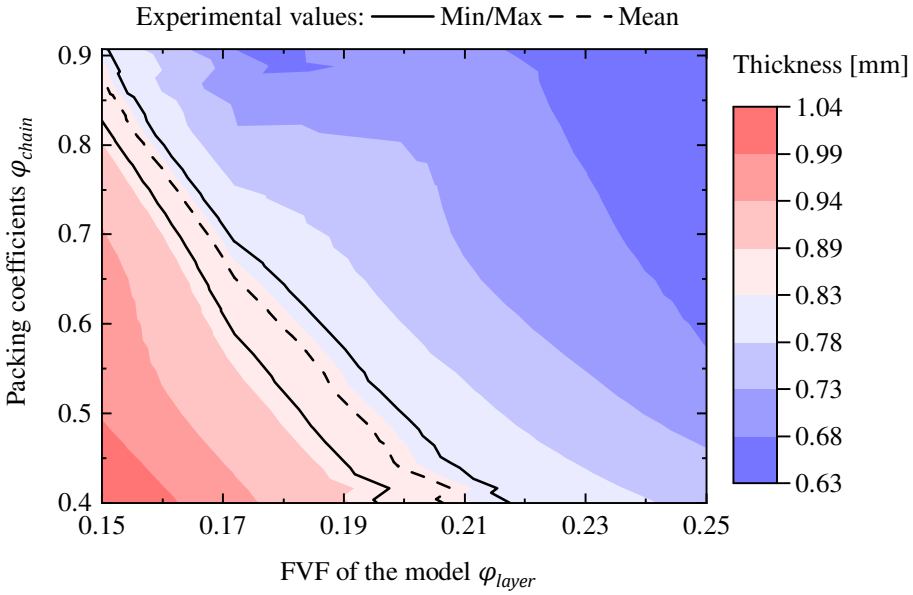

Fig. 5-17: Results of the virtual thickness measurement of the 0°/90° NCF.
The mean results of the 5 simulations are shown in the diagram (ref. Appendix f for the detailed results of each configuration). The mean and extreme experimental values are shown as contours on the response surface.

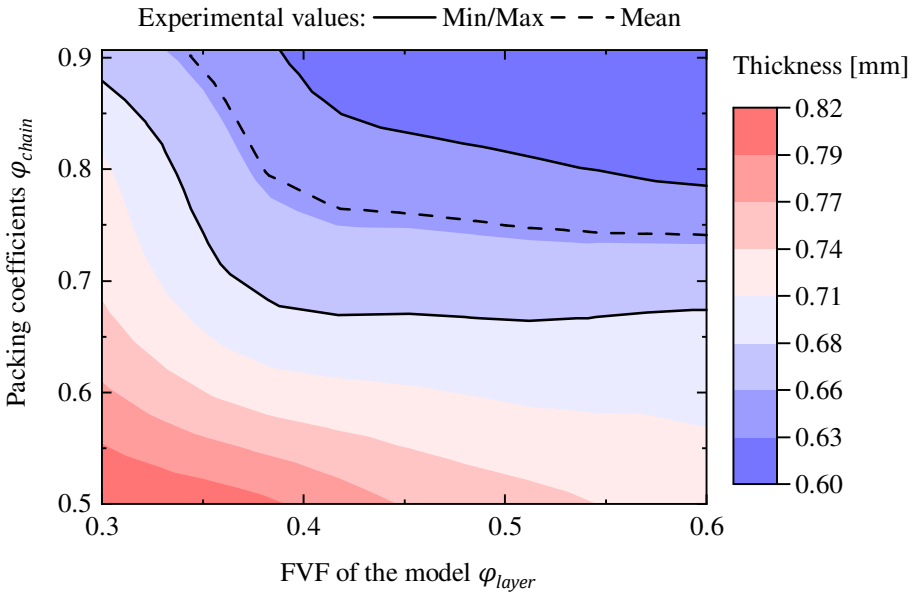

Fig. 5-18: Results of the virtual thickness measurement of the ±45° NCF.
The mean results of the 5 simulations are shown in the diagram (ref. Appendix f for the detailed results of each configuration). The mean and extreme experimental values are shown as contours on the response surface

Since the filaments are in a relaxed state, the packing coefficient φ_{chain} should target low values. As a consequence, a packing coefficient φ_{chain}= 75% is selected for the generation of the "as-manufactured" NCF geometries. Subsequently, a fit of the mean thickness values of the simulation and experimental results is performed to identify the

adequate input parameters φ_{layer}. Since high values of φ_{layer} lead to higher computational effort in the first simulation steps (due to the increased contacts of the chains), the lowest value for φ_{layer} will be selected if many solutions are found. Note that the scatter of the experimental results may have a strong influence on the selection of the coefficients, especially for the ±45° NCF where the experimentally measured thicknesses cover a wide range of potential input configurations. The resulting coefficients are listed in Tab. 5-6 for both reference textiles.

Tab. 5-6: Definition of the coefficients φ_{layers} and φ_{chain} for the simulation of the reference NCFs according to the experimental and virtual investigations of the textile thickness.

	0/90 NCF	**±45°NCF**
φ_{layer} [-]	0.16	0.52
φ_{chain} [-]	0.75	0.75

5.5 Conclusion

A numerical mechanical description of dry NCFs at the microscopic scale was developed in this chapter. This method can be applied to describe a wide range of NCF architectures with realistic description of the local defects in the fibrous layers. Its applicability was demonstrated on two different configurations (0°/90° and ±45° biaxial NCFs). Variability in the filament orientation distribution was observed on two specimens and introduced in the simulation in order to model all interaction mechanisms within the textile (inter-filament, inter-stitch and stitch-to-filament interactions). A stepwise generation of the numerical "as-manufactured" geometry considers the main manufacturing steps and models the manufacturing process induced local defects in the fibrous mats. Averaged periodic boundary conditions were developed to ensure an overall periodicity of the model while allowing reorientation of the chains at the smallest scale.

Varying the orientation distribution in the model, a correlation was found with the type of local defects induced at the stitching points. Also, the comparison of the filament orientation with the simulation results showed a good correlation and the detailed comparison of the local defects (cracks and channels) confirmed that the induced defects correlate with the experimental observations. Thus, the presented quantitative comparison validates the ability of the simulation to reproduce the local defects and the orientation variability of the fibrous layers.

Finally, a calibration of the thickness of the fibrous layers before the knitting process and of the packing coefficient in the digital chains was performed. Compaction experiments were carried out on single NCF plies to evaluate the thickness of the textile at a pressure of 1.0 kPa. A large virtual parametric study was conducted to calibrate the simulation input parameters. A constant value for the packing coefficient was selected for

both NCFs and the thickness of the layers before knitting was adjusted to fit the experimental results.

The final input parameters of the reference textiles are listed in Tab. 5-7. Note that these parameters can be used as a guideline for similar textile configurations if the calibration of the filament orientation, of the defects, or of the thickness cannot be performed.

The presented approach is a mechanical description of dry textiles that includes all relevant interaction mechanisms. Hence, this framework can be easily integrated in further simulations to predict the mechanical behavior of any NCF configuration.

Tab. 5-7: Summary of the input parameters for the simulation of the "as-manufactured" geometries of the reference NCFs with adequate defect and thickness description

		0°/90° NCF	**±45° NCF**
Filaments	Young's modulus [GPa]	120	127.5
	Density [g/cm³]	0.905	0.890
	Diameter [µm]	69	69
	Packing coefficient [-]	0.75	0.75
	Mesh length [mm]	0.2	0.2
Fibrous layers	Layer thickness before stitching [mm]	0.52	0.16
	FVF of the layers before stitching [-]	0.16	0.52
	Standard deviation for the sampling [°]	1.15 (0°-layer)	2.0 (+45°-layer)
		4.0 (90°-layer)	2.0 (-45°-layer)
Stitching yarn	Young's Modulus [GPa]	1.81	1.81
	Density [g/cm³]	1.25	1.25
	Diameter of the chains [µm]	88	71
	Mesh length [mm]	0.1	0.1
	Magnitude pretension [%]	16	17

6 Virtual shear characterization of NCFs

The objective of a virtual testing environment is to numerically investigate the properties of a material. Compared to conventional experimental approaches, a virtual approach can study the impact of a larger number of material configurations. Also, the quantification of interactions between manufacturing parameters is possible.

In the present doctoral thesis, the shear behavior of NCFs is investigated. An accurate shear stiffness is crucial for the prediction of the filament orientation and of local defects during the preforming process. As shown previously, the shear behavior of a NCF is closely related to knitting parameters, such as the stitch gauge or stich width. As a consequence, a virtual framework able to predict the shear behavior of NCFs is a strong benefit in the development of new composite parts.

The current chapter concentrates on the development of the virtual shear characterization of biaxial NCFs using the virtual NCF geometries presented in chapter 5. The focus is put on the characterization of the ±45° NCF due to its higher complexity compared to the 0°/90° NCF. First, the method to apply adequate shear deformations to the virtual NCF geometries is described. The adaptions of the methods required for the virtual shear characterization of NCFs with 0° and 90°-layers are detailed in Appendix g. Second, a validation of the kinematic behavior is presented. It is based on the measure of the shear angle of the virtual textile and on a comparison between experimental and numerical stitch sliding measurements. Third, a study on the influence of the RVE size on the shear behavior is performed to identify adequate RVEs for subsequent investigations. Fourth, the relation between the shear behavior and the orientation variability of the chains in the fibrous layers is examined. Fifth, the framework is applied to NCFs with different stitch lengths to study the dependency of the shear behavior on the stitch architecture. The simulations of this chapter are based on the reference parameters listed in Tab. 5-7.

6.1 Methodology of the virtual shear characterization

6.1.1 Normalization of shear forces

The shear angle of a biaxial textile is usually defined as the change of the angle between the orientations of the layers. The shear behavior can be investigated experimentally using various test setups, as reported in section 2.2.2. Nevertheless, the force required to shear the textile depends on the sample size and a method to compare experimental

results with simulation results (which are performed on reduced textile models) must be used. To that end, two common measures are found:

- The shear force F_{fabric} in N/mm (normalized using the width of the sheared zone of the sample). It is assimilated to the force induced in each arm of the picture frame rig (i.e. aligned with the filament orientation). As recommended by Peng et al. in [98], the shear force is normalized by the sample width if different sample geometries are compared. Nevertheless, this approach considers that the sheared field is a square (i.e. has equal side lengths).
- The shear torque C_{fabric} in N.mm/mm² (normalized using the area of the sample). It is a scalar that is directly derived from the shear energy and does not assume any sample geometry.

The shear torque C_{fabric} is selected in this chapter to measure the shear behavior. Since models of NCFs based on the periodicity of the stitching pattern lead to various rectangular shapes and sizes, the use of the normalized shear torque provides a direct comparison between the results of different RVE shapes and sizes.

The shear torque is related to the shear energy normalized by the surface of the sample $W_{fabric}(\gamma)$ as follows:

$$W_{fabric}(\gamma) = \int_0^{\gamma} C_{fabric}(\theta) d\theta \tag{6-1}$$

where γ is the current shear angle applied to the textile.

Note the direct relation between the normalized shear torque and normalized shear force in the case of picture frame tests with square sheared fields:

$$C_{fabric}(\gamma) = F_{fabric}(\gamma)\cos(\gamma) \tag{6-2}$$

The shear energy can be obtained using the history output E_W from ABAQUS, which calculates the work of external forces required to deform the simulation model. Therefore, C_{fabric} is derived as follows:

$$C_{fabric}(\gamma) = \frac{dE_W}{d\gamma}\frac{1}{w \times l} \tag{6-3}$$

where w and l are the width and length of the RVE, respectively.

6.1.2 Generation of a virtual shear deformation

The numerical definition of the textile presented in chapter 5 requires the boundaries of the model to be aligned with the machine directions. Since the layers of biaxial ±45° NCFs are not aligned with the boundaries of the RVE, the shear of ±45° NCFs resembles

the bias extension test method. Hence, the pure shear deformation of a layer is obtained through a combined extension and contraction of the RVE depending on the RVE size and on the layer orientations (see Fig. 6-1).

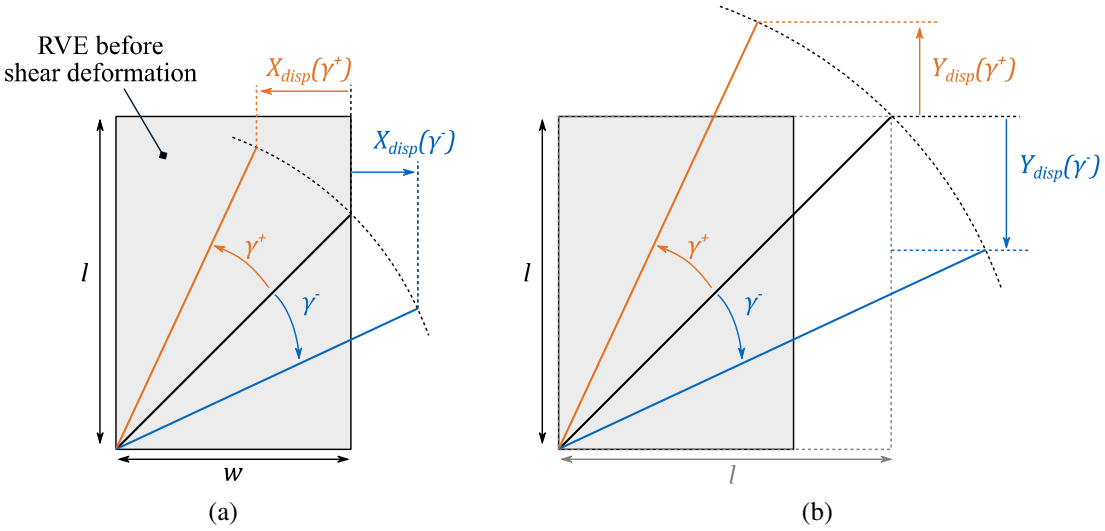

Fig. 6-1: Identification of the RVE deformation in x (a) and y (b) directions of a ±45° NCF in the case of positive (orange) and negative (blue) shear deformations.

The deformation of the RVE in x and y directions is related to the shear angle γ as follows:

$$X_{disp}(\gamma) = w\left(\cos\left(\frac{\gamma}{2}\right) - \sin\left(\frac{\gamma}{2}\right) - 1\right) \tag{6-4}$$

$$Y_{disp}(\gamma) = l\left(\cos\left(\frac{\gamma}{2}\right) + \sin\left(\frac{\gamma}{2}\right) - 1\right) \tag{6-5}$$

The shear deformation is applied to the RVE using the reference points of the regular mesh of the RVE. To that purpose, the displacement $u_{Shear12}$ of a dummy node is included in the equations of the periodic boundary conditions:

$$u_{RP2} = u_{RP1} + u_{Shear12} \tag{6-6}$$

where the subscripts 1 and 2 correspond to two opposite faces of the RVE boundaries.

The displacement $u_{Shear12}$ is given by Eqs. (6-4) and (6-5). It is the same displacement for all RPs of paired opposite faces of the RVE boundaries. The RPs remain free to move along the boundary faces of the RVE (ensuring the mesoscopic periodicity of the fibrous mat). The displacements of the end nodes of the stitching yarns are fully periodic.

Note that the virtual neighboring RVEs are modeled with lateral rigid surfaces, as illustrated in Fig. 5-6. Therefore, the lateral surfaces must follow the deformation of the RVE during the virtual characterization.

Two python scripts “main_Shear_neg.py” and “main_Shear_pos.py” were developed to automatically import the “as-manufactured” geometries and prepare the simulation models for a full virtual shear characterization. Since the positive and negative shear deformation are performed in separate simulations, they can be solved independently and in parallel.

6.2 Validation of the kinematic behavior

The ability of the simulation to reproduce the kinematic behavior of the textile is demonstrated in this section. To that end, the evolution of the shear angle is compared to the theoretical shear deformation. Moreover, the stitch sliding is used as a validation criterion to demonstrate that the simulation can reproduce the deformation mechanisms of biaxial NCFs.

6.2.1 Shear deformation

The validation of the shear deformation is performed with a 2x2 RVE. Fig. 6-2 illustrates the “as-manufactured” geometry of the NCF and the respective deformed geometries at applied shear angles of +30° and -30°.

First, an overall change of the directions of the chains is observed, which correlates with the onset of a shear angle in the textile. The geometry with negative shear deformation (see Fig. 6-2b) shows a significant compression of the loops. Moreover, the angle of the loops increases compared to the reference configuration. On the contrary, the stitching yarn is stretched in positive shear deformations (cf Fig. 6-2c). The loops are extended and align with the machine direction. A periodic displacement of the stitching yarn can be observed at the border of the model, highlighting the periodic sliding of the yarn. In both shear directions, local waviness (i.e. buckling) of the chains can be detected. Due to the absence of bending stiffness of the chains, the buckling is localized in zig-zag shapes. Even though the exact deformation of the chains differs from the out-of-plane deformations observed in section 3.3.2, this approach can help identifying critical regions and a potential onset of defects.

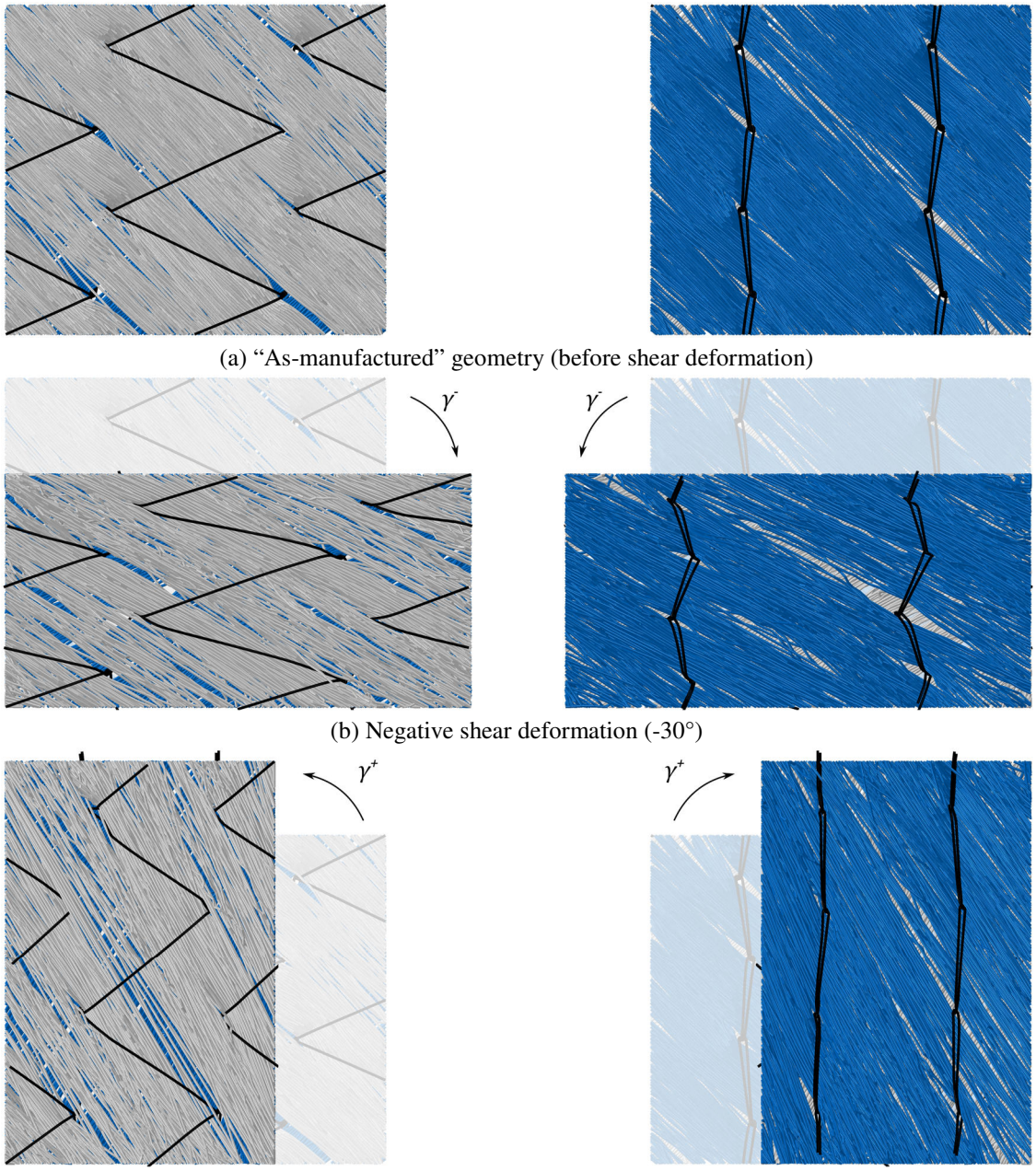

(a) “As-manufactured” geometry (before shear deformation)

(b) Negative shear deformation (-30°)

(c) Positive shear deformation (+30°)

Fig. 6-2: Simulation results of the ±45° NCF modeled with a 2x2 RVE before deformation (a), at a negative shear angle of -30° (b) and at a positive shear angle of +30° (c).
The front faces are illustrated on the left side and the back faces on the right side.

The deformation is applied to the RVE using the periodic mesh of the reference points. Thus, the shear deformation of the layers results from the overall deformation of the RVE. In order to measure the virtual shear angle, the directions of all DCEs of the layers are extracted at different stages of the simulation. The angle of a layer is defined as the median orientation of its elements.

The simulations were performed five times due to the stochastic approach used to distribute the orientation of the chains. The results of the virtual shear angle for positive and negative shear deformations are illustrated in Fig. 6-3.

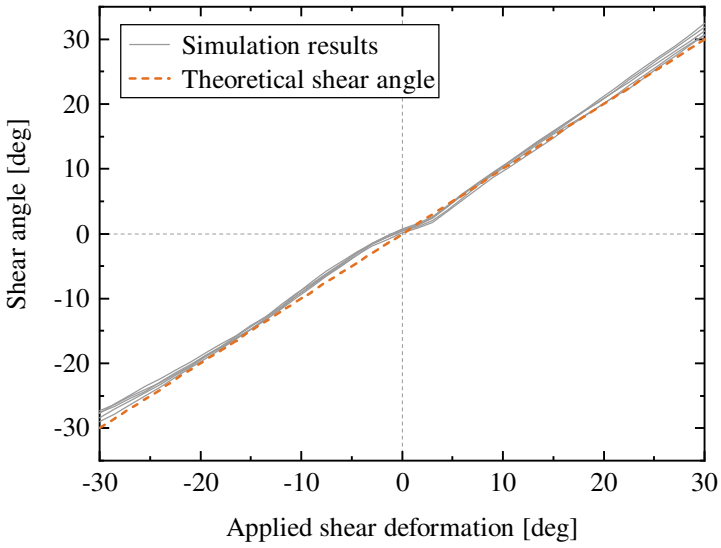

Fig. 6-3: Results of the virtual shear deformation of the NCF for positive and negative shear deformations.

It can be observed that the virtual shear angle correlates with the applied deformation. The measured virtual shear deformation is smaller than the applied shear deformation at low shear angles and slightly exceeds it afterwards. This can be explained by the use of mass scaling to speed-up the calculation. Nevertheless, the difference between the applied shear angle and the mean value from the five simulation results is smaller than 1.5° until ±27° shear angle. A maximum difference of 2.0° is reached at -30° shear angle (corresponding to a relative error of 6.6%). As a result, the virtual shear deformation of the NCF is considered to be equal to the applied shear deformation.

6.2.2 Stitch sliding

Wiggers [162] showed the occurrence of stitch sliding on a sheared sample and pointed out that the stitch passes from the back side to the front side. Thereby, a change in length of the stitch segments is accommodated, which ensures a uniform tension in the stitching yarns. Analytical calculations of the strain in the stitching yarn generally assume a free sliding of the yarn [61, 206]. However, the increase in tension may reduce the sliding, leading to a higher shear resistance. It results that a simulation aiming at the investigation of the mechanical behavior of dry NCFs must adequately reproduce the sliding of the stitching yarn during the shear deformation.

6.2.2.1 Experimental quantification of the stitch sliding

Experimental method

The content of this subsection is partly derived from [K3].

A PF testing rig is used to induce a controlled shear deformation in the textile, as shown in Fig. 6-4a. This method presents the advantage that each tow is clamped at the frame, ensuring a controlled inter-tow shear deformation.

Based on the stitch architecture (stitch gauge of 5.08 mm and stitch length of 4.4 mm), analytical calculations can predict the elongation of the stitch segments in bias direction. In the case of a positive shear deformation, it shows that the stitching yarn should pass from the back side to the front side in order to compensate the segment elongation. In order to study the stitch movement, a portion of the stitching yarns on the back side of the samples was colored black while the front face remained uncolored (see Fig. 6-4b and Fig. 6-4c). Hence, the stitching yarn movement can be observed if the uncolored regions on the back face elongate. It should be noted that regions with a length of ca. 0.5 mm are intentionally left uncolored on the back face of the sample to enable measures right from the beginning of the experiments.

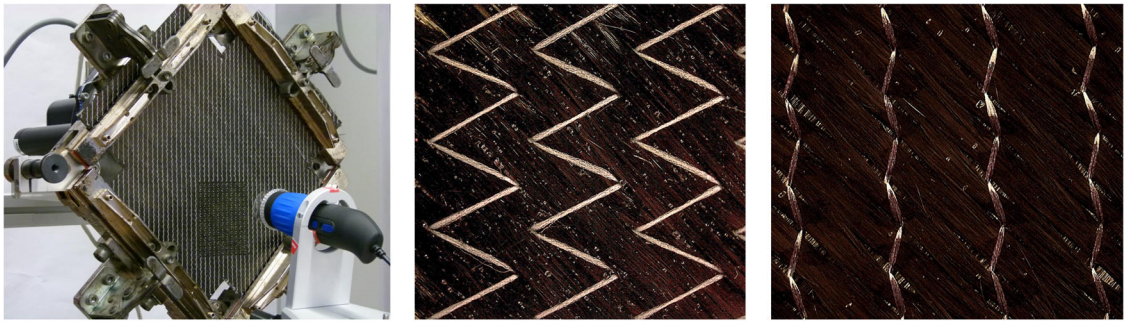

(a) (b) (c)

Fig. 6-4: Illustration of the experimental setup (a), front face of the NCF with uncolored stitching yarns (b) and back face with colored regions of the stitching yarns before testing (c).

A digital microscope MIRAZOOM® MZ902 with a resolution of 3,488x2,616 px² was used to record the back face of the samples on an approximate area of 33x25 mm² as shown in Fig. 6-4a. An automatic image post-treatment of the microscope pictures was implemented to study the length of the uncolored region at various shear angles of the sample.

First of all, a separation between the uncolored stitch regions and the rest of the sample is required. A direct segmentation of the image with threshold is not possible because of the reflection of the carbon fibers (see Fig. 6-5a). Therefore, an opening morphological operator [207] is used with a square structural element of 5px. The result of the segmentation with threshold after image opening is illustrated in Fig. 6-5b. One can observe that

the uncolored region is discontinuous, which is mainly due to the image noise. A subsequent closing morphological operator closes the gaps and connects the small regions (ref. Fig. 6-5c).

(a) (b) (c)

Fig. 6-5: Original microscope picture (a), segmented image after opening (b) and subsequent closing operations (c).

The dye introduced in the stitching yarn resulted in an elliptical shape of the uncolored regions, which appears on the front side as the stitching yarn is drawn through the fiber bed. In order to measure automatically these uncolored regions, the white spots were fitted with ellipses. The sliding distance is calculated as the increase of the major axis of the fitted ellipse between successive pictures. With this approach, the stitching yarn strain is neglected since any lengthening of the uncolored regions is attributed to a sliding of the yarn. A high scatter of the sliding distance was observed throughout the sample. Therefore, the elongation of the uncolored regions is measured at many spots in each picture (minimum of nine spots) and the mean value is calculated for each sample.

Results

The raw pictures of a same stitch segment recorded at various shear angles (0°, 10° and 27°) are illustrated in Fig. 6-6a. The results after segmentation and application of morphological operators are shown in Fig. 6-6b. The overlays of Fig. 6-6a and Fig. 6-6b with the corresponding fitted ellipses are depicted in Fig. 6-6c.

The results of the stitch sliding measurements are presented in Fig. 6-7. A total stitch sliding of approximately 0.45 mm is measured at the maximum shear deformation (30° shear angle), which corresponds to 20% of the initial segment length of the stitching pattern. The assumption of a stitch sliding is verified and matches well with the results presented by Wiggers [16]. Moreover, it can be observed that the sliding distance correlates with the theoretical segment elongation up to 22° shear angle (calculated by multiplying the percentage elongation of the diagonal frame length with the original segment length). Afterwards, the slope progressively reduces. This can be explained by the increased inter-stitch friction combined with a form closure of entangled stitching yarn loops occurring at high shear angles (i.e. when the segments are completely stretched). With increasing dominance of the inter-stitch friction, the free movement of the yarn is inhibited at the crossovers and potentially leads to an inhomogeneous distribution of the tension in the stitching yarns.

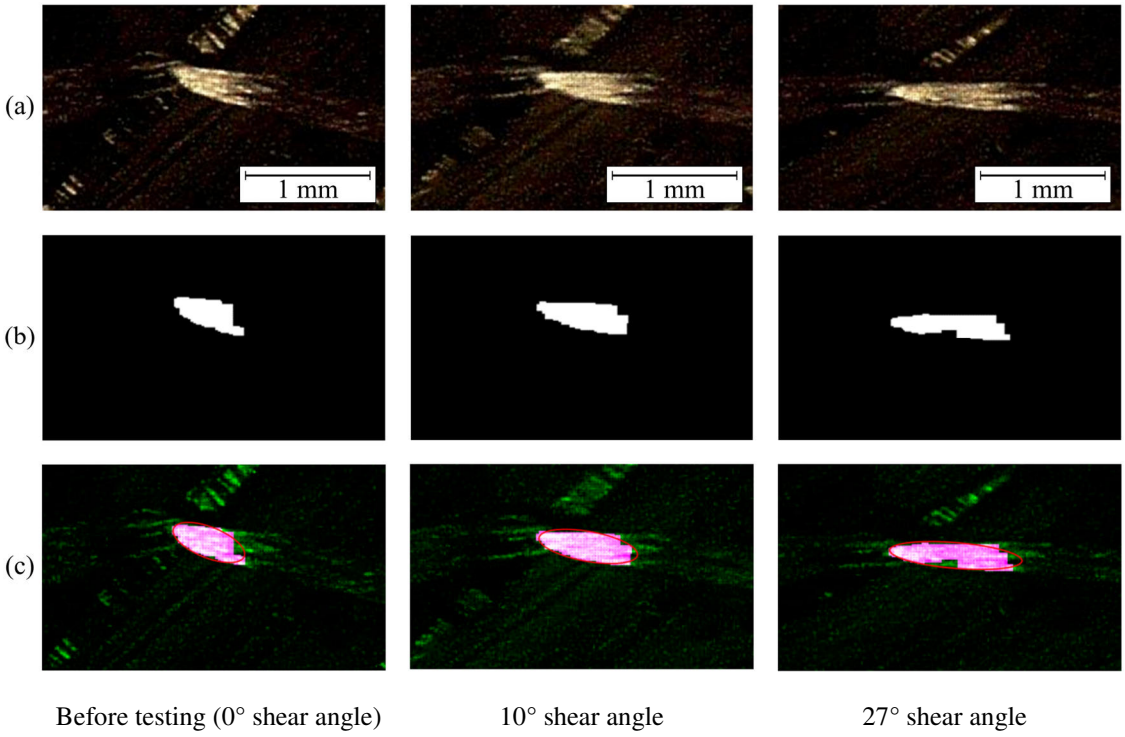

Fig. 6-6: **Image analysis (raw picture (a), image after post-treatment (b) and fitted ellipse (c)) of a same stitch segment before testing (i.e. 0° shear angle), at 10° and 27° shear angle.**

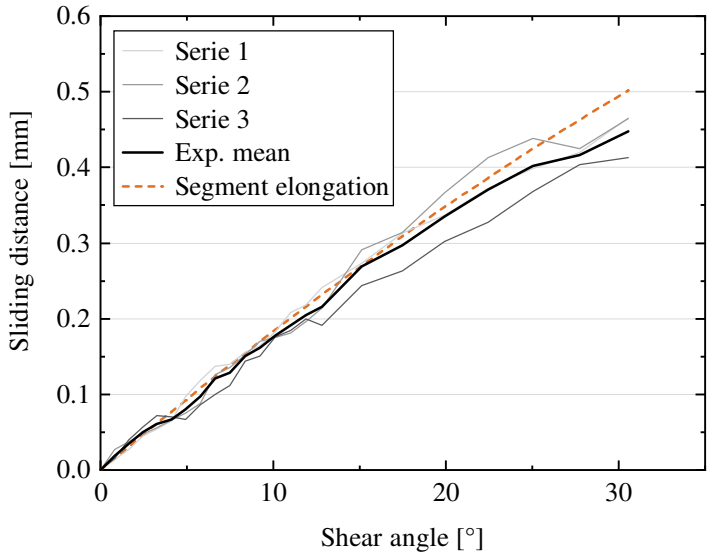

Fig. 6-7: **Comparison between the measured sliding distance and the theoretical segment elongation depending on the shear angle.**

6.2.2.2 Validation of the simulation results

A comparable approach was adopted to measure the stitch sliding of the simulation results showed in section 6.2.1. Due to the tricot stitching pattern of the NCF, a 2x2 RVE is constituted of eight crossovers at which the sliding can be measured. The mean value

of the eight measures is calculated for each simulation result. The sliding distance is defined as the change in projected length between the nodes at the apex and the nodes initially located at a distance of 0.5 mm from the apex (see Fig. 6-8a). Note that the middle point from the left and right parts of the loops is used to measure the sliding distance. Fig. 6-8b and Fig. 6-8c illustrate the results at 15° and 30° shear angle, respectively. A significant sliding is noticeable. Moreover, a rotation of the element at the apex can be seen in Fig. 6-8c, which is due to the interpenetration of the chains when the tension in the stitching yarn is high. The slight movement at the apex may lead to a difference of sliding between the left and right part of the loop for large shear deformations. Nevertheless, the difference is expected to remain smaller than half the length of the element of the apex (approximatively 70 µm).

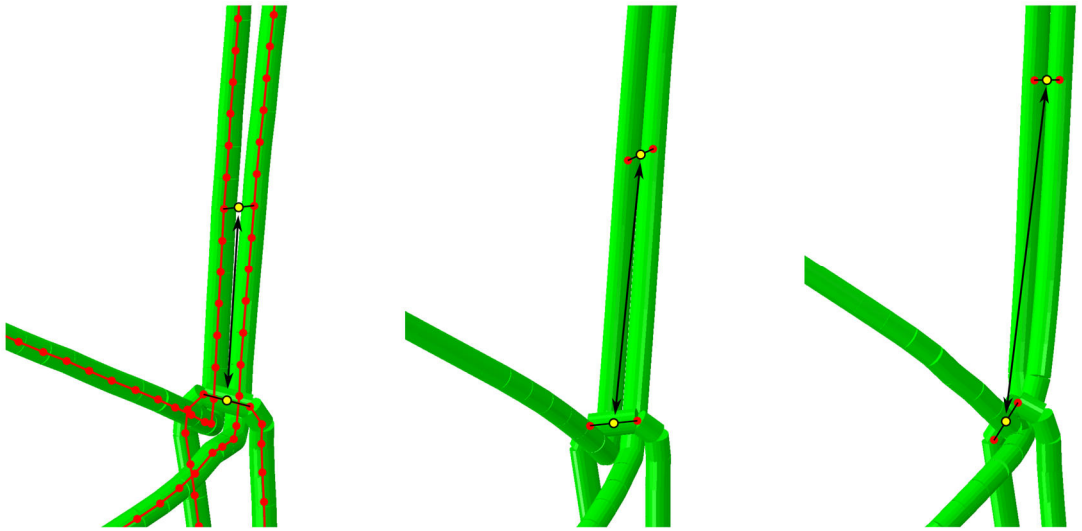

Fig. 6-8: Measure of the numerical stitch sliding of the simulation results: reference length (a) and corresponding lengths at a shear deformation of 15° (b) and 30° (c).
For better clarity, the fibrous layers are not illustrated.

The results of the stitching sliding for each simulation are plotted in Fig. 6-9. It can be observed that the stitch sliding accommodates the elongation of the stitch segment and an excellent correlation is found with the experimental results until a shear angle of 15°. It progressively deviates from the theoretical elongation at larger shear angles and a slight difference with experimental results can be noticed. The deviation is mainly due to the fact that the numerical sliding of the stitching yarn is already reduced at a shear deformation of 15° instead of 22° in the experiments. It can be attributed to the discretization of the yarn with numerical truss elements, which induces a higher interlocking of the stitching yarn and prevents a free sliding.

The maximum deviation between the simulation and experimental mean values is measured to 0.04 mm at the shear deformation of 30°. This difference remains small compared to the diameters of the chains (71 µm) and to the length of the chain elements (0.1 mm). The simulations were stopped at a shear angle of 30° due to an observed loss

of contact between the numerical chains of the stitching yarn for shear angles larger than 30°. This is also attributed to the chain interlocking and the high penetration of the chains due to the penalty stiffness of the interaction model.

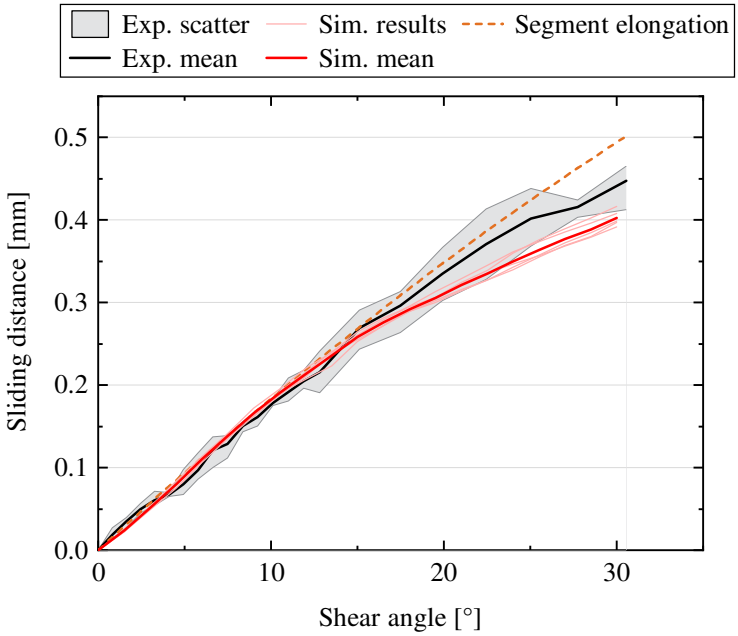

Fig. 6-9: Comparison between the experimental and numerical stitch sliding distance.

It can be concluded that the main deformation mechanisms are well reproduced by the numerical model. Also, it is expected that the simulation slightly overestimates the shear forces due to the interlock of the stitching yarn that results in higher extensional forces.

6.3 Numerical investigation of the mechanical behavior

It was identified in chapter 4 that the shear behavior until a shear angle of 11.5° has a major influence on the draping results of the ±45° NCF. Thus, the shear torque C_{fabric} measured at a shear deformation of 11.5° is used to quantify the influence of numerical and physical parameters on the virtual shear behavior. Moreover, specific attention is paid on the asymmetric behavior of the NCF.

The introduction of a stochastic approach to sample the orientation of the chains leads to variability of the simulation results, which requires many repetitions of the virtual characterization to calculate a representative mean value. Simulations were performed in order to obtain five results for each configuration (each simulation using a different "as-manufactured" geometry).

Note that spurious non-representative stresses were observed in some simulation results. On the one hand, these stresses can result from the sampling of the orientations of the chains, during which one chain may be generated with a large deviation from the

theoretical orientation. Thus, high tensile stresses are induced during the shear deformation, leading to non-realistically high shear forces. On the other hand, the lack of bending stiffness of the truss elements combined with the averaged periodic boundary conditions can lead to a folding of small elements at the corners. This induces non-physical forces that invalidate the simulation results. A method was developed to identify non-realistic simulation results (see Appendix g) and to restart them from the beginning with a new sampling of the orientations (i.e. with a new "as-manufactured" geometry).

6.3.1 Influence of the size of the RVE

The approach developed to model the textile at the level of the filaments reduces the textile to RVEs, whose dimensions are based on the periodicity of the stitching pattern. Even though the boundary conditions ensure an average periodicity of the fibrous layers, the impact of the RVE size must be studied in order to evaluate its influence on the shear behavior and to derive guidelines for further investigations.

To that end, the virtual shear characterization was performed on different configurations ranging from 1x1 to 5x5 RVEs, as listed in Tab. 6-1. Three examples are illustrated in Fig. 6-10. Local defects (cracks) are observed in all "as-manufactured" geometries.

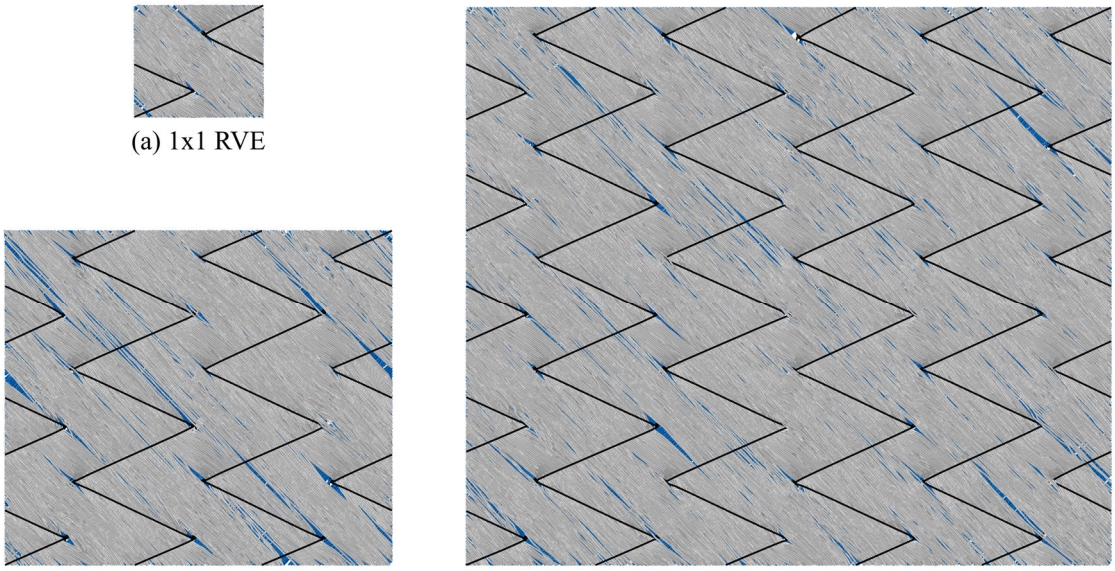

(a) 1x1 RVE

(b) 3x3 RVE

(c) 5x5 RVE

Fig. 6-10: Examples of the RVEs generated in order to study the influence of the RVE size on the shear behavior: 1x1 (a), 3x3 (b) and 5x5 RVEs (c).

The results of this study are illustrated in Fig. 6-11, in which the results derived from all simulations of each configuration are plotted in order to facilitate the interpretation of the data. First, it can be observed that the normalized shear torque increases with the size of the RVE. Moreover, a high scatter of the results is shown in all configurations. The variation of the shear stiffness with the RVE size can be justified by the larger number of filaments in the unit cell. It raises the probability of local defects and filaments

deviating from the theoretical direction, both of which intensify the interactions in the textile and, thus, increase the shear stiffness. A plateau is reached in negative direction for RVEs larger than 358 mm² (i.e. larger than 4x4 RVEs). In positive direction the reduction of the slope and the distribution of the data points suggest a slight convergence after 4x4 RVEs.

The mean values of the repetitions and the resulting asymmetric ratio for each configuration are presented in Tab. 6-1. The evolution of the asymmetric ratio, defined as the ratio between the positive and negative shear torque at 11.5°, is shown in Fig. 6-12. Apart from the 1x1 RVE, the ratio varies between 4.9 and 7.6 and no significant influence of the size of the RVE can be observed on the asymmetric ratio. The numerical NCFs show a higher asymmetric shear behavior than reported in chapter 3, where it was measured to 3.35. This means that the influence of the stitching yarn is overestimated in the simulation. It can be justified by different factors that increase the forces induced by the stitching yarn in a positive shear deformation:

- The discretization of the stitching yarn in numerical elements leads to interlocking of the elements. This prevents stitch sliding and induce higher tension in the yarn, as observed in the previous section.
- Merging all filaments of the stitching yarn into a single chain does not allow deformations (i.e. flattening) of the yarn cross-section, which might lead to higher interactions at the surface of the fibrous layers.
- The use of an overestimated friction coefficient of the stitching yarn.

Moreover, the binder present on the surface of the textile may increase the force required to shear the fibrous layers, reducing the influence of the stitching yarn on the shear forces.

The high computation times engendered by large RVEs suggest that the smallest acceptable RVEs should be selected. Using 4 CPUs, it was found that the computation time increases by approximately a factor of 4 for the simulation of a 4x4 RVE (30 hours) compared to a 2x2 RVE (7 hours). It can be concluded that simulations aiming at the calculation of absolute values must be performed with models larger than 4x4 RVEs, while studies on relative influences of the stitching yarn on the asymmetric ratio can be performed with 2x2 RVEs.

Tab. 6-1: Configurations and respective results of the numerical study on the influence of the RVE size on the shear behavior of the ±45° NCF.

RVE size	RVE Area [mm²]	Mean $C_{fabric}(11.5°)$ [mN/mm]	Mean $C_{fabric}(-11.5°)$ [mN/mm]	Asymmetric ratio [-]
1x1	22.4	19.7	0.485	40.5
2x2	89.4	14.4	2.00	7.22
3x3	201	29.1	5.90	4.92
4x4	358	65.6	12.1	5.44
5x5	559	87.1	11.5	7.56

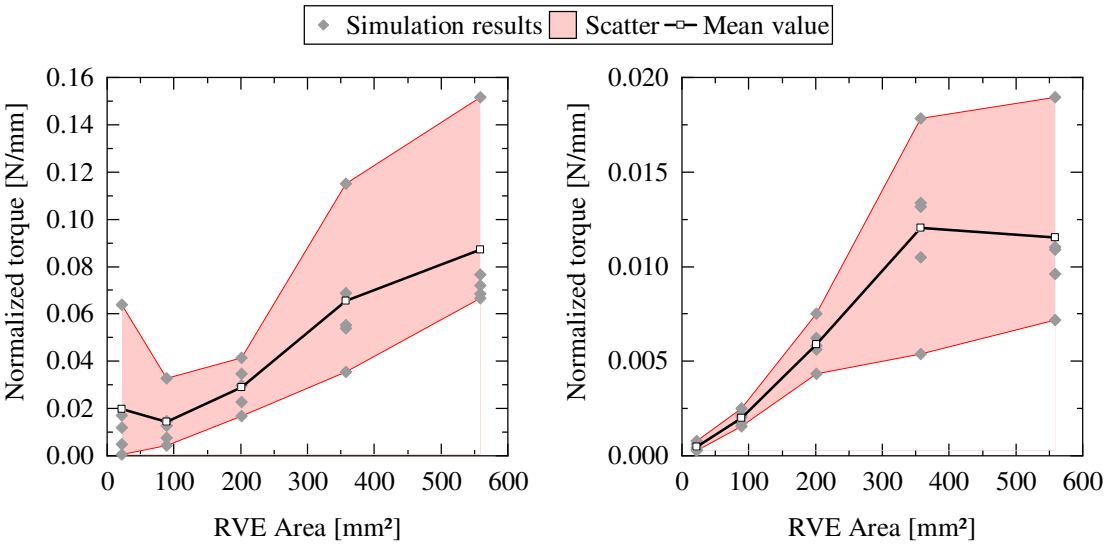

(a) Positive shear (b) Negative shear

Fig. 6-11: Normalized shear torque measured at a shear deformation of 11.5° in positive (a) and negative (b) directions depending on the RVE size.
The red surface represents the range of the results from the maximum and minimum values for each configuration.

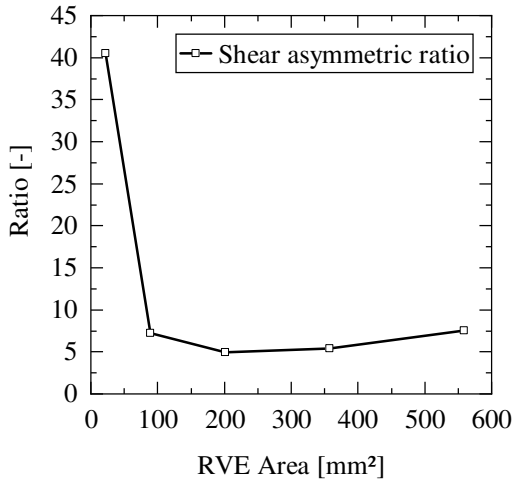

Fig. 6-12: Evolution of the shear asymmetric ratio depending on the RVE size.

6.3.2 Influence of the orientation variability

It was previously found that variability of the orientation of the chains is necessary to accurately model the orientation distribution of the filaments and reproduce local defects in the fibrous layers. In a pure shear deformation, deviations of the filament from the theoretical ±45° directions lead to an extension or contraction of the chain length. This induces tensile or compressive forces in the chains, impacting the shear behavior of the whole textile. Moreover, it changes the magnitude of the inter-filament, inter-stitch and stitch-to-filament interactions.

The influence of the variability in the fibrous layers on the shear behavior is investigated in this subsection. The standard deviation of the Gaussian distribution used to sample the orientation of the digital chains is varied from 0° to 4.0°, as listed in Tab. 6-2. Even though a standard deviation of 0° results in filaments aligned in +45° or -45° directions, the fibrous mats are not periodic, as the considered ratio between the stitch length and stitch gauge is not compatible with ±45° filament orientations. Two “as-manufactured geometries” (i.e. virtual fabrics before shear characterization) generated with standard deviations of 0° and 4.0° are illustrated in Fig. 6-13. The fabric without variability shows fibrous layers with filaments remaining mostly parallel after the pretension of the stitching yarn. Local deviations from the ±45° directions are only observed close to the stitching points. Note that local distortions in the fibrous mat are only generated in the direction in which the stitching yarn is pulling. This highlights the weak interactions between the chains in this configuration. On the contrary, strong deviations from the ±45° directions are noticed in Fig. 6-13b (highlighted by the red chain). Moreover, a waviness of the chain is observed. It results from the entanglement with other chains and suggests a higher level of interactions between the chains than in Fig. 6-13a.

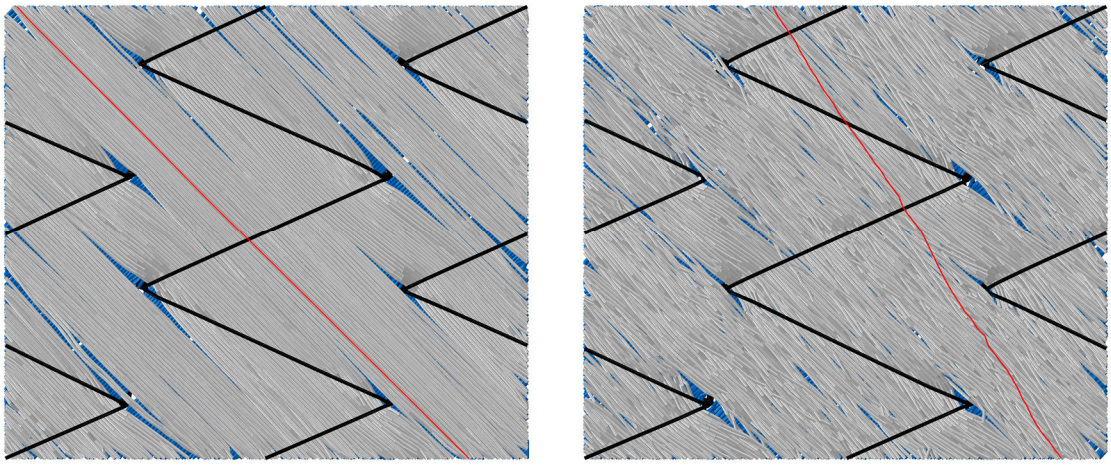

(a) $\sigma_G = 0°$ (b) $\sigma_G = 4.0°$

Fig. 6-13: Virtual NCFs (before virtual shear characterization) generated with various standard deviations of the Gaussian distribution used to sample used to sample the orientation of the digital chains.
One chain of the +45° layer is highlight in each picture to show the influence of the variability in the fibrous architecture of the layers.

The results of the virtual shear characterization are illustrated in Fig. 6-14. The mean results and the corresponding shear asymmetric ratios are listed in Tab. 6-2. As expected, the normalized shear torque increases with the standard deviation used to sample the orientation of the digital chains. Nevertheless, it is shown that the shear torque remains constant for low standard deviations (below 1.0°). With increasing variability, the dependency is noticeably stronger. This is justified by a higher degree of entanglement of the chains and superior interaction forces in the virtual fabric. In addition, tensile stresses induced in chains deviating from the theoretical path generate higher shear torques. Note that the scatter of the results increases with the standard deviation, which can be explained by a higher probability of chains deviating considerably from the theoretical path.

The shear asymmetric ratio shows a slight growth along the standard deviation. This means that the orientation variability influences the contribution of the stitching yarn and not only the forces generated in the fibrous layers. This can be attributed to a higher magnitude of the stitch-to-filaments interactions. As a consequence, the orientation variability of the chains increases the contribution of the stitching yarn on the shear torque.

This study suggests that the standard deviation used to sample the orientation of the digital chains is a key parameter of the numerical description of the NCF towards accurate predictions of the shear behavior. As a result, it is recommended to pay particular attention in the calibration of the orientation variability, as it was proposed in section 5.3.2.

Tab. 6-2: Configurations and respective results of the numerical study on the influence of the orientation variability on the shear behavior of the ±45° NCF.

Standard deviation [°]	**Mean $C_{fabric}(11.5°)$ [mN/mm]**	**Mean $C_{fabric}(-11.5°)$ [mN/mm]**	**Asymmetric ratio [-]**
0°	4.33	0.897	4.83
0.5°	5.51	1.14	4.85
1.0°	6.38	1.14	5.59
2.0°	14.4	2.00	7.22
3.0°	45.1	7.88	5.73
4.0°	75.4	10.4	7.29

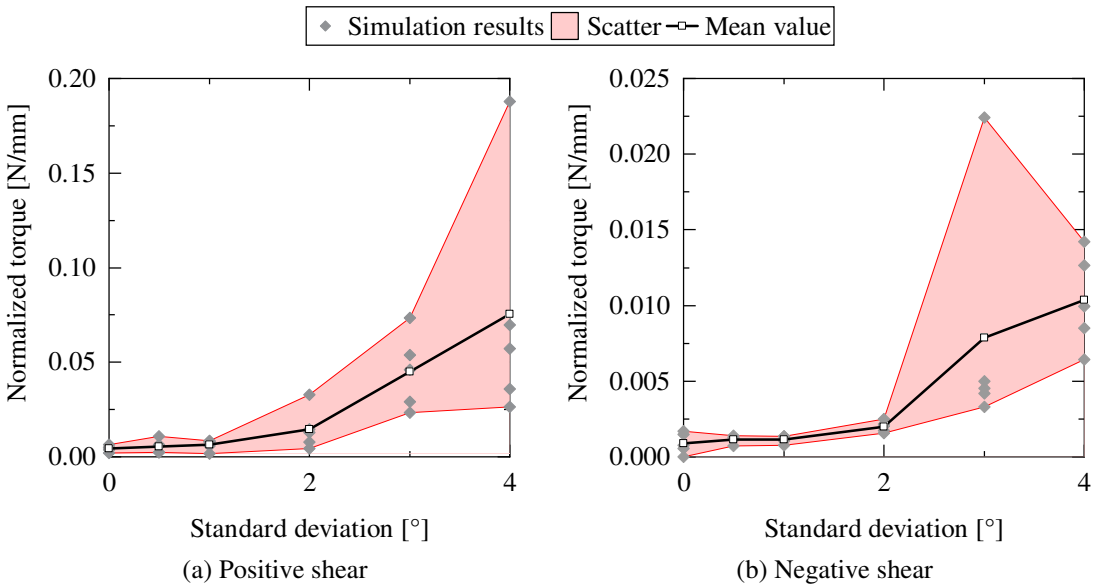

Fig. 6-14: **Normalized shear torque measured at a shear deformation of 11.5° in positive (a) and negative (b) directions depending on the standard deviation used to sample the orientation of the chains modeling the fibrous layers.**
The red surface represents the range of the results from the maximum and minimum values for each configuration.

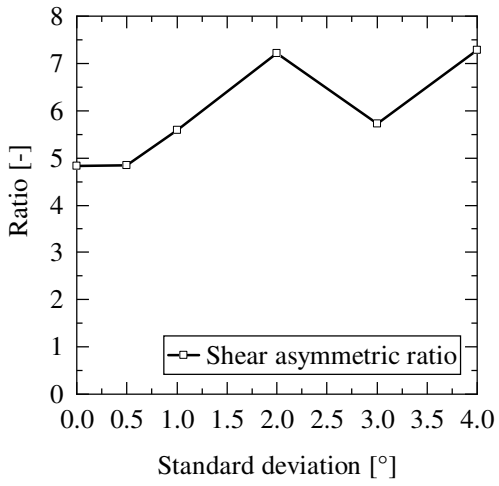

Fig. 6-15: **Evolution of the shear asymmetric ratio depending on the standard deviation used to sample the orientation of the chains modeling the fibrous layers.**

6.3.3 Influence of the stitch length

The main advantage of virtual approaches is the ability to study a large range of manufacturing parameters with reduced effort. So, the cost intensive production of the samples and their mechanical characterizations can be alleviated.

The architecture of the stitching pattern was identified in chapter 2 as a key parameter for the shear stiffness of biaxial NCFs. In this subsection, the influence of the stitch length on the shear torque and on the asymmetric ratio is investigated. Note that such

studies can be extended to further parameters of the stitch architecture (such as the stitch gauge or the stitching pattern).

The reference stitch length of the ±45° NCF is 2.2 mm. Configurations with one shorter and one longer stitch length are investigated, as listed in Tab. 6-3 and illustrated in Fig. 6-16. The angles of the overlapping part of the stitching yarn — which corresponds to the angle between two successive stitching points of a same yarn (ref. Fig. 6-16) — are calculated and listed in Tab. 6-3. It enables a direct comparison of the simulation results with the approach presented by Krieger et al. in [61]. Note that the number of repetitions of the stitching pattern in the machine direction is adapted in order to keep a consistent RVE size. This leads to a 4x2 RVE for the shortest stitch length and a 1x2 RVE for the longest.

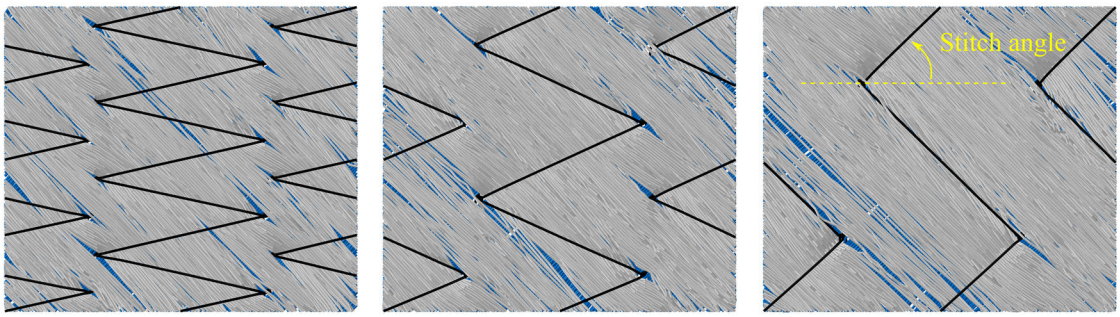

(a) 1.1 mm (b) 2.2 mm (c) 4.4 mm

Fig. 6-16: Virtual NCFs (before virtual shear characterization) with a constant stitch gauge of 5.08 mm and stitch lengths of 1.1 mm (a), 2.2 mm (b) and 4.4 mm (c).

The results of the virtual shear characterization are illustrated in Fig. 6-17 and summarized in Tab. 6-3. First, it is found that the shear torque in positive direction increases with the stitch length. On the contrary, the shear torque in the negative shear direction decreases with the stitch length. A significant drop of the shear torque in negative shear direction is observed for stitch lengths larger than 1.1 mm, whereas no significant difference can be observed between the results obtained with stitch lengths of 2.2 mm and 4.4 mm.

Fig. 6-18 shows the evolution of the asymmetric ratio. The configuration with a stitch length of 1.1 mm has an asymmetric ratio of 0.033. Asymmetric ratios smaller than 1 mean that the shear force required to shear the fabric in negative direction is higher than in positive direction. With 1.1 mm stitch length, the shear torque measured in negative direction is thirty-one times higher than in positive direction. The asymmetric ratio increases with the stitch length and is already larger than 1 with a stitch length of 2.2 mm.

These observations correlate with the results found in the literature. On the one hand, Steer reported in [60] that higher forces were measured in negative than in positive shear direction for a ±45° NCF with a very short stitch length. On the other hand, Krieger et al. published in [61] that there is a specific ratio between the stitch length and stitch gauge at which the behavior of a $\pm\alpha$ NCF is symmetric (i.e. has an asymmetric ratio of

1) because no strain is generated in the stitching yarn in both shear directions. According to this theory, a symmetric behavior is reached with a stitch angle of 68.5° for ±45° biaxial NCFs. With a stitch gauge of 5.08 mm, it would correspond to a stitch length of 2.0 mm. It correlates with the simulation results of the virtual shear characterization showed in Fig. 6-18, in which an asymmetric ratio of 1 is predicted for a stitch length between 1.1 mm and 2.2 mm.

As a consequence, this study shows that the simulation approach developed in this doctoral thesis is able to investigate the influence of the stitch architecture on the shear behavior. Thus, it can reduce the experimental effort during the development of adequate textile architectures.

Tab. 6-3: Configurations and respective results of the numerical study on the influence of the stitch length on the shear behavior of the ±45° NCF.

Stitch length [mm]	**1.1**	**2.2**	**4.4**
Stitch angle [°]	77.8	66.6	49.1
Mean $C_{fabric}(11.5°)$ [mN/mm]	4.95	14.4	126
Mean $C_{fabric}(-11.5°)$ [mN/mm]	152	2.00	1.84
Asymmetric ratio [-]	3.26E-2	7.22	68.3
Shear direction of highest torque	Negative	Positive	Positive

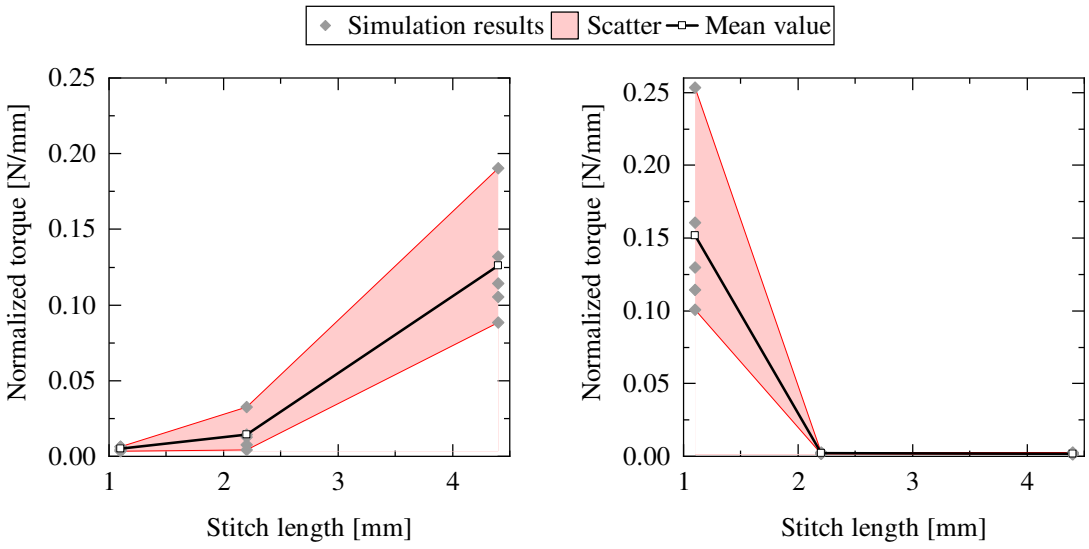

(a) Positive shear (b) Negative shear

Fig. 6-17: Normalized shear torque measured at a shear deformation of 11.5° in positive (a) and negative (b) directions depending on the stitch length.
The red surface represents the range of the results from the maximum and minimum values for each configuration.

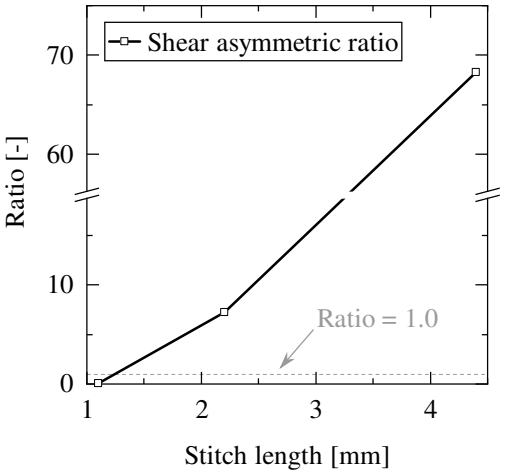

Fig. 6-18: Evolution of the shear asymmetric ratio depending on the stitch length.

6.4 Conclusion

An approach was established in this chapter to virtually characterize the shear behavior of a ±45° NCF. A pure shear deformation was applied to the numerical description of NCFs (developed in chapter 5) using the reference points of the periodic mesh.

Firstly, the kinematic behavior of the virtual textile was validated with experimental investigations on the stitch sliding. A method to quantify the stitch sliding depending on the shear deformation was applied to the ±45° NCF with a picture frame testing rig. A significant stitch sliding was observed compared to the original stitch length. Moreover, the correlation between the sliding distance and the theoretical segment elongation up to a shear angle of 22° supports the hypothesis of free stitch movement at the crossovers. For larger shear angles, this movement is progressively impeded due to the high degree of interaction of the stitching yarn at entangled loops once the stitch segments are straightened. A consistent method was used to quantify the stitch sliding in the simulation. An excellent correlation with the experiments was found for shear angles up to 15°. In the simulation, the stitch sliding is impeded at smaller angle due to the numerical discretization of the stitching yarn and the resulting interlocking. The elongation of the stitch segments must be adapted through additional extension of the stitching yarns. This validates the deformation mechanisms of the numerical model but suggests that higher shear forces might be observed in the simulation for shear angles larger than 15°.

Secondly, the shear torque was identified as an adequate measure of the shear behavior since it is neither related to the geometry of the sample nor to the loading conditions. The shear torque is normalized using the area of the RVE. According to the observations made in chapter 4, a focus is put on the shear torque at a shear deformation of ±11.5° and on the shear asymmetric ratio. A study on the influence of the RVE size suggested a convergence of the normalized shear torque for samples larger than 4x4 RVEs (meaning that the smallest unit-cell defined by the periodicity of the stitching pattern is

repeated four times in and perpendicular to the machine direction). Nevertheless, a convergence of the shear asymmetric ratio was observed starting from 2x2 RVEs. As a result, 2x2 RVE models are defined as reference models for virtual investigations aiming at relative results. It is recommended to perform simulations with models larger than 4x4 RVEs if one wishes to calculate absolute values.

Thirdly, the influence of the orientation variability in the fibrous layers was analyzed. It was found that the shear torque heightens with the standard deviation used to sample the orientation of the filaments due to higher level of interactions within the layers and of the chains with the stitching yarns. The intensification of the shear forces is also due to tensile stresses induced in the chains if their orientations deviate from the ±45° directions. In addition, a slight increase of the asymmetric shear ratio was observed, which suggests that the influence of the stitching yarn increases with the variability in the fibrous layer. This study highlights the importance of the calibration of the orientation of the chains to accurately predict the shear behavior of the textile.

Fourthly, the influence of the stitch architecture was examined. The stitch length was reduced and increased by a factor of two compared to the original length. The simulation results showed an augmentation of the shear torque in positive shear direction with the stitch length. On the contrary, the shear torque for negative shear deformations is higher for shorter stitch lengths. Moreover, it was found that the configuration with the shortest stitch length (1.1 mm) requires a higher shear torque in negative direction than in positive direction. The results are in complete agreement with experimental studies published by other researchers.

A high scatter of the simulation results was observed in all configurations. This can be justified by the high tensile stiffness of the chains and induced stresses if the chains are not exactly oriented in the ±45° directions (which result from the variability of the orientations in the fibrous material or from local deviations near the stitching points). Even though these effects are also observed in experimental trials with picture frame setups, the use of large samples reduce the influence of the boundary conditions and, thus, the scattering of the results. Moreover, a sliding in the clamps of misaligned filaments cannot be excluded in the experiments, reducing the high tensile stresses. This is not possible with the boundary conditions of the presented simulation method. As a consequence, the simulation is more sensitive to spurious forces and it is recommended to increase the number of simulation results per configuration.

The developed virtual characterization approach of biaxial NCFs represents a significant advantage for the investigation of relative changes of the shear behavior depending on the textile configurations. These numerical simulations can alleviate expensive experimental investigations to evaluate the influence of manufacturing parameters on the shear behavior of the textile.

7 Conclusions, potential application of the multiscale approach and future works

The large variety of NCF configurations and their resulting varying mechanical behaviors require high experimental effort in the selection and design of suitable textiles for the production of new composite parts. This doctoral thesis aimed at the development of methods able to support the design of new textiles for composite manufacturing. To that end, two main research goals have been defined. First, a simulation framework to predict the quality of the preforming process was targeted in order to find optimal deformation behaviors of the textile. Second, a numerical description of NCFs able to predict the shear behavior of dry NCFs was developed in order to study the influence of the textile architecture on the shear behavior of the textile.

The main results of these respective goals are discussed in the following sections and potential sources of improvement are identified. Moreover, a connection between the forming simulation and the virtual shear characterization is proposed to highlight the benefits of the multiscale approach presented in this doctoral thesis. Finally, future works and potential applications of the methods are detailed.

7.1 Identification of optimal deformation behaviors

Development of a macroscopic forming simulation

The forming process of dry NCFs was modeled using a macroscopic approach. It describes the textile reinforcement as a continuum and accounts for the material behavior to predict the shear and out-of-plane deformations of textiles (such as wrinkles or folds). Process parameters and interactions with other components were considered. The forming simulation was developed using the commercially available software package ABAQUS. The weak bending rigidity of dry textiles compared to their tensile stiffness required adaptions of the available *FABRIC material model. To that end, a bi-linear bi-material approach was introduced, which considers various elastic moduli in tension and compression directions. As such, the bending stiffness can be adequately reduced using standard shell formulations. Moreover, a bi-linear compressive stress-strain relationship allows for approximation of the non-linear bending behavior of textile reinforcements. This approach is an efficient method to model the deformation behavior of dry textiles for composite manufacturing at reduced development costs and using available constitutive equations.

The calibration of the material model and of the interaction properties was presented. An experimental method for the characterization of the bending parameters was developed using rudimentary equipment. It is based on the buckling of a textile sample to generate a bending deformation representative of the out-of-plane deformations in forming processes. The combined acquisition of the deformed geometry and of the reaction force during the experiments delivers the data for an indirect calibration of the input parameters. The experiments were simulated with a large number of input parameter sets (a total of 500 sets were generated) to calibrate the bending model. The best set was identified based on criteria defined on the reaction force and on the deformed geometry. This promising approach needs further developments to reduce the variability observed in the experiments. For example, the use of universal test machines and of an automatic extraction of the sample geometries can significantly reduce the experimental scatter. With a controlled displacement of the sample and a continuous recording of the deformed sample geometry, potential strain-rate dependencies of the material could be observed. In addition, the generation of a surrogate model using the high number of simulation results could enable a better fit of the experimental results.

A validation of the forming simulation was presented using a hemispherical stamp geometry. Criteria on the fiber orientation, on the wrinkling behavior and on the corner draw-in have validated the ability of the simulation to predict the deformed geometry of the textile. Nevertheless, the simulation failed to predict the stamp force and the blankholder displacement in the second half of the stamping process. This would suggest that the calibration of the bending behavior at high curvatures was not sufficiently considered in the characterization. As a result, further work is recommended to increase the robustness of the calibration method at high curvatures.

Finally, the forming simulation approach shall be enhanced to the simulation of preforms with many plies. Since simulations of multiple plies with their respective interactions considerably increase the computation times, the development of smeared descriptions of the preform is recommended.

Influence of the material behavior on the preform quality

A method to measure the quality of the preforming process based on simulation results was proposed in chapter 4. Thereby, the shear deformation, the onset of wrinkles and geometrical deviations of the textile from the stamp geometry were used in order to automatically measure the quality of the numerical preform.

These criteria were applied to a “Pole-Peak” stamp geometry and the influence of material parameters was extensively studied. It was found that the balance between the shear and bending stiffnesses is crucial for the preform quality, and that adequate change of the shear stiffness can compensate an unfavorable bending rigidity. Moreover, the importance of the shear stiffness at small shear angles (smaller than 11.5°) was highlighted. Finally, it was shown that the non-linear bending behavior of the textile has a predominant influence on the wrinkles and, thus, on the quality of the preforming process.

Since the stamp and the blank-holder geometries influence the deformation of the textile, it is expected that the guidelines derived in chapter 4 can vary with the tool geometries or forming processes. Moreover, further conclusions on the preform quality require extensive studies to quantify the influence of defects on the part performance and define adequate thresholds on the objective functions.

7.2 Prediction of the shear behavior of dry NCFs

Numerical description of NCFs at the scale of the filaments

Simulations aiming to predict the shear behavior of the textile must accurately reproduce all relevant deformation mechanisms. Due to the contribution of the stitching yarn to the rigidity of NCFs and its interaction with the fibrous layers, numerical descriptions of the textile at microscopic level were selected. A framework able to describe any NCF configuration was developed. It models the stitching yarns and the fibrous layers with digital chains. A stochastic distribution of the orientation of the chains was used to accurately reproduce the distribution of the filaments and the local defects in the textile. The size of the model is based on the stitching pattern and on its periodicity. Averaged periodic boundary conditions were developed to account for the mesoscopic periodicity of the fibrous layers.

The in-plane geometry of the virtual textile was validated based on the size of the local defects and on the orientation distributions of the layers. The thickness of the textile was used to calibrate the number of filaments modeled in one digital chain and to define the fiber volume fraction of the fibrous layers before the knitting process. During the calibration of the input parameters, it was found that the magnitude of pretension of the stitching yarn influences the orientation of the loops, the size of the defects and thereby the orientation of the chains. Therefore, extended investigations of the pretension in the stitching yarn may be performed to improve the accuracy of the description. Moreover, the entanglement of the chains characterized by the out-of-plane waviness of the filaments can be validated using X-ray computed tomography.

Since this framework is based on mechanical simulations that account for all deformation mechanisms of dry NCFs, it can be used in further simulations to predict various properties of the textile.

Virtual shear characterization

The shear characterization of the virtually generated NCFs was performed. The kinematic behavior of the virtual NCFs was analyzed through comparisons of the shear angles between the applied and measured deformation. Moreover, the stitch sliding was selected to validate the deformation behavior of the virtual textile. The mechanical behavior of the virtual NCFs was quantified using the normalized shear torque at a shear deformation of ±11.5°. It was observed that the size of the virtual sample influences the

shear behavior. It was concluded that studies on the asymmetric shear ratio can be performed with models repeating the stitching pattern two times in each direction. However, larger models are necessary to achieve a convergence of the absolute results in each shear direction. Moreover, the influence of the distribution of the chain orientations was examined, showing a significant impact on the deformability of the textile. The framework was also used to study the influence of the stitch length. The results showed that the stitch length is a key factor to adjust the shear stiffness of a textile. Furthermore, a significant impact on the asymmetric ratio was observed, correlating with the results and theories of other researchers. Similar investigations with the variation of further manufacturing parameters can deliver essential results for the development of new textiles.

Nevertheless, the simulation overpredicts the asymmetric shear ratio and failed to model the shear deformation of the reference material at shear angles larger than 30°. On the one hand, it is supposed that the contribution of the stitching yarn is overestimated due to the discretization of the yarn in truss elements. Thus, shorter elements may reduce the interlocking of the elements at the loop crossovers. On the other hand, the simulation of the stitching yarn with multiple chains or elements with enhanced kinematic relations (modeling the deformation of the cross section) could improve the accuracy of the simulation results.

The main limitation of the virtual shear characterization is the restriction to relative comparisons of the simulation results. Further work is required to achieve realistic absolute values of the shear forces. It was found in a supplementary study (not presented in this work) that the number of chains used to model the fibrous layers heightens the shear torque. This is justified by the increase of the number of contact surfaces between the chains of the fibrous layers. This suggests that the entanglement of the chains should be further calibrated or that interaction models should be developed to alleviate this dependency.

In the future, the bending stiffness of the digital chains can be introduced in the framework if the forces resulting from bending deformations of the chains cannot be neglected compared to the axial forces and interaction forces. In that case, the bending stiffness of the chains must be thoroughly studied to achieve a realistic deformation behavior depending on the number of filaments modeled in each chain. Approaches implemented with the solver ABAQUS/Explicit were studied in [S8], [S9] and [S10]. Even though they presented promising results, numerical instabilities raised due to the weak bending stiffness of the chains could not be solved in the context of this doctoral thesis. Methods based on new elements or other constitutive equations should be considered.

7.3 Potential application of the multiscale approach: example of the stitch length

In this subsection, a study presents a potential application of the methods developed in this doctoral thesis. By connecting the forming simulation at the macroscopic scale (chapters 3 and 4) with the virtual shear characterization at the microscopic scale (chapters 5 and 6), the influence of textile configurations on the preform quality can be predicted. In the following, the example of the stitch length is investigated.

To that end, input behaviors of three ±45° biaxial NCF configurations (stitch lengths of 1.1 mm, 2.2 mm, and 4.4 mm) are generated for the simulation of the "Pole-Peak" stamping process (ref. section 4.4.1). The shear input curves for the forming simulations are derived from the results of the virtual shear characterization, as follows:

- The experimentally measured shear behavior of the ±45° NCF (i.e. stitch length of 2.2 mm) in positive direction is taken as the reference curve (see Fig. 3-9a).
- The material behavior for positive shear deformation of the NCFs with stitch lengths of 1.1 mm and 4.4 mm is scaled from the reference curve according to the predicted evolution of the normalized shear torque illustrated in Fig. 6-17a.
- The material behavior for negative shear deformation of all NCFs is scaled from the experimental curve of the ±45° NCF in negative direction (see Fig. 3-9b) according to the predicted evolution of the asymmetric shear ratio from Fig. 6-18.

Note that the input parameters of the bending behavior are kept constant for all NCF configurations.

The forming simulation results of the three NCF configurations are presented in Fig. 7-1. The strong asymmetric deformation is found in all simulation results. The forming process with the smallest stitch length promotes a positive shear deformation in the textile, whereas stitch lengths of 2.2 mm and 4.4 mm show higher shear deformations in negative direction. These observations correlate with the evolution of the asymmetric shear ratio, which is smaller than 1 for a stitch length of 1.1 mm and larger for the other configurations.

The quality of the respective preforms is measured using the criteria developed in chapter 4 on the shear deformation and on the onset of wrinkles. The results are illustrated in Fig. 7-2. The strongest wrinkling and smallest shear deformations are reached with a stitch length of 1.1 mm. This is explained by the high shear stiffness of this configuration, promoting the onset of wrinkles to accommodate the stamp geometry. Focusing on the stitch lengths of 2.2 mm and 4.4 mm, it is important to note the opposite evolution of the local curvatures and geometrical deviations (criteria used to calculate the wrinkling objective function). The longest stitch length leads to a slight increase of the

wrinkling objective function, which is in accordance with the stronger wrinkling of the preform observed in the regions of positive shear deformations (see Fig. 7-1c).

Important findings about the expected deformations in the textile depending on the stitch length were derived. This study is an example of potential applications of the methods developed in this work to support the design of new textiles and to select adequate textiles improving the quality of the preforming process.

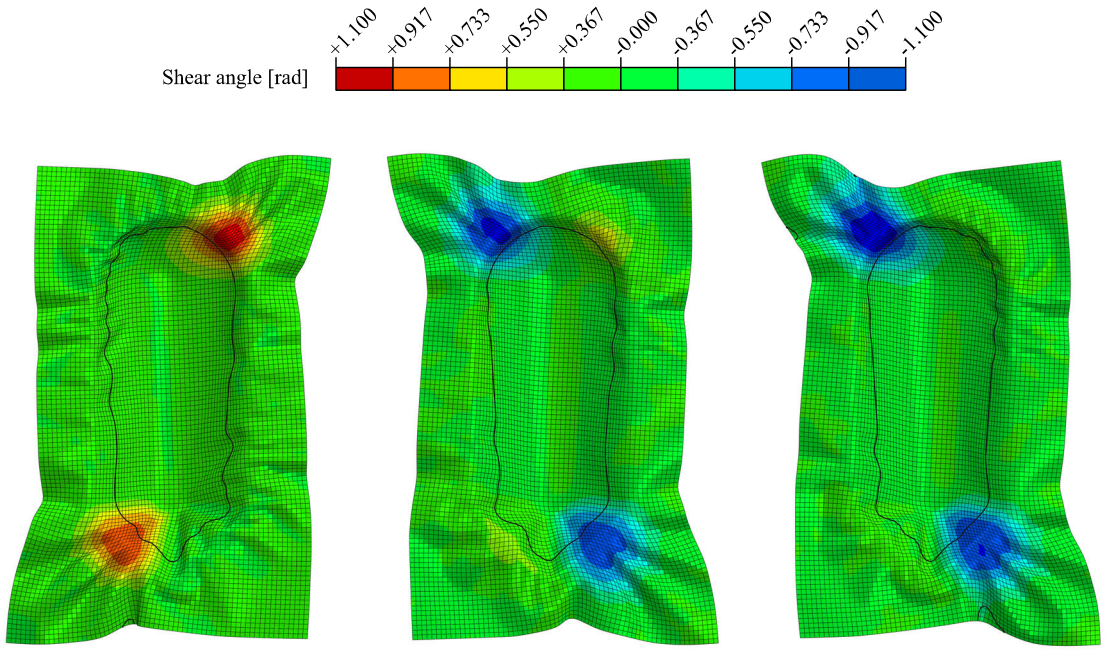

(a) Stitch length 1.1 mm (b) Stitch length 2.2 mm (c) Stitch length 4.4 mm

Fig. 7-1: Results of forming simulations using the virtual shear characterization to generate the shear input parameters of NCFs with various stitch lengths.
The black line shows the contour of the outer surface of the preform at a height of 25 mm.

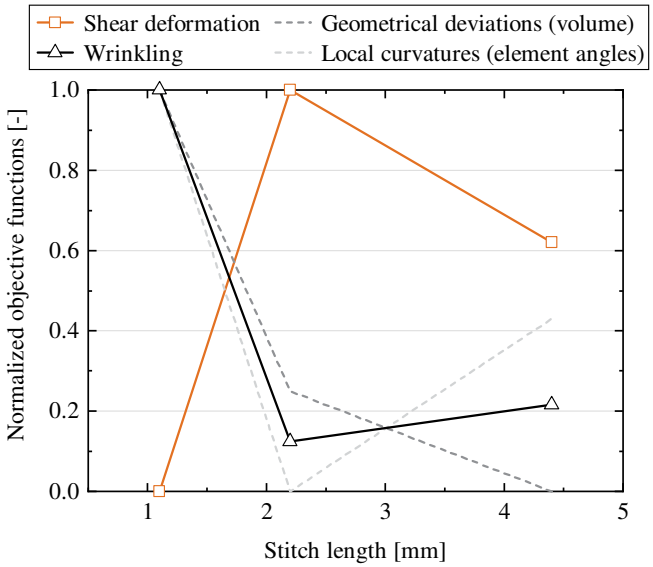

Fig. 7-2: **Criteria measuring the quality of the preform of forming simulations using the virtual shear characterization to generate the shear input parameters of NCFs with various stitch lengths.**
The winkling objective function is defined as the mean value of the geometrical deviations and local curvatures.

7.4 Future applications towards virtual textile development

This thesis is part of a long-term vision towards a virtual textile development. In the future, following improvements of the presented methods shall be considered:

- Extension of the virtual characterization: the method presented in this doctoral thesis focused on the shear behavior of the textile. Since the stitching pattern can influence the bending behavior further, the virtual characterization of the bending rigidity shall be considered. The boundary conditions of a bending deformation can be introduced using the periodic mesh of reference points but improvements are required in the case of beam elements to constraint the rotational degrees of freedom. In addition, the simulation of combined loading conditions (e.g. combined shear and tensile loads) can replace complex test setups to understand potential interactions between deformation modes.
- Automated workflow: a relation between the methods developed at the macroscopic scale (forming simulation) and at the microscopic scale (virtual shear characterization) was presented in section 7.3 for two stitch lengths. In the future, an automated coupling should be developed to identify adequate materials for different forming processes and for new component geometries. Due to the high computing times of the virtual shear characterization and need for many simulation results to achieve representative values, the use of dedicated optimization methods is recommended. For example, surrogate models

of the textile behavior — constructed based on simulation results of the virtual characterization — can be used to identify optimal textile architectures.

- Multiscale forming simulation: local irregularities in composite materials can lead to the failure of the whole structure due to stress concentrations, out-of-plane stresses and unexpected failure modes. As a result, local defects have a global influence on the whole design of the components. A recent work published by Iwata et al. [196] reported a coupled meso-macro forming analysis, in which the deformation field of a macroscopic forming simulation with woven fabrics is used to compute local defects in critical regions with mesoscopic simulation. Such approach could be adapted to the forming of NCFs through a coupling of microscopic analyses (using the developed virtual description of NCFs) with macroscopic forming simulations. This would enable the calculation of the overall textile deformation while accurately predicting local defects in critical regions.

Defects and variability during the preforming of textiles influence the subsequent manufacturing steps. As a consequence, the development of robust manufacturing processes requires the consideration of defects induced in the previous steps with a realistic description of the textile, rather than using ideal geometries of the preforms. Simulation methods can describe each process step but the consideration of defects and variability in the textile requires extensive supplementary experimental characterizations. As a result, the developed framework is valuable to predict further textile properties:

- Compaction of the preform: in resin transfer molding processes, the preform is placed in the tool and compacted to the final geometry for the injection of the resin. Local geometrical deviations of the preform are compressed, leading to various defects in the textile (such as gaps or waviness). The compaction stiffness of the preform plays an essential role in the distribution of the forces and resulting fiber volume fraction. The virtual characterization framework of the compaction behavior can support the calibration of macroscopic models as presented in [208] and can accurately predict the compaction state of the textile. Note that improvements of the contact models may be required to account for the strain-rate dependency of the textile compaction behavior.
- Permeability of the textile: the permeability of the textile influences the flow front of the resin during the injection process. An accurate description of the filling process is mandatory in order to develop adequate filling strategies, which aim at a full impregnation of the textile. Since the permeability of the textile strongly depends on the textile architecture, on its compaction state and on the microstructure of the filaments, extensive experimental characterization studies are required [209]. Even though virtual characterizations of the textile permeability were published in the recent years [210, 211], they rely on inputs from cost-intensive X-ray computed tomography or assume ideal architectures. The method presented in this doctoral thesis is able to predict the

"as-manufactured" geometry of NCFs with an accurate description of local defects. Hence, a connection of this method with a virtual characterization of the textile permeability could considerably reduce the effort of experimental characterizations. Moreover, the virtual characterization framework could be used to generate a realistic geometry of the textile at various compacted states (i.e. for a large range of fiber volume fractions) and with various deformation states (e.g. with a shear deformation). The virtual characterization can complement the experimental characterization of the textile permeability and, thus, improve the accuracy of the filling simulations.

References

[1] EUROPEAN COMMISSION, “Communication from the Commission to the European Parliament, the European Council, the Council, the European Economic and Social Committee and the Committee of the Regions: The European Green Deal,” COM(2019) 640, 2019.

[2] EUROPEAN COMMISSION, “Communication from the Commission to the European Parliament, the European Council, the Council, the European Economic and Social Committee, the Committee of the Regions and the European Investment Bank: A Clean Planet for all - A European strategic long-term vision for a prosperous, modern, competitive and climate neutral economy,” COM(2018) 773, 2018.

[3] European Environmental Agency, “Approximated EU GHG inventory: proxy GHG estimates for 2017,” No 17/2018, 2018.

[4] EUROPEAN COMMISSION, “In-Depth Analysis in Support of the Commission Communication COM(2018) 773: A Clean Planet for all A European long-term strategic vision for a prosperous, modern, competitive and climate neutral economy,” 2018.

[5] J. C. Kelly, J. L. Sullivan, A. Burnham, and A. Elgowainy, “Impacts of Vehicle Weight Reduction via Material Substitution on Life-Cycle Greenhouse Gas Emissions,” *Environmental science & technology*, vol. 49, no. 20, pp. 12535–12542, 2015, doi: 10.1021/acs.est.5b03192.

[6] G. Hellard, “Composites in Airbus: A Long Story of Innovations and Experiences,” 2008.

[7] A. G. Miller, “The Boeing 787 Dreamliner: More Than an Airplane,” 2005.

[8] J. Starke, “CARBON COMPOSITES IN AUTOMOTIVE STRUCTURAL APPLICATIONS,” Brussels, 2016.

[9] JEC Group, “JEC Observer: Overview of the Global Composites Market 2019-2024,” 2020. [Online]. Available: http://www.jeccomposites.com/e-store/jec-observer-overview-global-composites-market-2019-2024

[10] Lux Research, “The Future of Carbon Fiber Composites: Executive Summary,” 2020.

[11] A. Elmarakbi, Ed., *Advanced composite materials for automotive applications: Structural integrity and crashworthiness*. Chichester: Wiley, 2014.

[12] “DIEFFENBACHER Preform Technology: Advancements in the fully automated preform process for complex parts,”

[13] BMW Group, *BMW i3 Produktion BMW Werk Leipzig: CFK-Fertigung (09/13).* [Online]. Available: https://www.press.bmwgroup.com/austria/photo/detail/P90127346/bmw-i3-produktion-bmw-werk-leipzig-cfk-fertigung-09-13 (accessed: Feb. 14 2021).

[14] F. Nosrat Nezami, T. Gereke, and C. Cherif, "Active forming manipulation of composite reinforcements for the suppression of forming defects," *Composites Part A: Applied Science and Manufacturing*, vol. 99, pp. 94–101, 2017, doi: 10.1016/j.compositesa.2017.04.011.

[15] B. Sköck-Hartmann and T. Gries, "Automotive applications of non-crimp fabric composites," in *Non-Crimp Fabric Composites*: Elsevier, 2011, pp. 461–480.

[16] S. V. Lomov, Ed., *Non-Crimp Fabric Composites*: Elsevier, 2011.

[17] G. Creech and A. K. Pickett, "Meso-modelling of Non-Crimp Fabric composites for coupled drape and failure analysis," *J Mater Sci*, vol. 41, no. 20, pp. 6725–6736, 2006, doi: 10.1007/s10853-006-0213-6.

[18] S. V. Lomov *et al.,* "Carbon composites based on multiaxial multiply stitched preforms. Part 3: Biaxial tension, picture frame and compression tests of the preforms," *Composites Part A: Applied Science and Manufacturing*, vol. 36, no. 9, pp. 1188–1206, 2005, doi: 10.1016/j.compositesa.2005.01.015.

[19] S.V. Lomov, I. Verpoest, M. Barburski, and J. Laperre, "Carbon composites based on multiaxial multiply stitched preforms. Part 2. KES-F characterisation of the deformability of the preforms at low loads," *Composites Part A: Applied Science and Manufacturing*, vol. 34, no. 4, pp. 359–370, 2003, doi: 10.1016/S1359-835X(03)00025-3.

[20] C. Koch, "Eigenschaftsprofil von Carbonfasergelegen und deren Wirkzusammenhänge in der automobilen Großserienproduktion," Doctoral thesis, Chair of Carbon Composites, Technical University of Munich, München, 2021.

[21] P. Boisse, N. Hamila, E. Vidal-Sallé, and F. Dumont, "Simulation of wrinkling during textile composite reinforcement forming. Influence of tensile, in-plane shear and bending stiffnesses," *Composites Science and Technology*, vol. 71, no. 5, pp. 683–692, 2011, doi: 10.1016/j.compscitech.2011.01.011.

[22] M. Christ, A. Miene, and U. Mörschel, "Measurement and Analysis of Drapeability Effects of Warp-Knit NCF with a Standardised, Automated Testing Device," *Appl Compos Mater*, vol. 47, 3–4, p. 343, 2016, doi: 10.1007/s10443-016-9555-7.

[23] S. Bel, P. Boisse, and F. Dumont, "Analyses of the Deformation Mechanisms of Non-Crimp Fabric Composite Reinforcements during Preforming," *Appl Compos Mater*, vol. 19, 3-4, pp. 513–528, 2012, doi: 10.1007/s10443-011-9207-x.

[24] W. Jiang, “Vergleich des Drapierverhaltens von biaxialen Gelegen,” Term Project, Chair of Carbon Composites, Technical University of Munich, Munich, 2018.

[25] M. Christ, “Definition und Quantifizierung der Drapierbarkeit von multiaxialen Gelegen durch die Vermessung von Einzeleffekten,” Doctoral dissertation, Universität Bremen, Bremen, 2018. [Online]. Available: http://d-nb.info/1161096647/34

[26] P. Boisse, “Finite element analysis of composite forming,” in *Composites Forming Technologies*: Elsevier, 2007, pp. 46–79.

[27] J. W. Klintworth and A. C. Long, “The use of draping simulation in composite design,” in *Composites Forming Technologies*: Elsevier, 2007, pp. 277–292.

[28] P. Harrison, W.-R. Yu, and A. C. Long, “Modelling the deformability of biaxial non-crimp fabric composites,” in *Non-Crimp Fabric Composites*, S. V. Lomov, Ed.: Elsevier, 2011, pp. 144–165.

[29] S. T. Peters, Ed., *Handbook of composites,* 2nd ed. London [etc.]: Chapman & Hall, 1998.

[30] Gadow, Weichand, and Jiménez, “Process Technology, Applications and Thermal Resistivity of Basalt Fiber Reinforced SiOC Composites,” *Ceramics*, vol. 2, no. 2, pp. 298–307, 2019, doi: 10.3390/ceramics2020025.

[31] AVK, Industrievereinigung Verstärkte Kunststoffe, *Handbuch Faserverbundkunststoffe: Grundlagen, Verarbeitung, Anwendungen ; mit 46 Tabellen,* 3rd ed. Wiesbaden: Vieweg + Teubner, 2010.

[32] A. McIlhagger, E. Archer, and R. McIlhagger, “Manufacturing processes for composite materials and components for aerospace applications,” in *Polymer Composites in the Aerospace Industry*: Elsevier, 2020, pp. 59–81.

[33] BOGE Rubber & Plastics, *First all-plastic brake pedal for battery-electric sports car.* [Online]. Available: https://www.boge-rubber-plastics.com/en/first-all-plastic-brake-pedal-battery-electric-sports-car (accessed: Jan. 4 2021).

[34] S. Mazumdar, “Opportunity and Challenges in Automotive Composites Industry,” December 2013.

[35] Hexcel Corporation, “HexFlow® RTM 6: 180°C mono-component epoxy system for Resin Transfer Moulding and Infusion technologies,” Jan. 2016.

[36] M. Holmes, “High volume composites for the automotive challenge,” *Reinforced Plastics*, vol. 61, no. 5, pp. 294–298, 2017, doi: 10.1016/j.repl.2017.03.005.

[37] M. Dix, S. Beck, A. Repper, and R. Hinterhölzl, “Integrierte Materialmodellierung für die CFK-Prozesssimulation,” *Lightweight Des*, vol. 6, no. 5, pp. 24–29, 2013, doi: 10.1365/s35725-013-0276-7.

[38] A. Vita, V. Castorani, M. Germani, and M. Marconi, “Comparative life cycle assessment of low-pressure RTM, compression RTM and high-pressure RTM manufacturing processes to produce CFRP car hoods,” *Procedia CIRP*, vol. 80, pp. 352–357, 2019, doi: 10.1016/j.procir.2019.01.109.

[39] H. Tan and K. M. Pillai, “Processing polymer matrix composites for blast protection,” in *Blast Protection of Civil Infrastructures and Vehicles Using Composites*: Elsevier, 2010, pp. 54–87.

[40] C. Cherif, *Textile Werkstoffe für den Leichtbau: Techniken-- Verfahren-- Materialien-- Eigenschaften*. Heidelberg: Springer, 2011.

[41] R. Ernst-Siebert and S. Grasser, “Mass production of composite leaf springs,” *Lightweight des worldw*, vol. 11, no. 3, pp. 18–21, 2018, doi: 10.1007/s41777-018-0013-0.

[42] C. Kowtsch, C. Herzberg, and R. Kleicke, “Gewebte Halbzeuge und Webtechniken,” in *Textile Werkstoffe für den Leichtbau*, C. Cherif, Ed., Berlin, Heidelberg: Springer Berlin Heidelberg, 2011, pp. 171–224.

[43] A. Schnabel and T. Gries, “Production of non-crimp fabrics for composites,” in *Non-Crimp Fabric Composites*: Elsevier, 2011, pp. 3–41.

[44] R. Seuß, “Production Process of Non Crimp Fabrics for aviation applications,” Moskau, Oct. 15 2014. [Online]. Available: https://docplayer.net/21253654-Production-process-of-non-crimp-fabrics-ncf-for-aviation-applications-composites-without-borders-2014-10-15-moskau-rainer-seuss.html

[45] Lindauer DORNIER GmbH, “DORNIER Carbon Weaving Machine: Product information,”

[46] H. Schürmann, *Konstruieren mit Faser-Kunststoff-Verbunden,* 2nd ed. Berlin, Heidelberg: Springer-Verlag Berlin Heidelberg, 2007.

[47] P. Abel, C. Lauter, T. Gries, and T. Troester, “Textile composites in the automotive industry,” in *Fatigue of Textile Composites*: Elsevier, 2015, pp. 383–401.

[48] F. Kruse and T. Gries, “Standardisation of production technologies for non-crimp fabric composites,” in *Non-Crimp Fabric Composites*: Elsevier, 2011, pp. 42–66.

[49] *DIN EN 13473-1:2001-11, Verstärkungen_- Spezifikation für Multiaxialgelege_-Teil_1: Bezeichnung; Deutsche Fassung EN_13473-1:2001*, Berlin.

[50] KARL MAYER Textilmaschinenfabrik GmbH, “High-performance warp-knitting machine for the production of carbon-fibre multiaxial non-crimp fabrics,” [Online]. Available: https://www.karlmayer.com/ecomaXL/files/Factsheet_COP_MAX_5_encn.pdf?download=true

[51] B. Lehmann and C. Herzberg, “Garnkonstruktionen und Garnbildungstechniken,” in *Textile Werkstoffe für den Leichtbau*, C. Cherif, Ed., Berlin, Heidelberg: Springer Berlin Heidelberg, 2011, pp. 111–169.

[52] S. V. Lomov, “Understanding and modelling the effect of stitching on the geometry of non-crimp fabrics,” in *Non-Crimp Fabric Composites*, S. V. Lomov, Ed.: Elsevier, 2011, pp. 84–102.

[53] P. Middendorf and C. Metzner, “Aerospace applications of non-crimp fabric composites,” in *Non-Crimp Fabric Composites*: Elsevier, 2011, 441-449e.

[54] K. Wei, D. Liang, M. Mei, D. Wang, X. Yang, and Z. Qu, “Preforming behaviors of carbon fiber fabrics with different contents of binder and under various process parameters,” *Composites Part B: Engineering*, vol. 166, pp. 221–232, 2019, doi: 10.1016/j.compositesb.2018.11.143.

[55] A. C. Long and M. J. Clifford, “Composite forming mechanisms and materials characterisation,” in *Composites Forming Technologies*: Elsevier, 2007, pp. 1–21.

[56] S. Chen, O.P.L. McGregor, L. T. Harper, A. Endruweit, and N. A. Warrior, “Defect formation during preforming of a bi-axial non-crimp fabric with a pillar stitch pattern,” *Composites Part A: Applied Science and Manufacturing*, vol. 91, pp. 156–167, 2016, doi: 10.1016/j.compositesa.2016.09.016.

[57] A. C. Long, P. Boisse, and F. Robitaille, “Mechanical analysis of textiles,” in *Design and Manufacture of Textile Composites*: Elsevier, 2005, pp. 62–109.

[58] S. V. Lomov, “Deformability of textile performs in the manufacture of non-crimp fabric composites,” in *Non-Crimp Fabric Composites*: Elsevier, 2011, 117-144e.

[59] O. Stolyarov, T. Quadflieg, and T. Gries, “Characterization of shear behavior of warp-knitted fabrics applied to composite reinforcement,” *The Journal of The Textile Institute*, vol. 108, no. 1, pp. 89–94, 2017, doi: 10.1080/00405000.2016.1153876.

[60] Q. Steer, “Modélisation de la mise en forme des renforts fibreux cousus (NCF) : Etude expérimentale et numérique de l’influence de la couture,” Doctoral dissertation, Laboratoire de Mécanique des Contacts et des Structures (LaMCoS), INSA Lyon, Lyon, France, 2019.

[61] H. Krieger, T. Gries, and S. E. Stapleton, “Shear and drape behavior of non-crimp fabrics based on stitching geometry,” *Int J Mater Form*, vol. 11, no. 5, pp. 593–605, 2018, doi: 10.1007/s12289-017-1368-1.

[62] H. Kong, A. P. Mouritz, and R. Paton, “Tensile extension properties and deformation mechanisms of multiaxial non-crimp fabrics,” *Composite Structures*, vol. 66, 1-4, pp. 249–259, 2004, doi: 10.1016/j.compstruct.2004.04.046.

[63] P. Boisse, N. Hamila, and A. Madeo, “Modelling the development of defects during composite reinforcements and prepreg forming,” *Philosophical transactions. Series A, Mathematical, physical, and engineering sciences*, vol. 374, no. 2071, p. 20150269, 2016, doi: 10.1098/rsta.2015.0269.

[64] E. de Bilbao, D. Soulat, G. Hivet, and A. Gasser, “Experimental Study of Bending Behaviour of Reinforcements,” *Exp Mech*, vol. 50, no. 3, pp. 333–351, 2010, doi: 10.1007/s11340-009-9234-9.

[65] T. Gereke, O. Döbrich, M. Hübner, and C. Cherif, “Experimental and computational composite textile reinforcement forming: A review,” *Composites Part A: Applied Science and Manufacturing*, vol. 46, pp. 1–10, 2013, doi: 10.1016/j.compositesa.2012.10.004.

[66] T. K. Ghosh and N. Zhou, “Characterization of fabric bending behavior: A review of measurement principles,” 2003.

[67] K. Potter, B. Khan, M. Wisnom, T. Bell, and J. Stevens, “Variability, fibre waviness and misalignment in the determination of the properties of composite materials and structures,” *Composites Part A: Applied Science and Manufacturing*, vol. 39, no. 9, pp. 1343–1354, 2008, doi: 10.1016/j.compositesa.2008.04.016.

[68] S.V. Lomov, E.B. Belov, T. Bischoff, S.B. Ghosh, T. Truong Chi, and I. Verpoest, “Carbon composites based on multiaxial multiply stitched preforms. Part 1. Geometry of the preform,” *Composites Part A: Applied Science and Manufacturing*, vol. 33, no. 9, pp. 1171–1183, 2002, doi: 10.1016/S1359-835X(02)00090-8.

[69] M. Schneider, “Automated analysis of defects in non-crimp fabrics for composites,” in *Non-Crimp Fabric Composites*: Elsevier, 2011, pp. 103–114.

[70] R. Loendersloot, S. V. Lomov, R. Akkerman, and I. Verpoest, “Carbon composites based on multiaxial multiply stitched preforms. Part V: geometry of sheared biaxial fabrics,” *Composites Part A: Applied Science and Manufacturing*, vol. 37, no. 1, pp. 103–113, 2006, doi: 10.1016/j.compositesa.2005.04.013.

[71] Jones, *Mechanics of composite materials,* 2nd ed. New York, London: Brunner-Routledge, 1999.

[72] F. Dumont, C. Weimer, D. Soulat, J. Launay, S. Chatel, and S. Maison-Le-Poec, “Composites Preforms Simulations for Helicopters Parts,” *Int J Mater Form*, vol. 1, S1, pp. 847–850, 2008, doi: 10.1007/s12289-008-0268-9.

[73] *DIN SPEC 8100:2015-11, Textilien_- Verstärkungstextilien_- Automatische Prüfung der Drapierbarkeit an Gelegen und Geweben für endlosfaserverstärkte Werkstoffe; Text Deutsch und Englisch*, Berlin.

[74] N. Schur, “Drapieren und Handhaben von unidirektionalen Faserhalbzeugen in einer automatisierten Prozesskette zur Herstellung komplexer Preforms,” Doctoral dissertation, University of Stuttgart, Stuttgart.

[75] H. Ali, S. Noor, S. Huiqi, J. Jinhua, and C. Nanliang, “Characterization and analysis of wrinkling behavior of glass warp knitted non-crimp fabrics based on double-dome draping geometry,” *Journal of Engineered Fibers and Fabrics*, vol. 15, 155892502095852, 2020, doi: 10.1177/1558925020958521.

[76] W. Wu, B. Jiang, L. Xie, F. Klunker, S. Aranda, and G. Ziegmann, “Effect of Compaction and Preforming Parameters on the Compaction Behavior of Bindered Textile Preforms for Automated Composite Manufacturing,” *Appl Compos Mater*, vol. 20, no. 5, pp. 907–926, 2013, doi: 10.1007/s10443-012-9308-1.

[77] J. S. Lee, S. J. Hong, W.-R. Yu, and T. J. Kang, “The effect of blank holder force on the stamp forming behavior of non-crimp fabric with a chain stitch,” *Composites Science and Technology*, vol. 67, 3-4, pp. 357–366, 2007, doi: 10.1016/j.compscitech.2006.09.009.

[78] A. Schug, J. Winkelbauer, R. Hinterhölzl, and K. Drechsler, “Thermoforming of glass fibre reinforced polypropylene: A study on the influence of different process parameters,” in *ESAFORM 2017*, p. 30010.

[79] K. Tanaka, R. Ushiyama, T. Katayama, S. Enoki, and H. Sakamoto, “Formability evaluation of carbon fiber NCF by a non-contact 3D strain measurement system and the effects of blank folder force on its formability,” in Ostend, Belgium, 2014, pp. 317–326.

[80] S. Chen *et al.,* “Double diaphragm forming simulation for complex composite structures,” *Composites Part A: Applied Science and Manufacturing*, vol. 95, pp. 346–358, 2017, doi: 10.1016/j.compositesa.2017.01.017.

[81] S. Chen, A. Endruweit, L. T. Harper, and N. A. Warrior, “Inter-ply stitching optimisation of highly drapeable multi-ply preforms,” *Composites Part A: Applied Science and Manufacturing*, vol. 71, pp. 144–156, 2015, doi: 10.1016/j.compositesa.2015.01.016.

[82] F. T. Peirce, “26—THE “HANDLE” OF CLOTH AS A MEASURABLE QUANTITY,” *Journal of the Textile Institute Transactions*, vol. 21, no. 9, T377-T416, 1930, doi: 10.1080/19447023008661529.

[83] *DIN 53362:2003-10, Prüfung von Kunststoff-Folien und von textilen Flächengebilden (außer Vliesstoffe), mit oder ohne Deckschicht aus Kunststoff_- Bestimmung der Biegesteifigkeit_- Verfahren nach Cantilever*, Berlin, 2003.

[84] *DIN EN 14882:2005-11, Mit Kautschuk oder Kunststoff beschichtete Textilien_- Bestimmung der Koeffizienten von Haftreibung und Bewegungsreibung; Deutsche Fassung EN_14882:2005*, Berlin.

[85] *ASTM G115-9: Guide for Measuring and Reporting Friction Coefficients,* G02 Committee, West Conshohocken, PA.

[86] L. Dong, C. Lekakou, and M.G. Bader, “Solid-mechanics finite element simulations of the draping of fabrics: a sensitivity analysis,” *Composites Part A: Applied Science and Manufacturing*, vol. 31, no. 7, pp. 639–652, 2000, doi: 10.1016/S1359-835X(00)00046-4.

[87] *ASTM D1894-01: Test Method for Static and Kinetic Coefficients of Friction of Plastic Film and Sheeting,* D20 Committee, West Conshohocken, PA.

[88] D. M. Leutz, “Forming simulation of AFP material layups: Material characterization, simulation and validation,” Dissertation, Chair of Carbon Composites, Technical University of Munich, München, 2016.

[89] D. Hermann, S. S. Ramkumar, P. Seshaiyer, and S. Parameswaran, “Frictional study of woven fabrics: The relationship between the friction and velocity of testing,” *J. Appl. Polym. Sci.*, vol. 92, no. 4, pp. 2420–2424, 2004, doi: 10.1002/app.20213.

[90] B. S. GUPTA, J. O. AJAYI, and M. KUTSENKO, “Experimental methods for analyzing friction in textiles,” in *Friction in Textile Materials*: Elsevier, 2008, pp. 174–221.

[91] A. Margossian, “Forming of tailored thermoplastic composite blanks: Material characterisation, simulation and validation,” Dissertation, Chair of Carbon Composites, Technical University of Munich, München, 2017.

[92] R. Akkerman, M. P. Ubbink, M. B. de Rooij, and R. H. W. ten Thije, “Tool-Ply Friction In Composite Forming,” in *AIP Conference Proceedings*, Zaragoza (Spain), Apr. 2007, pp. 1080–1085.

[93] A. F. Schug, “Unidirectional Fibre Reinforced Thermoplastic Composites: A Forming Study,” Doctoral dissertation, Chair of Carbon Composites, Technical University of Munich, München, 2020.

[94] P. Boisse, N. Naouar, and A. Charmetant, “Finite element analysis of composite forming at macroscopic and mesoscopic scale,” in *Advances in Composites Manufacturing and Process Design*: Elsevier, 2015, pp. 297–315.

[95] J. Launay, G. Hivet, A. V. Duong, and P. Boisse, “Experimental analysis of the influence of tensions on in plane shear behaviour of woven composite reinforcements,” *Composites Science and Technology*, vol. 68, no. 2, pp. 506–515, 2008, doi: 10.1016/j.compscitech.2007.06.021.

[96] J. Cao *et al.,* “Characterization of mechanical behavior of woven fabrics: Experimental methods and benchmark results,” *Composites Part A: Applied Science and Manufacturing*, vol. 39, no. 6, pp. 1037–1053, 2008, doi: 10.1016/j.compositesa.2008.02.016.

[97] G.B. McGuinness and C.M. ÓBrádaigh, “Development of rheological models for forming flows and picture-frame shear testing of fabric reinforced thermoplastic

sheets," *Journal of Non-Newtonian Fluid Mechanics*, vol. 73, 1-2, pp. 1–28, 1997, doi: 10.1016/S0377-0257(97)00040-2.

[98] X. Q. Peng, J. Cao, J. Chen, P. Xue, D. S. Lussier, and L. Liu, "Experimental and numerical analysis on normalization of picture frame tests for composite materials," *Composites Science and Technology*, vol. 64, no. 1, pp. 11–21, 2004, doi: 10.1016/S0266-3538(03)00202-1.

[99] F. Nosrat-Nezami, T. Gereke, C. Eberdt, and C. Cherif, "Characterisation of the shear–tension coupling of carbon-fibre fabric under controlled membrane tensions for precise simulative predictions of industrial preforming processes," *Composites Part A: Applied Science and Manufacturing*, vol. 67, pp. 131–139, 2014, doi: 10.1016/j.compositesa.2014.08.030.

[100] S. Orawattanasrikul, "Experimentelle Analyse der Scherdeformationen biaxial verstärkter Mehrlagengestricke," Doctoral thesis, Technische Universität Dresden, Dresden, Germany, 2006.

[101] L. M. Dangora, C. J. Hansen, C. J. Mitchell, J. A. Sherwood, and J. C. Parker, "Challenges associated with shear characterization of a cross-ply thermoplastic lamina using picture frame tests," *Composites Part A: Applied Science and Manufacturing*, vol. 78, pp. 181–190, 2015, doi: 10.1016/j.compositesa.2015.08.015.

[102] P. Boisse, N. Hamila, E. Guzman-Maldonado, A. Madeo, G. Hivet, and F. dell'Isola, "The bias-extension test for the analysis of in-plane shear properties of textile composite reinforcements and prepregs: a review," *Int J Mater Form*, vol. 10, no. 4, pp. 473–492, 2017, doi: 10.1007/s12289-016-1294-7.

[103] P. Harrison, M. J. Clifford, and A. C. Long, "Shear characterisation of viscous woven textile composites: A comparison between picture frame and bias extension experiments," *Composites Science and Technology*, vol. 64, 10-11, pp. 1453–1465, 2004, doi: 10.1016/j.compscitech.2003.10.015.

[104] B. Zhu, T. X. Yu, and X. M. Tao, "Large deformation and slippage mechanism of plain woven composite in bias extension," *Composites Part A: Applied Science and Manufacturing*, vol. 38, no. 8, pp. 1821–1828, 2007, doi: 10.1016/j.compositesa.2007.04.009.

[105] J. Pourtier, B. Duchamp, M. Kowalski, P. Wang, X. Legrand, and D. Soulat, "Two-way approach for deformation analysis of non-crimp fabrics in uniaxial bias extension tests based on pure and simple shear assumption," *Int J Mater Form*, vol. 61, no. 4, p. 341, 2019, doi: 10.1007/s12289-019-01481-8.

[106] *DIN EN ISO 14125:2011-05, Faserverstärkte Kunststoffe - Bestimmung der Biegeeigenschaften (ISO_14125:1998_+_Cor.1:2001_+_Amd.1:2011); Deutsche Fassung EN_ISO_14125:1998_+_AC:2002_+_A1:2011*, Berlin.

[107] L. M. Dangora, C. J. Mitchell, and J. A. Sherwood, “Predictive model for the detection of out-of-plane defects formed during textile-composite manufacture,” *Composites Part A: Applied Science and Manufacturing*, vol. 78, pp. 102–112, 2015, doi: 10.1016/j.compositesa.2015.07.011.

[108] T. G. Clapp, H. Peng, T. K. Ghosh, and J. W. Eischen, “Indirect Measurement of the Moment-Curvature Relationship for Fabrics,” *Textile Research Journal*, vol. 60, no. 9, pp. 525–533, 1990, doi: 10.1177/004051759006000906.

[109] A. Pilger, “Weiterentwicklung eines Biegeprüfstands zur Charakterisierung von Prepreg-Materialien für Luftfahrtanwendungen,” Term Project, Chair of Carbon Composites, Technical University of Munich, Munich, 2019.

[110] U. Sachs, “Friction and bending in thermoplasctic composites forming processes,” PhD Thesis, University of Twente, Enschede, 2014.

[111] J. Wang, A. C. Long, and M. J. Clifford, “Experimental measurement and predictive modelling of bending behaviour for viscous unidirectional composite materials,” *Int J Mater Form*, vol. 3, S2, pp. 1253–1266, 2010, doi: 10.1007/s12289-009-0670-y.

[112] W.-R. Yu, P. Harrison, and A. Long, “Finite element forming simulation for non-crimp fabrics using a non-orthogonal constitutive equation,” *Composites Part A: Applied Science and Manufacturing*, vol. 36, no. 8, pp. 1079–1093, 2005, doi: 10.1016/j.compositesa.2005.01.007.

[113] S. Bel, N. Hamila, P. Boisse, and F. Dumont, “Finite element model for NCF composite reinforcement preforming: Importance of inter-ply sliding,” *Composites Part A: Applied Science and Manufacturing*, vol. 43, no. 12, pp. 2269–2277, 2012, doi: 10.1016/j.compositesa.2012.08.005.

[114] N. Naouar, E. Vidal-Salle, J. Schneider, E. Maire, and P. Boisse, “3D composite reinforcement meso F.E. analyses based on X-ray computed tomography,” *Composite Structures*, vol. 132, pp. 1094–1104, 2015, doi: 10.1016/j.compstruct.2015.07.005.

[115] J. Sirtautas, A. K. Pickett, and P. Lépicier, “A mesoscopic model for coupled drape-infusion simulation of biaxial Non-Crimp Fabric,” *Composites Part B: Engineering*, vol. 47, pp. 48–57, 2013, doi: 10.1016/j.compositesb.2012.09.088.

[116] M. Sherburn, “Geometric and Mechanical Modelling of Textiles,” Doctoral dissertation, University of Nottingham, Nottingham, 2007. [Online]. Available: http://eprints.nottingham.ac.uk/10303/

[117] H. Lin, M. J. Clifford, A. C. Long, and M. Sherburn, “Finite element modelling of fabric shear,” *Modelling Simul. Mater. Sci. Eng.*, vol. 17, no. 1, p. 15008, 2009, doi: 10.1088/0965-0393/17/1/015008.

[118] University of Nottingham, *TexGen: Non-Crimp Fabrics.* [Online]. Available: http://texgen.sourceforge.net/index.php/Main_Page (accessed: Apr. 11 2021).

[119] KU Leuven, *WiseTex suite.* [Online]. Available: https://www.mtm.kuleuven.be/onderzoek/scalint/Composites/software/wisetex (accessed: Jan. 5 2021).

[120] D. Durville, "Microscopic approaches for understanding the mechanical behaviour of reinforcement in composites," in *Composite Reinforcements for Optimum Performance*: Elsevier, 2011, pp. 461–485.

[121] S. D. Green, A. C. Long, B.S.F. El Said, and S. R. Hallett, "Numerical modelling of 3D woven preform deformations," *Composite Structures*, vol. 108, pp. 747–756, 2014, doi: 10.1016/j.compstruct.2013.10.015.

[122] A. J. Thompson, B. El Said, J. P.-H. Belnoue, and S. R. Hallett, "Modelling process induced deformations in 0/90 non-crimp fabrics at the meso-scale," *Composites Science and Technology*, vol. 168, pp. 104–110, 2018, doi: 10.1016/j.compscitech.2018.08.029.

[123] D. Durville, "Simulation of the mechanical behaviour of woven fabrics at the scale of fibers," *Int J Mater Form*, vol. 3, S2, pp. 1241–1251, 2010, doi: 10.1007/s12289-009-0674-7.

[124] G. Zhou, X. Sun, and Y. Wang, "Multi-chain digital element analysis in textile mechanics," *Composites Science and Technology*, vol. 64, no. 2, pp. 239–244, 2004, doi: 10.1016/S0266-3538(03)00258-6.

[125] L. Huang, Y. Wang, Y. Miao, D. Swenson, Y. Ma, and C.-F. Yen, "Dynamic relaxation approach with periodic boundary conditions in determining the 3-D woven textile micro-geometry," *Composite Structures*, vol. 106, pp. 417–425, 2013, doi: 10.1016/j.compstruct.2013.05.057.

[126] C. Mack and H. M. Taylor, "39—The Fitting of Woven Cloth to Surfaces," *Journal of the Textile Institute Transactions*, vol. 47, no. 9, T477-T488, 1956, doi: 10.1080/19447027.1956.10750433.

[127] S. G. Hancock and K. D. Potter, "The use of kinematic drape modelling to inform the hand lay-up of complex composite components using woven reinforcements," *Composites Part A: Applied Science and Manufacturing*, vol. 37, no. 3, pp. 413–422, 2006, doi: 10.1016/j.compositesa.2005.05.044.

[128] A. K. Pickett, G. Creech, and P. de Luca, "Simplified and advanced simulation methods for prediction of fabric draping," *Revue Européenne des Éléments Finis*, vol. 14, 6-7, pp. 677–691, 2005, doi: 10.3166/reef.14.677-691.

[129] L. Delsart and O. Le Roy, "A fully-integrated composite part design solution," *JEC Magazine*, no. 24, 2006.

[130] M. Körber and C. Frommel, “Automated Planning and Optimization of a Draping Processes Within the CATIA Environment Using a Python Software Tool,” *Procedia Manufacturing*, vol. 38, pp. 808–815, 2019, doi: 10.1016/j.promfg.2020.01.113.

[131] C. Ward, S. Hancock, and K. Potter, “Forming Complex Shaped Components Using Drape Simulation Software: Informing Manual and Automated Production Needs,” *SAE Int. J. Aerosp.*, vol. 1, no. 1, pp. 798–810, 2009, doi: 10.4271/2008-01-2316.

[132] L. Ye and H. R. Daghyani, “Characteristics of woven fibre fabric reinforced composites in forming process,” *Composites Part A: Applied Science and Manufacturing*, vol. 28, 9-10, pp. 869–874, 1997, doi: 10.1016/S1359-835X(97)00053-5.

[133] A. C. Long and C. D. Rudd, “A Simulation of Reinforcement Deformation during the Production of Preforms for Liquid Moulding Processes,” *Proceedings of the Institution of Mechanical Engineers, Part B: Journal of Engineering Manufacture*, vol. 208, no. 4, pp. 269–278, 1994, doi: 10.1243/PIME_PROC_1994_208_088_02.

[134] C.-l. Lai and W.-b. Young, “Modeling fiber slippage during the preforming process,” *Polym. Compos.*, vol. 20, no. 4, pp. 594–603, 1999, doi: 10.1002/pc.10382.

[135] A. C. Long, B. J. Souter, F. Robitaille, and C. D. Rudd, “Effects of fibre architecture on reinforcement fabric deformation,” *Plastics, Rubber and Composites*, vol. 31, no. 2, pp. 87–97, 2002, doi: 10.1179/146580102225001391.

[136] A. C. Long, J. Wiggers, and P. Harrison, “Modelling the effect of blank-holder pressure and material variability on forming of textile preforms,” Cluj-Napoca, Romania, 27-29 April, 2005.

[137] Y. Denis, F. Morestin, and N. Hamila, “A hysteretic model for fiber-reinforced composites at finite strains: fractional derivatives, computational aspects and analysis,” *Computational Materials Science*, vol. 181, p. 109716, 2020, doi: 10.1016/j.commatsci.2020.109716.

[138] E. Guzman-Maldonado, N. Hamila, N. Naouar, G. Moulin, and P. Boisse, “Simulation of thermoplastic prepreg thermoforming based on a visco-hyperelastic model and a thermal homogenization,” *Materials & Design*, vol. 93, pp. 431–442, 2016, doi: 10.1016/j.matdes.2015.12.166.

[139] P. Boisse, N. Hamila, and A. Madeo, “The difficulties in modeling the mechanical behavior of textile composite reinforcements with standard continuum mechanics of Cauchy. Some possible remedies,” *International Journal of Solids and Structures*, vol. 154, pp. 55–65, 2018, doi: 10.1016/j.ijsolstr.2016.12.019.

[140] Dassault Systèmes / SIMULIA, *ABAQUS.* Accessed: Jan. 6 2021. [Online]. Available: https://www.3ds.com/products-services/simulia/products/abaqus/

[141] F. J. Schirmaier, D. Dörr, F. Henning, and L. Kärger, "A macroscopic approach to simulate the forming behaviour of stitched unidirectional non-crimp fabrics (UD-NCF)," *Composites Part A: Applied Science and Manufacturing*, vol. 102, pp. 322–335, 2017, doi: 10.1016/j.compositesa.2017.08.009.

[142] S. Chen, O. P. L. McGregor, A. Endruweit, L. T. Harper, and N. A. Warrior, "Simulation of the forming process for curved composite sandwich panels," *Int J Mater Form*, vol. 13, no. 6, pp. 967–980, 2020, doi: 10.1007/s12289-019-01520-4.

[143] Dassault Systèmes / SIMULIA, "ABAQUS user manual 2017: Fabric material behavior," 2017.

[144] *Software PLASFIB*, 2011.

[145] P. Wang, X. Legrand, P. Boisse, N. Hamila, and D. Soulat, "Experimental and numerical analyses of manufacturing process of a composite square box part: Comparison between textile reinforcement forming and surface 3D weaving," *Composites Part B: Engineering*, vol. 78, pp. 26–34, 2015, doi: 10.1016/j.compositesb.2015.03.072.

[146] H. Xiong, N. Hamila, and P. Boisse, "Consolidation Modeling during Thermoforming of Thermoplastic Composite Prepregs," *Materials (Basel, Switzerland)*, vol. 12, no. 18, 2019, doi: 10.3390/ma12182853.

[147] Q. Steer, J. Colmars, and P. Boisse, "Modeling of tricot stitch non crimp fabric in forming simulations," in Vitoria-Gasteiz, Spain, 2019, p. 20004.

[148] ESI Group, "PAM-COMPOSITES 2016.5, PAM-FORM User's Guide," 2016.

[149] J.-I. Kim, Y.-T. Hwang, K.-H. Choi, H.-J. Kim, and H.-S. Kim, "Prediction of the vacuum assisted resin transfer molding (VARTM) process considering the directional permeability of sheared woven fabric," *Composite Structures*, vol. 211, pp. 236–243, 2019, doi: 10.1016/j.compstruct.2018.12.043.

[150] J. Wollmann *et al.,* "Virtual and experimental analysis of a continuous 3D hybrid metal-composite process for automotive applications," *Advanced Metal Forming Processes in Automotive Industry (AutoMetForm 2016), Wroclaw, Poland.*, 2016.

[151] B. Kaiser, T. Pyttel, and F. Duddeck, "A generalised method for the coupling of a parallelogram-like unit cell with a macroscopic finite element to simulate the behaviour of textiles," *Int J Mater Form*, vol. 64, no. 1, p. 21, 2019, doi: 10.1007/s12289-019-01472-9.

[152] R.H.W. ten Thije, R. Akkerman, and J. Huétink, “Large deformation simulation of anisotropic material using an updated Lagrangian finite element method,” *Computer Methods in Applied Mechanics and Engineering*, vol. 196, 33-34, pp. 3141–3150, 2007, doi: 10.1016/j.cma.2007.02.010.

[153] AniForm Engineering B.V., *AniForm Virtual Forming.* Accessed: Jan. 6 2021. [Online]. Available: https://aniform.com/features

[154] B. Eck, “Composites forming simulations in LS-Dyna using the material law 249,” 10-12 October, 2016.

[155] D. Dörr *et al.,* “A Benchmark Study of Finite Element Codes for Forming Simulation of Thermoplastic UD-Tapes,” *Procedia CIRP*, vol. 66, pp. 101–106, 2017, doi: 10.1016/j.procir.2017.03.223.

[156] M. Q. Pham, O. Döbrich, W. Trümper, T. Gereke, and C. Cherif, “Numerical Modelling of the Mechanical Behaviour of Biaxial Weft-Knitted Fabrics on Different Length Scales,” *Materials (Basel, Switzerland)*, vol. 12, no. 22, 2019, doi: 10.3390/ma12223693.

[157] M. Q. Pham, O. Döbrich, J. Mersch, T. Gereke, and C. Cherif, “Meso-scale model for the forming process of biaxial reinforced weft-knitted fabrics,” *IOP Conf. Ser.: Mater. Sci. Eng.*, vol. 406, p. 12026, 2018, doi: 10.1088/1757-899X/406/1/012026.

[158] O. Vorobiov, T. Bischoff, and A. Tulke, “Micro-meso draping modelling of non-crimp fabrics,” *10th European LS-DYNA Conference 2015, Würzburg, Germany*.

[159] D. Durville, I. Baydoun, H. Moustacas, G. Périé, and Y. Wielhorski, “Determining the initial configuration and characterizing the mechanical properties of 3D angle-interlock fabrics using finite element simulation,” *International Journal of Solids and Structures*, vol. 154, pp. 97–103, 2018, doi: 10.1016/j.ijsolstr.2017.06.026.

[160] X. Sun, A. J. Thompson, B. El Said, and S. R. Hallett, “A Comparative Study of Numerical Modelling Methods for Deformation of Dry Textile Composites,” Lyon, France, Mar. 13 2019.

[161] T. Gereke, M. Q. Pham, M. Hübner, O. Döbrich, and C. Cherif, “Discrete Finite Element Models of Textile Structures,” Lyon, France, Mar. 13 2019.

[162] J. Wiggers, “Analysis of textile deformation during preforming for liquid composite moulding,” Doctoral dissertation, University of Nottingham, Nottingham, 2007. [Online]. Available: http://eprints.nottingham.ac.uk/10414/

[163] L. Li, Y. Zhao, H.-g.-n. Vuong, Y. Chen, J. Yang, and Y. Duan, “In-plane shear investigation of biaxial carbon non-crimp fabrics with experimental tests and

finite element modeling," *Materials & Design*, vol. 63, pp. 757–765, 2014, doi: 10.1016/j.matdes.2014.07.007.

[164] N. Moustaghfir, S. El-Ghezal Jeguirim, D. Durville, S. Fontaine, and C. Wagner-Kocher, "Transverse compression behavior of textile rovings: finite element simulation and experimental study," *J Mater Sci*, vol. 48, no. 1, pp. 462–472, 2013, doi: 10.1007/s10853-012-6760-0.

[165] L. Daelemans *et al.,* "Finite element simulation of the woven geometry and mechanical behaviour of a 3D woven dry fabric under tensile and shear loading using the digital element method," *Composites Science and Technology*, vol. 137, pp. 177–187, 2016, doi: 10.1016/j.compscitech.2016.11.003.

[166] TIOBE Software BV, *TIOBE Index for January 2021: Python is TIOBE's Programming Language of 2020!* [Online]. Available: https://www.tiobe.com/tiobe-index/

[167] M. Komeili, "Multi-scale characterization and modeling of shear-tension interaction in woven fabrics for composite forming and structural applications," Dissertation, University of British Columbia, 2014.

[168] D. Dörr, T. Joppich, D. Kugele, F. Henning, and L. Kärger, "A coupled thermomechanical approach for finite element forming simulation of continuously fiber-reinforced semi-crystalline thermoplastics," *Composites Part A: Applied Science and Manufacturing*, vol. 125, p. 105508, 2019, doi: 10.1016/j.compositesa.2019.105508.

[169] W. R. Yu, M. Zampaloni, F. Pourboghrat, K. Chung, and T. J. Kang, "Analysis of flexible bending behavior of woven preform using non-orthogonal constitutive equation," *Composites Part A: Applied Science and Manufacturing*, vol. 36, no. 6, pp. 839–850, 2005, doi: 10.1016/j.compositesa.2004.10.026.

[170] *DIN EN ISO 5084:1996-10, Textilien_- Bestimmung der Dicke von Textilien und textilen Erzeugnissen (ISO_5084:1996); Deutsche Fassung EN_ISO_5084:1996*, Berlin.

[171] H. Eschenauer, N. Olhoff, and W. Schnell, *Applied Structural Mechanics: Fundamentals of Elasticity, Load-Bearing Structures, Structural Optimization,* 1st ed. Berlin: Springer, 1996.

[172] G. R. Liu and S. S. Quek, *The finite element method: A practical course*. Oxford: Elsevier Butterworth-Heinemann, 2003.

[173] ABAQUS, Inc., "ABAQUS/Explicit: Advanced Topics: Lecture 5: Quasi-Static Analyses," 2005.

[174] K. Bletzinger, *Structural Optimization I*, 2017.

[175] F. Duddeck, *Structural Optimization II*, 2018.

[176] T. Sarkar, *DOEPY: Design of Experiment Generator in Python*, 2019. [Online]. Available: https://doepy.readthedocs.io/en/latest/

[177] Dassault Systèmes / SIMULIA, "ABAQUS user manual 2017: Frictional behavior," 2017.

[178] S. Thumfart, W. Palfinger, M. Stöger, and C. Eitzinger, "Accurate Fibre Orientation Measurement for Carbon Fibre Surfaces," in *Computer Analysis of Images*, pp. 75–82.

[179] PROFACTOR GmbH, *Machine Vision in Composite Parts: FScan – measurement of fibre angles on composite parts.* [Online]. Available: https://www.profactor.at/en/solutions/machine-vision/composite-parts/ (accessed: Jan. 10 2021).

[180] S. E. Arnold, M.P.F. Sutcliffe, and W.L.A. Oram, "Experimental measurement of wrinkle formation during draping of non-crimp fabric," *Composites Part A: Applied Science and Manufacturing*, vol. 82, pp. 159–169, 2016, doi: 10.1016/j.compositesa.2015.12.011.

[181] S. Ward, W. McCarvill, and J. Tomblin, "Guidelines and Recommended Criteria for the Development of a Material Specification for Carbon Fiber/Epoxy Fabric Prepregs," National Institute for Aviation Research, May. 2007.

[182] Airbus, "Process Specification 80-T-31-2910: Manufacture of Structural Fiber-reinforced Plastic (FRP) Components, General," Jul. 2007.

[183] H. Krieger, A. Schnabel, L. Appel, and T. Gries, "Experimental Setup to Validate Textile Material Models for Drape Simulation," *KEM*, 554-557, pp. 456–464, 2013, doi: 10.4028/www.scientific.net/KEM.554-557.456.

[184] C. Krogh, J. A. Sherwood, and J. Jakobsen, "Generation of feasible gripper trajectories in automated composite draping by means of optimization," *Advanced Manufacturing: Polymer & Composites Science*, vol. 5, no. 4, pp. 234–249, 2019, doi: 10.1080/20550340.2019.1699691.

[185] H. M. Hsiao and I. M. Daniel, "Effect of fiber waviness on stiffness and strength reduction of unidirectional composites under compressive loading," *Composites Science and Technology*, vol. 56, no. 5, pp. 581–593, 1996, doi: 10.1016/0266-3538(96)00045-0.

[186] K. Potter, "Manufacturing defects as a cause of failure in polymer matrix composites," in *Failure Mechanisms in Polymer Matrix Composites*: Elsevier, 2012, pp. 26–52.

[187] T. A. Bogetti and J. W. Gillespie, "Process-Induced Stress and Deformation in Thick-Section Thermoset Composite Laminates," *Journal of Composite Materials*, vol. 26, no. 5, pp. 626–660, 2016, doi: 10.1177/002199839202600502.

[188] S. Mukhopadhyay, M. I. Jones, and S. R. Hallett, “Compressive failure of laminates containing an embedded wrinkle; experimental and numerical study,” *Composites Part A: Applied Science and Manufacturing*, vol. 73, pp. 132–142, 2015, doi: 10.1016/j.compositesa.2015.03.012.

[189] M. Thor *et al.,* “Numerical and experimental investigation of out-of-plane fiber waviness on the mechanical properties of composite materials,” *Int J Mater Form*, 2020, doi: 10.1007/s12289-020-01540-5.

[190] M. Dickert and G. Ziegmann, “Influence of binder on the mechanical properties and the permeability of a non-crimp carbon fabric preform,” *ECCM15 - 15TH EUROPEAN CONFERENCE ON COMPOSITE MATERIALS, Venice, Italy, 24-28 June 2012*.

[191] M. Thor, M. G. R. Sause, and R. M. Hinterhölzl, “Mechanisms of Origin and Classification of Out-of-Plane Fiber Waviness in Composite Materials—A Review,” *J. Compos. Sci.*, vol. 4, no. 3, p. 130, 2020, doi: 10.3390/jcs4030130.

[192] P. Hallander, J. Sjölander, and M. Åkermo, “Forming induced wrinkling of composite laminates with mixed ply material properties; an experimental study,” *Composites Part A: Applied Science and Manufacturing*, vol. 78, pp. 234–245, 2015, doi: 10.1016/j.compositesa.2015.08.025.

[193] D. Dörr, “Sensitivity of material properties on wrinkling behavior and fiber reorientation of thermoplastic UD-Tape laminates during forming analyzed by Finite Element forming simulation,” *ECCM17 - 17th European Conference on Composite Materials Munich, Germany, 26-30th June 2016*.

[194] ESI Group, “Composites Simulation Solution 2015.5: Release Notes & Installation Guide,” 2015.

[195] D. Dörr, T. Joppich, F. Schirmaier, T. Mosthaf, L. Kärger, and F. Henning, “A method for validation of finite element forming simulation on basis of a pointwise comparison of distance and curvature,” in Nantes, France, 2016, p. 170011.

[196] A. Iwata, T. Inoue, N. Naouar, P. Boisse, and S. V. Lomov, “Coupled meso-macro simulation of woven fabric local deformation during draping,” *Composites Part A: Applied Science and Manufacturing*, vol. 118, pp. 267–280, 2019, doi: 10.1016/j.compositesa.2019.01.004.

[197] P. Virtanen *et al.,* “SciPy 1.0: fundamental algorithms for scientific computing in Python,” *Nature methods*, vol. 17, no. 3, pp. 261–272, 2020, doi: 10.1038/s41592-019-0686-2.

[198] B. Zouari, J.-L. Daniel, and P. Boisse, “A woven reinforcement forming simulation method. Influence of the shear stiffness,” *Computers & Structures*, vol. 84, 5-6, pp. 351–363, 2006, doi: 10.1016/j.compstruc.2005.09.031.

[199] C. M. Eisenhauer and K. Drechsler, “Integration of excess material into a semi-finished product to form complex composite parts,” *Textile Research Journal*, vol. 87, no. 19, pp. 2420–2431, 2016, doi: 10.1177/0040517516671119.

[200] Dassault Systèmes / SIMULIA, “ABAQUS user manual 2017: Contact constraint enforcement methods in Abaqus/Explicit,” 2017.

[201] C. Cherif, Ed., *Textile materials for lightweight constructions: Technologies - methods - materials - properties*. Heidelberg: Springer, 2016. [Online]. Available: http://search.ebscohost.com/login.aspx?direct=true&scope=site&db=nlebk&AN=1051787

[202] T. N. Hans, “Finite Element Simulation of the braiding process,” Doctoral dissertation, Chair of Carbon Composites, Technical University of Munich, München.

[203] T. Hans, J. Cichosz, M. Brand, and R. Hinterhölzl, “Finite element simulation of the braiding process for arbitrary mandrel shapes,” *Composites Part A: Applied Science and Manufacturing*, vol. 77, pp. 124–132, 2015, doi: 10.1016/j.compositesa.2015.06.003.

[204] E. Vidal-Sallé and F. Massi, “Friction Measurement on Dry Fabric for Forming Simulation of Composite Reinforcement,” *KEM*, 504-506, pp. 319–324, 2012, doi: 10.4028/www.scientific.net/KEM.504-506.319.

[205] B. Cornelissen, B. Rietman, and R. Akkerman, “Frictional behaviour of high performance fibrous tows: Friction experiments,” *Composites Part A: Applied Science and Manufacturing*, vol. 44, pp. 95–104, 2013, doi: 10.1016/j.compositesa.2012.08.024.

[206] J. Wiggers, A. C. Long, P. Harrison, and C. D. Rudd, “The effects of stitch architecture on the shear compliance of non-crimp fabrics,” *Proceedings of sixth ESAFORM Conference on Material Forming*, pp. 851–854, 2003.

[207] D. Vernon, *Machine vision: Automated visual inspection and robot vision*. New York: Prentice Hall, 1991.

[208] D. Bublitz, M. Angstl, M. Hartmann, and K. Drechsler, “Implementation of a viscoelastic material model to predict the compaction response of dry carbon fiber preforms,” in *SICOMP Conference, Trollhättan, Sweden; 2019*.

[209] D. May *et al.,* “In-plane permeability characterization of engineering textiles based on radial flow experiments: A benchmark exercise,” *Composites Part A: Applied Science and Manufacturing*, vol. 121, pp. 100–114, 2019, doi: 10.1016/j.compositesa.2019.03.006.

[210] M. A. Ali, R. Umer, K. A. Khan, and W. J. Cantwell, “Application of X-ray computed tomography for the virtual permeability prediction of fiber reinforcements for liquid composite molding processes: A review,” *Composites Science*

and Technology, vol. 184, p. 107828, 2019, doi: 10.1016/j.compscitech.2019.107828.

[211] I. Straumit, C. Hahn, E. Winterstein, B. Plank, S. V. Lomov, and M. Wevers, "Computation of permeability of a non-crimp carbon textile reinforcement based on X-ray computed tomography images," *Composites Part A: Applied Science and Manufacturing*, vol. 81, pp. 289–295, 2016, doi: 10.1016/j.compositesa.2015.11.025.

A Appendix

a Definition of the ROIs for the comparison of the fiber orientation

The validation of the forming simulation approach presented in chapter 3 was performed using various criteria. In this appendix, the ROIs defined to compare the fiber orientation at the surface of the textile samples with the simulation results are presented. Fig. A-1 gives a detailed overview of the ROIs and their respective coordinates are listed in Tab. A-1.

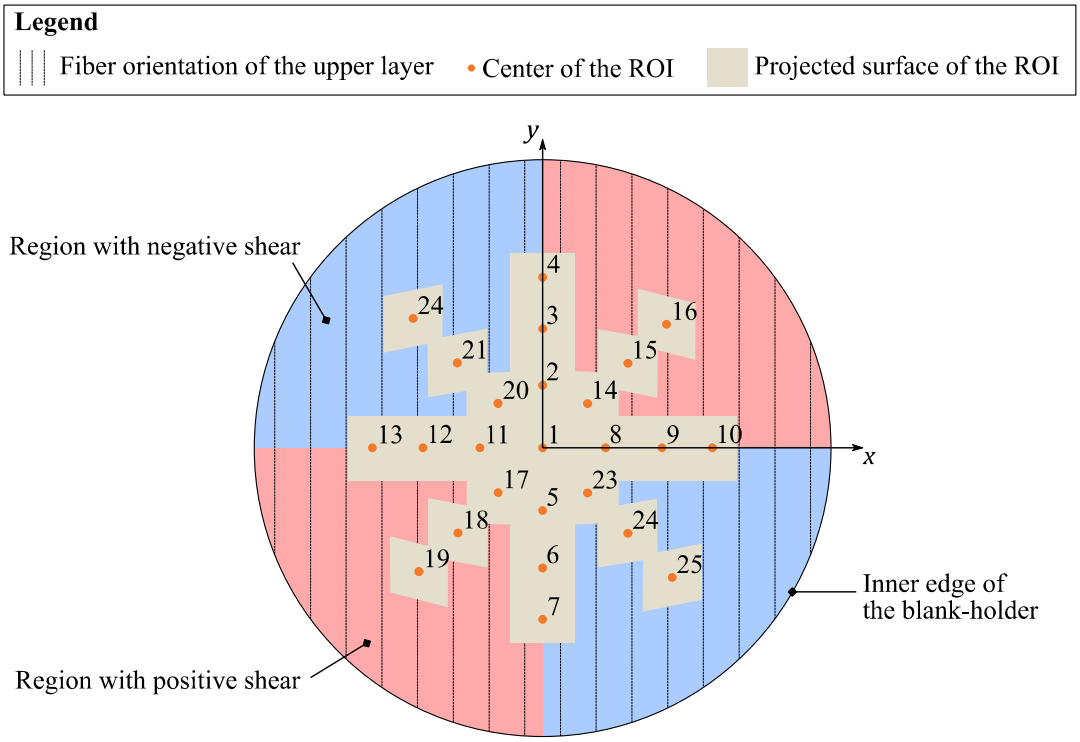

Fig. A-1: **Identification of the ROIs for the comparison of the fiber orientation at the surface of the textile samples from the forming experiments.**

Tab. A-1: Coordinates of the ROIs

Label of the ROI	x-coordinate [mm]	y-coordinate [mm]
1	0.0	0.0
2	0.0	19.5
3	0.0	37.2
4	0.0	52.9
5	0.0	-19.5
6	0.0	-37.2
7	0.0	-52.9
8	19.5	0.0
9	37.2	0.0
10	53.0	0.0
11	-19.5	0.0
12	-37.2	0.0
13	-53.0	0.0
14	13.9	13.9
15	26.4	26.4
16	40.3	40.3
17	-13.9	-13.9
18	-26.4	-26.4
19	-40.3	-40.3
20	-13.9	-13.9
21	-26.4	-26.4
22	-38.5	-38.5
23	13.9	13.9
24	26.4	26.4
25	38.5	38.5

b *FABRIC material card of the ±45° NCF

The *FABRIC material card, resulting from the material calibration of the ±45° NCF presented in chapter 3, is detailed here. For better clarity, the input parameters of the shear behavior are reduced to twenty data points for each shear direction.

```
*Material, name=Material-Fabric
*Density
4.84e-08,
*Damping, beta=3e-06
*Fabric, stress free initial slack=yes
*Uniaxial, Component=1
*Loading data, regularize=off, type=elastic, direction=compression
0.000E+00, 0.000E+00
7.958E-02, 3.934E-03
2.436E-01, 1.813E-01
1.638E+03, 1.000E+00
*Loading data, regularize=off, type=elastic, direction=tension
0.00E+00, 0.00E+00
2.00E+03, 1.00E+00
*Uniaxial, Component=2
*Loading data, regularize=off, type=elastic, direction=compression
0.000E+00, 0.000E+00
7.958E-02, 3.934E-03
2.436E-01, 1.813E-01
1.638E+03, 1.000E+00
*Loading data, regularize=off, type=elastic, direction=tension
0.00E+00, 0.00E+00
2.00E+03, 1.00E+00
*Uniaxial, Component=Shear
*Loading data, regularize=off, direction=compression
0.00E+00,0.00E+00
8.22E-03,3.35E-03
1.60E-02,1.01E-02
2.02E-02,1.68E-02
2.30E-02,2.36E-02
2.54E-02,3.38E-02
2.70E-02,4.40E-02
2.91E-02,6.47E-02
3.11E-02,8.56E-02
```

```
3.30E-02,1.07E-01
3.46E-02,1.28E-01
3.61E-02,1.50E-01
3.68E-02,1.79E-01
3.59E-02,2.32E-01
3.45E-02,2.86E-01
3.29E-02,3.43E-01
3.07E-02,4.01E-01
2.87E-02,4.63E-01
2.77E-02,5.28E-01
2.62E-02,6.38E-01
2.53E-02,7.61E-01
2.65E-02,8.91E-01
*Loading data, regularize=off, direction=tension
0.00,0.00
1.02E-02,3.35E-03
2.01E-02,1.01E-02
2.61E-02,1.68E-02
3.10E-02,2.36E-02
3.77E-02,3.38E-02
4.53E-02,4.40E-02
6.47E-02,6.47E-02
8.36E-02,8.56E-02
9.93E-02,1.07E-01
1.11E-01,1.28E-01
1.18E-01,1.50E-01
1.22E-01,1.79E-01
1.20E-01,2.32E-01
1.13E-01,2.86E-01
1.04E-01,3.43E-01
9.36E-02,4.01E-01
8.40E-02,4.63E-01
7.45E-02,5.28E-01
6.49E-02,6.38E-01
5.92E-02,7.61E-01
6.02E-02,8.91E-01
```

c Case study 1: shear and bending input parameters of the extreme cases

This appendix presents the shear and bending curves of the extreme sets of input parameters from case study 1 (ref. section 4.4.2). This corresponds to shear scaling factors C_{shear} of 0.1 and 2.0, and bending scaling factors $C_{bending}$ of 0.1 and 2.0.

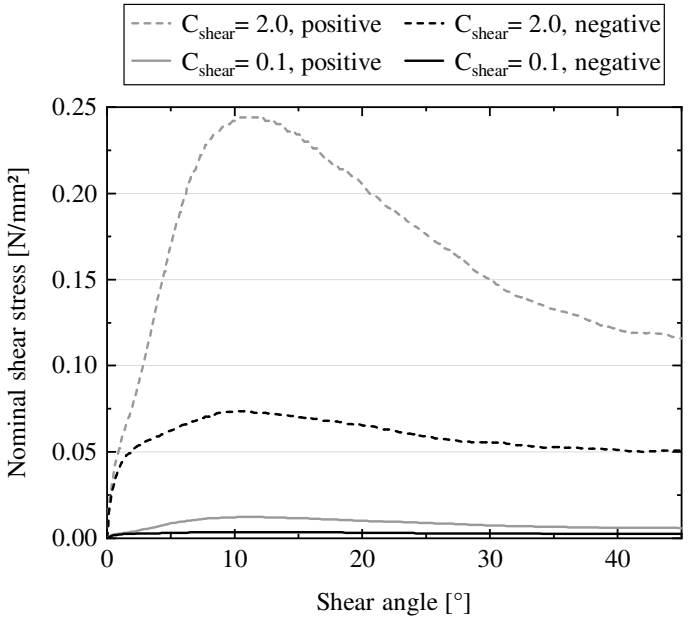

Fig. A-2: Shear input curves of the case study 1 calculated with the extreme values of the shear scaling factor C_{shear}.

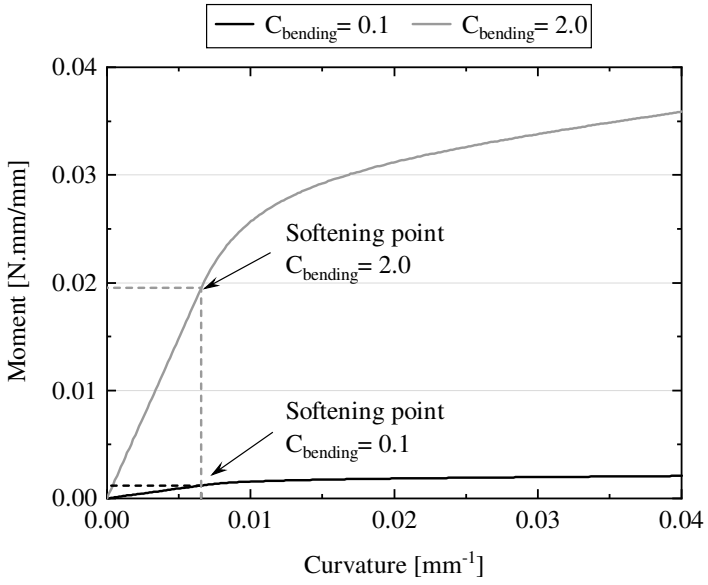

Fig. A-3: Bending-moment relationships of the case study 1 calculated with the extreme values of the bending scaling factor $C_{bending}$.

d Case study 3: bending moment-curvature relationships

This appendix presents the parameters of the four configurations illustrating the influence of the bending behavior on the forming simulation from Fig. 4-11. The bending moment-curvature relationships of these four sets of input parameters and of the reference configuration are shown in Fig. A-4. For ease of interpretation, the input parameters are listed in Tab. A-2 with the respective curvatures and normalized bending moments at each softening point.

Tab. A-2: Parameters of the BLBM model of the four configurations illustrated in Fig. 4-11.

Designation	B18	B31	B256	B269	Reference
E_{tens} [GPa]	2.00	2.00	2.00	2.00	2.00
E_{comp} [MPa]	20.2	20.2	20.2	20.2	20.2
E_{soft} [MPa]	0.406	0.406	4.69	4.69	0.925
ε_{soft} [-]	0.593E-3	7.01E-3	0.593E-3	7.01E-3	3.90E-03
κ_{soft} [m^{-1}]	0.990	11.7	0.990	11.7	10.5
M_{soft} [mN.mm/mm]	1.58	18.7	1.58	18.7	6.56

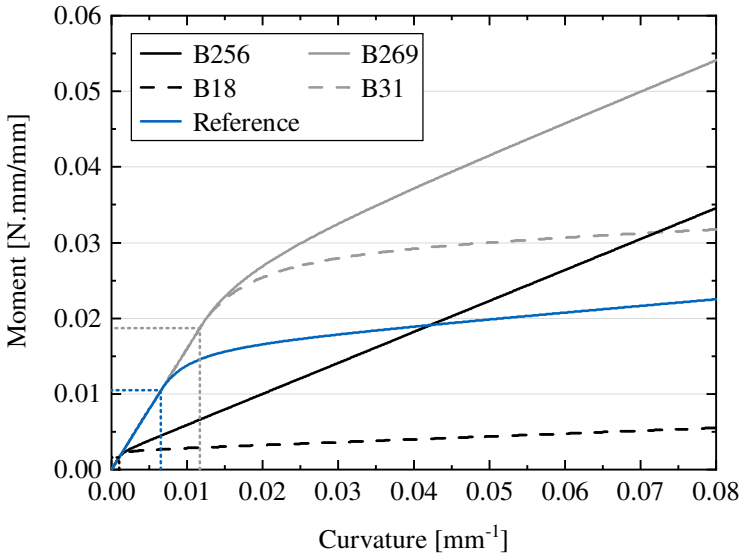

Fig. A-4: Bending moment-curvature relationships of the four sets of input parameters used in section 4.4.4 and of the reference configuration (resulting from the calibration presented in chapter 3).

e Influence of the RVE size on the virtual material thickness

The numerical description of the NCFs at the scale of the filaments introduced in chapter 5 reduces the textile geometry to RVEs. The size of the RVEs is based on the periodic repetition of the stitching pattern of the textiles. In order to investigate the influence of the RVE size on the thickness of the numerical "as-manufactured" geometry, virtual compaction experiments were performed. Note that the thickness of the textile is defined in this doctoral thesis as the gap between two parallel and rigid plates when a compaction pressure of 1.0 kPa is applied. The area of the RVE is increased until it equals the area of the platens used in the experiments (i.e. 491 mm²). The configurations used for this study are listed in Tab. A-3. Moreover, the input parameters for both textiles are summarized in Tab. A-4. The simulations are performed five times for each RVE size since the stochastic distribution of the chain orientation introduces variability in the thickness of the virtual textiles.

The resulting thicknesses depending on the RVE size are illustrated in Fig. A-5. Firstly, it can be observed that the RVE size of the 0°/90°NCF has no significant influence on the thickness. Only the scatter of the results changes (reduction of the scattering for simulations with large RVEs). Note that the difference between the maximum and minimum thicknesses of the 1x1 RVE corresponds to 6.7% of the mean value, which is comparable with that of the experimental results (5.6%, see section 5.4.1).

Secondly, a convergence of the thickness is noticed in the simulation results of the ±45° NCF for RVE areas greater than 89.4 mm² (i.e. larger than 2x2 RVEs, see Fig. A-5b). A reduction of the scatter is also observed with increasing RVE size. For the 2x2 RVE, the maximum difference between the results equals 7.4% of the mean value, which is smaller than the scattering of the experimental results.

Tab. A-3: RVE configurations used to investigate the influence of the RVE size on the virtual textile thickness.

0°/90° NCF		**±45° NCF**	
Repetitions ($r_W \times r_L$)	**Area [mm²]**	**Repetitions ($r_W \times r_L$)**	**Area [mm²]**
1x1	56.9	1x1	22.4
1x2	114	2x2	89.4
2x2	228	3x3	201
2x4	455	4x4	358
		5x5	559

Based on these observations and in order to reduce the computing time, the 1x1 RVE is identified as the optimal configuration for the virtual thickness measurement of the 0°/90° NCF. Similarly, 2x2 RVEs are recommended for the ±45° NCF.

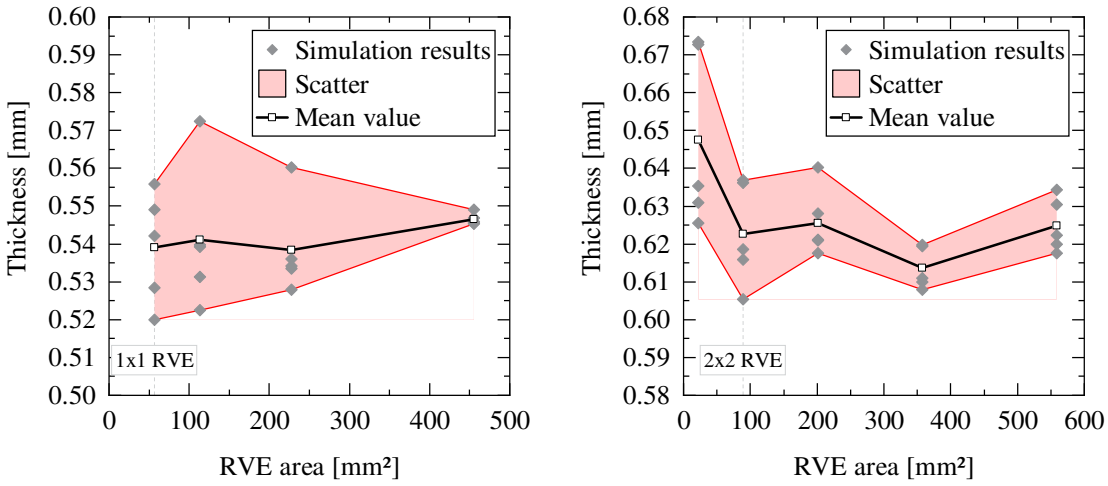

Fig. A-5: **Thickness at 1.0 kPa of the 0°/90° NCF (a) and ±45° NCF (b) depending on the area of the RVE.**

Tab. A-4: **Input parameters of the simulation for the investigation of the influence of the RVE size on the textile thickness.**

		0°/90° NCF	**±45° NCF**
Filaments	Young's modulus [GPa]	120	127.5
	Density [g/cm³]	0.905	0.890
	Diameter [µm]	69	69
	Packing coefficient [-]	0.83	0.83
	Mesh length [mm]	0.2	0.2
Fibrous layers	Layer thickness before stitching [mm]	0.20	0.21
	Standard deviation for the sampling [°]	1.15 (0°-layer)	2.0 (+45°-layer)
		4.0 (90°-layer)	2.0 (-45°-layer)
Stitching yarn	Young's Modulus [GPa]	1.81	1.81
	Density [g/cm³]	1.25	1.25
	Diameter of the chains [µm]	88	71
	Mesh length [mm]	0.1	0.1
	Magnitude pretension [%]	16	17
	Stitching pattern	Tricot-chain	Tricot
	Stitch gauge [mm]	5.08	5.08
	Stitch length [mm]	2.8	2.2

f Results of the sensitivity analysis of the virtual thickness measurement

The parametric investigation of the virtual textile thickness is performed depending on the parameters φ_{layer} and φ_{chain}. A full factorial design matrix with five levels for each parameter was determined. The resulting configurations are listed in Tab. A-5 for the 0°/90° and ±45° NCFs. The simulations were performed five times for each configuration of each material. The results are illustrated in Fig. A-6 and Fig. A-7, in which the set of design parameters are identified using their respective identification numbers.

Tab. A-5: Detail of the configurations for the parametric analysis of the virtual thickness.

	0°/90° NCF		**±45° NCF**	
Configuration ID	φ_{layer} **[-]**	φ_{chain} **[-]**	φ_{layer} **[-]**	φ_{chain} **[-]**
0	0.15	0.4	0.3	0.5
1	0.175	0.4	0.375	0.5
2	0.2	0.4	0.45	0.5
3	0.225	0.4	0.525	0.5
4	0.25	0.4	0.6	0.5
5	0.15	0.52675	0.3	0.60175
6	0.175	0.52675	0.375	0.60175
7	0.2	0.52675	0.45	0.60175
8	0.225	0.52675	0.525	0.60175
9	0.25	0.52675	0.6	0.60175
10	0.15	0.6535	0.3	0.7035
11	0.175	0.6535	0.375	0.7035
12	0.2	0.6535	0.45	0.7035
13	0.225	0.6535	0.525	0.7035
14	0.25	0.6535	0.6	0.7035
15	0.15	0.78025	0.3	0.80525
16	0.175	0.78025	0.375	0.80525
17	0.2	0.78025	0.45	0.80525
18	0.225	0.78025	0.525	0.80525
19	0.25	0.78025	0.6	0.80525
20	0.15	0.907	0.3	0.907
21	0.175	0.907	0.375	0.907
22	0.2	0.907	0.45	0.907
23	0.225	0.907	0.525	0.907
24	0.25	0.907	0.6	0.907

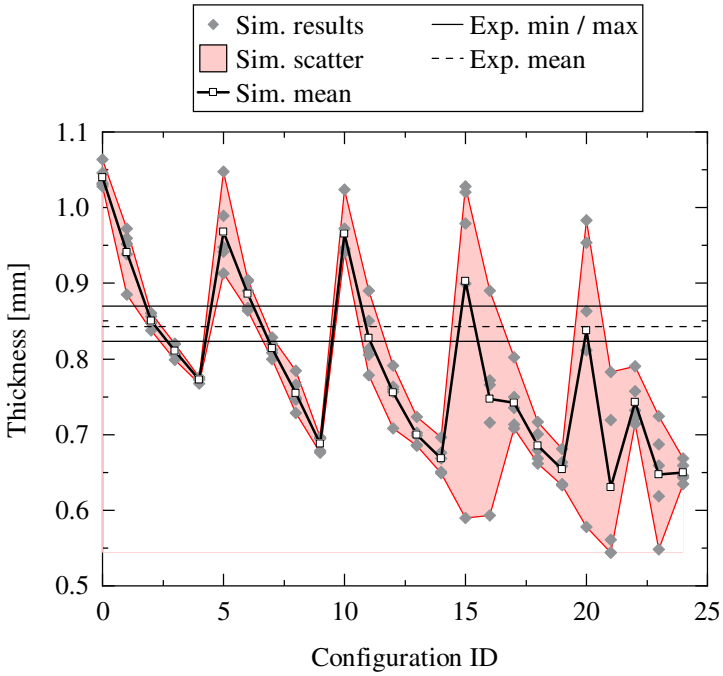

Fig. A-6: **Results of the virtual thickness measurements for each repetition and configuration of the 0°/90°NCF listed in Tab. A-5.**

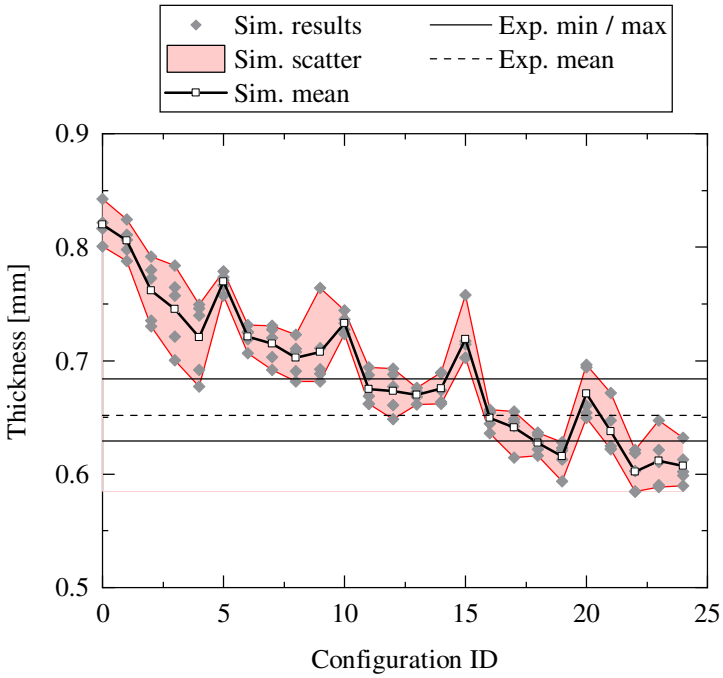

Fig. A-7: **Results of the virtual thickness measurement for each repetition and configuration of the ±45°NCF listed in Tab. A-5.**

g Virtual shear deformation of NCFs with 0° and 90°-layers

In the case of NCFs exclusively constituted of 0° and 90°-layers, the boundaries of the RVE align with the layer orientations. Therefore, the deformation of the RVE shown in Fig. A-8 corresponds to the usual definitions of the shear deformations. Note that a simple shear deformation is applied to the RVE in order to reduce the kinetic energy of the model.

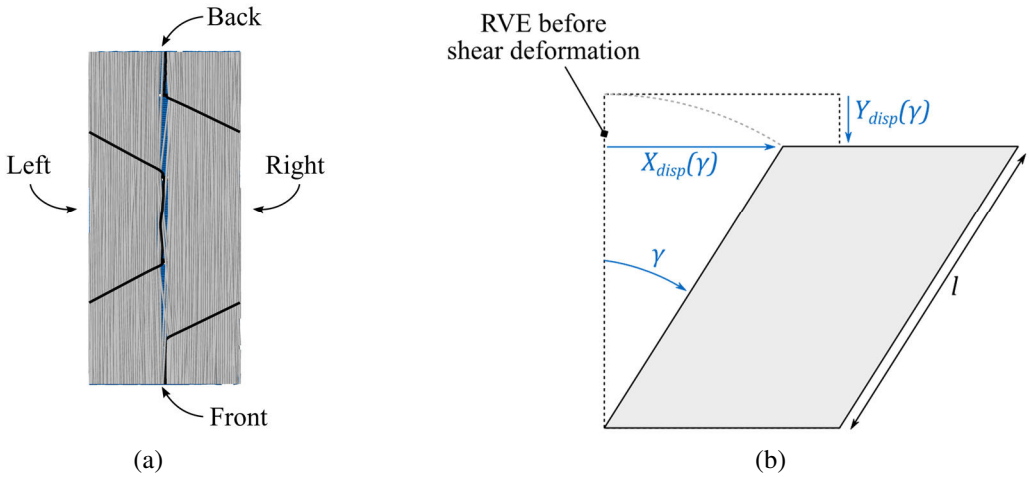

Fig. A-8: Identification of the RVE boundaries (a), as well as x and y deformations of the back face of a NCF with 0° and 90°-layers for an applied shear angle γ.

As a result, the front boundary of the RVE remains fixed, the left and right boundaries are rotating, whereas the back boundary is translating. The displacements of the back boundary of the RVE in x and y directions are related to the shear angle γ as follows:

$$X_{disp}(\gamma) = l \sin(\gamma) \; ; \tag{A-1}$$

$$Y_{disp}(\gamma) = l(1 - \cos(\gamma)) \tag{A-2}$$

The shear deformation is applied to the back boundary of the RVE using the reference points of the regular mesh of the RVE. To that purpose, the displacement $u_{Shear,back}$ of a dummy node is included in the equations of the periodic boundary conditions:

$$u_{RP,back} = u_{RP,front} + u_{Shear,back} \tag{A-3}$$

where the subscripts “front” and “back” correspond to the front and back boundaries of the RVE, respectively.

Constraints are applied to the RPs of the left boundary in order to ensure a displacement of the RPs along the rotated boundary of the RVE. This can be done using kinematic couplings available in ABAQUS. Periodic displacements between the RPs of the right and lefts boundaries ensure a mesoscopic periodicity of the fibrous mat.

h Identification procedure of non-realistic results of the virtual shear characterization

The method developed to model NCFs at the microscopic scale uses a stochastic process to sample the orientations of the digital chains. Due to the high stiffness of the digital chains, deviations of the chain orientation from the theoretical path can result in high tensile stresses and in a significant increase of the shear force. Even though this variability can be observed experimentally, it is considered that a small number of DCEs should not influence the behavior of the whole RVE. As a consequence, a method was developed to identify non-representative simulation results.

In the case of a 1x1 RVE with reference parameters (listed in Tab. 5-7), the virtual descriptions of the ±45° NCFs are constituted of 224 digital chains. It is considered that a virtual shear test result is representative if the high tensile stresses are located at least in more than one digital chain (i.e. in more than 0.5% of the elements). The simulation result is accepted if the tensile stress in more than 0.5% of the elements is above a threshold set to 10% of the maximum tensile stress. This means that the ratio between the 99.5th percentile and the maximum stress in the model must be greater than 0.1.

This identification procedure also applies for simulations with larger RVEs.

Two cases are illustrated in Fig. A-9 to highlight the results of the identification procedure. The result shown in Fig. A-9a has a high ratio, showing that the high tensile stresses of the model are achieved in a large number of chains. On the contrary, Fig. A-9b shows a simulation result in which high tensile stresses are only located in one chain (i.e. in less than 0.5% of the model).

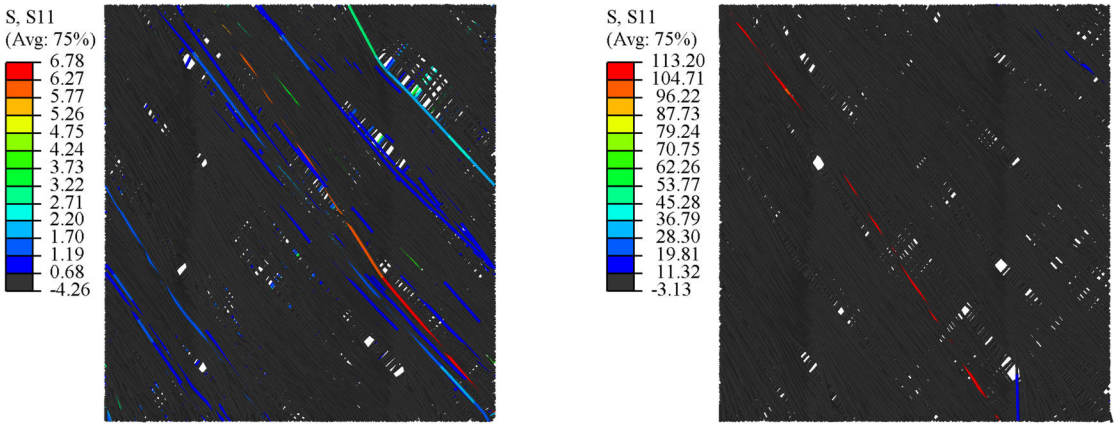

Ratio = 0.45
Simulation result accepted

Ratio = 0.09
Simulation result rejected

Fig. A-9: Examples of tensile stresses during virtual shear characterization and ratios between the 99.5th percentile and the maximum tensile stress in the respective models.
Elements with tensile stresses lower than 10% of the maximum tensile stress are colored black.

Due to the lack of bending rigidity of numerical chains modeled with truss elements, spurious deformations of small chains can be observed at the corner of the model. The high stresses induced in the elements result in non-realistic energies and invalidate the simulation results. Since the high stresses are only located in a few elements, the selection procedure described above is able to identify these spurious effects. In the case illustrated in Fig. A-10, the ratio between the 99.5th percentile and the maximum tensile stress is calculated at 0.03, which is significantly smaller than the threshold.

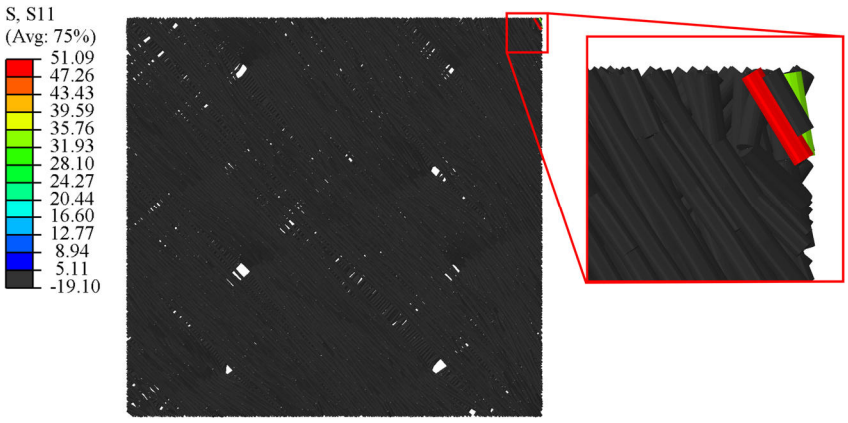

Fig. A-10: Example of spurious localized stresses at the corner of a simulation result during virtual shear characterization.
Elements with tensile stresses smaller than 10% of the maximum tensile stress are colored black.

B Publications

Scientific journal papers

[P1] D. Colin, S. Bel, T. Hans, M. Hartmann, and K. Drechsler, "Virtual Description of Non-Crimp Fabrics at the Scale of Filaments Including Orientation Variability in the Fibrous Layers," *Appl Compos Mater*, vol. 27, no. 4, pp. 337–355, 2020, doi: 10.1007/s10443-020-09819-1.

[P2] K. Heller, M. Hallmannseder, D. Colin, K. Kind, and K. Drechsler, "Comparing Test Methods for the Intra-ply Shear Properties of Uncured Prepreg Tapes," *Science and Engineering of Composite Materials*, vol. 27, no. 1, pp. 89–96, 2020, doi: 10.1515/secm-2020-0009.

Conferences

[K1] J. Krollmann, D. Colin, Avila Gray L., S. Zaremba, and K. Drechsler, "Bending characterization of axis and off-axis fiber-reinforced hinges at large deflection," in *Society for the Advancement of Material and Process Engineering 2016 (SAMPE)*, Long Beach, CA, 2016.

[K2] D. Colin, T. N. Hans, and S. Bel, "A Numerical Framework to Quantify the Influence of the Material Behavior of Dry Textiles on the Preform Quality," in *SAMPE Europe Conference 2021*, Baden/Zürich, Switzerland, 2021. (submitted)

[K3] D. Colin, S. Bel, T. Hans, and M. Hartmann, "On the inter-stitch interaction in biaxial non-crimp fabrics," in *PROCEEDINGS OF THE 21ST INTERNATIONAL ESAFORM CONFERENCE ON MATERIAL FORMING: ESAFORM 2018*, Palermo, Italy, 2018, p. 20004.

[K4] D. Colin, S. Bel, T. Hans, and M. Hartmann, "Towards a Virtual Characterization of a Biaxial Non-Crimp Fabric," in *18th European Conference on Composite Materials (ECCM18)*, Athens, Greece, 2018.

[K5] D. Colin, S. Bel, T. Hans, and M. Hartmann, "Virtual Description of a Biaxial 0/90° Non-Crimp Fabric with Normally Distributed Filament Directions," in *22nd International Conference on Material Forming (ESAFORM 2019)*, Vitoria-Gasteiz, Spain, 2019.

[K6] K. Heller, M. Hallmannseder, D. Colin, K. Kind, K. Drechsler, "Comparing Test Methods for the Deformation Behavior of Uncured Prepreg Tapes.", in *Concordia Centre for Composites (CONCOM) (Ed.): The Fourth International Symposium on Automated Composites Manufacturing, ACM4*, Montreal, Canada, 2019.

[K7] M. Feuchtgruber, D. Colin, S. Zaremba, K. Drechsler, “Modeling thermal behaviour of cooling channels in big area additive manufactured structures”, in *SAMPE Europe Conference 2020*, Amsterdam, Netherlands, 2020.

[K8] A. J. Imbsweiler, Y. Shinoura, D. Colin, S. Zaremba, K. Drechsler, “Optimization of the determination of Kamal’s parameters in SMC Process simulation.”, in *SAMPE Europe Conference 2020*, Amsterdam, Netherlands, 2020.

C Supervised student theses

During my employment at the Chair of Carbon Composites of the Technical University of Munich (TUM-LCC) I supervised the following student theses:

[S1] J. Hornung, “Entwicklung eines biaxialen Kohlenstofffasergeleges für Sichtanwendungen mit Hexagonalstich und optimierten Drapiereigenschaften” Master's Thesis in cooperation with SGL Automotive Carbon Fibers GmbH & Co. KG, Chair of Carbon Composites, TUM, 2017.

[S2] S. Bichlmaier, “Materialcharakterisierung eines trockenen Geleges für die Entwicklung von numerischen Drapiermodellen”, Term Project (Semesterarbeit), Chair of Carbon Composites, TUM, 2018

[S3] S. Bichlmaier, “Validation of Forming Simulations Applied to Non-Crimp Fabric Dry Carbon Fiber Reinforcement”, Master's Thesis, Chair of Carbon Composites, TUM, 2019.

[S4] Lennart Frey, “Development of a New Test Bench to Characterize the Bending Behaviour of Reinforcement Textiles for Forming Process Simulations”, Term Project (Semesterarbeit), Chair of Carbon Composites, TUM, 2019.

[S5] K. Krastev, “Simulation and Improvement of a Test Bench for the Characterization of the Bending Behavior of Reinforcement Textiles for Forming Process Simulation”, Term Project (Semesterarbeit), Chair of Carbon Composites, TUM, 2020.

[S6] Y. Chen, “Validation of Forming Simulations with Quantifiable Criteria Applied to Dry Carbon Fiber Reinforcements”, Bachelor's Thesis, Chair of Carbon Composites, TUM, 2020.

[S7] Y. Zhou, “Reduction of Forming Process Induced Defects of Non-Crimp Fabrics with Numerical Optimization”, Master's Thesis, Chair of Carbon Composites and Professur für Computational Mechanics, TUM, 2018.

[S8] M. R. Winastwan, “Numerical Implementation of Bending Stiffness for Compaction Behavior of Non-Crimp Fabrics”, Master's Thesis, Chair of Carbon Composites and Professur für Computational Mechanics, TUM, 2019.

[S9] I. Haider, “Sensitivity Analysis and Surrogate Modeling of Compaction Behavior of Dry Non-Crimp Fabrics with the Inclusion of Bending Stiffness”, Master's Thesis and Professur für Computational Mechanics, Chair of Carbon Composites, TUM, 2020

[S10] A. Janakiraman, “Convergence Analysis Applied to Virtual Shear Characterization of Non-Crimp Fabrics at the scale of filaments,” Master's Thesis, Chair of Carbon Composites, TUM, 2020.

[S11] S. Wiesnet, “Untersuchung von Faserrichtungsänderungen bei Heissumformungen von CFK Bauteilen”, Term Project (Semesterarbeit) in cooperation with Automation W+R GmbH, Chair of Carbon Composites, TUM, 2017.

[S12] I. Küçük, “Simulation of the Forming Process of Non-Crimp Fabrics”, Master's Thesis, Chair of Carbon Composites and Professur für Computational Mechanics, TUM, 2018.

[S13] E. Helfrich, “Entwicklung einer Methode zur Kalibrierung und Validierung von Simulationsansätzen zur Umformsimulation vorimprägnierter FVK-Halbzeuge,” Master's Thesis in cooperation with Voith Composites GmbH & Co. KG, Chair of Carbon Composites, TUM, 2018.

[S14] S. Wiesnet, “ Konzept eines Referenzverfahrens zur Bestimmung der Genauigkeit von Faserrichtungsbestimmungsmethoden und mögliche Anwendung in der algorithmischen Optimierung der Erkennung”, Master's Thesis in cooperation with Automation W+R GmbH, Chair of Carbon Composites, TUM, 2019.

[S15] M. Feuchtgruber, “Development of a thermal simulation of a 3D printed RTM mould for aerospace industry”, Master's Thesis, Chair of Carbon Composites, TUM, 2019.

[S16] L. Frey, “Entwicklung einer sich definiert über eine aerodynamische Druckbelastung verformbaren Frontspoilerlippe mithilfe eines Hybridmaterials aus Faserverbund und Elastomer”, Master's Thesis in cooperation with BMW M GmbH, Chair of Carbon Composites, TUM, 2020.

[S17] M. Mayerhofer, “Entwicklung und Implementierung einer adaptiven graphenbasierten Entwurfssprache zur Auslegung und Dimensionierung eines Leichtbaubiegebalkens”, Bachelor's Thesis in cooperation with Fraunhofer IGCV, Chair of Carbon Composites, TUM, 2021.

Parts of the above listed theses contributed to the underlying doctoral dissertation, as indicated in the text.